Hindustan College of Science and Technology
Farah-Mathura

(AICTE approved & affiliated to AKTU)

Key Indicator 3.1

Resource Mobilization for Research

Metric 3.1.1

Grants received from Government and non-governmental agencies for research projects / endowments in the institution during the last five years

Grants received from Government and non-governmental agencies for research projects / endowments in the institution during the last five years (INR in Lakhs)

Name of the research project / endowment	Name of the Principal Investigator/ Co-investigator	Department of Principal Investigator	Year of Award	Amount Sanctioned (INR in Lakhs)	Duration of the project	Name of the Funding Agency	Type (Government / non-Government)
Elaboration nanocomposites coating based on carbonaceous materials for active components of gas sensing system	Dr. M.S. Gaur	Department of Physics	2018	11.24	3 Years	Indo-Belarus Cooperation in Science and Technology, Sanctioned by DST New Delhi	Government
Development of novel epoxy resin/graphene nanocomposite coating material for aircraft structures	Dr. M.S. Gaur / Dr. R. K. Tiwari	Department of Physics	2019	11.50	3.8 Years	DRDO, Aeronautics R & D Board, New Delhi	Government
Development of test methods for control of heavy metals in water for environmental monitoring	Dr. M.S. Gaur	Department of Physics	2019	31.82	2 Years	DST-Russian Science Foundation (RSF) sanctioned by DST New Delhi	Government

Hindustan College of Science and Technology
Farah-Mathura
(AICTE approved & affiliated to AKTU)

Project: I

Elaboration Nano-composites coating based on carbonaceous materials for active components of gas sensing system

Sanctioned Agency:

(DST, India - Skorina State University, Belarus)

Sanctioned letter

Government of India
Ministry of Science and Technology
Department of Science & Technology
(International Bilateral Cooperation Division)

Technology Bhavan, New Mehraulli Road
New Delhi-110016

DST/INT/BLR/P-13/2016 Date: 29.08.2018

ORDER

Subject: Implementation of Indo- Belarus Joint project entitled: **"Elaboration nanocomposite coatings based on carbonaceous materials for active components of gas monitoring system"** coordinated by **Dr. M.S. Gaur,** Department of Physics, Hindustan College of Science and Technology, Mathura - regarding.

Sanction of the President is hereby accorded for incurring an expenditure not exceeding **Rs. 11,24,000/- (Rupees Eleven Lakh and Twenty four Thousand only)** for implementation of the Indo- Belarus joint project entitled "Elaboration nanocomposite coatings based on carbonaceous materials for active components of gas monitoring system" coordinated by **Dr. M.S. Gaur,** Department of Physics, Hindustan College of Science and Technology, Mathura with **Prof. Cor. Mem. A.V.** Rector of Francisk Skorina, Gomel State University Belarus for a total duration of Three years from the date of issue of the Sanction Order. The detailed breakup of the grant for General as well as Capital Components are given below:-

General Component	:	Rs. 11,24,000/-
Capital Component	:	Rs. NIL

2. As per the terms and conditions, agreed by both side, under the project the sending side will bear the cost related to the International air travel, medical insurance and visa charges whereas the receiving side shall bear the cost of accommodation, hospitality and local travels of the visiting scientist. The break-up of approved expenditure is as indicated below :

Item of Expenditure	Amount		
	1st year	2nd year	3rd year
1. Mobility of scientists Two visits each side each year			
• For visit of Indian scientists to Belarus	1,74,000	1,74,000	1,74,000
• For visit of Belarus Scientists to India (as calculated below in para 3 and 4 below)	1,44,000	1,44,000	1,44,000
2. Consumables	50,000	30,000	20,000
3. Contingency	20,000	20,000	20,000
Year wise Cost	3,88,000	3,68,000	3,58,000
Overhead 10% on consumable	5,000	3,000	2,000
Total Year wise Cost	3,93,000	3,71,000	3,60,000
Grand Total	Rs 11,24,000/-		

Director
Hindustan College of
Science & Technology
FARAH (MATHURA)

3. Sanction of the President is hereby accorded for release of 1st instalment amounting of **Rs. 3,93,000/- (Rupees Three Lakh and Ninety Three Thousand only)** to the grantee Institute. The amount of grant will drawn by the Drawing and Disbursing Officer, DST and will be disbursed to **Hindustan College of Science and Technology, Mathura**. The bank details for electronic transfer of funds through RTGS are given below:-

Account Holders name/ designation	Hindustan College of Science and Technology, Mathura
Name of Bank	Punjab National Bank
Bank Account Number	1841002100004382
IFSC Code	PUNB0184100
E-Mail	mulayamgaur@rediffmail.com

Condition for placing of grant amount :

4. All interest or other earnings against Grant-in-aid or advances (other than reimbursement) released to any grantee institution should be mandatorily remitted to the Consolidated Fund of India immediately after finalization of the accounts. Such advances should not be allowed to be adjusted against future releases.

Conditions for submission of SE/UC and Progress report:

5. (a) the grantee organisation will furnish to the Department of Science & Technology, financial year wise Utilization Certificate (UC) in the proforma prescribed as per GFR 2017 and audited statement of expenditure (SE) along with up to date progress report at the end of each financial year duly reflecting the interest earned / accrued on the grants received under the project. This is also subject to the condition of submission of the final statement of expenditure, utilization certificate and project completion report within one year from the scheduled date of completion of the project.

(b) While submitting Utilisation Certificate/Statement of Expenditure, the organisation has to ensure submission of supporting documentary evidences with regard to purchase of equipment/capital assets as per the provisions of GFR 2017. Subsequent release of grants under the project shall be considered only on receipt of the said documents.

(c) a transparent procurement procedure in line with the Provisions of General Financial Rules 2017 will be followed by the Institute/ Organisation under the appropriate rules of the grantee organisation while procuring capital assets sanctioned for the above mentioned project and a certificate to this effect will be submitted by the Grantee organisation immediately on receipt of the grant;

6. The grantee organisation will have to enter & upload the Utilization Certificate in the PFMS portal besides sending it in physical form to this Division. The subsequent/final instalment will be released only after confirmation of the acceptance of the UC by the Division and entry of previous Utilization Certificate in the PFMS.

7. In the event grant has been released under capital head through separate sanction order under the same project for purchase of equipment(s), separate SE/UC has to be furnished for the released Capital head grant.

Conditions of Assets (if any) :

8.(a) DST reserves sole rights on the assets created out of grants. Assets acquired wholly or substantially out of government grants (except those declared as obsolete and unserviceable or condemned in accordance with the procedure laid down in GFR 2017), shall not be disposed of without obtaining the prior approval of DST.

Director
Hindustan College of
Science & Technology
FARAH (MATHURA)

(b) The equipment/instrument shall have to be purchased within twelve months from the date of release of the capital grant. Fresh permission shall have to be sought from DST, in the event, the Institute fails to purchase the equipment/instrument within the prescribed period of twelve months from the date of release of sanctioned amount.

Conditions for International Visits :

9. All project related visits to be undertaken by the Scientists from either side in connection with the implementation of the project shall require prior approval from this Department separately on a case to case basis before any expenditure is incurred in this regard.

10. As per MoF instructions, it has been decided that in all cases of air travel, both domestic and international, where the Government of India bears the cost of air passage, the officials concerned may travel only by Air India. For travel to stations not connected by Air India, the officials may travel by Air India to the hub/point closest to their eventual destination, beyond which they may utilize the services of another airline which should also preferable be an alliance partner of Air India.

Other Conditions:

11. The account of the grantee organisation shall be open to inspection by the sanctioning authority and audit (both by C&AG of India and Internal Audit by the Principal Accounts Office of the DST), whenever the organisation is called upon to do so, as laid down under Rule 236(1) of General Financial Rules 2017.

12. Due acknowledgement of technical support / financial assistance resulting from this project grant should mandatorily be highlighted by the grantee organisation in bold letters in all publications / media releases as well as in the opening paragraphs of their Annual Reports during and after the completion of the project.

13. In case the scheme provides for payment of honorarium / remuneration / fellowship / scholarship to the PI, a para may suitably be incorporated in the DSO to the effect that "PI is not drawing any emoluments/ salary/ fellowship from any other project either supported by DST or by any other funding agency.

14. **Failure to comply with the terms and conditions of the sanction order will entail full refund with interest in terms of Rule 231 (2) of GFR 2017.**

15. The expenditure involved is debitable to Demand No.84, Department of Science & Technology for the year 2017-18:

3425 : Other Scientific Research (Major Head)
60 : Others
60.798 : International Cooperation (Minor Head)
14 : Research & Development
14.00.31 : Grants-in-aid General for the year 2017-18 (Plan)
(**Previous** : ICD-3425.60.798.12.00.31)

16. This sanction order being 1st instalment for implementation of this project, no SE/UC is due from the grantee institution against this project.

17. This issues with the concurrence of IFD vide their concurrence Dy. No. **C/2097 /IFD 2017-18 dated 14.08.2018.**

18. As per Rule 234 of GFR 2017, this sanction has been entered at S. No. ...154....in the register of grants maintained in the Division.

19. NGO Darpan portal ID. UP/2017/0116810

(Rajiv Kumar)
Scientist 'E'

Director
Hindustan College of
Science & Technology
FARAH (MATHURA)

To,

The Pay & Accounts Officer,
Department of Science & Technology,
New Delhi-110016

Copy to:

1. Office of the Principal Director of Audit, AGCR Bldg., IP Estate, New Delhi-110002
2. Cash Section (3 copies), DST
3. I.F. Division/Accounts Section, DST
4. Sanction Folder
5. Project File.
6. **Dr. M.S. Gaur,** Department of Physics, Hindustan College of Science and Technology, Mathura
7. **Registrar**, Department of Physics, Hindustan College of Science and Technology, Mathura
8. **Finance Officer**, Department of Physics, Hindustan College of Science and Technology, Mathura

(Rajiv Kumar)
Scientist 'E'

Break up of expenditure on each visit of Indian Scientists visiting collaborative Institute is calculated broadly as below:

a. International Fare Delhi - Gomel and back By excursion economy class	Rs 70,000
b. Medical Insurance (Silver class)	Rs 2,000
c. Visa Fee (as per actuals)	Rs 5,000
d. Local Transport	Rs.10,000
Total:	Rs 87,000

4. Break up of expenditure on each visit of Belarus scientists and project staff visiting the Indian collaborative Institute (for an average duration of two weeks):

I. Per diem@ Rs 2500 *14 days	Rs 35,000
II. Accommodation @ Rs 2500 * 14 days	Rs 35,000
III. Local Transport	Rs 2,000
Total:	Rs 72,000

(Rajiv Kumar)
Scientist 'E'

Director
Hindustan College of
Science & Technology
FARAH (MATHURA)

DST/INT/BLR/P-13/2016
Government of India
Ministry of Science and Technology
Department of Science & Technology
(International Bilateral Cooperation Division)

Technology Bhavan, New Mehraulli Road
New Delhi-110016
Date: 16-09-19

ORDER

Subject: Release of 2nd installment

In continuation of orders of even number dated 29-08-18, sanction of the President is hereby conveyed for carry forward of the unspent balance of Rs. **1,93,726/- (Rupees One Lakh Ninety Three Thousand Seven Hundred Twenty Six Only)** from 2018-19 to 2019-20 for utilization by the grantee institution in connection with the implementation of the Indo-Belarus joint research project entitled "Elaboration .... monitoring systems" coordinated by Dr. M.S. Gaur, Hindustan college of Science and Technology, Mathura.

2. Sanction of the President is hereby accorded for release of 2nd instalment of Rs. **1,77,274/- (Rupees One Lakh Seventy Seven Thousand Two Hundred Seventy Four Only)** to Hindustan college of Science and Technology, Mathura. The amount of grant will drawn by the drawing and disbursing officer, DST and will be disbursed to Hindustan college of Science and Technology, Mathura. The bank details for electronic transfer of funds through RTGS are given below:

Account Holders name/ designation	Hindustan college of Science and Technology, Mathura
Name of Bank	Punjab National Bank
Bank Account Number	1841002100004382
IFSC Code	PUNB0184100
E-Mail	mulayamgaur@rediffmail.com

3. The terms and conditions as communicated earlier vide this Ministry's Sanction order of even number dated 29-08-18 shall remain unchanged and shall be applicable in the present sanction also.

Condition for placing of grant amount :

4. The grantee organisation will maintain separate audited account for the project and the entire amount of grant will be kept in an interest bearing account. For Grants released during F.Y. 2017-18 and onwards, all interest or other earnings against Grant shall be remitted to the Consolidated Fund of India (through Non-Tax Receipt Portal (NTRP), i.e. www.bharatkosh.gov.in), immediately after finalization of the accounts, as it shall not be allowed to be adjusted against future releases of grant. **A certificate to this effect shall have to be submitted along with Statement of Expenditure / Utilisation Certificate for considering subsequent release of Grant/ closure of Project accounts.**

Conditions for submission of SE/UC and Progress report:

5. (i) The grantee organisation will furnish to the Department of Science & Technology, financial year wise Utilization Certificate (UC) in the proforma prescribed as per GFR 2017 and audited statement of expenditure (SE) along with up to date progress report at the end of each financial year duly reflecting the interest earned / accrued on the grants received under the project. This is also subject to the condition of submission of the final statement of expenditure, utilization certificate and project completion report within one year from the scheduled date of completion of the project.

Director
Hindustan College of
Science & Technology
FARAH (MATHURA)

Hindustan College of Science and Technology
Farah-Mathura
(AICTE approved & affiliated to AKTU)

Project: I

Elaboration Nano-composites coating based on carbonaceous materials for active components of gas sensing system

Sanctioned Agency:

(DST, India - Skorina State University, Belarus)

Statement of Expenditure

Annexure-II

REQUEST FOR ANNUAL INSTALMENT WITH UP-TO-DATE STATEMENT OF EXPENDITURE

1. **Sanction Order No. and date:** DST/INT/BLR/P-13/2016 dated 29.08.2018
2. **Total Project Cost** : Rs. 11,24000/-
3. **Revised Project Cost (if applicable)** : NA
4. Date of Commencement : 29.08.2018
5. Statement of Expenditure :
   (Month wise expenditure incurred during current financial year)

Month & Year	Expenditure incurred/ Committed
01.04.2021 to 28.08.2021	Rs. 17,106/-

6. Grant received in each year:

a. 1st Year : Rs. 3,93,000/-
b. 2nd Year : Rs.1,77, 274/-
c. 3rd Year : Nil
d. Interest, if any: Rs.4,441/-(FY 2018-2019) + Rs.8, 355/- (FY 2019-2020) + Rs. 9,542/- (FY 2020-2021) +Rs.4,546/- (FY 2021-2022) = Rs. 26,884/- (Deposited)
e. Total (a+b+c+d): Rs. 5,97, 158/-

Statement of Expenditure

(to be submitted financial year wise i.e. DOS* to 31st March of that financial year say 2021-22, **(01.04.2021 to 28.08.2021)**

Sr. No. (I)	Sanctioned Heads (II)	Funds Allocated (indicate sanctioned or revised) (III)	Expenditure Incurred				Total Expenditure IV+V+VI+VII (VIII)	Balance as on (date) II–(IV+V+VI+VII) (IX)	Requirement of Funds up to 31st March next year X	Remarks (if any) XI
			Ist Year (*DOS to 31st March next year) (IV)	IInd Year (1st April to 31st March next year) (V)	IIIrd Year and so on (1st April to 31st March next year) (VI)	IVth Year and so on (1st April to 31st March next year) (VII)				
1.	Mobility of Scientists	9,54,000/-	1,61,885/-	71,420	Nil	Nil	2,33,305/-	7,20,695/-	Nil	
2.	Consumables	1,00000/-	37,338/-	11,820/-	51,106/-	Nil	100,264/-	–264*	Nil	*Excess of Rs. 264 /- is born by institute
3.	Contingency	60,000/-	53/-	12,543/-	32,298/- +	16,227/-	61,121/**-	–1,121**	Nil	**Excess of Rs. 1,121 /- is born by institute
4	Overhead	10,000/-		8000/-	Nil	2000/-	10,000/-	Nil	Nil	
6	Interest Earned	Rs. 4546 (FY 2021-22)								Refunde-d Rs. 4546/-
7.	Total	Rs. 11,24,000/-	Rs. 1,99,276/-	Rs. 1,03783/-	Rs. 83,404/-	Rs. 18,227 – Rs. 1121**/- = Rs. 17,106/-	Rs. 4,04,690 –Rs.264* – Rs.1.121** = Rs 4.03,305/-	Rs. 7,20,695/-	Nil	Refunded Rs. 1.66.969/-

For Hindustan College of Science & Technology

Name and Signature of Principal Investigator:
Date: 12.03.2022

12/03/2022
Account officer
PAWAN KUMAR GOYAL

(with seal)

Signature of Competent financial authority:
Date: CA Deepa Khanna
FRN 013795C
AGRA
12/03/2022

*DOS-Date of start of project

Note:Expenditure under the sanctioned heads, at any point of time, should not exceed funds allocated under that head. without prior approval of DST i.e. Figures in Column (VIII) should not exceed corresponding figures in Column (II).

1.Utilisation Certificate (Annexure III) for each financial year ending 31st March has to be enclosed along with request for carry forward permission to the next year.

Hindustan College of Science and Technology
Farah-Mathura
(AICTE approved & affiliated to AKTU)

Project: I

Elaboration Nano-composites coating based on carbonaceous materials for active components of gas sensing system

Sanctioned Agency:

(**DST, India - Skorina State University, Belarus**)

Utilization Certificate

Annexure-III

UTILISATION CERTIFICATE (2 COPIES)
FOR THE FINANCIAL YEAR – (ENDING 31ST MARCH)

1. **Title of the Project/ Scheme:** "Elaboration nanocomposites coatings based on carbonaceous materials for active components of gas monitoring system"
2. **Name of the Institution:** Hindustan College of Science & Technology, Farah, Mathura-281122.
3. **Principal Investigator:** Dr. M. S. Gaur, Professor, Department of Physics
4. **Department of Science & Technology sanction order No & Date sanctioning the project:** DST/INT/BLR/P-13/2016 dated 29.08.2018
5. **Head of account as given in the original sanction order:**

S. No.	Budget Head	Original sanction Amount in Rs.
1.	Mobility of Scientists	Rs. 9,54,000/-
2.	Consumables	Rs. 1,00000/-
3.	Contingency	Rs. 60,000/-
4	Overhead	Rs. 10,000/-
Total		Rs. 11,24,000/-

6. **Amount brought forward from the previous Financial year quoting DST letter no and date in which authority to carry forward the said amount was given :**
    - i. Amount: Rs.1,84,075/-
    - ii. Letter No :
    - iii. Date :
7. **Amount received during the financial year (Please give DST letter/order no and date):**
    - i. Amount : Rs. Nil
    - ii. Letter No. : Nil
    - iii. Date : Nil
8. **Interest earned:** Rs. 4,546/- *(Deposited in Bharatkosh)*
9. **Total amount that was available for expenditure (excluding commitments) during the financial year (Sr. No. 6+7+8):** Rs. 1,84,075/- + Rs. 4,546/- *(Deposited in Bharatkosh)* = Rs. 1,84,075/-
10. **Actual Expenditure (excluding commitments) Incurred during the financial year (upto 31st March):** Rs. 17,106/-
11. **Balance amount available at the end of the financial year:** Rs.1,66,969/-
12. **Unspent balance refunded, if any (please give details of cheque no etc.) :** Rs,1,66,969/-
13. **Amount to be carried forward to the next financial year (if applicable): NA**
    - i. Amount : Nil
    - ii. Letter No. Nil
    - iii. Date: Nil

12/03/2022

UTILISATION CERTIFICATE

Certified that out of Rs. 1,77, 274/- of grants-in-aid sanctioned during the year 2019-2020 in favour of The Director, HCST, Farah, Mathura under this Ministry/ Department letter/ order No. DST/INT/BLR/P-13/2016 dated 16.09.2019 and Rs. 1,93,724 /- on account of unspent balance of the previous year (2018-2019), a sum of Rs. 1,03783/- has been utilised in 2019-2020 for the purpose of project for which it was sanctioned. A sum of Rs.2,67,215/- is available for FY 2020-2021, a sum of Rs. 83,140/ has been utilised for the purpose of project for which it was sanctioned. A sum of Rs. 1,84,075/- is available for FY 2021-2022, a sum of Rs. 17,106/- has been utilised for the purpose of project for which it was sanctioned and balance of Rs.1,66,969/- is refunded back to DST.

Hindustan College of Science & Technology
12/03/2022 Account Officer

Signature of PI　Signature of Director　Accounts Officer of the Institute

Date 12.03.2022　Date 12.03.2022　Date 12/03/2022

(To be filled in by DST)

Certify that I have satisfied that the conditions on which the grants-in-aid was sanctioned have been fulfilled/ are being fulfilled and that I have exercised the following checks to see that the money was actually utilized for the purpose for which it was sanctioned:-

Kinds of checks exercised.

1.
2.
3.
4.
5.

Signature:____________
Designation:____________
Date:____________

Hindustan College of Science and Technology
Farah-Mathura
(AICTE approved & affiliated to AKTU)

Project: I

Elaboration Nano-composites coating based on carbonaceous materials for active components of gas sensing system

Sanctioned Agency:

(DST, India - Skorina State University, Belarus)

Project Outcomes (Publications)

List of Publications (Joint Project)

Entitled “Elaboration Nanocomposite coatings based on carbonaceous materials for active components of gas monitoring system”

Department of Science and Technology, New Delhi – Franciska Skronia, Gomel State University, Belarus

S.No.	Name of the author	Title of the article	Name of the journal	Year of publication	Issue	Pages	Impact factor	ISSN No.	*Web link*
1	Rohan Sagar, MS Gaur, AA Rogachev	Nanoarchitecture of PANI/CNT/GO hybrid nanocomposites with enhanced dielectric and gas sensing properties	Polymer Bulletin (Springer)	2022	1	22	2.87	0170-0839	https://doi.org/10.1007/s00289-022-04127-z
2	Rohan Sagar, MS Gaur, AA Rogachev	Piezoelectric and pyroelectric properties of ceramic nanoparticles-based nanostructured PVDF/PVC blend nanocomposites	Journal of Thermal Analysis and Calorimetry (Springer)	2020	2	645-655	4.67	1388-6150	https://doi.org/10.1007/s10973-020-09979-z
3	Rohan Sagar, MS Gaur, Vinod Kushwah, Aakash Rathore, DG Piliptsou, AA Rogachev	Preparation, characterization and micro hardness measurements of hybrid nanocomposites based on PMMA+P(VDF-TrFE) and graphene oxide,	Polymer Bulletin (Springer),	2020	12	7279-7300	2.87	0170-0839	https://doi.org/10.1007/s00289-020-03457-0
4	Mamta Kushwah, Rohan Sagar, AA Rogachev, MS Gaur	Dielectric, pyroelectricand polarizationbehaviorofpolyvinylidene fluoride (PVDF) –Gold nanoparticles (AuNPs) nanocomposites	Vacuum, Elsevier,	2019	1	298-306	3.67	0042-207X	https://doi.org/10.1016/J.VACUUM.2019.05.010

Home > Polymer Bulletin > Article

Original Paper | Published: 04 March 2022

Nanoarchitecture of PANI/CNT/GO hybrid nanocomposites with enhanced dielectric and gas sensing properties

Rohan Sagar, M. S. Gaur & A. A. Rogachev

Polymer Bulletin **80**, 1773–1793 (2023)

328 Accesses | Metrics

Abstract

The polyaniline (PANI) and PANI/carbon nanotubes (CNT)/graphene oxide (GO) thin film were prepared in indium tin oxide coated glass plate by spin coating method. The molecular structure and physical properties of PANI and its hybrid nanocomposites were characterized by UV–Vis spectra, field emission scanning electron microscope (FE-SEM) and atomic force microscopy (AFM). UV–Vis spectra show the agreement with formation of π–π^* electron interaction between PANI and CNT/GO. This interaction causes the decrease of bandgap due to confinement of the electrons and holes. The FE-SEM and AFM image of hybrid nanocomposites is different than PANI due to globular morphologies in the presence of CNT and GO. The surface free energy of PANI and hybrid nanocomposites thin films was analyzed by measuring contact angles. The dielectric permittivity and tangential loss (tan δ) of hybrid nanocomposites with different frequency were investigated at room temperature. The incorporation of CNT and GO in PANI matrix possesses high dielectric constant, low dielectric loss and high energy density. The excellent C_3H_6O gas sensing performance of PANI/CNT/GO hybrid nanocomposites thin film may be attributed to more oxygen vacancies and narrower bandgap. The response of PANI/CNT/GO sensor was four times better than PANI sensor with the recovery time of 506 s.

Data availability

The data that support the findings of this study are available from the corresponding author on request.

References

1. Moliton A, Hiorns RC (2004) Review of electronic and optical properties of semiconducting p-conjugated polymers: applications in optoelectronics. Polym Int 53:1397–1412. https://doi.org/10.1002/pi.1587

2. Patil YS, Salunkhe PH, Navale YH, Ubale VP, Patil VB, Maldar NN, Ghanwat AA (2018) Synthesis, characterization and conductivity study of co-polyazomethine polymer containing thiazole active ring. AIP Conf Proc 1989:020034. https://doi.org/10.1063/1.5047710

3. Yan B, Zhang W, Qin X, Piao Y (2020) Salt powder assisted synthesis of nanostructured materials and their electrochemical applications in energy storage devices. Chem Eng J 400:125895. https://doi.org/10.1016/j.cej.2020.125895

4. Prateek VK, Thakur RK (2016) Recent progress on ferroelectric polymer-based nanocomposites for high energy density capacitors: synthesis, dielectric properties and future aspec. Chem Rev 116:4260–4317. https://doi.org/10.1021/acs.chemrev.5b00495

5. Vijayalakshmi S, Nithya S (2020) Investigation on polyaniline with manganese dioxide nanostructure by using an in situ oxidative

63. Liu C, Tai HL, Zhang P, Su YJ, Jiang YD (2017) Enhanced ammonia-sensing properties of PANI-TiO_2-Au ternary selfassembly nanocomposite thin film at room temperature. Sens Actuators B Chem 246:85–95. https://doi.org/10.1016/j.snb.2017.01.046

64. Huang X, Hu N, Gao R, Wang Y, Wei H, Zhang Y (2012) Reduced graphene oxide–polyaniline hybrid: preparation, characterization and its applications for ammonia gas sensing. J Mater Chem 22:22488–22495. https://doi.org/10.1039/C2JM34340A

65. Bai X, Ji H, Gao P, Zhang Y, Sun X (2014) Morphology, phase structure and acetone sensitive properties of copper-doped tungsten oxide sensors. Sens and Actuators B: Chem 193:100–106. https://doi.org/10.1016/j.snb.2013.11.059

66. Kulkarni S, Patil P, Naik J (2018) Synthesis and evaluation of gas sensing properties of PANI, PANI/SnO_2 and PANI/SnO_2/rGO nanocomposites at room temperature. Inorg Chem Commun 96:90–96. https://doi.org/10.1016/j.inoche.2018.08.008

67. Gaikwad G, Patil P, Patil D, Naik J (2017) Synthesis and evaluation of gas sensing properties of PANI based graphene oxide nanocomposites. Mater Sci Eng B 218:14–22. https://doi.org/10.1016/j.mseb.2017.01.008

Acknowledgements

We gratefully acknowledge the financial support of Indo–Belarus joint project (Project no. DST/INT/BLR/P-13/2016) by Department of Science and Technology (DST), New Delhi (India). One of the authors Rohan Sagar acknowledge the University Grant Commission (UGC), New Delhi (India), for a providing research fellowship (Award number RGNF-2017-18-SC-UTT-29088).

Author information

Authors and Affiliations

Department of Physics, Hindustan College of Science and Technology (Affiliated to Dr. A.P.J. Abdul Kalama Technical

University, Lucknow, U.P. 226031, India), Farah, Mathura, Uttar Pradesh, 281122, India

Rohan Sagar & M. S. Gaur

Francisk Skorina Gomel State University, Sovetskaya, Str. 104, 246019, Gomel, Republic of Belarus

A. A. Rogachev

Corresponding author

Correspondence to M. S. Gaur.

Ethics declarations

Conflict of interest

The authors declare that they have no conflicts of interest.

Additional information

Publisher's Note

Rights and permissions

Reprints and Permissions

About this article

Cite this article

Sagar, R., Gaur, M.S. & Rogachev, A.A. Nanoarchitecture of PANI/CNT/GO hybrid nanocomposites with enhanced dielectric and gas sensing properties. *Polym. Bull.* **80**, 1773–1793 (2023). https://doi.org/10.1007/s00289-022-04127-z

Received
07 May 2021

Revised
09 December 2021

Accepted
02 February 2022

Published
04 March 2022

Issue Date
February 2023

DOI
https://doi.org/10.1007/s00289-022-04127-z

Keywords

Polyaniline **FE-SEM** **Atomic force microscopy**

Journal of Thermal Analysis and Calorimetry
https://doi.org/10.1007/s10973-020-09979-z

Piezoelectric and pyroelectric properties of ceramic nanoparticles-based nanostructured PVDF/PVC blend nanocomposites

Rohan Sagar[1] · **M. S. Gaur**[1] · **A. A. Rogachev**[2]

Received: 7 January 2020 / Accepted: 20 June 2020

Abstract

$BaZrO_3$ and $BaTiO_3$ nanofillers were incorporated in pristine PVDF and pristine PVC blend matrix separately to prepare blend nanocomposites using the solution casting technique. The mass ratios of PVDF/PVC/$BaTiO_3$ were chosen to be 80/16/4. The structure morphology of nanocomposites was analyzed by Fourier transform infrared spectroscopy (FTIR), atomic force microscopy (AFM), and X-ray diffraction. The FTIR, AFM, XRD and pyroelectric results indicate the strong interaction between the nanofiller and PVDF/PVC blend matrix. The nanocomposite exhibits a high pyroelectric coefficient due to proper dispersion of nanofillers. The maximum piezoelectric coefficients (d_{33}) were 39, 88, 79.72, 112pC N^{-1} for pristine PVC, pristine PVDF, PVDF/PVC/$BaZrO_3$ and PVDF/PVC/$BaTiO_3$ blend nanocomposites, respectively. The remnant polarization of blend nanocomposites is also measured by *P–E* loop. *P–E* loop shows that the polarization of the blend nanocomposites increases under influence of nanofiller. The pyroelectric coefficient for PVDF/PVC/nanofiller blend nanocomposite is very sensitive in the temperature range of 30 to 180 °C and greater than PVC (i.e. $351\ \mu C\ m^{-2}\ K^{-1} > 15\ \mu C\ m^{-2}\ K^{-1}$).

Keywords FTIR · XRD · AFM · Piezo-/pyroelectric coefficient · *P–E* loop · Blend polymer nanocomposite

Introduction

The pyroelectric and piezoelectric properties of ferroelectric materials are depending upon the structure and internal polarization of the material. These materials are intrinsically multifunctional and have found a broad range of applications [1–3]. The fluoro polymers are most suitable candidate for this purpose [4]. The fluoro polymer like PVDF and its copolymer offer several benefits in micro- and nanosystem due to large molecular motion that can be respond with low hysteresis and high-available energy densities. This class of polymers possesses unique properties including sensing ability of different stimuli [5, 6].

This new class of nanocomposites material may have excellent properties as compare to traditional materials such as polymers, single crystals, and ceramics. PVDF and PVC have unusual properties and widely used in industrial applications because they possesses favorable chemical, mechanical and electroactive properties with biocompatibility. The combination of pyroelectric and piezoelectric properties of $BaZrO_3$ and $BaTiO_3$ nanofiller make it interesting in nonlinear optics, miniaturized organic electronic devices, etc.

This class of polymer (fluoro polymers) distinguish themselves with a high bandwidth, high frequency, low-power requirements, fast response, and high-generative forces. Therefore, they qualify the properties for actuators and sensors applications [7, 8]. Other environmental effects such as humidity, temperature, and others cannot effect the performance of these materials. Several publications in the field of nanocomposite material are appeared in recent years [9]. The dispersion of nanoparticle is the big problem with two polymer matrix. But hybrid system of two or more than one polymer could be able to bind the nanoparticles in different interfaces by increasing van der Waals interaction. The application of polyvinylidene fluoride (PVDF) cannot be applied as a piezoelectric/pyroelectric sensor without

---

✉ M. S. Gaur
mulayamgaur@rediffmail.com

[1] Department of Physics, Hindustan College of Science and Technology, Farah, Mathura, U.P. 281122, India affiliated to Dr. A.P.J. Abdul Kalama Technical University, Lucknow, U.P. 226031, India

[2] Francisk Skorina Gomel State University, Sovetskaya Str. 104, 246019 Gomel, Republic of Belarus

enhancing their respective properties by incorporation of nanofillers.

PVDF and PVC are one of the most important polymers for various electronics and optoelectronic device applications [10] because of their excellent transparency and thin-film-forming ability. Owing to these merits, large numbers of research groups are exploring the chemistry of PVDF/PVC in order to improve its pyroelectric coefficient. The pyroelectric properties of PVDF/PVC could be improved by introducing nanofillers [11]. The addition of PVC into PVDF can enhance the flexibility and durability of the blend thin films [12]. In this study, PVC is blended with PVDF which renders the formation of free-standing thin film. $BaTiO_3$ and $BaZrO_3$ have some superior properties such as high ion-exchange and high adsorption capacity. It can absorb large quantities of vapor, such as DMF, at low partial pressures [13]. This allows the formation of nanonetwork in polymer matrix.

$BaTiO_3$ and $BaZrO_3$ nanofillers are the most favorable nanofillers for polymers due to the highly ordered porous structure with very small size. In the present work, $BaZrO_3$ and $BaTiO_3$ with different concentrations have been used as nanofiller for PVDF/PVC matrix. PVDF/PVC/nanofiller blend nanocomposites were prepared using simple solution casting technique. The nanocomposites were characterized using different analytical techniques including FTIR and piezo–pyroelectric coefficient. The main purpose of this study is to compare the pyroelectric response and structural properties of PVDF/PVC/$BaZrO_3$ and PVDF/PVC/$BaTiO_3$ blend nanocomposite thin films.

Experimental

Materials and methods

PVDF and PVC of molecular weight (Mw) 64.03 g mol^{-1} and 62.50 g mol^{-1}, respectively, were procured from redox (India). $BaZrO_3$ and $BaTiO_3$ nanoparticles of size < 100 nm with 98.5% trace metals basis from Sigma-Aldrich have been used in the present study. The analytical-grade Merck (99% pure) *N-N*-dimethylformamide (DMF) was used as a solvent for preparation of blend nanocomposite thin film.

The PVDF and PVC of mass ratio 4:1 were taken and dissolved in dimethylformamide (DMF). $BaZrO_3$ and $BaTiO_3$ were also dissolved in DMF. The solution of nanopartical (i.e. $BaZrO_3$, $BaTiO_3$) was added to the polymer solution drop by drop. Then the solution was stirred with sonicator at frequency of 20 kHz and power of 100 W for 15 min before. The mixture was cast to a glass petri dish and kept in vacuum oven at temperature of 60 °C for 2 h. After 2 h, oven was switched off, and samples remained inside the oven for 24 h. After drying, the samples were peeled from the petri dishes. The dried samples were subjected to room temperature in vacuum oven outgassing at 10^{-5} torr for a further period of 24 h to remove any residual solvent. The thickness of samples was observed to be in the range of 50–100 µm. The aluminum electrode of diameter 2.5 cm was prepared in both surface of sample using vacuum coating unit (Model no, VEQCO Delhi, India) for measurement of pyro- and piezoproperties.

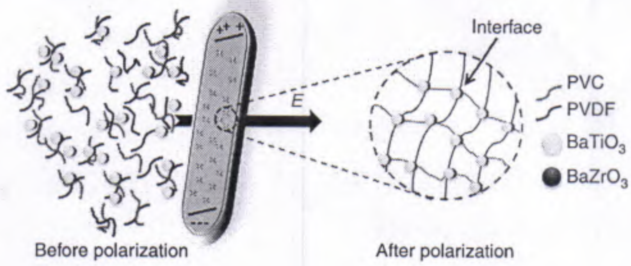

Fig. 1 Schematic diagram for polarization of blend nanocomposites

Polarization process

The both-side-aluminized nanocomposite samples were thermally poled according to method reported in the literature [14]. The detailed theoretical model to understand the polarization of polymer-ceramic nanocomposites is reported in the literature [15, 16]. According to this model the induce piezoelectricity and pyroelectricity within a polymer-ceramic composite, a strong electric field is applied to the sample, to orient the dipoles in each phase (i.e. polymeric and ceramic phase). However, since the ceramics has a much larger permittivity than the polymer, the electric field is greatly reduced in the ceramic phase. The polarization of polymer-ceramic nanocomposites samples at elevated temperature causes the accumulation of space charges at polymer-ceramic interface. Thus, internal field increases in the ceramics phase and removes the discontinuity of electric displacement at the interface. The polarization process of blend nanocomposite is schematically shown in Fig. 1.

Result and discussion

Mechanism of formation of blend nanocomposites

The fluoromethyl group ($–CF_3$) in PVDF and Cl group in PVC differentiated their chemical structure. The chemical structures of PVDF, PVC, and both nanoparticles are shown in Fig. 2. In general, PVDF has the highest thermal stability due to its regular packing of $–CF_2$ crystalline unit driven by

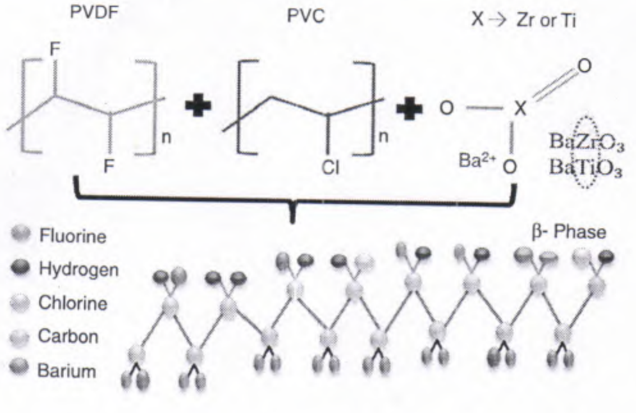

Fig. 2 Schematic representation of the chain conformation for the β-phases of blend nanocomposite

the mutual repulsion of adjacent fluorine atoms. PVDF has high molecular weight and infinite melt viscosity, however, PVC can be broken down into different scales at different temperatures. This structure of PVC is not suitable for ferroelectric. On the other hand, the bulk group of $-CF_3$ in PVC disturbs crystalline packing to main chain and increases amorphous fraction. Additionally, $-CF_3$ group can be considered as defects in the crystallites.

PVC and PVDF interact via the formation of a hydrogen bond between the carbonyl group of PVC and hydroxyl group of PVDF. The miscibility between the two polymers can be attributed to the existence of this hydrogen bonding interaction with nanoparticles (i.e. $BaZrO_3$ and $BaTiO_3$). The amorphism of PVDF takes place with the engagement of PVDF and PVC segments along the periphery of spherules phases in PVDF, as depicted in Fig. 2. This is the reason for enhancement of PVDF β-phase.

FTIR spectroscopy

FTIR spectra of PVDF/PVC/$BaTiO_3$ blend nanocomposites were carried out by Fourier transform infrared spectrophotometer BRUKER (Model VERTEX-70) in the wave number range of 500–3500 cm^{-1} in absorbance mode.

Figure 3 shows the FTIR spectra of PVDF, PVC, PVDF/PVC thin film and PVDF/PVC/$BaZrO_3$ and PVDF/PVC/$BaTiO_3$ blend nanocomposites thin film. The FTIR spectrum of PVC shows various characteristic peaks at 832 and 763 cm^{-1}, which are attributed to skeletal vibration of PVC [17, 18].

The characteristic bands at 2990 and 1088 cm^{-1} are assigned to O–H extending and C–O extending vibrations, separately. The band at 2910 cm^{-1} compares to C–H lopsided extending vibration of the alkyl group, and the band at 1721 cm^{-1} is ascribed to the C=O extending vibration of the carbonyl gathering. Additionally, the band at 1500 cm^{-1} can be due to vibration of an acetyl gathering. The bands at 1381 cm^{-1} and 1251 cm^{-1} are ascribed to CH_2 and C–H swaying vibrations separately. The band at 1425 cm^{-1} compares to CH_2 twisting [17, 19].

The FTIR spectra of PVDF/PVC thin film (Fig. 3 (c)) show small shifts in the bands as compared to the pristine PVC. This indicates the considerable interactions between two polymers.

The characteristic peaks of $BaZrO_3$ and $BaTiO_3$ have been observed at 976 cm^{-1}, which is corresponding to stretching vibration of nanocomposite [20]. A significant change in

Fig. 3 FTIR spectra of **a** pristine PVC, **b** pristine PVDF, **c** PVDF/PVC blend, **d** PVDF/PVC/$BaZrO_3$ and **e** PVDF/PVC/$BaTiO_3$ blends nanocomposite

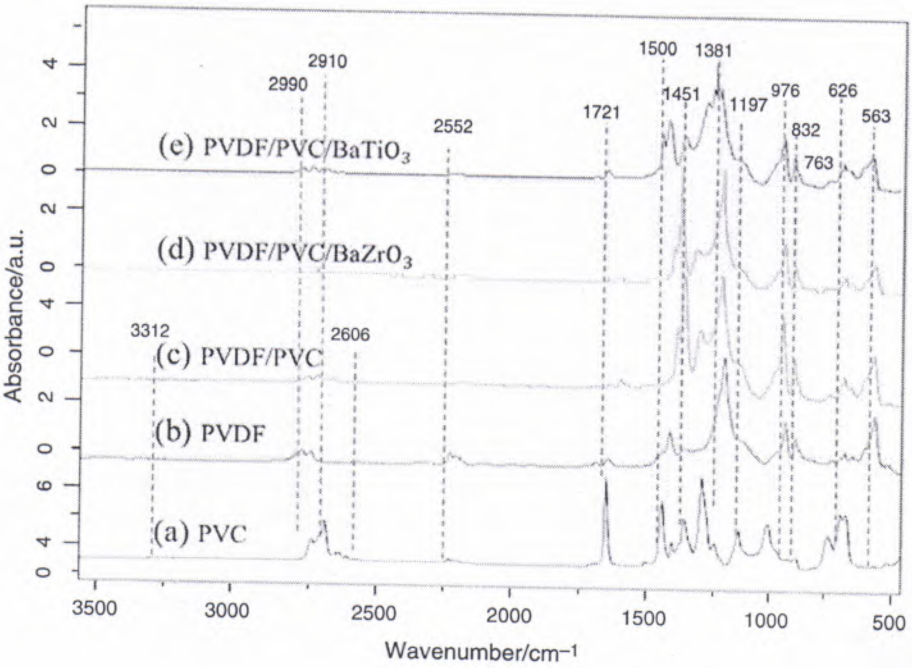

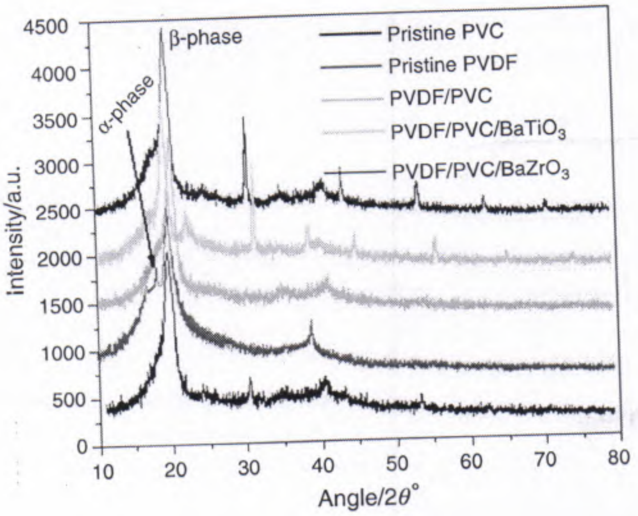

Fig. 4 XRD spectra of pristine PVC, pristine PVDF, PVDF/PVC blend, PVDF/PVC/$BaTiO_3$ and PVDF/PVC/$BaZrO_3$ blend nanocomposite

the intensity and shifts of bands were observed in the FTIR spectra. The peak heights at 763 cm^{-1} are assigned to α-form of PVDF; however, peak appeared at 835 cm^{-1} assigned to β-form of PVDF. The PVC and $BaTiO_3$ nanofiller enhance the β phase and reduce α phase. The β-content $F\beta$ of the samples was calculated by the following relation [21–23]:

$$F\beta = \frac{A_\beta}{(1.45)A_\alpha + A_\beta} \tag{1}$$

where A_α and A_β correspond to the height of absorption bands at 763 and 832 cm^{-1}, respectively. The β-crystal contents of PVDF/PVC/nanofillers blend nanocomposite thin film are shown in Table 3. The position and shape of the peaks are changed, but their relative height is almost the same. It is observed that the β-content increases in blend nanocomposites as compared to PVDF.

X-ray analysis

Figure 4a–e shows the XRD pattern of pristine PVC, pristine PVDF, PVDF/PVC and their blends nanocomposites. The XRD parameters such as interplanar distance (*d*), FWHM (*β*), average crystallite size (*L*), interchain separation (*R*), crystalline (%), primitive (*P*) and miller indices *(h k l)*, 2*θ* corresponding to different peaks are summarized in Table 2. The method for calculation of these parameters is reported in the literature [24–27].

Table 1 XRD analysis of various calculated structural parameters for pristine PVC, pristine PVDF, PVDF/PVC blend and PVDF/PVC blend nanocomposite

Samples	2*θ*	*β*	Intensity	*L*/Å	*d*/Å	*R*	%	*P*	*hkl*	*fcc*	*bcc*
Pristine PVC	19.03	09.51	2000	0.80	4.65	5.82	45.41	0.87	100		
1st	30.80	15.40	645	0.29	2.90	3.62		2.24	110		2
2nd	40.00	20.00	667	0.37	2.25	2.81		3.72	200	4	4
Pristine PVDF	19.03	09.51	1846	0.25	4.66	5.82	43.50	0.87	100		
1st	20.35	10.17	2441	1.63	4.36	5.45		0.99	100		
2nd	40.10	20.05	1262	0.03	2.24	2.80		3.74	200	4	4
PVDF/PVC blend	19.13	09.56	3201	0.77	4.63	5.79	38.66	0.88	100		
1st	40.90	20.45	1714	0.03	2.20	2.75		3.88	200	4	4
PVDF/PVC/$BaTiO_3$	19.10	09.55	3631	1.25	4.64	5.80	28.65	0.87	100		
1st	22.28	11.14	2451	0.81	3.98	4.98		1.18	100		
2nd	31.44	15.72	2970	6.34	2.84	3.55		2.33	110		2
3rd	39.55	19.77	2253	0.58	2.27	2.84		3.64	200	4	4
4rd	43.09	21.54	2177	4.56	2.09	2.62		4.29	200	4	4
5th	56.51	28.25	2111	0.66	1.62	2.03		7.13	–	–	–
6th	65.80	32.90	1945	0.30	1.41	1.77		9.39	221,300		
PVDF/PVC/$BaZrO_3$	19.09	09.54	4391	0.79	4.64	5.80	29.12	0.87	100		
1st	30.22	15.11	3487	5.62	2.95	3.69		2.16	110		2
2nd	40.42	20.21	2915	0.65	2.22	2.78		3.80	200	4	4
3nd	43.24	21.62	2750	4.23	2.09	2.61		4.32	210		
4rd	53.76	26.88	2684	0.30	1.70	2.12		6.51	211		6
5th	62.76	31.38	2517	3.27	1.47	1.84		8.63	221,300		
6th	71.55	35.77	2451	0.02	1.31	1.64		10.8	311	11	

Note: Peak position *(2θ)*, FWHM *(β)*, crystallite size *(L)*, interplanar distance *(d)*, interchain separation *(R)*, crystalline *(%)*, primitive *(P)*, miller indices *(h k l)*, face-centered cubic *(fcc)* and body-centered cubic *(bcc)*

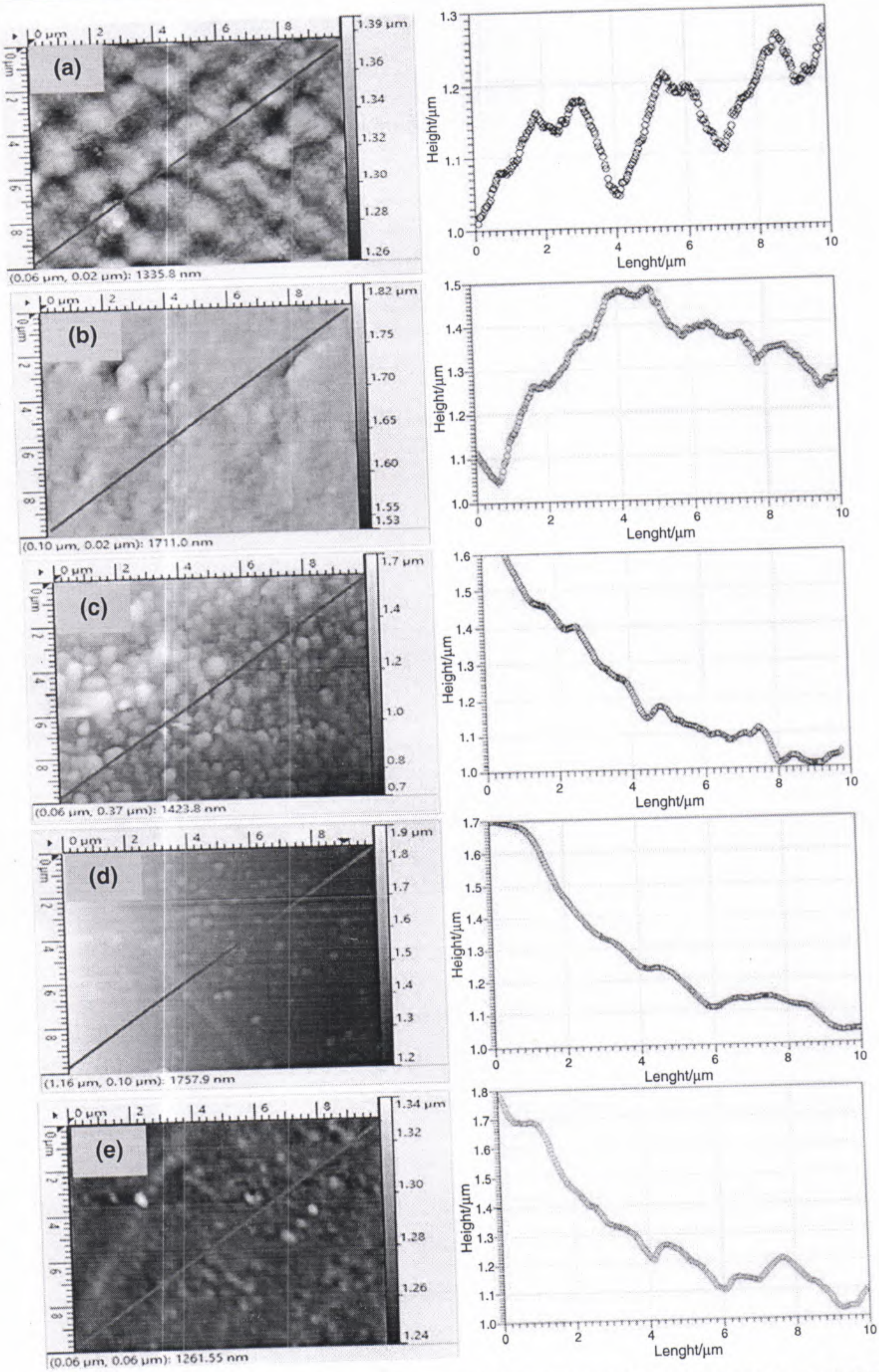

Fig. 5 AFM-2D topographic images of **a** pristine PVC, **b** pristine PVDF, **c** PVDF/PVC blend, **d** PVDF/PVC/BaTiO$_3$ and **e** PVDF/PVC/BaZrO$_3$ with height curves along read diagonals in the corresponding surface images of blend nanocomposite

The XRD peak at $2\theta = 18.48^\circ$ (020), 38.99° (002), and 41.8° (220) is assigned to α-phase of PVDF, while 2θ peak at 20.58° (110 or 200), 35.8° (001), and 36.68° (101) is assigned to *β*-phase of PVDF. However, 2θ peak at 26.58° (022) and 44.48° (114) confirms the *γ*-phase of PVDF [28, 29]. It is further observed that 2θ value at 16.72°, 19.58°, 23.54° corresponds to (200), (101), (210) planes of pristine PVC, respectively [30].

It is noticed for XRD spectra that no significant variation is observed by the addition of $BaZrO_3$ and $BaTiO_3$ PVDF/PVC blend matrix. It may be due to good dispersion of nanofillers in polymer matrix [31]. The % of crystallinity is affected by nanofillers as observed in Table 1 because nanofiller in general responsible for amorphous or crystalline phases in polymer matrix [32]. In the present study decrease in crystallinity is corresponding to amorphous phase attributed by $BaZrO_3$ and $BaTiO_3$. It is further responsible for higher conductivity and affirms the complexation between nanoparticle ($BaZrO_3$, $BaTiO_3$) and the PVDF/PVC blend.

It is clear that for pristine PVDF, the diffraction peak observed at $2\theta = 20.35^\circ$, corresponding to the plane (101), is due to crystalline structure of PVDF β-phase. The diffraction peaks at $2\theta = 19.03^\circ$ and 40.10°, corresponding to the planes (100) and (200), are due to crystalline structure of PVDF α-phases. PVC exhibits amorphous structure with polar chlorine atoms in the molecular structure. Pristine PVC exhibits a maximum intensity peak at $2\theta = 19^\circ$, 30° and a relatively less intense peak at 40°, respectively, and no sharpness in other small peaks.

Atomic force microscopy

The surface morphology of pristine and blend polymer nanocomposites were investigated by atomic force microscopy. The 2D and 3D AFM images of pristine and blend nanocomposites are shown in Figs. 5 and 6, respectively. The calculated particle size, average grain size and roughness are presented in Table 2. The higher value of grain size in blend matrix with $BaTiO_3$ could be correlated with uniform dispersion of the nanofiller within blend matrix [33, 34]. This proves the strong connectivity between $BaTiO_3$ and PVDF/PVC blend.

AFM recognizes two phases (i.e. hard and soft phases) in 3D images. XRD results support that the blend nanocomposite is more crystalline as well as hard in comparison with pristine system and finally exhibits mostly hard phases.

As a result, in 4 mass% loaded nanofiller, both the hard phases PVC and PVDF together increase surface roughness. In this case of different nanofillers (i.e., $BaTiO_3$, $BaZrO_3$), the roughness is a bit lower than that of 4 mass% loading because in this case PVDF/PVC blend nanocomposites is distributed over both phases. The height profiles curve right

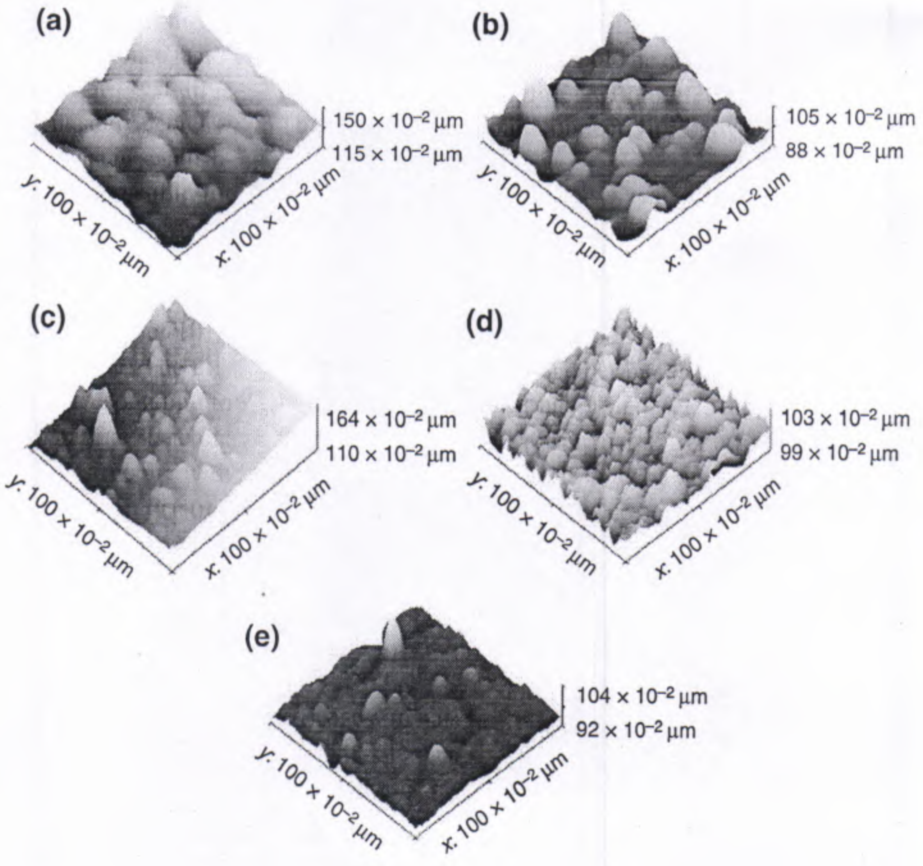

Fig. 6 AFM-3D topographic images of **a** pristine PVC, **b** pristine PVDF, **c** PVDF/PVC blend, **d** PVDF/PVC/$BaTiO_3$ and **e** PVDF/PVC/$BaZrO_3$ blend nanocomposite

Table 2 AFM parameters of pristine PVC, pristine PVDF, PVDF/PVC blend and PVDF/PVC blend nanocomposite

Samples	Particle size/nm	Grain size/nm	Roughness size/nm
Pristine PVC	77	12.41	7.12
Pristine PVDF	85	14.07	4.03
PVDF/PVC blend	92	16.55	4.31
PVDF/PVC/$BaTiO_3$	94	18.13	1.45
PVDF/PVC/$BaZrO_3$	88	16.98	2.12

side across the red diagonal of 2D height images (Fig. 5a–e) also supports this argument. The range of height is the highest in the case of PVDF/PVC/$BaTiO_3$ (1 to 1.8 μm), whereas the ranges in PVDF/PVC/$BaZrO_3$ (1.0 to 1.7 μm) and PVDF/PVC (1.0 to 1.6 μm) are very close to each other. AFM study suggests that a large number of interphases are introduced by incorporation of nanofillers. [35].

Pyroelectric activity

The pyroelectric current was recorded at different heating rates (i.e., 1, 2 and 3 °C min^{-1}) by electrometer (Keithley 6514) as shown in Fig. 7a–e. For pristine PVC and PVDF, the calculated value of p is 15.62 and 20.46 μC m^{-2} K^{-1}. With the growth of ceramic powder content, value of p increases too. The pyroelectric coefficients of PVDF/PVC, PVDF/PVC/$BaZrO_3$ and PVDF/PVC/$BaTiO_3$ have been calculated to be 88.58, 153.04 and 351.4 μC m^{-2} K^{-1}, respectively, as shown in Table 3. The increase in volume friction in PVDF/PVC matrix in the presence of nanofillers

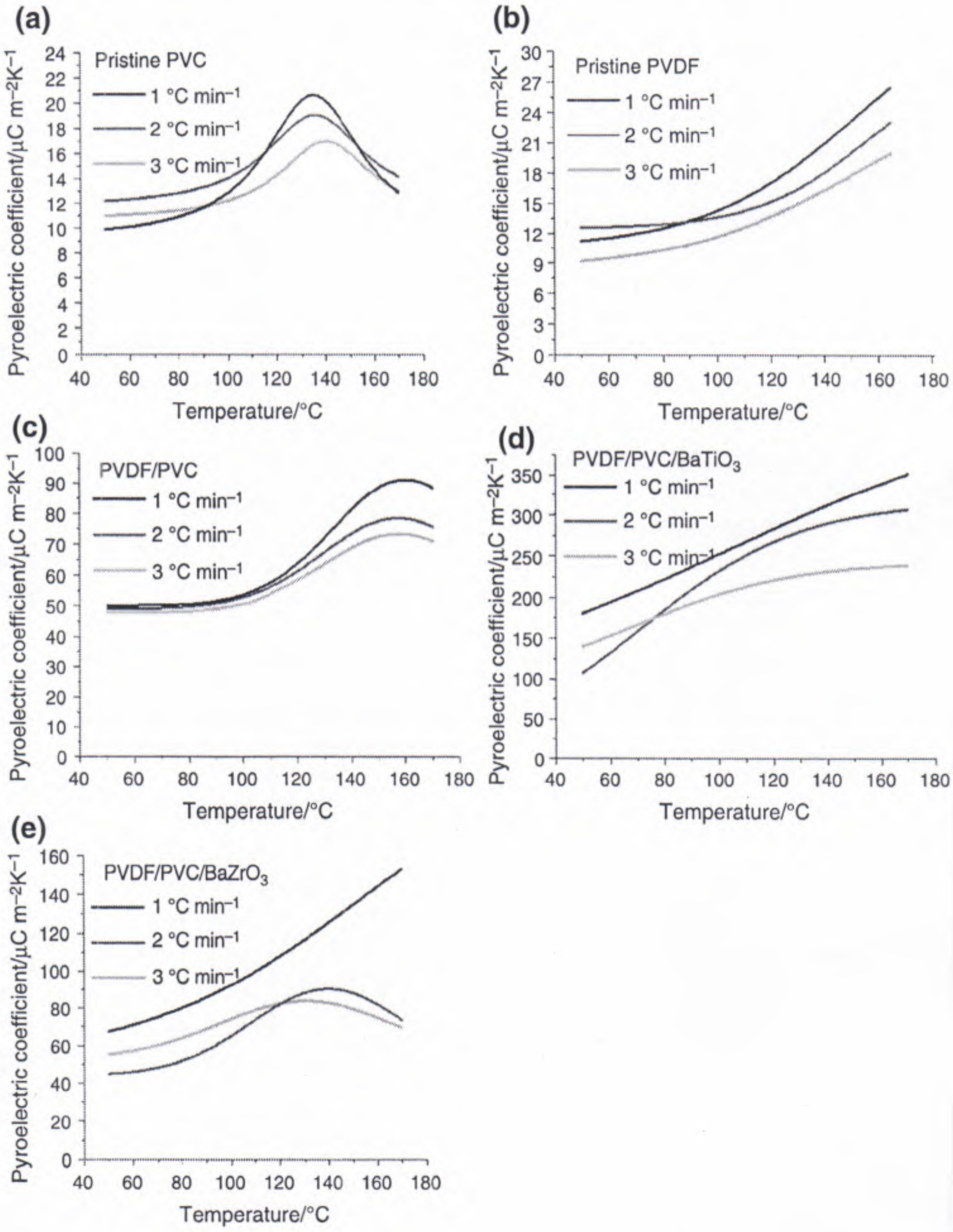

Fig. 7 Temperature-dependent pyroelectric coefficient of **a** pristine PVC, **b** pristine PVDF, **c** PVDF/PVC blend, **d** PVDF/PVC/$BaTiO_3$ and **e** PVDF/PVC/$BaZrO_3$ blend nanocomposites at different heating rates

Table 3 The comparative analysis of the present work with previously reported work in the literature PVDF/PVC blend nanocomposite

Samples	p/μC m^{-2} K^{-1} 1 °C min^{-1}	d_{33}/pC N^{-1}	$F\beta$/%	References
M2-HS1-ZnO	–	3.89 ± 1.48	75	[47]
HAp-60 mass% BaTiO3	16.2	1	–	[48]
P(VDF-TrFE) 50%PZTM2	113	–	–	[49]
(1%)PTCA/PVDF-TRFE	295.6	72.8	–	[50]
PVDF/ZnO(0.25%)	26	–	–	[51]
P(VDF-CTFE)	–	140	–	[52]
(0.7%)PZT/PVC	3.68	22		[53]
PZT/P(VDF-TrFE)	25.7	−37	–	[54]
P(VDF-TrFE)-BNT–BKT–BT	95	40	–	[14]
Pristine PVC	15.62	23	39.30	Present work
Pristine PVDF	20.46	66	09.94	
PVDF/PVC blend	88.58	44	79.72	
PVDF/PVC/$BaTiO_3$	351.64	236	88.93	
PVDF/PVC/$BaZrO_3$	153.04	127	80.01	

Note: Pyroelectric coefficient *(p)*, piezoelectric coefficients *(d_{33})*, and β content *($F\beta$)*

attributed the higher value of pyroelectric coefficient. This suggests that the presence of nanofiller (i.e. $BaZrO_3$ or $BaTiO_3$) contributes to the pyroelectric activity of the blend nanocomposites together with the PVDF/PVC polymer [36, 37]. The higher magnitude of the *p* for blend nanocomposites in comparison with PVDF/PVC blend may be due to the presence of high pore density.

The heating rate-dependent pyroelectric coefficients of PVDF/PVC blend nanocomposites are shown in Fig. 8. It is observed that 1 °C min^{-1} heating rate plays significant role to enhance the pyroelectric coefficients of PVDF/PVC blend nanocomposites samples because of sufficient relaxation time for relaxation of dipoles, atoms or ions.

It is observed that the pyroelectric parameters in the blend nanocomposites are much greater than individual polymer and polymer blend (i.e. PVDF + PVC), which could be associated with the proper dispersion of nanofiller in polymer matrix leading to a strong poling of the nanophases.

Piezoelectric activity

The piezoelectric coefficient *(d_{33})* for polar PVDF and blend nanocomposites is shown in Fig. 9. PVDF/PVC/$BaTiO_3$ blend nanocomposites are having d_{33} coefficient of 112pC N^{-1}. The strong piezoelectric behavior of PVDF depends on strong β-phase and poling condition. This means that higher piezoelectricity is subjected to structural morphology of PVDF. However, the orientation of β- phase dipoles have much pronounced effect on d_{33} than the amount of β-phase inside the PVDF-based blend nanocomposites [38, 39].

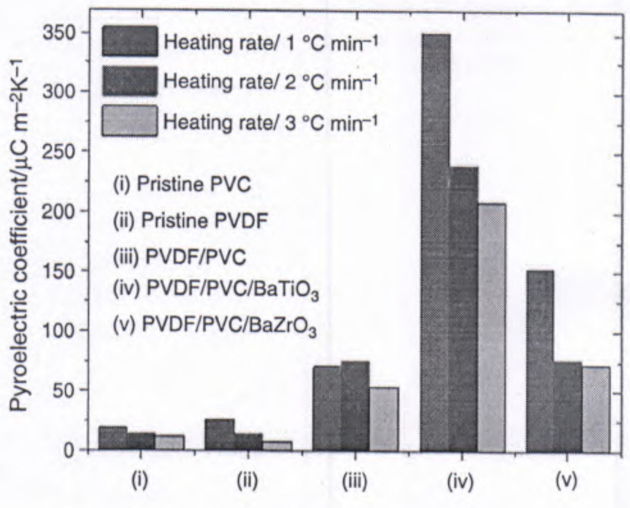

Fig. 8 Heating rate-dependent pyroelectric coefficient *(p)* of (i) pristine PVC, (ii) pristine PVDF, (iii) PVDF/PVC blend, (iv) PVDF/PVC/$BaTiO_3$ and (v) PVDF/PVC/$BaZrO_3$ blend nanocomposites

Further, piezoelectricity could be improved by uniaxial stretching applied to the PVDF or PVDF blend system at room temperature. Stretching provides the transformation of PVDF into β-polymorph. The origin of piezoelectricity in polymer is different than inorganic material because change in dipole moment of polymers is the most complex issue. All trans bonds (TTTT) in β-phase PVDF possess the highest net dipole moment among the four different polymorphs, which displays large piezoelectric and dielectric properties [40, 41].

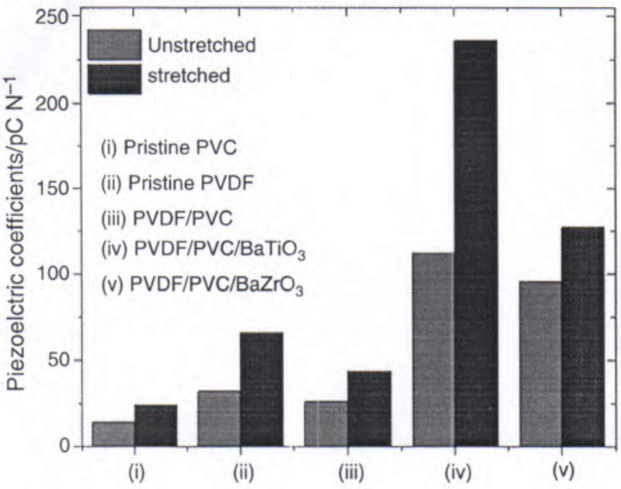

Fig. 9 Piezoelectric coefficient of (d_{33}) stretched and unstretched samples

PVDF nanocomposites could encourage the interface charge stockpiling yielding an expanded proficiency of dipolar polarization and subsequently, better piezoelectricity [42]. The improvement of β-phase contributed to the electroactive ionic phase stability in PVDF/PVC/BaTiO$_3$ blend nanocomposites. Therefore, this combination of polymer and nanofiller displays a higher piezoelectric coefficient [43].

The deformation of PVDF and its blend nanocomposites during stretching reduces the structural defects by decreasing thickness, which leads to much improved piezoelectric performance. The stretching also enhances the breakdown strength of PVDF and allows it to polarize by higher electric field [44].

The stretched sample induces almost 99% of β-phase PVDF allows the orientation crystallites in the drawing direction. The poling electric field is perpendicular to the surface of the stretched PVDF and orient to crystallites in poling direction. This orientation in stretched samples is stronger than unstretched samples, leading to enhanced d_{33} coefficient. In addition, since the stretching of PVDF blend nanocomposites possesses larger voids size due to nanofillers, the electric field applied to orient the dipoles could also be strong enough to breakdown the gas in the voids (such as creating electrets) to some extent and create more dipoles, which might also contribute to the improved piezoelectricity.

P–E hysteresis loops

The *P–E* hysteresis loops of pristine PVC, pristine PVDF, PVDF/PVC, and PVC/PVDF/nanofiller blend nanocomposite are shown in Fig. 10. The ferroelectric effect in PVDF is mainly due to the presence of fluorine atom, which is strong electronegative [45].

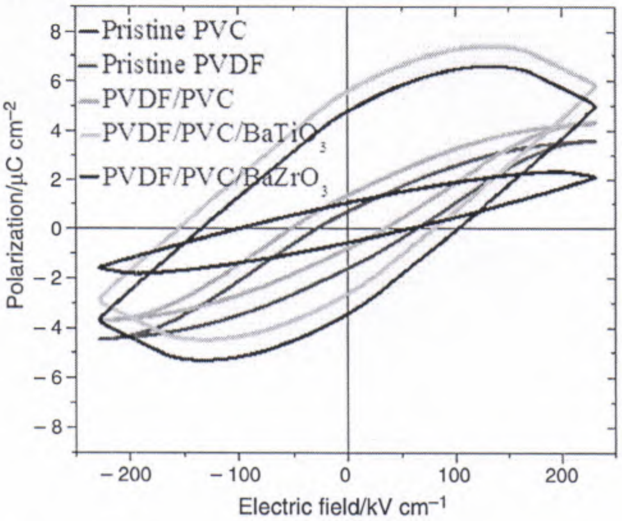

Fig. 10 Electric field-dependent polarization (*P–E* loop) pristine PVC, pristine PVDF, PVDF/PVC blend, and PVDF/PVC blend nanocomposite at room temperature

P–E hysteresis loops have been recorded at same electric field of polarization (i.e. 200 kV/cm) with frequency of 100 Hz at room temperature. All the loops clearly speak the effect of nanofillers by means of their area.

Pristine PVDF shows polar β-phase-dependent polarization P_r under influence of electric field. PVDF is combination of polar and nonpolar phases. The strength of polarization in PVDF depends on the amount of β-phase present (i.e. polar phase). In this study, pristine PVDF is dominated by nonpolar α-phase with a small amount of polar β-phase and hence the PVDF thin film shows a weak P_r vs. E curve (Fig. 10).

Figure 10 shows the increase in P_r value with the addition of nanofiller in polymer matrix may be due to redistribution of charges at the interface of polymer dielectric (i.e. PVDF, PVC, and their blend composites), which facilitates the complex polarization. Higher value of P_r indicates the significant change in ferroelectricity of polymeric system. The addition of BaTiO$_3$ in PVDF/PVC system produces 4.9 μC cm^{-2} (Fig. 10) value of P_r which is higher than that of the pristine PVC and PVDF (i.e. 1.9 and 3.0 μC cm^{-2}).

In the case of PVDF/PVC and PVDF/PVC/BaZrO$_3$ films, the saturation polarization values are around 3.2 and 4.0 μC cm^{-2}, respectively, which are higher than that of the pristine PVDF. The decrease in polarization values have been observed in PVDF/PVC and PVDF/PVC/BaZrO$_3$ samples as compared to the PVDF/PVC/BaTiO$_3$ blend nanocomposites. It may be due to the presence of nanoparticles with high conductivity in multiferroics is normally attributed to oxygen vacancies created due to the presence of Fe^{3+} and Fe^{2+} (polar on mechanism) [46]. The saturation of polarization depends on stabilization polarization domain and β-phase. The remnant polarization and coercive field both increase with increase in dielectric constant. This confirms that the presence of dielectric nanofiller like $BaZrO_3$ and $BaTiO_3$ significantly influences the polarization response.

Conclusions

It is concluded that enhanced β-phase crystallinity, reduced crystallite size and oriented structure of blend nanocomposites yielded the highest piezo/pyro response (112 $pC\ N^{-1}$, 351.64 $\mu C\ m^{-2}\ K^{-1}$ for PVDF/PVC/$BaTiO_3$) as compared to pristine and blend of PVDF and PVC. XRD pattern shows the structural analysis of blend nanocomposites including separation between crystalline and noncrystalline phases in polymer matrix. The interaction between the carbonyl groups of PVC and the CH_2 groups of PVDF causes the shift of C-O as noticed by FTIR spectra. The numbers of defects/interfaces are introduced by nanofillers as noticed in AFM images. Finally, it is concluded that the modification of β-phase by nanofillers is directly affecting the polarization capacity, pyroelectricity and piezoelectricity. This novel blend nanocomposite is a suitable candidate for ferroelectric device applications.

Acknowledgements Financial assistance from Indo-Belarusian Scientific Cooperation, DST, New Delhi (India) (letter no.INT/BLR/P-13/2016), is gratefully acknowledged. One of the authors Rohan Sagar acknowledges the University Grant commission (UGC), New Delhi (India), for proving research fellowship award number RGNF-2017-18-SC-UTT-29088. We are thankful to Dr. Satyendra Singh, Asstt. Professor, Jawahar lal Nehru University, New Delhi to provide the facility of P-E loop.

References

1. Bowen CR, Kim HA, Weaver PM, Dunn S. Piezoelectric and ferroelectric materials and structures for energy harvesting applications. Energy Environ Sci. 2014;7(1):25–44.
2. Ibrahim IR, Hashim M, Ismail I, Matori KA, Azis RS, Nazlan R, Mat Daud NH. Systematic microstructural development with thermal diffusivity behaviour from nanometric to micronic grains of strontium titanate. J Therm Anal Calorim. 2018;2:7954–8.
3. Dariusz B, Przemysław N, Izabela SW, Grzegorz D. Multi-component PZT ceramics obtained by mechanochemical activation and conventional ceramic technology. J Therm Anal Calorim. 2019;4:09141–4.
4. Jayalakshmy MS, Philip J. Pyroelectric figures of merit and associated properties of $LiTaO_3$/polyvinylidene difluoride nanocomposites for thermal/infrared sensing. Sens Actuat A. 2014;206:121–6.
5. Parket KI, Minbaek L, Ying L, San ZG, Keon JL. Flexible nanocomposite generator made of $BaTiO_3$ nanoparticles and graphitic carbons. Adv Mater. 2012;24(22):2999–3004.
6. Vacche SD, Oliveira F, Leterrier Y, Michaud V, Damjanovic D, Manson JAE. The effect of processing conditions on the morphology, thermomechanical, dielectric, and piezoelectric properties of P(VDF-TrFE)/$BaTiO_3$ composites. J Mater Sci. 2012;47(11):4763–74.
7. Cortellessa G, Arpino F, Dell'Isola M, Ficco G, Iacomini L, Fernicola V, Bertiglia F. Experimental and numerical analysis in heat flow sensors calibration. J Therm Anal Calorim. 2019;7:08321–6.
8. Bennaji N, Mami A, Mellouki I, Yacoubi N. A new method for thermo-electrical properties of GaSb by electro-pyroelectric technique. J Therm Anal Calorim. 2016;127(1):641–4.
9. Sagar R, Gaur SS, Grace AN, Gaur MS. Enhanced energy storage in polyvinylidenefluoride (PVDF) + $BaZrO_3$ electroactive nanocomposites. Ion. 2018;24(7):1965–75.
10. Mahajan R, Koros WJ. Factors controlling successful formation of mixed-matrix gas separation materials. Ind Eng Chem Res. 2000;39:2692.
11. Sagar R, Gaur SS, Gaur MS. Effect of $BaZrO_3$ nanoparticles on pyroelectric properties of polyvinylidene fluoride (PVDF). J Therm Anal Calorim. 2016;128(2):1235–9.
12. Mohanapriya MK, Deshmukh K, Ahamed MB, Chidambaram K, Khadheer PSK. Zeolite 4A filled poly (3, 4-ethylenedioxythiophene): (polystyrenesulfonate) (PEDOT: pSS) and polyvinyl alcohol (PVA) blend nanocomposites as high-k dielectric materials for embedded capacitor applications. Adv Mater Lett. 2016;7(12):996–1002.
13. Ahmad J, Hagg MB. Effect of zeolite preheat treatment and membrane post heat treatment on the performance of polyvinyl acetate/zeolite 4A mixed matrix membraneSep. Pure Tech. 2013;115:163–7.
14. Mahdi RI, Abd Majid WH. Piezoelectric and pyroelectric properties of BNT-base ternary lead-free ceramic–polymer nanocomposites under different poling conditions. RSC Adv. 2016;6:81296–309.
15. Furukawa T, Ishida K, Fukada E. Piezoelectric properties in the composite systems of polymers and PZT ceramics. J Appl Phys. 1979;50:4904–12.
16. Furukawa T, Suzuki K, Date M. Switching process in composite system of pzt ceramics and polymer. Ferroelectrics. 1986;68:33–44.
17. Pawde SM, Deshmukh K, Parab S. Functionalized engineering materials and their applications. J Appl Polym Sci. 2008;109:1328.
18. Deshmuk K, Ahamed MB, Deshmukh RR, Pasha SKK, Sadasivuni KK. Synergistic effect of vanadium pentoxide and graphene oxide in polyvinyl alcohol for energy storage application. Euro Polym J. 2016;76:14–27.
19. Pawde SM, Deshmukh K. Characterization of polyvinyl alcohol/gelatin blend hydrogel films for biomedical applications. J Appl Polym Sci. 2008;109:3431–7.
20. Rondon W, Freire D, Benzo Z, Sifontes AB, Gonzalez Y, Valero M. Application of 3A zeolite prepared from venezuelan kaolin for removal of Pb(II) from wastewater and its determination by flame atomic absorption spectrometry. Am J Anal Chem. 2013;4:584.
21. Yousefi AA. Influence of polymer blending on crystalline structure of polyvinylidene fluoride. Iran Polym J. 2011;20(2):109–21.
22. Salimi A, Yousefi AA. FTIR studies of β-phase crystal formation in stretched PVDF films. Polym Test. 2003;22:699–704.
23. Gregorio JR. Determination of the α, β, and γ crystalline phases of poly(vinylidene fluoride) films prepared at different conditions. J Appl Polym Sci. 2006;100:3272–9.
24. Mallick B, Patel T, Behera RC, Sarangi SN, Sahu SN, Choudhar RK. Microstrain analysis of proton irradiated PET microfiber. Nucl Instrum Methods Phys Res Sect B. 2006;248(2):305–10.
25. Madani M. Structure optical and thermal decomposition characters of LDPE graft copolymers synthesized by gamma irradiation. Bull Mater Sci. 2010;33(1):65–73.

26. Vij A, Chawla AK, Kumar R, Lochab SP, Chandra R, Singh N. Effect of 120 MeVAg 9 + ion beam irradiation on the structure and photoluminescence of SrS: Ce nanostructures. Phys B Condens Matter. 2010;405(11):2573–6.
27. Singh P, Kumar R. Influence of high-energy ion irradiation on the structural, optical, and chemical properties of polytetrafluoroethylene. Adv Polym Technol. 2014;33(3):21410–9.
28. Jurczuk K, Galeski A, Mackey M. Anne Hiltner and Eric Baer orientation of PVDF α and γ crystals in nanolayered films. Colloid Polym Sci. 2015;293(4):1289–97.
29. Satapathy S, Pawar S, Gupta PK, Varma KRV. Effect of annealing on phase transition in poly(vinylidene fluoride) films prepared using polar solvent. Bull Mater Sci. 2011;34:727.
30. Gilbert M, Ross DH, Bowen A. X-ray pole figures for oriented PVC. Polym. 1999;40:1233–9.
31. Abdelrazek EM, Hezma AM, El-khodary A, Elzayat AM. Spectroscopic studies and thermal properties of PCL/PMMA biopolymer blend. Egypt J Basic Appl Sci. 2016;3(1):10–5.
32. Alghunaim NS. Spectroscopic analysis of PMMA/PVC blends containing $CoCl_2$. Result Phys. 2015;5:331–6.
33. Joseph J, Deshmukh K, Chidambaram K, Faisal M, Selvarajan E, Sadasivuni KK, Ahamed MB, Pasha SKK. Dielectric and electromagnetic interference shielding properties of germanium dioxide nanoparticle reinforced poly(vinyl chloride) and poly(methylmethacrylate) blend nanocomposites. J Mater Sci Mater Electron. 2018;29(23):20172–88.
34. Sagara R, Gaura MS, Bhadoria BS. Investigation of TSDC and dielectric modulus of PVDF–$BaZrO_3$ nanocomposites thin film. Vacuum. 2018;156:375–83.
35. Tong JD, Leclere P, Rasmont A, Bredas JL, Lazzaroni R, Jerome R. Morphology and rheology of poly(methyl methacrylate)-block-poly(isooctyl acrylate)-block-poly(methyl methacrylate) triblock copolymers, and potential as thermoplastic elastomers. Macromol Chem Phys. 2000;201:1250.
36. Olszowy M. Dielectric and pyroelectric properties of the composites of ferroelectric ceramic and poly(vinyl chloride). Condens Matter Phys. 2003;2(34):307–13.
37. Jayasuriya AC, Tasaka S, lnagaki N. Pyroelectric properties of linear aromatic polyurethanes. IEEE Trans. 1996;3:765–9.
38. Mohammadi B, Yousefi AA, Bellah SM. Effect of tensile strain rate and elongation on crystalline structure and piezoelectric properties of PVDF thin films. Polym Test. 2007;26:42–50.
39. Yang L, Ji K, Zhu J, Wang J. Dramatically improved piezoelectric properties of poly(vinylidene fluoride) composites by incorporating aligned TiO_2@ MWCNTs. Compos Sci Technol. 2016;123:259–67.
40. Ye H, Yang L, Shao W, Sun S, Zhen L. Effect of electroactive phase transformation on electron structure and dielectric properties of uniaxial stretching poly(vinylidene fluoride) films. RSC Adv. 2013;45(3):23730–6.
41. Jahana N, Mighria F, Rodriguea D, Ajjia A. Synergistic improvement of piezoelectric properties of PVDF/$CaCO_3$/montmorillonite hybrid nanocomposites. Appl Cla Sci. 2018;152:93–100.
42. Baur C, DiMaio JR, McAllister E, Hossini R, Wagener E, Ballato J, Priya S, Ballato A, Smith JDW. Enhanced piezoelectric performance from carbon fluoropolymer nanocomposites. J Appl Phys. 2012;112:124104.
43. Chang-Mou W, Min-Hui C, Wun-Yuan Z. Piezoelectric response of aligned electrospun polyvinylidene fluoride/carbon nanotube nanofibrous membranes. Nanomaterials (Basel). 2018;8(6):420–5.
44. Chang J, Shen Y, Chu X, Zhang X, Song Y, Lin Y, Li L. Large d_{33} and enhanced ferroelectric/dielectric properties of poly(vinylidene fluoride)-based composites filled with $Pb(Zr0.52Ti0.48)O_3$ nanofibers. RSC Adv. 2015;5(63):51302–7.
45. Osińska K, Czekaj D. Thermal behavior of BST//PVDF ceramic–polymer composites. J Therm Anal Calorim. 2013;113(1):69–76.
46. Varshney M, Rawat M, Yadav KL. Structural, dielectric, ferroelectric and magnetic properties of (x) $CoFe_2O_4$-$(1-x)$ $BaTiO_3$ composite. IEEE Trans Dielectric Electric Insul. 2015;22:3.
47. Fortunato M, Chandraiahgari CR, Bellis GD, Ballirano P, Sarto F, Tamburrano F, Sarto MS. Piezoelectric effect and electroactive phase nucleation in self-standing films of unpoled PVDF nanocomposite films. Nanomaterials. 2018;8:743.
48. Dubey AK, Basu B, Balani K, Guo R, Bhalla AS. Dielectric and pyroelectric properties of HAp-$BaTiO_3$ composites. Ferroelectrics. 2011;423(1):63–76.
49. Wu C, Cai G, Luo W, Peng Q, Sun X, Zhang W. Enhancement of pyroelectric properties of composite thick films using Mn-doped PZT. Sens Actuat A. 2013;199:24–9.
50. Chan HLW, Chan WK, Zhang Y, Choy CL. Pyroelectric and piezoelectric properties of lead titanate/polyvinylidene fluoride-trifluoroethylene 0–3 composites. IEEE Tran Insul. 1998;5:4.
51. Tan KS, Gan WC, Velayutham TS, Majid WHA. Pyroelectricity enhancement of PVDF nanocomposite thin films doped with ZnO nanoparticles. Smart Mater Struct. 2014;23:125006–11.
52. Liu XF, Xiong CF, Sunb HJ, Li Z. Electromechanical properties of poly(vinylidene fluoridechlorotrifluoroethylene) copolymer. Appl Phys Lett. 2006;88:062904.
53. Donga LJ, Lia R, Liu Y. Piezoelectric and dielectric properties of PZT/PVC and graphite doped with PZT/PVC composites. Mater Sci Eng B. 2006;127:261–6.
54. Ng KL, Chan HLW, Choy CL. Piezoelectric and pyroelectric properties of PZT/P(VDF-TrFE) composites with constituent phases poled in parallel or antiparallel directions. IEEE Trans Freq Control. 2000;47:6–8.

③

Polymer Bulletin
https://doi.org/10.1007/s00289-020-03457-0

ORIGINAL PAPER

Preparation, characterization and microhardness measurements of hybrid nanocomposites based on PMMA + P(VDF–TrFE) and graphene oxide

Rohan Sagar[1] · **M. S. Gaur**[1] · **Vinod Kushwah**[1] · **Aakash Rathore**[2] · **D. G. Piliptsou**[3] · **A. A. Rogachev**[3]

Received: 18 May 2020 / Revised: 14 September 2020 / Accepted: 1 November 2020

Abstract

The polymer nanocomposites samples of the poly (methyl methacrylate) (PMMA)—poly (vinylidene fluoride–trifluoroethylene) P(VDF–TrFE) with graphene oxide (GO) were prepared by solution casting method. The impact of GO on electroactive polar β-phase of PMMA + P(VDF–TrFE) was investigated through the Fourier transform infrared spectroscopy (FTIR) and atomic force microscopy. The mechanical properties of nanocomposites samples have been investigated by measurement of microhardness. The value of microhardness and indentation depends on applied load on samples. The experimental result suggests that mechanical properties of samples decrease in presence of GO due to decrease in uniaxial orientation or agglomeration of GO. Surface characteristics such as surface free energy, interfacial free energy and hydrophobicity were determined by measuring the contact angle.

Keywords Graphene oxide · FTIR · AFM · Contact angles · Microhardness of thin films

Introduction

The combination of poly (methyl methacrylate) (PMMA) with poly (vinylidene fluoride–trifluoroethylene) P(VDF–TrFE) is a standout among the most promising ferroelectric polymers. The previous studied in these polymers have been

---

✉ M. S. Gaur
mulayamgaur@rediffmail.com

[1] Department of Physics, Hindustan College of Science and Technology (affiliated to Dr. A.P.J. Abdul Kalama Technical University, Lucknow, U.P. 226031, India), Farah, Mathura, Uttar Pradesh 281122, India

[2] Department of Mechanical Engineering, J.S.S. Academy of Technical Education, Noida, Uttar Pradesh 201301, India

[3] Francisk Skorina Gomel State University, Gomel, Belarus

successfully demonstrated their non-volatile and low cost memory devices applications [1, 2]. The PMMA + P(VDF–TrFE) can crystallize in different phases (α and β) depending on the heating conditions. Among these two phases, the β-phase is found to have most noteworthy ferroelectric properties. Nonpolar α-phases of PMMA + P(VDF–TrFE) composite are often reborn into polar β-phase by stretching or by heat treatment [3]. The interface formed in blend and nanocomposites system plays an important role to modify electrical and mechanical properties of ferroelectric polymers [4–11].

The ferroelectric polymer P(VDF–TrFE) (vinylidene fluoride-co-trifluoroethylene) was chosen as the dielectric material for its extremely high permittivity. Linear PMMA polymer was introduced into P(VDF–TrFE) matrix in order to minimize the ferroelectric effect of P(VDF–TrFE) and thus increase the reversibility. In addition, dynamic hysteresis is also associated with the friction force between water droplets and the insulator surface [12, 13].

In recent years, micro- and nanoindentation have been established as a means of detecting a wide variety of mechanical, morphological and nanostructural changes in amorphous and semicrystalline polymers [14–35], including hybrids [16], copolymers [20, 36], polymer composites [19] and multilayer systems [15], however, no report is available in hybrid nanocomposites system of PMMA + P(VDF–TrFE) + GO. The precise mechanical properties of polymers and polymer nanocomposites cannot be easily determined because, so far, there is no comprehensive visco-elasto-plastic theory to account for their micromechanical properties. However, valuable attempts have been made in the past to explain the mechanical behavior of materials that do not exhibit fully plastic behavior [37, 38].

The novelty of this work lies in the new properties arising from the combination of two polymers with GO and different dispersion characteristics, which have not been reported previously [39, 40]. The graphene oxide is important filler in polymer matrix because nanocomposites have stemmed from their high surface area and mechanical stability [41]. Consequently, studying the mechanical properties of PMMA + P(VDF–TrFE) + GO hybrid nanocomposites brings a great interest as the researchers are trying to find an answer to the question: how can hybrid nanocomposites system change to pave the way for new practical applications [42, 43].

Synthesis of graphene oxide (GO) is achieved by placing graphite in concentrated acid in the presence of an oxidizing agent. The Tour method demonstrated a less hazardous and more efficient method for graphite oxidation. This method and its modified versions are presently the most commonly used methods for the oxidation of graphite [44, 45].

Graphene oxide (GO) is one of those materials—it is a single-atomic layered material, made by the powerful oxidation of graphite, which is cheap and abundant. Graphene oxide is an oxidized form of graphene, laced with oxygen-containing groups [46].

The mechanical properties of several polymers are strongly influenced by GO because of its good dispersion and good interaction with main chain of many polymers. Nevertheless, very high dispersion of GO is difficult to reach after a certain amount of loading above which it adversely affects modulus, strength and surface wettability of polymer nanocomposites. The GO finally affected the pore structure, surface roughness and surface wettability of the polymer, which in turn is correlated with the mechanical properties of polymers [47–52].

The various mechanical properties varied with variation in applied load. Generally, there are two types of load (1) static load and (2) dynamic load. The applied load is the main parameter for testing of mechanical properties. For example, fatigue toughness is one of the most important properties of materials which can be determined by the behavior of the material under applied variable load. Various other material properties such as tensile strength, fracture toughness, toughness, ductility, elastic modulus and microhardness are investigated under application of static load [53–55].

In this paper, we report a study on GO-modified microhardness of PMMA + P(VDF–TrFE) hybrid nanocomposites samples. FTIR, AFM, contact angle measurement studies have been made to characterize the structural and surface properties of hybrid nanocomposites.

Experimental details

Materials

P(VDF–TrFE) (Mw ~ 146.06 g mol^{-1}), PMMA (Mw ~ 100.12 g mol^{-1}) and graphite powder (Mw ~ 1201.6 g mol^{-1}) were purchased from Sigma-Aldrich. Sulfuric acid (H_2SO_4), sodium nitrate ($NaNO_3$), hydrogen peroxide (H_2O_2), hydrochloric acid (HCL) and potassium permanganate ($KMnO_4$) were procured from Sigma-Aldrich. Acetone, distilled water (DW) and *N*, *N*-dimethylformamide (DMF) were used as a solvent for preparation of hybrid nanocomposite thin film.

Fabrication of GO and PMMA + P(VDF–TrFE) hybrid nanocomposites

Graphene oxide (GO) was prepared by modified Hummer's method [56]. In this method, 0.5 g of graphite powder and 0.5 g $NaNO_3$ were mixed with 25 ml of concentrated H_2SO_4. The mixture was continuously stirred for 30 min at the temperature range of 0–5 °C. Thereafter, 3 g of $KMnO_4$ flakes were slowly added to the suspension and the temperature was maintained below 25 °C under stirring, until this solution becomes light brownish. This solution was added with 45 ml of distilled water (DW) and 5 ml of H_2O_2 to reduce the excess of $KMnO_4$. It was then sonicated for 24 h. The dark suspension was then centrifuged to remove ionic contaminants for 15 min at 10,000 rpm. The whole reaction mixture was washed by 1 M HCl and ethanol for 3–4 times and filtered to get the gray color of GO separate sheets in oxidized state. The GO was dried in the form of precipitate to stay away from aggregation. For the preparation of blend sample, different weight % of P(VDF–TrFE) was added with PMMA. We have optimized the wt% of GO in PMMA + P(VDF–TrFE) matrix and observed that 2 wt% of GO is the best choice to enhance morphological and mechanical properties.

We have prepared the 50-µm-thick nanocomposite thin films of PMMA + P(VDF–TrFE) with GO by using solution casting method. In this method, polymer powder of (PMMA + P(VDF–TrFE)) with ratio of 80:20 was added in 50 ml of DMF and kept in stirrer for 2 h at 45 °C. Again we have added dried graphene oxide and stirred magnetically for 1 h at 45 °C. The solution was subjected to ultrasonic vibration for 20 min and stirred again for 6 h at 45 °C for a homogeneous distribution of GO. The resultant solution was poured in optically plane glass plate inside vacuum oven. The samples were kept at 60 °C inside vacuum oven for 24 h to remove the effect of all volatile contents before use.

Mechanism

The concentration fluctuation of PMMA and P(VDF–TrFE) around GO will disturb homogeneous entanglements of hybrid samples. Especially, GO strongly interacts with polymer due to the largest surface area.

The GO will act as entanglement points in hybrid sample and its density increases with increasing concentration, finally leading to the enhancement of phase stability [49].

The polar C–O–C and C=O groups of PMMA interact with strong polar fluoride groups of P(VDF–TrFE) (Fig. 1). The PMMA segment in nanocomposite film suppresses the free volume (or defect) existing in the normal P(VDF–TrFE) copolymers due to decrease in crystallinity and crystal size. The resultant properties of polymer GO hybrid nanocomposites depend on the intrinsic characters of GO (i.e., size). The functional groups, –OH and –COOH, exist on the surface and pores of the GO which promote the hydrogen bonds between the GO to amine, benzenoid and quinoid of the polymer chain [57, 58].

Results and discussion

P(VDF–TrFE) and PMMA are known to polar polymer and having excellent miscibility in common solvent. The addition of PMMA affected the crystallinity of P(VDF–TrFE), including the dilution and impeding the influence on the overall

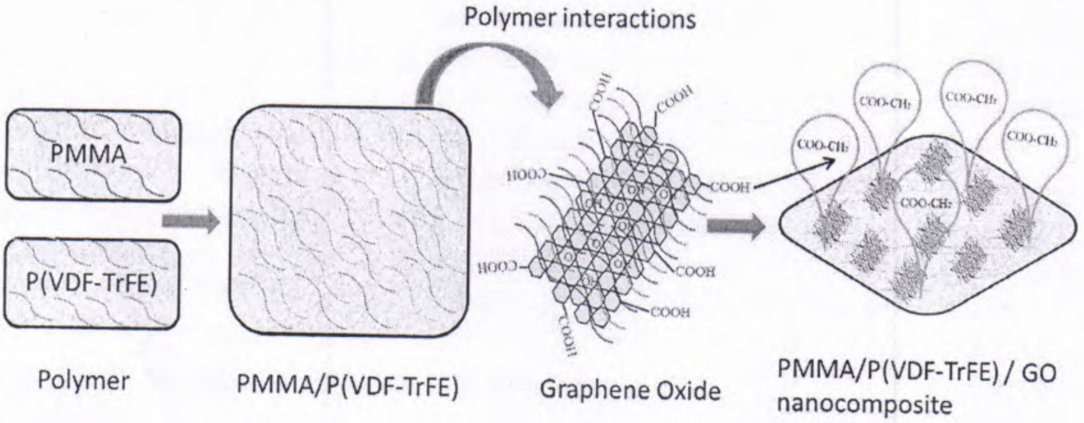

Fig. 1 Schematic diagram of polymer chain interactions with graphene oxide among polar groups of hybrid nanocomposites

crystallization of ferroelectric phase. The van der Waals forces and dipolar interactions strengthened the interfacial interactions. There are the van der Waals forces between the layers that can induce particle agglomeration, which will negatively affect the desirable properties [59]. The nanofiller aggregation means less surface contact between the polymers and GO consequently the polymer chains are free to move. The rigidity of PMMA + P(VDF–TrFE) and defects induced by GO agglomeration is responsible for measured microhardness. The tensile strength is strongly influenced by interfacial defects which lead to structure collapses. The GO and polymer have different surface energy; it causes agglomeration of GO in polymer matrix. This difference in surface energy could be minimized by proper sonication of solution or by using any inorganic chemical binder.

FTIR spectroscopy

Figure 2 shows the FTIR vibrational spectra of PMMA + P(VDF–TrFE) hybrid samples from 400 to 3600 cm^{-1}. The position of different functional groups of pristine and hybrid nanocomposites samples is given in Table 1.

The characteristic absorption bands of α-phase are observed at 482, 1175, 1271 and 1725 cm^{-1}, while characteristic absorption bands of β-phase are observed at 507, 658, 841 and 1436 cm^{-1} for pure P(VDF–TrFE) [60, 61] as shown in Fig. 2. The vibrational band at 507 cm^{-1} corresponds to bending vibrations mode of CF_2

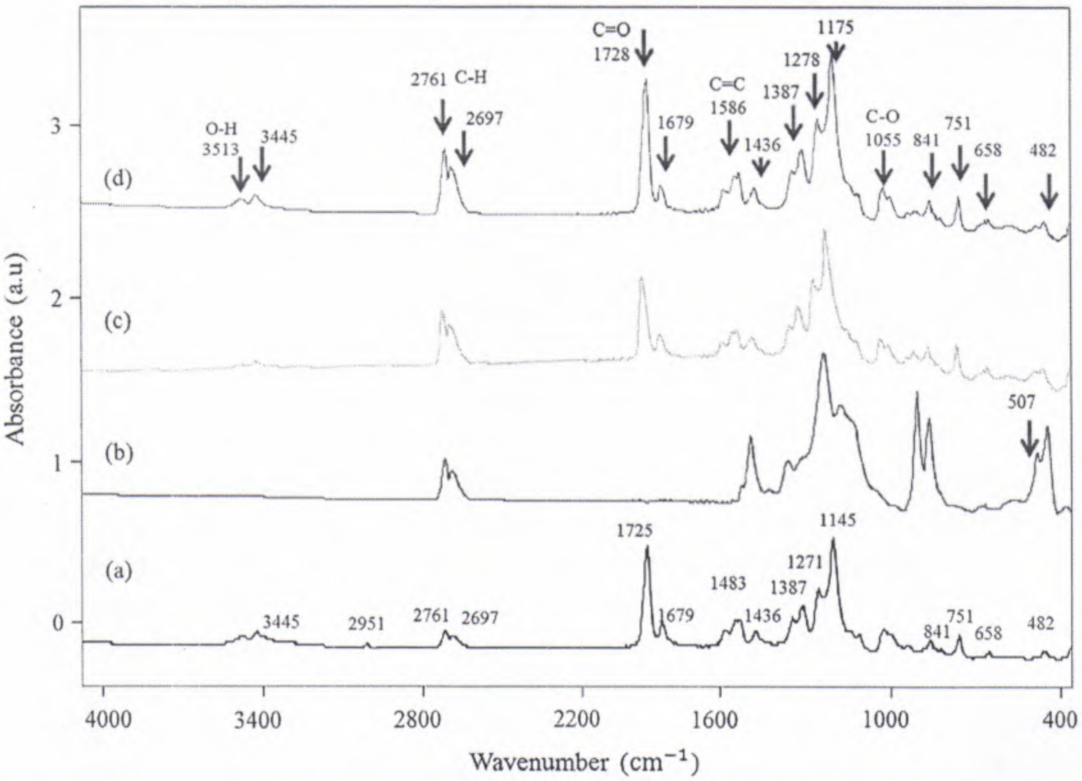

Fig. 2 FTIR spectrum of the **a** PMMA, **b** P(VDF–TrFE), **c** PMMA + P(VDF–TrFE) and **d** PMMA + P(VDF–TrFE) + 2 wt% GO for hybrid nanocomposites

Table 1 Characteristic of FTIR absorption for hybrid nanocomposites

Samples	Peak position (cm^{-1})	Phase	Assignment
PMMA	751		Wagging deformation (–CH_3)
	989		Bending (CH_3–O)
	1192		Skeletal chain
	1251		Stretching deformation (C=O)
	1435		Stretching (CH_2) and stretching, asymmetric(O–CH_3)
	1482		Bending asymmetric (CH_2)
	1712		Stretching (C=O)
	2951		$\nu_s(CH_2)$ vibration asymmetric
	3445		O–H symmetric, hydroxyl group
P(VDF–TrFE)	482	α	CF_2 bending and wagging
	507	β	CF_2 bending
	841	β	CH_2 rocking and CF_2 asymmetric stretching
	875	γ	CF_2 symmetric stretching
	1175	α	CH_2 wagging deformation
	1271	α	CF_2 symmetric stretching
	1436	β	CH_2 wagging deformation
	1725	α	CF out of plane deformation
PMMA + P(VDF–TrFE)	658	β	CF_2 bending and wagging
	1387		C–H stretching
	1679		Stretching vibration peaks of (C=C) groups
	2761		C–H stretching symmetric
	2697		C–H stretching
PMMA + P(VDF–TrFE) + 2 wt% GO	1055		C–O stretching bond
	1586		C=C stretching
	1728		C=O stretching
	3513		O–H symmetric, intermolecular bonded

dipoles and characteristic of TT (trans) conformation of the ferroelectric β-phase of P(VDF–TrFE). The O-CH_3 bending and stretching of PMMA are assigned to vibrational bands at 987 and 1483 cm^{-1}. The stretching frequency of C = O band corresponds to 1679 and 1271 cm^{-1}. Absorption band at 841 cm^{-1} shows the characteristic frequency of vinylidene compound. Stretching frequency at 1679 cm^{-1} is shifted to 1725 cm^{-1} which corresponds to C=O band of PMMA, in the hybrids (i.e., PMMA + P(VDF–TrFE) sample). This shift is due to carbonyl stretching frequencies of hybrids. This is also caused by specific interaction between the carbonyl groups of PMMA and the CH_2 groups of P(VDF–TrFE) which indicates the formation of hybrids. The results are supported by the analysis of PMMA + P(VDF–TrFE) hybrid by Coleman et al. [62]. We have investigated the influence of PMMA chains on formation of crystalline β-phase of P(VDF–TrFE). We found that the intensity of

841 cm^{-1} band is the function of PMMA and GO content. For example, intensity of PMMA + P(VDF–TrFE) hybrid at 841 cm^{-1} band decreases, when 2 wt.% of GO is added.

Figure 2 shows the FTIR characteristics of PMMA, P(VDF–TrFE), PMMA + P(VDF–TrFE) and 2 wt% GO contents samples. The P(VDF–TrFE) sample presents α-phase absorptions peak at 482, 1175 and 1271 cm^{-1}. It is clear from Fig. 2(b) that P(VDF–TrFE) sample exhibits nonpolar α-phase. FTIR results show that all absorption bands of the α-phase disappear, while new absorption bands at 841, 1271 and 1387 cm^{-1} have been observed, implying the transformation of the nonpolar α-phase to both electroactive β- and γ-phases [63, 64]. However, several absorption bands of pure PMMA at 841 and 1271 cm^{-1} are nearly according with these characteristic absorptions at 838, 1145 and 1271 cm^{-1} and disturb our judgment of whether electroactive β- and γ-phases do exist [65, 66]. Considering FTIR results, it is reasonable to understand that addition of PMMA transforms nonpolar α-phase to electroactive β- and γ-phases, but introduction of GO into PMMA + P(VDF–TrFE) hybrid sample gives the further change in FTIR spectra. In the FTIR spectra of P(VDF–TrFE) + PMMA + GO hybrid nanocomposites, though absorptions at 838 and 1271 cm^{-1} still exist, the absorption of the β-phase at 1278 cm^{-1} is hard to observe, which indicates that GO addition further induces electroactive γ-phase dominant phase structure.

The bands of PMMA + P(VDF–TrFE) + GO at 2995 cm^{-1} and 2951 cm^{-1} represent the asymmetrical and symmetric stretching of CH_2, respectively. The presence of different oxygen functionalities in the graphene oxide was confirmed at 3513 cm^{-1} (O–H stretching). The FTIR results confirm with XRD results by exposing the same phenomenon for electroactive β-phase intensity variation with the GO concentration and show a linear increasing trend up to 2 wt% GO within PMMA + P(VDF–TrFE) polymer matrix [67].

Atomic force microscopy

The grain size, particle size and roughness of the film (~ 32.21 nm, 79.65 nm and 41.02 nm), respectively, for 2 wt% GO of PMMA + P(VDF–TrFE) hybrid nanocomposite film were estimated by using AFM. The particle distribution and surface 2D topography images are shown in Fig. 3a–d. AFM demonstrates the structural morphology of PMMA + P(VDF–TrFE) + 2 wt% GO. In addition to that, a new observation is seen, i.e., at the surface of thin films, GO particles are present having size less than 2 μm. Roughness and average grain size are found to be increased for PMMA + P(VDF–TrFE) + GO hybrid nanocomposites. The RMS roughness and average grain size of GO and its hybrid nanocomposite were found to be 41.02 and 32.21 nm, respectively.

The topography AFM images for all samples in the contact mode are displayed in Fig. 3(a–d) which shows the topography of surface PMMA, P(VDF–TrFE), PMMA + P(VDF–TrFE) and PMMA + P(VDF–TrFE) + GO hybrid nanocomposite samples. P(VDF–TrFE) sample of this type of structure differs from hybrid nanocomposites. The detailed heights along with the yellow

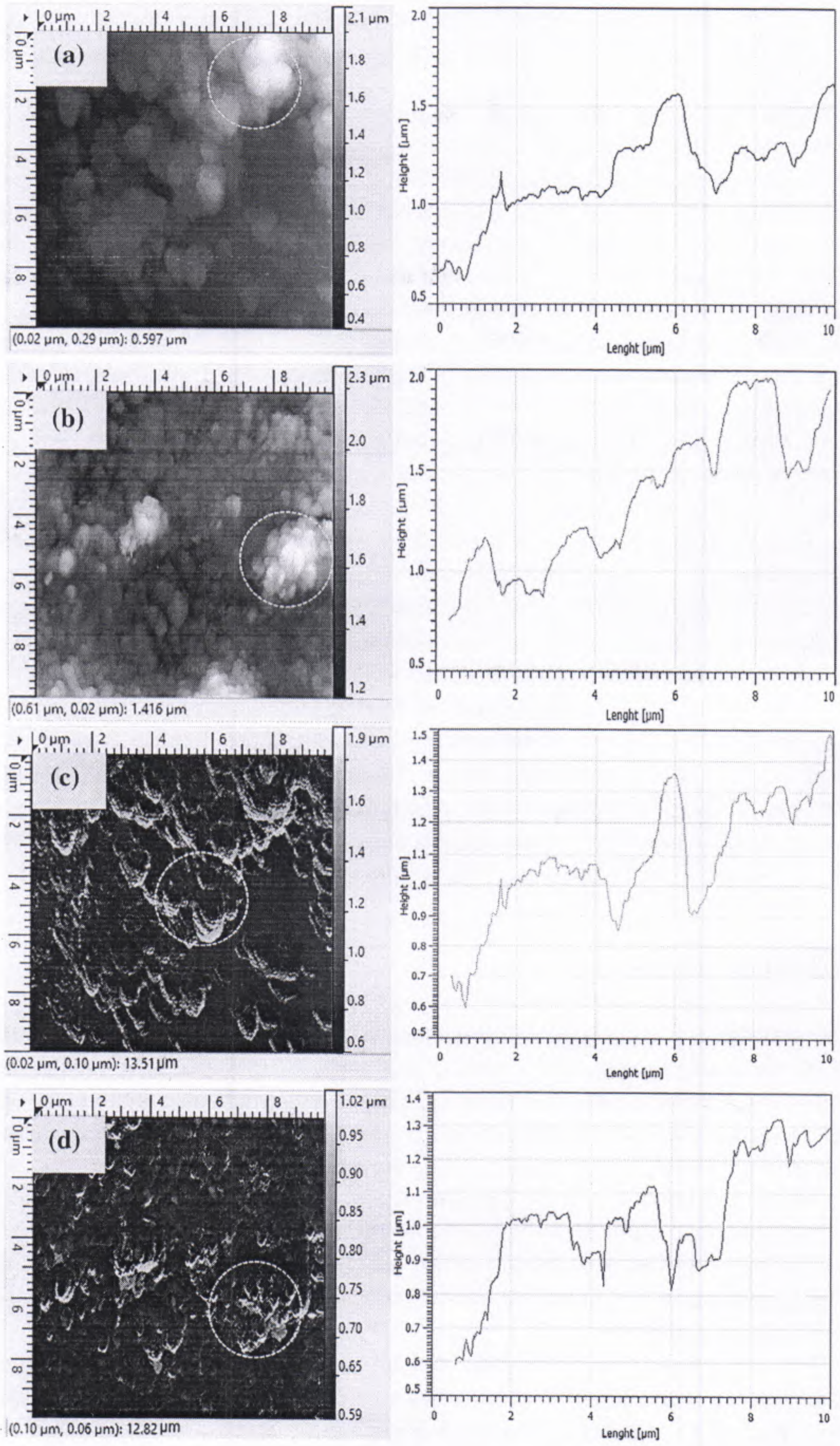

Fig. 3 AFM 2D images of the **a** PMMA, **b** P(VDF–TrFE), **c** PMMA + P(VDF–TrFE) and **d** PMMA + P(VDF–TrFE) + 2 wt% GO for hybrid nanocomposites

dotted circle of Fig. 3a–d are shown by the right sided height curve. The roughness of P(VDF–TrFE) and PMMA sample is 44.11 and 48.02 nm, respectively. The roughness of hybrid sample significantly enhances as shown in Fig. 3c, while roughness of PMMA + P(VDF–TrFE) + GO hybrid nanocomposites decreases (i.e., Fig. 3d). Figure 3 shows the several wide and lofty peaks, manifesting the current aggregation of large grains. The microhardness of material is the function of grain size. AFM images are characterized by separate lamellar crystallites have different grain size, which affects the microhardness.

AFM recognizes two phases (i.e., hard and soft phase) in 3D images. Microhardness results support the hybrid nanocomposites, which are more crystalline as well as hard in comparison with pristine system and finally exhibit mostly hard phases as shown in Fig. 4a–b. The PMMA and P(VDF–TrFE) samples have hard phases with higher value of surface roughness. However, surface roughness of hybrid sample decreases in presence of GO.

Structural changes in hybrid nanocomposite samples are caused by change in sizes of lamellar crystal by introducing GO in polymer matrix. AFM also illustrates the surface morphology of PMMA, P(VDF–TrFE) and PMMA + P(VDF–TrFE) + GO hybrid nanocomposite samples. The P(VDF–TrFE) images display small voids in the interconnected morphology. The 2D and 3D images of AFM represent the reduction in microvoids with 2 wt% of GO, which corresponds to a reduction in surface roughness as shown in Table 2. The surface roughness is observed to be lower for lower concentration of 2 wt% GO in PMMA + P(VDF–TrFE) hybrid nanocomposites. The decrease in void size in nanocomposite samples represents uniform dispersion of GO. This finally causes the reduction in particle size and grain size as shown in Table 2. In a nanocomposites sample, the particle size is macrophenomenon, while grain size is

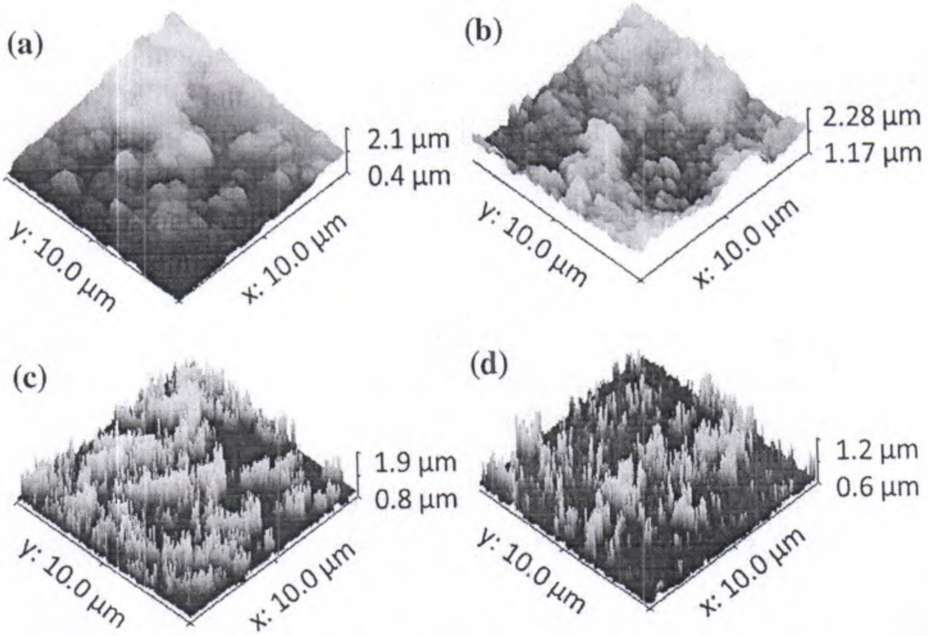

Fig. 4 AFM 3D images of the **a** PMMA, **b** P(VDF–TrFE), **c** PMMA + P(VDF–TrFE) and **d** PMMA + P(VDF–TrFE) + 2 wt% GO for hybrid nanocomposites

Table 2 AFM parameters of hybrid nanocomposites

Samples	Particle size(nm)	Average grain size (nm)	Average roughness size (nm)
PMMA	86.52	80.40	48.02
P(VDF–TrFE)	58.26	53.18	44.11
PMMA + P(VDF–TrFE)	90.91	26.72	53.17
PMMA + P(VDF–TrFE) + 2 wt% GO	79.65	32.21	41.02

microphenomenon. In the present study, grain size was in the range of 48 nm. This range of grain size occurs due to the quantum effect [68–70].

Microhardness and tensile strength

The measurement of the microhardness variation at room temperature is subjected to volume fraction of spherulites during primary crystallization of a number of polymer materials [71–73]. The following equation relates the microhardness parameters of polymers:

$$H = H_{\mathrm{sph}}\varnothing + H_{\mathrm{a}}\left(1 - \varnothing\right) \tag{1}$$

where H_{sph} and H_{a} are the microhardness values of the spherulitic and the amorphous inter-spherulitic regions in polymer, respectively. In general, microhardness values during primary crystallization are shown to be directly proportional to the total emerging crystallinity in the sample [74, 75]. It arises from the direct proportionality between the microhardness of the spherulites and the fraction of crystalline material within them (i.e., α_L) [71, 76, 77]:

$$H_{sph} = H_{c\alpha_L} + H_a\left(1 - \alpha_L\right) \tag{2}$$

Combination of Eqs. (1 and 2) yields:

$$H = H_{c\alpha} + H_\alpha(1 - \alpha) \tag{3}$$

It is reported that the microhardness and other mechanical properties of polymers are enhances with carbonaceous nanofiller, however, it is not necessary for electrical properties of GO based polymer nanocomposites [78, 79].

The decrease in microhardness of PMMA + P(VDF–TrFE) + GO hybrid nanocomposites is due to less uniaxial orientation of GO or aggregation of GO. The GO exhibits hydroxyl, carboxyl and carbonyl oxygen-containing functional groups, which are hydrophilic and highly reactive nano-reinforcements in aqueous system. The decrease in microhardness of GO nanocomposites sample as compared to pure PMMA and PMMA + P(VDF–TrFE) hybrid is due to uniaxial orientation of GO [80, 81].

Microhardness test is developed to measure the microhardness of materials. It can be used for all materials and has one of the broadest scales among microhardness tests. Microhardness is determined when force is applied by an indenter to

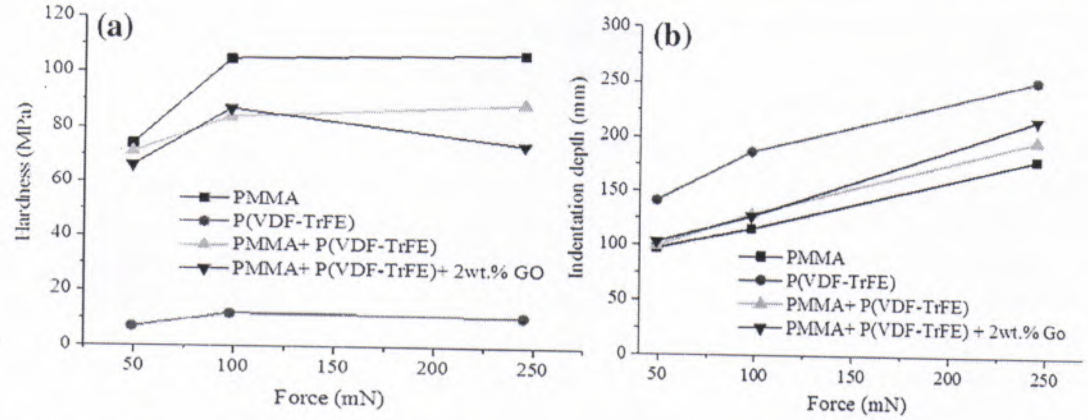

Fig. 5 The variations in force **a** microhardness at room temperature and **b** force–displacement curves of indentation depth for hybrid nanocomposites

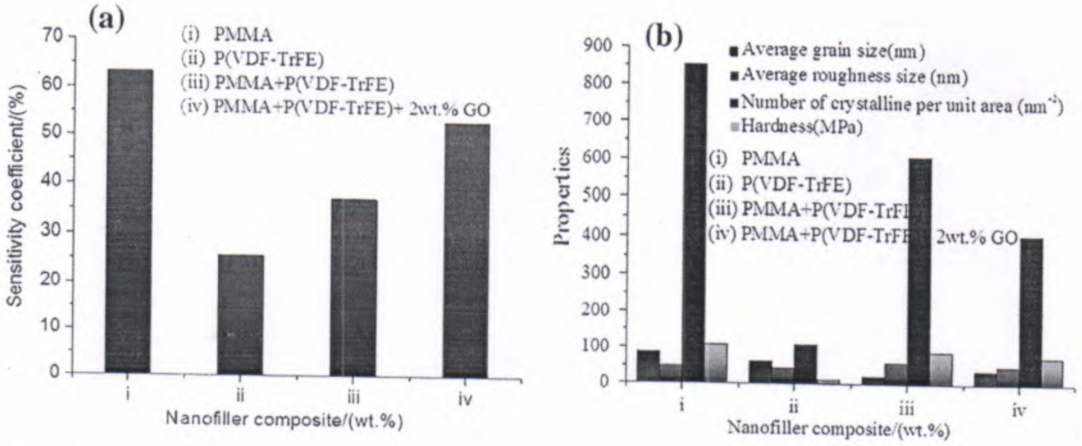

Fig. 6 Effect of nanofiller on, **a** sensitivity coefficients and **b** related properties of hybrid nanocomposites

the surface of samples. In this study, the mechanical characterizations of nanocomposites materials are performed using AFFRI brand DM-8 motorized digital microhardness tester. The microhardness values (H) of different applied loads are in the range of 49.03–245.2 Nm. This was calculated by using Eqs. 4 and 5 [82]. F is the load applied in sample surface, *A* is the micrometer square surface area and d is the indented edge length.

$$H = \frac{F}{A} \tag{4}$$

$$H = 14.22F/d^2 \tag{5}$$

The load-dependent microhardness and indentation depth are shown in Fig. 5a–b. Figure 6a–b shows representative load displacement curves from nanoindentation measurement performed on PMMA + P(VDF–TrFE) + GO hybrid nanocomposites. The standard Oliver and Pharr method was used for the analysis of microhardness (H), yield strength (Y_S), average grain size (G_a), average roughness (*R*a), tensile strength (T_S) and number of crystalline per unit area (*N*) [83–86]. These parameters are presented in Table 3.

The indentation depths of less than 250 mm (245 mN) are observed in load–displacement curve. Figure 5a shows linear elastic (reversible) loading and unloading behaviour of load–displacement curve. It is due to fact that indentation at lower value of load did not prove the damage of polymer surface.

Figure 5a reveals that the microhardness is maximum at 100 mN force for all samples, however, PMMA shows maximum value of microhardness. After 100 mN force, the microhardness is gradually decreased.

The microhardness of polymer nanocomposites depends on the nature of polymer nanofiller interface. The microhardness will increase, if nanofiller concentrates on the interface due to good interface adhesion, however, microhardness decreases due to poor interface adhesion. The decrease in microhardness in hybrid nanocomposites samples with GO is probably due to uniaxial orientation of GO or agglomeration of the GO in polymer matrix [87, 88]. The agglomeration of GO is discarded from AFM study, therefore, uniaxial orientation of GO is the only reason for decrease in microhardness.

The indentation depth of P(VDF–TrFE) is the highest as compared to PMMA, PMMA + P(VDF–TrFE) and PMMA + P(VDF–TrFE) + GO samples. We have observed that the addition of GO in PMMA + P(VDF–TrFE) composite slightly decreases the indentation depth in general. It is due to fact that the plastic deformation of PMMA + P(VDF–TrFE) is controlled by GO.

Tensile and yield strengths were computed from the following relation [89, 90]:

$$T_s = -99.8 + 3.734\mathrm{H} \tag{6}$$

$$Y_s = -90.7 + 2.876H \tag{7}$$

where T_s tensile strength, Y_s yield strength and H microhardness.

The microhardness parameters of PMMA, P(VDF–TrFE), PMMA + P(VDF–TrFE) and PMMA + P(VDF–TrFE) + 2 wt% GO samples are shown in Table 3. The addition of GO in PMMA + P(VDF–TrFE) reduces the T_S due to its uniaxial orientation. The tensile strength values of P(VDF–TrFE) decreases with combination of PMMA and GO. The P(VDF–TrFE) showed the lowest yield strength and its Y_S increases with combination of PMMA/GO due to brittle essence of PMMA [91].

It is seen that tensile and yield strengths are negatively correlated with average grain size and surface roughness, whereas they are positively correlated with the number of crystalline or number of particle per unit area (i.e., Table 3).

The P(VDF–TrFE) is a crystalline as well as amorphous polymer. P(VDF–TrFE) is the copolymers of PVDF that have offered a straight forward approach to obtaining the electroactive phase due to presence of pores. Consequently, it will decrease the mechanical properties [92–94].

In the present study, the nanoindentation measurements are also correlated with AFM images (Fig. 2a–d) due to similar surface profile of all samples after nanoindentation. The GO is harder than PMMA + P(VDF–TrFE) in

Table 3 Microhardness parameters of hybrid nanocomposites

Samples	F (mN)	H (MPa)	Y_S (N mm^{-2})	T_S (N mm^{-2})	G_a (nm)	R_a (nm)	(N) (1 mm^{-2})
PMMA	245	107	217	299.7	86	47	851.6
P(VDF–TrFE)	245	11	59	232.5	61	43	107.2
PMMA + P(VDF–TrFE)	245	89	165.2	158.7	22	59	607.7
PMMA + P(VDF–TrFE) + 2 wt% GO	245	74	122.2	176.5	38	51	404.4

Microhardness (H), Applied load (F), Yield strength (Y_S), Average grain size (G_a), Average Roughness (Ra), Tensile strength (T_S) and Number of crystalline per unit area (N)

nanocomposites samples, hence during indentation run, if indenter falls in the nanocomposites matrix, where GO is present, the depth of indentation would reduce significantly and there would be an increase in surface deformation around the region.

Sensitivity coefficient

The several parameters such as force, diameter/thickness of sample and depth are affecting the microhardness of sample. They are also responsible for uncertainty on measurement. The uncertainty in measurement is given by following relation [86]:

$$c = \frac{\Delta H}{\Delta x} \tag{8}$$

where Δx *is* the input parameter that has been changed (load) and ΔH is the change in microhardness. The sensitivity coefficient represents accuracy of microhardness measurement. The sensitivity coefficients (c) can be analyzed from microhardness measurements. For sensitivity analysis, we observed that the sensitivity of PMMA is more than P(VDF–TrFE) and PMMA + P(VDF–TrFE) and PMMA + P(VDF–TrFE) + GO samples as shown in Fig. 6a.

Contact angles

The contact angle for PMMA, P(VDF–TrFE), PMMA + P(VDF–TrFE), PMMA + P(VDF–TrFE) + GO samples with respect to water and glycerin has been measured by very simple sessile drop method [95].

The surface energy associated with polymer nanocomposites samples with respect to water and glycerin was determined by measuring contact angle. It is reported in the literature [96] that PMMA is more hydrophobic than P(VDF–TrFE). The mixing of P(VDF–TrFE) in PMMA matrix will significantly affect the hydrophobicity of PMMA. The surface of the PMMA + P(VDF–TrFE) + GO hybrid nanocomposites contains some of the GO particles and this eventually decreased the hydrophobic nature. It could be clearly seen in Fig. 7a–d by variation in contact angle.

It is clearly observed that contact angles for PMMA + P(VDF–TrFE) + GO samples with respect to water and glycerin are 79.24°, 83.08°, 62.30°, 81.20° and 69.55°, 81.64°, 61.36°, 75.27°, respectively, as shown in Fig. 8a. The forces acting on surface of the PMMA + P(VDF–TrFE) and PMMA + P(VDF–TrFE) + GO samples are vanished as compared to pristine sample of PMMA and PMMA + P(VDF–TrFE) samples due to polar nature of water and glycerine. Therefore, surface free energy decreases at the surface of PMMA + P(VDF–TrFE) and PMMA + P(VDF–TrFE) + GO samples.

The contact angles were measured in four different places of sample with 1 μl of liquid. Owens and Wendt equation [97, 98] was used to calculate the solid surface energy:

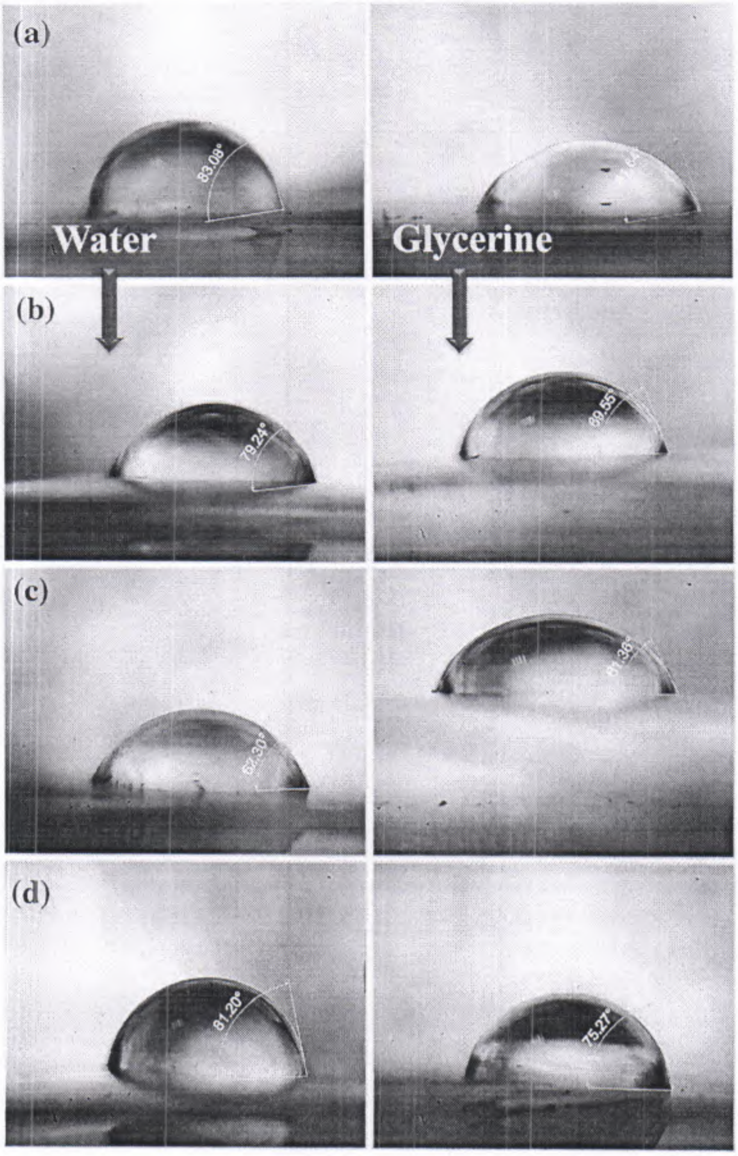

Fig. 7 Contact angle images of the **a** PMMA, **b** P(VDF–TrFE), **c** PMMA + P(VDF–TrFE) and **d** PMMA + P(VDF–TrFE) + 2 wt% GO for hybrid nanocomposites

$$\cos\theta = \left[2\sqrt{\gamma_{\mathrm{s}}^{\mathrm{d}}} \left(\frac{\sqrt{\gamma_{\mathrm{L}}^{\mathrm{d}}}}{\gamma_{\mathrm{L}}} \right) + 2\sqrt{\gamma_{\mathrm{s}}^{\mathrm{p}}} \left(\frac{\sqrt{\gamma_{\mathrm{L}}^{\mathrm{p}}}}{\gamma_{\mathrm{L}}} \right) - 1 \right] \tag{9}$$

where θ is the contact angle, γ_{s} and γ_{L} are the solid and liquid surface energy, respectively. γ_s^d and γ_s^p are dispersion forces and polar forces of total surface energy ($\gamma = \gamma_s^d + \gamma_s^p$).

The surface energy with respect to polar liquid in polymer is caused by interaction of polar molecules with solid surface that has permanent dipole moment. However, dispersive part is originated due to random fluctuations in the electron density when solid and liquid interacted together.

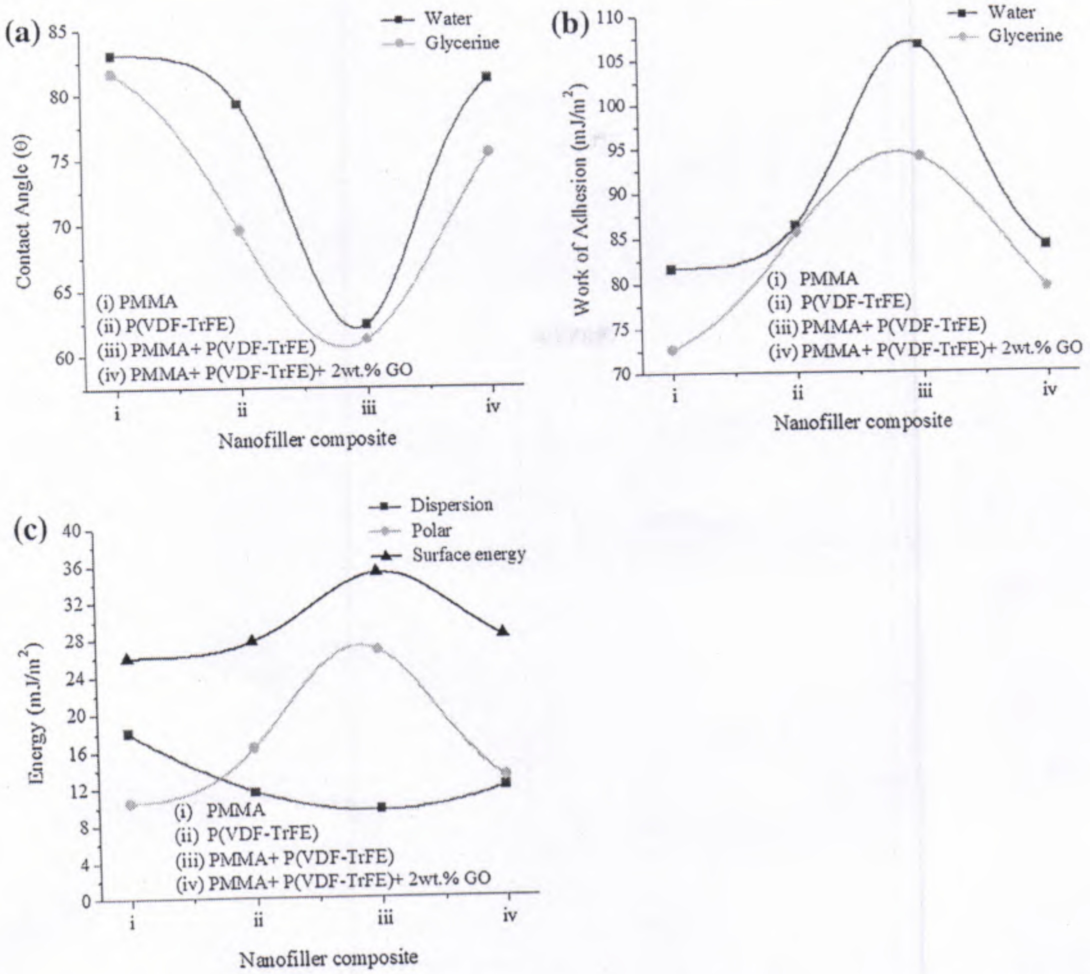

Fig. 8 The effect of nanofiller composite **a** contact angle, **b** work of adhesion and **c** surface energy for hybrid nanocomposites

The measurement of contact angle of polymer nanocomposites with two kinds of liquids with known surface energy components, γ_s^d and γ_s^p explained by Rohan et. al [99].

The calculated value of surface energy for PMMA-based nanocomposites samples is presented in Table 4. The surface energy of PMMA is increased from 26.04 to 35.46 mJ m^{-2} when P(VDF–TrFE) is added. However, hydrophilicity of PMMA is related to the contributions of dipole–dipole and dipole–induced dipole interactions.

Table 4 Contact angle (θ) of work of adhesion (W_A) and surface energy (γs) of hybrid nanocomposites

Samples	(θ)		(W_A) (mJ m^{-2})		(γs) (mJ m^{-2})
	Water	Glycerine	Water	Glycerine	
PMMA	83.08	81.64	81.62	72.61	26.04
P(VDF–TrFE)	79.24	69.55	86.38	85.58	27.62
PMMA + P(VDF–TrFE)	62.30	61.36	106.65	93.98	35.46
PMMA + P(VDF–TrFE) + 2 wt% GO	81.20	75.27	84.01	79.35	28.47

Also, the contact angle and adhesion work for PMMA + P(VDF–TrFE) + 2 wt% GO hybrid nanocomposites are affected by the water. The surface roughness and molecular interactions are the main reasons for these results shown in Fig. 8(b).

The weak interaction of $-CF_2$ groups of P(VDF–TrFE) is the reason of its weak hydrophobicity [95]. The PMMA and PVDF have almost similar dispersion component (γ_s^d), but addition of P(VDF–TrFE) in PMMA enhances the polar component (γ_s^p) and finally increases the surface energy of nanocomposites as presented in Fig. 8(c). It has been observed that the surface composition of PMMA+P(VDF–TrFE) +GO sample was highly influenced by GO, which reflects the variation in surface energy.

Generally, the crystalline nuclei are formed at the end of the polymer chain, and size of the nuclei is independent on isolated amorphous chains of polymer like PMMA. Table 3 shows that the crystallinity of PMMA is greater than crystallinity of P(VDF–TrFE), however, PMMA+ P(VDF–TrFE) + GO hybrid nanocomposites have higher crystalline than the P(VDF–TrFE) and less crystalline than PMMA. It may be due to agglomeration of GO being able to reduce the electrostatic force between the hybrid polymer matrix and the graphene oxide, which is responsible for reduction in crystallinity of the hybrid nanocomposites (Fig. 6b) [100, 101].

Thus, hydrophilicity of individual and composite samples is affected the microhardness, surface enrichment and crystallization. Factors affecting the surface hydrophilicity of polymer nanocomposites are reported in the literature [98]. In general, the hydrophilicity of polymer is the part of (i) crystallization domains contraction on the sample surface and (ii) surface enrichment tendency of polymer. The literature [102] demonstrates that contact angle measurement provides the information about level of intercalation between nanofiller and the polymer.

The decrease in contact angle is subjected to increase in nanofiller concentration. This means that intercalation between nanofiller and polymer enhances. It has been verified by AFM technique.

Conclusions

FTIR and AFM characterization results confirm the formation of hybrid nanocomposite of PMMA with P(VDF–TrFE) and GO. The contact angle measurement confirms the intercalation of GO with polymer matrix and its hydrophobic properties.

In summary, we have emphasized attractive applications of the microindentation method to the study of the mechanical properties of polymer nanocomposites surfaces. The isolated microhardness (H) of value up to 107 MPa could be easily scaled down to develop submicron level uniform small crystal of P(VDF–TrFE). In addition, the surface structural analysis of polymer/hybrid nanocomposites samples by AFM technique and contact angle measurement supports the results of mechanical properties by means of uniaxial orientation of GO and its dispersion in polymer matrix. The improvement in microhardness and yield strength of hybrid nanocomposites is found to mainly depend on the concentration of GO in polymer interface adhesion. It is concluded that our attempt of this study will help to understand the fundamental concept of "nano" effect in polymer, liquid–solid interaction in hybrid nanocomposites system by measuring contact angle and pave the way for industrial applications in several flexible electronic devices.

Acknowledgements This work was financially supported by Indo-Belarusian Scientific Cooperation, DST, New Delhi (India) (Letter No.INT/BLR/P-13/2016) which is gratefully acknowledged. One of the authors Rohan Sagar acknowledges the University Grant commission (UGC), New Delhi (India) for proving research fellowship award number (RGNF-2017-18-SC-UTT-29088).

References

1. Reece TJ, Ducharme S, Sorokin AV, Poulsen M (2003) Nonvolatile memory element based on a ferroelectric polymer Langmuir–Blodgett film. Appl Phys Lett 82:142–144
2. Naber RCG, Tanase C, Blom PWM, Gelinck GH, Marsman AW, Touwslager FJ, Setayesh S, de Leeuw DM (2005) High-performance solution-processed polymer ferroelectric field-effect transistors. Nat Mater 4:243–248
3. Mir SH, Hasan PMZ, Danish EY, Aslam M (2020) Pd-induced phase separation in poly (methyl methacrylate) telopolymer: synthesis of nanostructured catalytic Pd nanorods. Colloid Polym Sci 298:441–448
4. Fujisaki S, Ishiwara H, Fujisaki Y (2007) Poly (vinylidene fluoride–trifluoroethylene)/barium titanate nanocomposite for ferroelectric nonvolatile memory devices. Appl Phys Lett 90:162–192
5. Salimi A, Yousef AA (2004) Conformational changes and phase transformation mechanisms in PVDF solution-cast films. J Polym Sci Part B Polym Phys 42:3487–3495
6. Naber RCG, Blom PWM, Marsman AW, de Leeuw DM (2004) Low voltage switching of a spin cast ferroelectric polymer. Appl Phys Lett 85:2032–2034
7. Noda K, Ishida K, Kubono A, Horiuchi T, Yamada H, Matsushige K (2003) Remanent polarization of evaporated films of vinylidene fluoride oligomers. J Appl Phys 93:2866–2870
8. Xia F, Xu HH, Razavi B, Cheng Z-Y, Zhang QM (2002) Dependence of threshold thickness of crystallization and film morphology on film processing conditions in poly(vinylidene fluoride–trifluoroethylene) copolymer thin films. J Appl Phys 92(6):3111–3115
9. Xia F, Xu H, Fang F, Razavi B, Cheng Z-Y, Lu Y, Xu B, Zhang QM (2001) Thickness dependence of ferroelectric polarization switching in poly(vinylidene fluoride–trifluoroethylene) spin cast films. Appl Phys Lett 78:1122–1124
10. Urayama K, Tsuji M, Neher D (2000) Layer-thinning effects on ferroelectricity and the ferroelectric to paraelectric phase transition of vinylidene fluorid trifluoroethylene copolymer layers. Macromolecules 33:8269–8279
11. Xia F, Zhang QM (2004) Schottky emission at the metal polymer interface and its effecton the polarization switching of ferroelectric poly(vinylidenefluoride-trifluoroethylene) copolymer thin films. Appl Phys Lett 85(10):1719–1721
12. Choudhuri JR, Vanzo D, Madden PA, Salanne M, Bratko D, Luzar A (2016) Dynamic response in nanoelectrowetting on a dielectric. ACS Nano 10:8536–8544
13. Schneemilch M, Welters WJJ, Hayes RA, Ralston J (2000) Electrically induced changes in dynamic wettability. Langmuir 16:2924–2927
14. Gersappe D (2002) Molecular mechanisms of failure in polymer nanocomposites. Phys Rev Lett 89:058301–058311
15. Puente Orench I, Ania F, Baer E, Hiltner A, Bernal T, Baltá Calleja FJ (2004) Basic aspects of microindentation in multilayered poly (ethylene terephthalate)/polycarbonate films. Philos Mag 84(18):1841–1852
16. Baltá-Calleja FJ, Cagiao ME, Adhikari R, Michler GH (2004) Relating microhardness to morphology in styrene/butadiene block copolymer/polystyrene blends. Polymer 45(1):247–254
17. Henning S, Michler GH, Ania F, Balta-Calleja FJ (2005) Microhardness of α-and β-modified isotactic polypropylene at the initial stages of plastic deformation: analysis of micromechanical processes. Colloid Polym Sci 283(5):486–495
18. Flores A, Pieruccini M, Stribeck N, Funari SS, Bosch E, Balta´-Calleja FJ (2005) Structure formation in poly (ethylene terephthalate) upon annealing as revealed by microindentation hardness and X-ray scattering. Polymer 46(22):9404–9410

19. Ania F, Broza G, Mina MF, Schulte K, Roslaniec Z, Balta-Calleja FJ (2006) Micromechanical properties of poly (butylene terephthalate) nanocomposites with single-and multi-walled carbon nanotubes. Compos Interfac 13(1):33–45
20. Flores A, Mathot VBF, Michler GH, Adhikari R, Balta´ -Calleja FJ, (2006) Novel aspects of microindentation hardness in very low crystallinity ethylene-1-octene copolymers: a model for deformation. Polymer 47(15):5602–9
21. Uchiyama T, Suyama M, Alam MM, Asano T, Henning S, Flores A, Mina MF (2007) Layer structure formation in oriented poly (ethylene terephthalate) relating to micromechanical properties. Polymer 48(2):542–555
22. Shahdad SA, McCabe JF, Bull S, Rusby S, Wassell RW (2007) Hardness measured with traditional Vickers and Martens hardness methods. Dent Mater 23(9):1079–1085
23. Bembey AK, Oyen ML, Bushby AJ, Boyde A (2006) Viscoelastic properties of bone as a function of hydration state determined by nanoindentation. Philos Mag 86:5691–5703
24. Godara A, Raabe D, Green S (2007) The influence of sterilization processes on the micromechanical properties of carbon fiber-reinforced PEEK composites for bone implant applications. Acta Biomater 3(2):209–220
25. Liu Y, Wang M (2007) Fabrication and characteristics of hydroxyapatite reinforced polypropylene as a bone analogue biomaterial. J Appl Polym Sci 106(4):2780–2790
26. Vaziri A, Lee H, Mofrad MK (2006) Deformation of the cell nucleus under indentation: mechanics and mechanisms. J Mater Res 21(8):2126–2135
27. Kaufman JD, Miller GJ, Morgan EF, Klapperich CM (2008) Time-dependent mechanical characterization of poly (2-hydroxyethyl methacrylate) hydrogels using nanoindentation and unconfined compression. J Mater Res 23(5):1472–1481
28. Lu HB, Huang G, Wang B, Mamedov A, Gupta S (2006) Characterization of the linear viscoelastic behavior of single-wall carbon nanotube/polyelectrolyte multilayer nanocomposite film using nanoindentation. Thin Solid Film 500(2):197–202
29. Owens FJ (2006) Raman and mechanical properties measurements of single walled carbon nanotube composites of polyisobutylene. J Mater Chem 16(5):505–508
30. Chiu WM, Chang YA, Kuo HY, Lin MH, Wen HC (2008) A study of carbon nanotubes/biodegradable plastic polylactic acid composites. J Appl Polym Sci 108(5):3024–3030
31. Liu T, Phang IY, Shen L, Chow SY, Zhang WD (2004) Morphology and mechanical properties of multiwalled carbon nanotubes reinforced nylon-6 composites. Macromolecules 37(19):7214–7222
32. Chavarria F, Paul DR (2006) Morphology and properties of thermoplastic polyurethane nanocomposites: effect of organoclay structure. Polymer 47(22):7760–7773
33. Shen Lu, In YP, Tianxi L, Kaiyang Z (2004) Nanoindentation and morphological studies on nylon 66/organoclay nanocomposites II effect of strain rate. Polymer 45(24):8221–8229
34. Wornyo E, Gall K, Yang F, King W (2007) Nanoindentation of shape memory polymer networks. Polymer 48(11):3213–3225
35. Chen CH, Sun YY (2006) Mechanical properties of blocked polyurethane/epoxy interpenetrating polymer networks. J Appl Polym Sci 101(3):1826–1832
36. Flores A, Pietkiewicz D, Stribeck N, Roslaniec Z, Baltá Calleja FJ (2001) Structural features of random polyester: amide copolymers as revealed by X-ray scattering and microindentation hardness. Macromolecules 34(23):8094–8100
37. Marsh DM (1964) Alan Howard cottrell plastic flow in glass. Proc R Soc Lond A279420–435
38. Hirst W, Howse MGJW (1969) The indentation of materials by wedges. Pro R Soc Lond Math Phys Sci 311(1506):429–444
39. Mir SH, Ochiai B (2016a) Development of hierarchical polymer@Pd nanowire-network: synthesis and application as highly active recyclable catalyst and printable conductive ink. Chem Open 5(3):213–218
40. Mir SH, Ochiai B (2017) One-pot fabrication of hollow polymer@Ag nanospheres for printable translucent conductive coatings. Adv Mater Interfaces 4(14):1601198
41. Theophile N, Jeong HK (2017) Electrochemical properties of poly (vinyl alcohol) and graphene oxide composite for supercapacitor applications. Chem Phys Lett 669:125–129
42. Parrey KA, Aziz A, Ansari SG, Mir SH, Khosla A, Niazi A (2018) Synthesis and characterization of an efficient hole-conductor free halide perovskite $CH_3NH_3PBI_3$ semiconductor absorber based photovoltaic device for IOT. J Electrochem Soc 165(8):3023–3029

43. Mir SH, Nagahara LA, Thundat T, Mokarian-Tabari P, Furukawa H, Khosla A (2018) Review: organic-inorganic hybrid functional materials—an integrated platform for applied technologies. J Electrochem Soc 165(8):3137–3156
44. Morozov SV, Novoselov KS, Katsnelson MI (2008) Giant intrinsic carrier mobilities in graphene and its bilayer. Phy Rev Lett 100:016602
45. Hirata M, Gotou T, Horiuchi S, Fujiwara M, Ohba M (2004) Thin-film particles of graphite oxide 1: high-yield synthesis and flexibility of the particles. Carbon 42(14):2929–2937
46. Habte AT, Ayele DW (2019) Synthesis and characterization of reduced graphene oxide (rGO) started from graphene oxide (GO) using the tour method with different parameters. Adv Mater Sci Eng 5:1–9
47. Ali A, Al-Enizi AM, M, Ali AM, Alamgir K, (2016) Influence of graphene oxide on mechanical, morphological, barrier, and electrical properties of polymer membranes. Arab J Chem 9(2):274–286
48. Mir SH, Ochiai B (2016b) Fabrication of polymer-Ag honeycomb hybrid film by metal complexation induced phase separation at the air/water interface. Macromol Mater Eng 301(9):1026–1031
49. Sahin O, Uzun O, Kölemen U, Uçar N (2007) Dynamic hardness and reduced modulus determination on the (001) face of B-Sn single crystals by a depth sensing indentation technique. J Phys Condens Matter 19:306001
50. Sangwal K, Surowska B, Blaziak P (2002) Analysis of the indentation size effect in the microhardness measurement of some cobalt-based alloys. Mater Chem Phys 77:511
51. Graaf DD, Braciszewicz M, Hintzen HT, Sopicka-Lizer M, De WG (2004) The influence of the composition on (the load-dependence of) the microhardness of Y–;Si–;Al–;O–;N glasses as measured by Vickers indentation. J Mater Sci 39:2145
52. Lopesa ESN, Cremascoa A, Afonsob CRM, Caram R (2011) Effects of double aging heat treatment on the microstructure, vickers hardness and elastic modulus of Ti–Nb alloys. Mater Charact 62:673–680
53. Tosun M, Ataoglu S, Arda L, Ozturk O, Asikuzun E, Akcan D, Cakiroglu O (2014) Structural and mechanical properties of ZnMgO nanoparticles. Mater Sci Eng 590:416–422
54. Ozturk O, Cetinkara HA, Asikuzun E, Akdogan M, Yilmazlar M, Terzioglu C (2011) Investigation of mechanical and superconducting properties of iron diffusion-doped Bi-2223 superconductors. J Mater Sci Mater Electron 22(9):1501–1508
55. Arda L, Ozturk O, Asikuzun E, Ataoglu S (2013) Structural and mechanical properties of transition metals doped ZnMgO nanoparticles. J Powder Technol 235:479–484
56. Cote LJ, Kim F, Huang J (2009) Langmuir-Blodgett assembly of graphite oxide single layers. J Am Chem Soc 131:1043–1049
57. Wang H, Hao Q, Yang X, Lu L, Wang X (2010) Effect of graphene oxide on the properties of its composite with polyaniline. ACS Appl Mater Interfaces 2(3):821–828
58. Konwer S, Guha AK, Dolui SK (2012) Graphene oxide-filled conducting polyaniline composites as methanol-sensing materials. J Mater Scie 48(4):1729–1739
59. Hermann J, DiStasio RA, Tkatchenko A (2017) First-principles models for van der waals interactions in molecules and materials: concepts, theory, and applications. Chem Rev 117(6):4714–4758
60. Gregorio R, Captao RC (2000) Morphology and phase transition of high melt temperature crystallized poly(vinylidene fluoride). J Mater Sci 35:299–306
61. Elashmawi I, Hakeem N (2008) Effect of PMMA addition on characterization and morphology of PVDF. Polym Eng Sci 48(5):895–901
62. Coleman MM, Painter PC (1995) Hydrogen bonded polymer blends. Prog Polym Sci 1:20
63. Mao D, Bruce EG, Manuel A, Quevedo L (2011) Ferroelectric Properties and Polarization Switching Kinetic of Poly (vinylidene fluoride-trifluoroethylene) Copolymer. Ferroelectr Phys Effe 4:644–654
64. Singh PK, Gaur MS (2018) Enhancement of β-phase of P (VDF–TrFE) 60/40 by $BaTiO_3$ nanofiller. Ferroelectrics 524(1):37–43
65. Martins P, Lopes AC, Lanceros-Mendez S (2014) Electroactive phases of poly(vinylidene fluoride): Determination, processing and applications. Prog Polym Sci 39(4):683–706
66. Martins P, Lopes A, Lanceros-Mendez S (2013) Electroactive phases of poly(vinylidene fluoride): determination, processing and applications. Prog Polym Sci 39:683–706
67. Liu ZD, Feng Y, Li WL (2015) High dielectric constant and low loss of polymeric dielectric composites filled by carbon nanotubes adhering BaTiO3 hybrid particles. RSC Adv 5:29017–29021

68. Gupta AS, Sarkar CK (2015) Introduction to nano quantum effect on properties of nanomaterials by Chandan Kumar Ghosh. Springer, Berlin
69. Takagahara T, Takeda K (1992) Theory of the quantum confinement effect on excitons in quantum dots of indirect-gap materials. Phys Rev B 46:15578
70. Zaman S, Mansoor M, Abubakar AMM (2016) AFM investigation and optical band gap study of chemically deposited PbS thin films. IOP Conf Ser Mater Sci Eng 146:012034–012040
71. Santa-CruzBalta´-Calleja CFJ, Zachmann HG, Stribeck N, Asano T (1991) Relating microhardness of poly (ethylene terephthalate) to microstructure. J Polym Sci Part B Polym Phys 29:819–824
72. Cagiao ME, ConnorBalta´-Calleja MFJ, Seferis JC (1999) Structure development in a thermoplastic polyimide: cold crystallization as revealed by microhardness. Polym J 31(9):739–746
73. Rueda DR, Viksne A, Malers L, Balta-Calleja FJ, Zachmann HG (1994) Influence of morphology on the microhardness of poly(ethylene naphthalene-2,6-dicarboxylate. Macromol Chem Phys 195:3869–3876
74. Kajaks J, Flores A, García-Gutiérrez MC, Rueda DR, Baltá-Calleja FJ (2000) Crystallization kinetics of poly(ethylene naphthalene-2,6-dicarboxylate) as revealed by microhardness. Polymer 41(21):7769–7772
75. Baltá-Calleja FJ, Santa Cruz C, Asano T (1993) Physical transitions and crystallization phenomena in poly(ethylene terephthalate) studied by microhardness. J Polym Sci Part B Polym Phys 31:557–565

76 Balta-Calleja FJ, Flores A, Ania F, Michler GH, Balta-Calleja FJ (eds) (2005) Mechanical properties of polymers based on nanostructure and morphology, 1st edn. Taylor and Francis, Boca Raton (Florida), p 784

77 Baltá-Calleja FJ (2000) Structure-microhardness correlation of polymers and blends. In: Cunha AM, Fakirov S (eds) Structure development during polymer processing: NATO science series. Kluwer Academic Publishers, Dordrecht, pp 145–162

78. Jiang X, Bin Y, Matsuo M (2005) Electrical and mechanical properties of polyimide carbon nanotubes composites fabricated by in situ polymerization. Polymer 46:7418–7424
79. Meincke O, Kaempfer D, Weickmann H, Friedrich C, Vathauer M, Warth H (2004) Mechanical properties and electrical conductivity of carbon-nanotube filled polymide-6and its blends with acrylonitrile/butadiene/styrene. Polymer 45:739–748
80. Luo J, Chen S, Li Q, Liu C, Gao S, Zhang J, Guo J (2019) Influence of graphene oxide on the mechanical properties, fracture toughness, and microhardness of recycled concrete. Nanomaterials 9(3):325–335
81. Gaur A, Rana D, Maiti P (2019) Mechanical and wear behaviour of poly (vinylidene fluoride)/clay nanocomposite. J Mater Res Technol 8(6):5874–5881
82. Smith WF (1996) Principles of materials science and engineering, potential energy curves and material properties, 3rd edn. McGraw-Hill, Columbus
83. Oliver WC, Pharr GM (1992) An improved technique for determining hardness and elastic modulus using load and displacement sensing indentation experiments. J Mater Res 7:1564–1583
84. Lin I, Chen CT, Bdikin I, Ball V, Gracio J, Buehler MJ (2014) Tuning heterogeneous poly(dopamine) structures and mechanics: in silico covalent cross-linking and thin film nanoindentation. Sof Mattter 10:457–464
85. Kariper IA (2015) Hardness of Mn2V2O7 thin films and its influential factors. Int J Miner Mettal Mater 22:987–991
86. Kariper IA (2016) Hardness of thin films and the influential factors, chapter 1. Diamond and Carbon Composites and Nanocomposites 1–20.
87. José AC, Maria CP (2019) Monitoring Dispersion and Re-agglomeration Phenomena during the Manufacture of Polymer Nano composites. Processi of Poly Nano 12(1):97–120
88. Fornes TD, Paul DR (2003) Crystallization behavior of nylon 6 nanocomposites. Polymer 44(14):3945–3961
89. Cahoon JR, Broughton WH, Kutzak AK (1971) The determination of yield strength from hardness measurements. Metall Trans 2:1979–1983
90. Pavlina EJ, Van Tyne CJ (2008) Correlation of yield strength and tensile strength with hardness for steels. Int J Miner Metall Mater 17(6):888–893
91. Haihe S, Sijia Y, Shulin S, Huixuan Z (2013) Effect of Miscibility and Crystallization on the Mechanical Properties and Transparency of PVDF/PMMA Blends. Polym Plast Technol Eng 52:221–227

92. Ionita M, Pandele AM, Crica L, Pilan L (2014) Improving the thermal and mechanical properties of polysulfone by incorporation of graphene oxide. Compos Part B 59:133–139
93. Eggedi O, Valiyaneerilakka U, Dar MR, Varghese S (2014) Nanoindentation and thermal characterization of poly(vinylidenefluoride)/MWCNT nanocomposites. AIP Adv 4:047102
94. Shrungi M, Goswami A, Bajpai J, Bajpai AK (2019) Designing kaolin-reinforced bionanocomposites of poly(vinyl alcohol)/gelatin and study of their mechanical and water vapor transmission behavior. Polym Bull 76(11):5791–5811
95. Skinner FK, Rotenberg Y, Neumann AW (1989) Contact angle measurements from the contact diameter of sessile drops by means of a modified axisymmetric drop shape analysis. J Colloid Interface Sci 130(1):25–34
96. Thabet A, Ebnalwaled AA (2017) Improvement of surface energy properties of PVC nanocomposites for enhancing electrical applications. Measurement 110:78–83
97. Ma W, Zhang J, Wang X, Wang S (2007) Effect of PMMA on crystallization behavior and hydrophilicity of poly(vinylidene fluoride)/poly(methyl methacrylate) blend prepared in semi-dilute solutions. Appl Surf Sci 253(20):8377–8388
98. Owens DK, Wendt RC (1969) Estimation of the surface free energy of polymers. J Appl Polym Sci 13:1741–1747
99. Sagar R, Gaur MS, Bhadoria B (2018) SInvestigation of TSDC and dielectric modulus of PVDF+$BaZrO_3$ nanocomposites thin film. Vacuum 156:375–383
100. Kumar P, Kumar A, Cho KY (2017) An asymmetric electrically conducting self-aligned graphene/polymer composite thin film for efficient electromagnetic interference shielding. AIP Adv 7:15103
101. Narayan R, Kim JE, Kim JY (2016) Graphene oxide liquid crystals: discovery, evolution and applications. Adv Mater 28:3045–3068
102. Alateyah AI, Dhakal HN, Zhang ZY (2013) Processing, properties, and applications of polymer nanocomposites based on layer silicates: a review. Adv Polym Technol 32(4):212–216

4.

Vacuum 166 (2019) 298–306

Contents lists available at ScienceDirect

Vacuum

journal homepage: www.elsevier.com/locate/vacuum

Dielectric, pyroelectric and polarization behavior of polyvinylidene fluoride (PVDF) - Gold nanoparticles (AuNPs) nanocomposites

Mamta Kushwah[a], Rohan Sagar[a,*], A.A. Rogachev[b], M.S. Gaur[a,*]

[a] Department of Physics, Hindustan College of Science and Technology, Farah, Mathura, 281122 U.P., India, Affiliated to Dr. A.P.J. Abdul Kalama Technical University, U. P, Lucknow, India
[b] Francisk Skorina Gomel State University, Sovetskaya Str. 104, 246019, Gomel, Belarus

ARTICLE INFO

Keywords:
Synthesized AuNPs
Vacuum
Pristine PVDF
FTIR
XRD
P-E loop
Pyroelectric coefficient

ABSTRACT

In this study, the polymorphism of poly (vinylidene fluoride) (PVDF) was control by gold nanoparticles (AuNPs). Simple one step method was used for synthesis of AuNPs using $HAuCl_4{\cdot}3H_2O$, and N, N-dimethylformamide (DMF). The AuNPs of size 20–30 nm have been prepared by chemical method. DMF was act as reducing agent and solvent of PVDF. The circular samples of diameter 3.5 cm and thickness 10–25 µm were prepared. It has been observed that AuNPs modify the structural morphology of PVDF. The β-phase of PVDF was modified due to interaction between electric charge at the surface of AuNPs and CF_2 dipoles. This is further verified by increase of remanent polarization in P-E loop. XRD spectra address the crystallographic phase identification of PVDF in presence of AuNPS. The AuNPs in PVDF matrix significantly enhances 72.2% expansion of remanent polarization (P_r), 19.23% depletion of coercive field (E_c) and 70–100% expansion of shifting speed of the ferroelectric polarization. Fourier transform infrared spectroscopy (FTIR) and X-ray diffraction (XRD) of pristine and NPs mixed PVDF illustrates the structural properties and reason of enhanced ferroelectric properties.

1. Introduction

Dielectric polymer nanocomposites lead to great interest due to their several applications in the field of electronics and electrical industry [1–4]. Poly (vinylidene fluoride) (PVDF) is an semicrystalline with diverse crystalline phases (α, β, γ, δ, and ε) depending on the crystallization conditions. Generally, PVDF mainly contains active nonpolar α-phase (*TGTG*) and polar β-phase (*TTTT*). β-phase has all-trans planner zigzag structure and the dipole moments of the two C–F and C–H bonds add up in such a way that the monomer get an effective dipole moment in the direction perpendicular to the carbon backbone. β-phase PVDF is a prime interest for electronic applications such as piezoelectric or pyroelectric sensors, microwave transducers as well as nonvolatile memories[5].

The β-phase of PVDF was enhanced by several methods as reported in literature [6–13]. However, direct mixing of nanoparticles in PVDF matrix is new trends of research to enhance the α and β-phase. Earlier ceramic nanoparticles are used [14] to enhance β-phase of PVDF, however, uniform dispersion and bonding of ceramic nanoparticles in PVDF matrix is major challenge. But crosslinking of AuNPs with PVDF is easily possible due to presence of functional group. The effect of gold nanoparticle on ferroelectric properties of pristine PVDF has been reported earlier [15,16]. ZnO nanoparticles have shown their potential to improve the pyroelectric response in PVDF [17]. β-phase crystals in PVDF are significantly improved by doping of palladium and AuNPs [18–20]. The effect of AuNPs in polymorphism of PVDF for ferroelectric switching and energy storage applications have been recently reported [20–23], however, reason of polymorphism is still unclear.

The dispersion of nanoparticles in polymer matrix is main concern of nowdays research. Generally, dissimilar surface energy of organic and inorganic (i.e. NPs) material causes aggregation of NPs. It also effect the processability of thin films, defect density and dielectric properties [24,25]. The agglomeration of nanoparticles directly increase the dielectric loss and reduced dielectric breakdown strength of polymer dielectrics. Therefore, uniform dispersion of nanoparticles in organic matrix is essential to achieve optimum device performance.

It is well known that PVDF exhibit high energy density, high breakdown strength, high dielectric constant etc and having several industrial applications [26,27]. Metal nanoparticles embedded polymers have created enormous interest for the fabrication of energy storage devices because nanoscale conductive fillers can increase the overall dielectric permittivity of composites [28–31]. The direct mixing of nanoparticles has been attractive due to the functionalization of the nanoparticles by the polymer chain. The dielectric and ferroelectric

---

* Corresponding authors.
E-mail addresses: mrrohansagar@gmail.com (R. Sagar), msgaur.hcst@sgei.org (M.S. Gaur).

https://doi.org/10.1016/j.vacuum.2019.05.010
Received 5 April 2019; Received in revised form 26 April 2019; Accepted 7 May 2019

properties of PVDF-AuNPs nanocomposites are rarely reported in literature. Therefore, the objective of present work is to synthesis/characterization of AuNPs, preparation of PVDF-AuNPs nanocomposites samples. Further, dielectric and pyroelectric characteristics were undertaken for energy storage applications. To understand the nature of enhancing dielectric, pyroelectric and energy storage properties of PVDF by mixing of AuNPs, Fourier transform infrared spectroscopy (FTIR), X-ray diffraction (XRD) and P-E loop were recorded. The results show that PVDF-AuNPs nanocomposites samples display an excellent charge storage performance as compared to pristine PVDF.

2. Experimental details

AuNPs were synthesized by DMF (N,N-Dimethylformamide) as a solvent. DMF (N,N-Dimethylformamide) is a best known solvent and reducing agent for Au^{3+} to Au^0 [32]. 1 mM of $HAuCl_4{\cdot}3H_2O$ (Sigma-Aldrich,India) powder were added into 100 ml of DMF and were kept in stirrer at 60 °C for 5 h. After 5 h colourless solution were convert in pink colour. This indicate the formation of AuNPs. *It was found that the size and morphology of the AuNPs could be controlled by keeping the colloidal AuNPs in vacuum pressure of 10^{-5} Torr at room temperature, and by considering that spherical particles were found in all samples.* In order to develop the stable AuNPs, the pH of solution was maintained 5. This is the simple functionaliation process of nanoparticles as reported in literature [33,34]. The solution of pristine PVDF were poured onto optically plane circular glass plate of diameter 5 cm. The glass plates were kept in vacuum oven at 50 °C for 2 h and then switch off the oven for 24 h for prepration of pristine PVDF samples. Finally, the dried pristine PVDF films (thickness ~10–25 µm) were lifted off from the glass substrates. In order to prepare PVDF-AuNPs nanocomposite samples, the 1 and 2 mM concentration were added drop by drop in PVDF solution. AuNPs doped solution of PVDF stirred at 50 °C for 1 h and sonicated for 20 min. The final solution was poured into optically plan glass plate. The rest of the thin film preparation process is similar to preparation of pristine PVDF sample. The dried samples were out gassed in air for 24h, and this was followed by room temperature outgassing at a vacuum pressure of 10^{-5} torr for further period of 24 h to remove the residual solvent..

AuNP_s were characterized by UV–Vis spectra (PerkinElmer, Lambda 25 Spectrophotometer). The size of nanoparticles were confimed by cross-sectional Transmission Electron Microscopy (TEM, JEOL 2100F, USA). Zeta potential estimation from zetasizer (Malvern Panalytical) However, pristine PVDF and PVDF-AuNPs nanocomposites samples are characterized by Fourier Transform Infrared Spectroscopy (FTIR) BRUKER (Model VERTEX-70) and XRD spectra to study the structural morphology. The LCR (Model no, Hioki 3532-50 LCR Hi- TESTER, India) meter was used to record the dielectric parameters. The aluminium electrodes of diameter 2.5 cm were prepared by using vacuum coating unit (Model no, VEQCO Delhi, India). The pyroelectric current was recorded with heating rate of 1 °C min^{-1} by electrometer (Keithley 6514). The polarization-electric field (P-E) hysteresis loops were recorded at 100 Hz using the ferroelectric test system (Marine India).

3. Results and discussion

3.1. Characterization of AuNPs

The AuNPs were characterized apparently transparent pink colour of the solution ensures the AuNPs formation primarly. The characteristic plasmon bond of AuNPs was observed at 544 nm in UV–Vis spectra as shown in Fig. 1. The TEM image of AuNPs is illustrated in Fig. 2(a). The dark-field image confirms the spherical nanoparticles. TEM and selected-area electron diffraction (SAED) confirm the size (i.e. 20–30 nm) and shape (i.e. spherical) of $AuNP_S$.

SAED pattern was explored for gold nanoparticle, as shown in Fig. 2(b). This is corresponding to crystalline behavior of AuNPs, that has spots superimposed on the ring. The SAED pattern of the spherical nanoparticle showed clear lattice fringes with bright circular rings corresponding to (111), (200), (220), and (311) planes. There are four sets of spots that could be identified from this diffraction pattern as shown in Fig. 2(b). AuNPs also showed strong intensity at (111) plane. TEM analysis revealed that the synthesized gold nanoparticles are stable in solution. The zeta potential of AuNPs was observed to be −25 to −18 mV (Fig. 3). This shows the nanoparticles are stable in collolidal form.

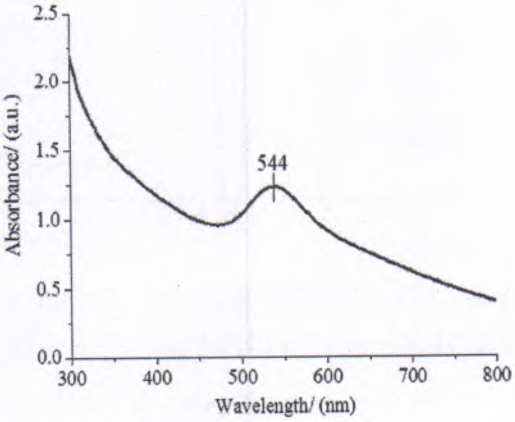

Fig. 1. UV–Vis spectra of AuNPs.

3.2. TEM of PVDF-AuNPs nanocomposite

The TEM of pristine PVDF and PVDF-AuNPs nanocomposites were recorded by TEM (JEOL 2100F, USA). Fig. 4(a) and (b) shows representative images of pristine PVDF and PVDF-AuNPs (2 mM) nanocomposites. The TEM of pristine PVDF possessed a fine morphology (Fig. 4(a)). It can also be seen that the AuNPs dispersed uniformly in the PVDF matrix forming continuous conductive paths (Fig. 4(b)). It could be observed from Fig. 4(b) that AuNPs are dispersed in PVDF matrix with minimum particle agglomeration. The reduction in nanoparticles agglomeration is caused by steric repulsion between the nanoparticles and polymer chains [41].

3.3. Mechanism of PVDF-AuNPs nanocomposite formation

Mixing of AuNPs with PVDF gives strong interaction with PVDF as shown in Fig. 5. The PVDF will stabilize the AuNPs, while AuNPs is stabilized by binding with fluorine ion (F^-). So that the shift of binding energy of Au ($4f_{7/2}$ and $4f_{5/2}$) and increase of fluorine ion (F^-) in PVDF nanocomposites is expected. An interface is formed due to interaction of AuNPs with PVDF backbone. The interface plays very important role in dielectric and polarization properties of PVDF-AuNPs nanocomposites such as dielectric constant, remanent polarization, coercive field, and switching speed.

3.4. FTIR

FTIR illustrate compositional, molecular structural and physical characteristics analysis of PVDF-AuNPs nanocomposites. FTIR spectra of pristine PVDF, PVDF-AuNPs (1 mM), PVDF-AuNPs (2 mM), PVDF-AuNPs (5 mM) and PVDF-AuNPs (10 mM) are shown in Fig. 6(a and b). The α- and γ-crystalline phases of pristine PVDF were characterize by peaks at 978, 764, 612, 538 cm^{-1} (α) and 815, 1213 cm^{-1} (γ), respectively [35–38].

The AuNPs mixed PVDF thin films (PVDF-AuNPs (1 mM) and PVDF-AuNPs (2 mM)) are having new peak at 1265 and 443 cm^{-1}, which attributes β-phase [37,38]. In this case γ-phase peak at 1213 cm^{-1} is

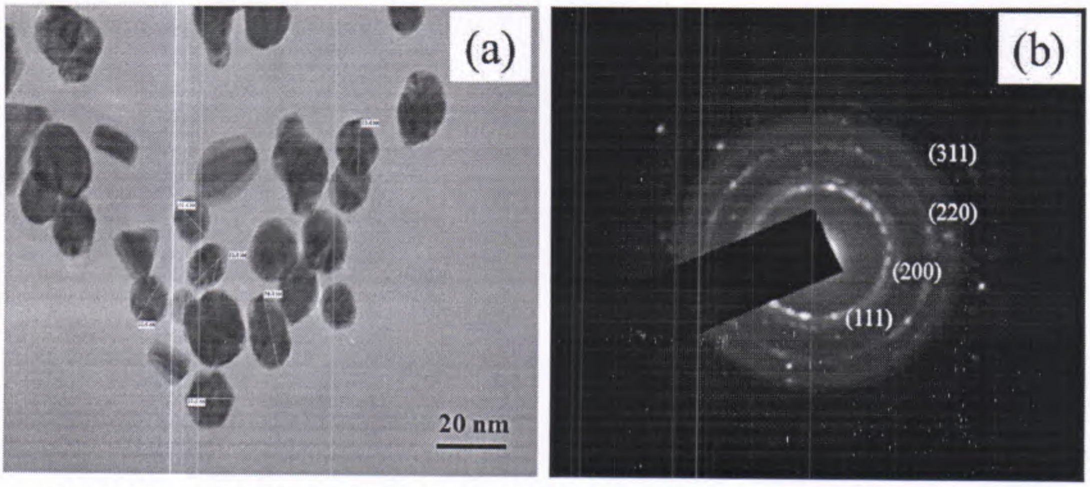

Fig. 2. (a) Transmission electron microscopy (TEM) and (b) Selected area electron diffraction (SAED) images of AuNPs.

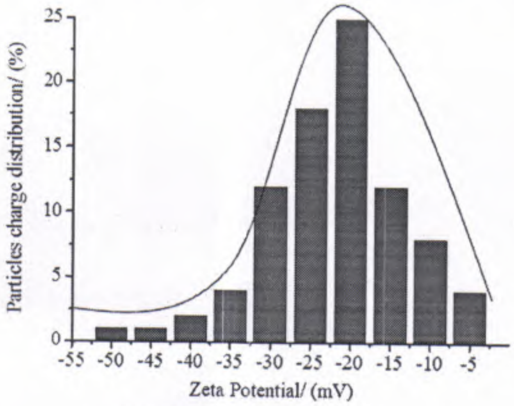

Fig. 3. Zeta potential of AuNPs.

reduced.

The chain (TTTT) of PVDF confirms both β-phases and γ-phases in PVDF. The vibrational bands corresponds to these two phases appear almost at same frequencies in FTIR spectra. Thus peak at 831 and 500 cm^{-1} carry a dual signature of the γ-phases as well as of the β-phases [37–39]. AuNPs mixed in PVDF can control the crystalline polymorph and improves the content of the polar β-phase.

The similar peaks of polar β-phases also observed at 3050 and 2950 cm^{-1} (i.e. Fig. 6(b)). These peaks are due to $\nu_{as}(CH_2)$ and $\nu_s(CH_2)$ vibrational bands. AuNPs causes the minor shifting towards higher wavelength corresponding to lower energy states. This is an evidence for strong interaction of AuNPs with PVDF.

The peak at 1407 cm^{-1} (Fig. 6(a).) attributes $\nu_{as}(CC)$ and $\omega(CH_2)$ modes of vibration because of electronegativity difference of fluorine atoms in PVDF and surface charge of AuNPs. This interaction of PVDF and AuNPs minimizes potential energy of stereo chemical conformation and induces β-phases. This particular characteristics have been observed by FTIR spectra by modification of β-phase peak (i.e. 443, 500, 831 and 1265 cm^{-1}) with increasing concentration of AuNPs in PVDF matrix.

3.5. X-ray diffraction

The XRD patterns of nanocomposite thin films are shown in Fig. 7. The peaks corresponding to 2θ are 14.67°, 16.11°, 19.48° and 40.03° for pure PVDF. First two peaks corresponding to diffraction planes of (100), (110) attributes the nonpolar α-phases formed during crystallization process [40]. However, the peak at 40.03° is corresponding to (200) diffraction plane. This peak is due to the β phase present in PVDF.

There are some new peaks (i. e 34.58°, 61.05° and 76.78°) are

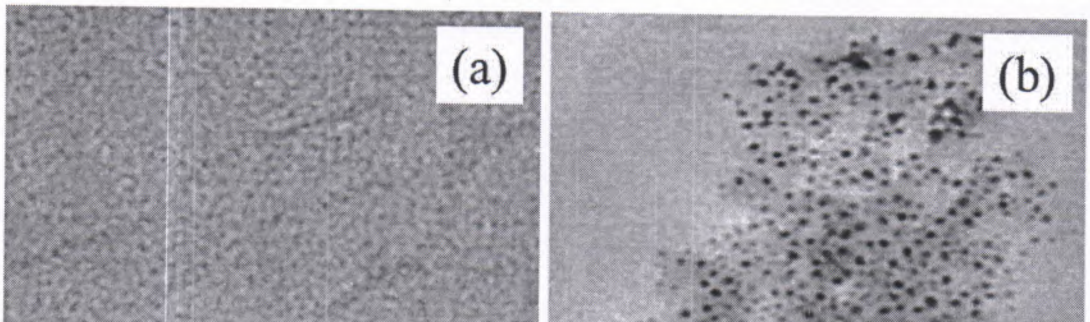

Fig. 4. TEM image of pristine PVDF and PVDF-AuNPs nanocomposites.

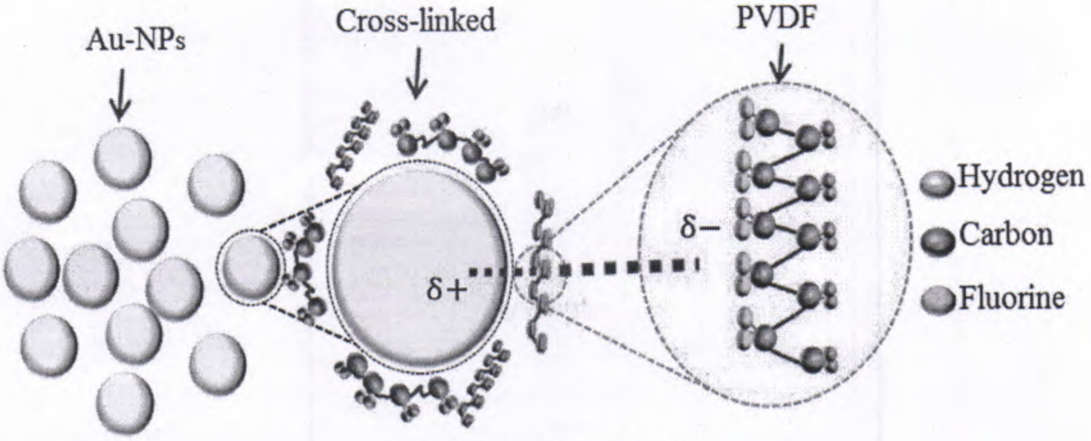

Fig. 5. Synthesis mechanism of PVDF-AuNPs nanocomposites.

observed in PVDF-AuNPs nanocomposite samples. It can be seen from Fig. 7 that PVDF-AuNPs nanocomposites samples shows six diffraction peaks (i.e. 15.96°, 19.01°, 34.57°,39.55°, 61.05° and 76.61°). AuNPs possesses four prominent Bragg reflections at 34.42°, 39.71°, 61.21°, and 76.92° corresponding to (111), (200), (220) and (311) diffraction plane. These peaks are clearly matches with XRD data of gold solution [41]. The increase of XRD peak intensity with AuNPs concentration is an direct evidence for modification of α and β phase [42]. The diffraction planes observed by XRD are same as observed by SAED pattern.

XRD parameters such as average crystallite size (L), inter planer distance (d), inter chain separation (R), crystallinity (%), primitive (P), Miller Indices (h k l), Face centered cubic (Fcc) and Body centered cubic (bcc) are calculated and summarized in Table 1. These parameters are calculated by method as reported in literature [43–46]. XRD result shows that crystal structure of PVDF is significantly modified by AuNPs mixing.

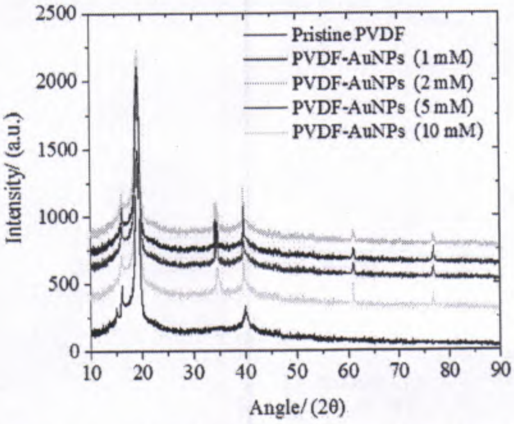

Fig. 7. XRD spectra of pristine PVDF sample, PVDF-AuNPs (1 mM), PVDF-AuNPs (2 mM), PVDF-AuNPs (5 mM) and PVDF-AuNPs (10 mM) nanocomposites.

3.6. Dielectric properties

Fig. 8(a) shows the variation of the dielectric permittivity with frequency over the range of 1×10^3 Hz to 5×10^6 Hz for nanocomposite samples with different concentration of AuNPs. For AuNPs (1 mM) and AuNPs (2 mM) nanocomposite samples, the dielectric permittivity decreases gradually with the increase in frequency.

The permittivity of the PVDF thin film has been observed to be less than permittivity of PVDF-AuNPs nanocomposites. It is much higher for 2 mM and 5 mM concentration of AuNPs in PVDF, however, permittivity decreases with further increase of AuNPs concentration. This is because of aglomoration of AuNPs followed by reduction of free volume for orientation of dipoles for higher concentration of AuNPs.

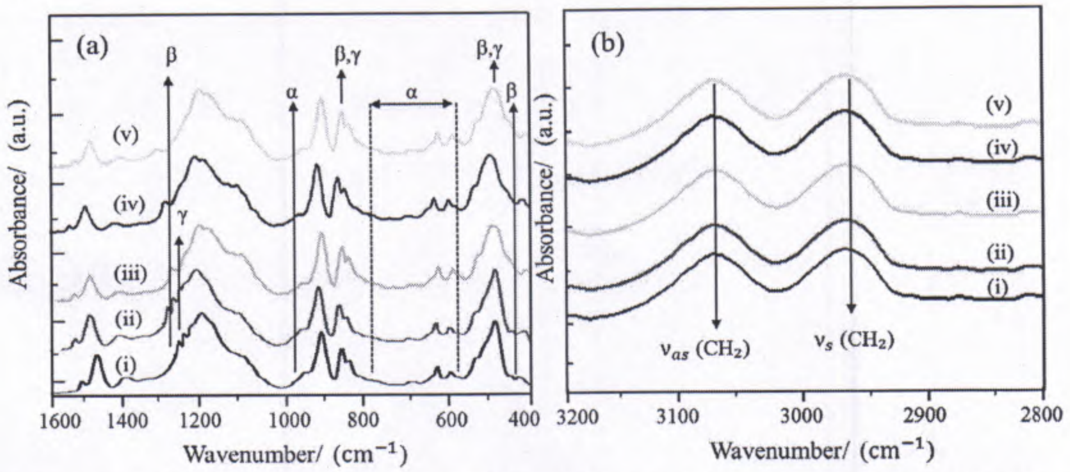

Fig. 6. FTIR spectra of pristine PVDF sample, PVDF-AuNPs (1 mM), PVDF- AuNPs (2 mM), PVDF- AuNPs (5 mM) and PVDF-AuNPs (10 mM) nanocomposites in different frequency regions; (a) 1600 to 400 cm^{-1} and (b) 3200 to 2800 cm^{-1}.

Table 1
XRD parameters of pristine PVDF sample and PVDF-AuNPs nanocomposites.

Samples	2θ	β	Intensity	L(Å)	d (Å)	R	%	P	hkl	Fcc (F)	Bcc (I)
Pristine PVDF	14.67	0.00	321	73.37	6.03	7.54	44.41	0.51	100		
2nd	16.11	3.81	487	0.37	5.49	6.87		0.62	–		
3rd	19.48	0.98	1497	1.44	4.55	5.69		1.91	110		
4th	40.03	2.27	331	0.59	2.25	2.81		3.73	200		4
AuNPs (1 mM)	16.11	4.21	959	0.34	5.49	6.87	42.19	0.62	100		
2nd	19.18	0.72	1987	1.95	4.62	5.78		0.88	–		
3rd	34.58	0.42	817	3.25	2.59	3.24		2.81	111	3	
4th	39.86	1.99	872	0.68	2.26	2.82		3.69	200	4	4
5th	61.05	65.55	652	0.01	1.51	1.89		8.21	220	8	8
6th	76.78	61.38	615	0.01	1.24	1.55		11.27	311	11	
AuNPs (2 mM)	16.11	4.22	1197	0.33	5.49	6.87	38.24	0.62	100		
2nd	19.32	0.72	2231	1.95	4.59	5.73		0.89	–		
3rd	34.42	0.45	1098	3.04	2.60	3.25		2.78	111	3	
4th	39.71	2.15	1197	0.63	2.26	2.83		3.67	200	4	4
5th	61.21	65.49	909	0.01	1.51	1.89		8.25	220	8	8
6th	76.92	62.03	879	0.01	1.23	1.54		11.25	311	11	
AuNPs (5 mM)	15.96	4.22	1062	0.33	5.55	6.93	40.8	0.61	100		
2nd	19.32	0.71	2072	1.98	4.59	5.73		0.89	–		
3rd	34.25	0.45	970	3.06	2.61	3.27		2.76	111	3	
4th	39.55	2.15	1043	0.63	2.27	2.84		3.64	200	4	4
5th	60.88	65.48	774	0.02	1.52	1.90		8.17	220	8	8
6th	76.78	62.31	780	0.01	1.24	1.55		11.27	311	11	
AuNPs (10 mM)	15.96	4.22	713	0.34	5.55	6.93	48.44	0.61	100		
2nd	19.01	0.72	1988	1.96	4.66	5.83		0.86	–		
3rd	34.57	0.45	621	3.05	2.59	3.24		2.81	111	3	
4th	39.55	2.15	731	0.63	2.27	2.84		3.64	200	4	4
5th	61.05	65.49	511	0.02	1.51	1.89		8.21	220	8	8
6th	76.61	62.03	413	0.01	1.24	1.55		11.26	311	11	

It is known that the dielectric behavior of polymers could be investigated by studying the polarization component of polymer. The polarization components of PVDF are electronic, ionic or orientational polarization. The electronic polarization occurs due to shifting of electron cloud under applied electric field [47,48]. Ionic polarization is caused by variation of distance between the positive and negative ions in the polymeric dielectric by an applied electric field [47,48]. The arrangement of dipoles according to direction of electric fieled in dielectric polymers attributed the orientational polarization. The interfacial polarization is occurred in multiphase polymer matrix such as composite materials. These polarization phenomena are frequency dependent [49], therefore, to determine how much each polarization changes and affects the dielectric properties by incorporation of AuNPs in PVDF matrix is important.

In order to study the contribution of each type of polarization, we have calaculated the ionic (α_i),electronic (α_e), orinatation (α_o) and interfacial polarizability [47,50–52] and summarized in Table 2. It has been observed that the role of ionic and electronic polarization is negligible due to lower value of polarizability, however, orientational and space charge/interfacial polarization play significant role. It is well known that [53,54] orientational and space charge polarization (α_s)are responsible for dielectric properties of PVDF. However, incorporation of AuNPs in PVDF significantly change the nature of polarization. It could

Table 2
Dielectric and polarization parameters of pristine PVDF sample and PVDF-AuNPs nanocomposites.

Samples	ε' (1 kHz)	α_i (Fm^2)	α_o (Fm^2)	α_e (Fm^2)	α_s (Fm^2)	η (%)
Pristine PVDF	8.26	0.32	0.10	0.48	7.15	59.4
AuNPs (1 mM)	13.77	2.17	3.31	5.06	12.69	68.5
AuNPs (2 mM)	15.88	2.78	4.19	6.15	16.52	72.2
AuNPs (5 mM)	14.78	1.59	2.73	2.52	13.11	60.8
AuNPs (10 mM)	11.07	7.64	9.87	10.20	12.20	53.4

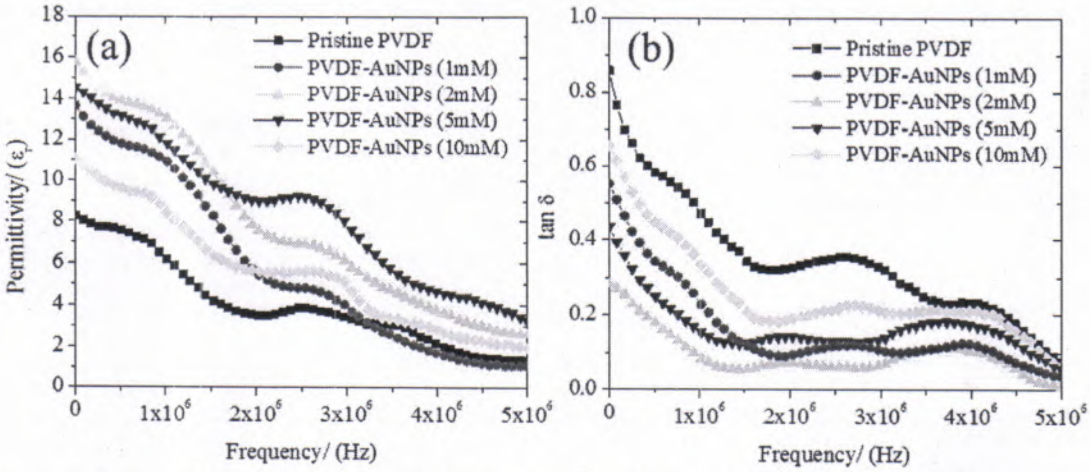

Fig. 8. Frequency dependent (a) dielectric permittivity and (b) tangent (tan δ) loss for pristine PVDF sample and PVDF- AuNPs nanocomposites.

be observed from Table 2 that PVDF-AuNPs nanocomposite exhibit the higher value of ionic, electronic and interfacial polarizability. Infact, ionic and electronic polarization in polymers occur at very high frequency, but in present case they appear even at lower frequency due to formation of charge transfer complex between polymer and nanofillers. During polarization the large numbers of electrons and ions appears due to presence of highly conductive nanofillers attributed the ionic and electronic polarization. It has been observed that the value of orientational polarizability is very small in nanocomposites. It means the motion of dipole is masked by other type of polarizatiuon. The interfacial polarization/space charge between the AuNPs and the pure PVDF polymer matrix is reported earlier [55].

The interfacial polarization mechanism of the PVDF-AuNP$_S$ nanocomposites with different molecular concentrations of PVDF matrix is schematically represented in Fig. 5. The yellow circle represents the cross section of AuNPs, the light blue and brown chains represents the PVDF surrounding the AuNPs and entangling with one another, the yellow edge represents the PVDF-AuNPs interface, the green dot refers to the polar fluorine ion of the PVDF chains, and the other ion represents the hydrogen and carbon ion. The higher value of interfacial polarizability shows its maximum contribution with other type of polarization as shown in Table 2. The calculated value of polarizability is an evidence that total polarization in PVDF-AuNPs matrix is the sum of ionic, electronic and interfacial polarization.

Fig. 8(b) shows the frequency dependence of the tangent loss and AuNPs modified PVDF samples at room temperature and atmospheric pressure. The tangent loss spectra show two relaxation peak, however, first peak attributed to interfacial polarization or Maxwell–Wagner–Sillars (MWS) polarization. Usually this polarization occurs in heterogeneous materials like nanocomposites, polymer blends, hybrid etc [56,57]. At lower frequencies the space charge accumulation and short-range dipole-dipole interactions at the AuNPs-conducting PVDF interfaces result in strong interfacial polarization [58,59].

The interfacial polarization of AuNPs is restricted due to confinement of charge carriers and molecular movement causes the increase of loss. The Debye like relaxations loss peaks (second peak) are mainly for large dielectric response. Interesting fact is that with increasing concentration of AuNPs, the tangent loss peaks are shifted towards higher frequencies(5×10^6 Hz) [58,59]. This shifting in relaxation peaks are attributed to the strong Van der waal type of interaction between AuNPs and PVDF matrix.

3.7. *Pyroelectric response*

The effect of AuNPs on the pyroelectric properties of pristine PVDF and PVDF-AuNP$_S$ nanocomposites were investigated. The pyroelectric current was recorded as a function of temperature with constant heating rate of 1 °C min^{-1} (i.e. Fig. 9). The pyroelectric current represents the polarization induced from thermal stress. It was observed that the behavior of pyroelectric coefficient with AuNPs concentration in PVDF matrix are similar to that of the dielectric permittivity as shown in Fig. 7(a). These results suggest that the mixing of AuNPs could enhance dielectric and pyroelectric properties of PVDF and thus modifying the polarization behavior. The pyroelectric coefficients was calculated using following relation [60,61]:

$$I = pA\frac{dT}{dt} \tag{1}$$

where p is the pyroelectric coefficient, I is the pyroelectric current, A is the area of the electrode and (dT/dt) is the heating rate.

The pyroelectric coefficient reaches its lowest value, 25.22 μC m^{-2} K^{-1}, at a temperature of 120 °C, this temperature corresponds to maximum polarization and phase difference. The other phase transitions are clearly noticeable at 100 °C and 140 °C where the peak values of the pyroelectric current are 6.99(pA) and 5.22(pA) respectively. Polarization gradually decreases at 30 °C–180 °C with further increase of temperature, polarization decreases rapidly and finally, a small phase change occurs at 140 °C.

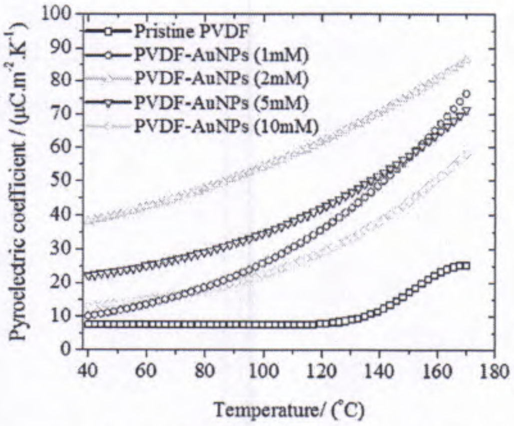

Fig. 9. Temperature dependent pyroelectric coefficient for pristine PVDF sample and PVDF-AuNPs nanocomposites.

It is clearly observed that the polarization decreases rapidily with increase of temperature. Fig. 9 shows that the pyroelectric coefficient increases with increase of temperature. PVDF- AuNPs (2mM) nanocomposites shows the maximum value of pyroelectric coefficietnts as compare to other nanocomposites.

The incorporation of AuNPs in PVDF matrix directly enhances the β-phase (TTTT conformance) of PVDF as verified from FTIR spectra. β-phase causes the strong piezoelectric and pyroelectric response of PVDF [62] as observed in this study.

3.8. *Pyroelectric figure of merit*

The pyroelectric figure of merit was calculated by following relation [63]:

$$F_v = \frac{p}{\sqrt{\varepsilon_r \tan\delta}} \tag{2}$$

where ε_r is the real part of permittivity, tangent loss (tanδ) and p is the pyroelectric coefficient.

The figure of merits (μC.m^{-2} K^{-1}) is varied from 9.5 to 32.5. Figure of merit was maximum for PVDF-AuNPs (2 mM) nanocomposites due to maximum pyro response of polymer matrix. This result is well agreed with maximum value of pyroelectric coefficient with PVDF-AuNPs (2 mM) nanocomposites. The pyroelectric figure of merit in our study is stronger than other pyroelectric material [63–66]. Therefore, AuNPs significantly enhances the pyroelectric response of PVDF.

3.9. *P–E loop*

P-E loops at room temperature with applied electric field of 100 kV cm^{-1} for different concentration of AuNPs in PVDF nanocomposite samples with frequency of 100 Hz are shown in Fig. 10(a–b). The P-E loop start expansion at lower value of field and saturated in higher value of field. The area of P-E loop measure the loss of energy during polarization and depolarization process [67]. The saturation polarization (P) value increases from 1.2 μC cm^{-2} to 3.1 μC cm^{-2} for the applied field of 10 kV cm^{-1} to 100 kV cm^{-1} in PVDF-AuNPs nanocomposite. This increment denotes the higher energy density as well as increasing the dielectric strength of the nanocomposite. P-E loop decreases from 3.5 μC cm^{-2} to 0.6 μC cm^{-2}, as the concentration of AuNPs increases from 1 mM to 2 mM. The dielectric material has electric energy storage properties and can be obtained from the P-E loop. In the presence of an electric field, PVDF shows polar β-phase dependent polarization. The strength of polarization in pristine PVDF

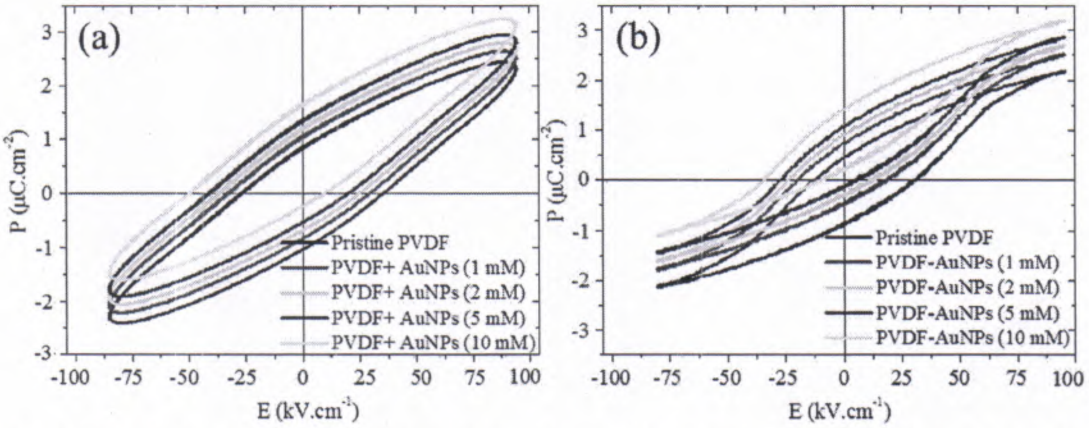

Fig. 10. Electric field dependent polarization (P–E loop) at 100 Hz (a) Sin waveform and (b) Triangle waveform for pristine PVDF sample and PVDF-AuNPs nanocomposites at room temperature.

depends on the amount of β-phase.

PVDF sample is dominated by nonpolar α-phase with a small amount of polar β-phase and hence the PVDF thin film shows a weak polarization (p) vs electric field (E) Sin waveform and triangle waveform curve (Fig. 10(a–b)). The recoverable electric energy density (S_{reco}) and the energy density stored per unit (S_{stre}) volume of the nanocomposites are generally determined the P-E hysteresis loop scanned between $-E_{min}$ to $+ E_{max}$, for ferroelectric polymer, the electrical energy storage density and efficiency can be obtained for P-E hysteresis loop from following relations [68,69]:

$$S_{reco} = \int_{P_2}^{P_{max}} EdP \tag{3}$$

$$S_{store} = \int_{P_1}^{P_{max}} EdP \tag{4}$$

$$\eta = \frac{S_{reco}}{S_{store}} x100\% \tag{5}$$

where η is energy storage efficiency of the nanocomposites. The polarization increases from P_2 to P_{max} along a different loop than when the full loop is scanned. Sin waveform and triangle waveform shows change in the recoverable (S_{reco}) and efficiency (η%) of PVDF and PVDF- AuNPs nanocomposited for 100 $kV\,cm^{-1}$ applied electric field at room temperature.

The S_{reco} for PVDF-AuNPs (2 mM) is 1.3 $J\,cm^{-3}$, which is higher than other nanocompositions (i.e. Fig. 11). The calculated efficiency for pristine PVDF, PVDF-AuNPs (1 mM), PVDF-AuNPs (5 mM), PVDF-AuNPs (10 mM) are 59, 68.5 and 53.4% respectively, however, PVDF-AuNPs (2 mM) exihibits higher efficiency (i.e. 72.2%). These results can be attributed to the growing formation of β-phase in aggregate by the addition of AuNPs and its synergistic effect.

The area under the curve is caused by internal heterogeneous charge, which provide the charge storage ability of material. It is cleary reflected in P-E loop that incorporation of AuNPs causes an increase of *P*. The increase in *P* value of nanocomposite samples can be due to accumulation of charges at the interface, which facilitates the heterogeneous polarization in the systems, which further enhances the ferroelectric behavior of the sample.

The remnant polarization and coercive field increase with the addition of AuNPs. This confirms that the presence of AuNPs in PVDF significantly influences the polarization response of the polymer matrix.

4. Conclusion

We have demonstrated the enhancement of the ferroelectric properties of PVDF by mixing of AuNPs. It is concluded that AuNPs in PVDF matrix enhances electroactive polar β-phase due to interactions of AuNPs and CF_2 dipoles existing PVDF and increases charge storage. The size of AuNPs was 24 nm, which is the same order of magnitude as the crystallite size of β-phase in PVDF. Theerefore, enhancement of ferroelectric properties especially energy storage efficiency, dielectric and pyroelectric is due to strong intraction between AuNPS and ferroelectric crystals of PVDF. Dielectric permittivity increases with increasing of AuNPs content in PVDF due to its conductive nature. The increase in permittivity is attributed to the improved interfacial polarization due to entrapment of charged particle at the interfaces between AuNPs surfaces and the PVDF matrix. The pyroelectric response of the nanocomposite suggest its application in designing of pyroelectric sensor. Finally, it is concluded that novel nanocomposites material is important for fabrication of acutuators, IR-sensors, pyroelectric sensor and transducers.

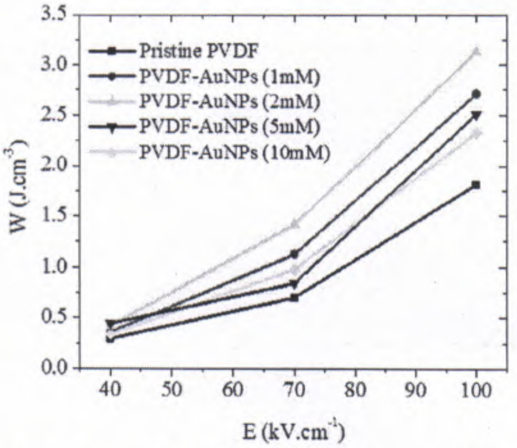

Fig. 11. Energy density for pristine PVDF sample and PVDF-AuNPs nanocomposites.

Acknowledgements

Financial assistance from Indo-Belarusian Scientific Cooperation, DST, New Delhi (India) (letter no. INT/BLR/P-13/2016) is gratefully acknowledged. One of the author Rohan Sagar acknowledge the University Grants Commission, New Delhi (India) for proving research fellowship award number RGNF-2017-18-SC-UTT-29088. We are also thankful to Dr. Satyendra Singh from Special Centre for Nanoscience, Jawaharlal Nehru University, New Delhi (India) for providing the

characterization facilities.

Appendix A. Supplementary data

Supplementary data to this article can be found online at https://doi.org/10.1016/j.vacuum.2019.05.010.

References

[1] L. Xie, X. Huang, Y. Huang, K. Yang, P. Jiang, Core @ doubleshell structured BaTiO$_3$-polymer nanocomposites with high dielectric constant and low dielectric loss for energy storage application, J. Phys. Chem. C 117 (44) (2013) 22525–22537.

[2] A. Toor, J.C. Cheng, A.P. Pisano, Synthesis and characterization of gold nanoparticle/SU-8 polymer based nanocomposite, Proc. IEEE NEMS. Hawaii, USA, 2014, pp. 664–668.

[3] V. Tomer, G. Polizos, E. Manias, C.A. Randall, Epoxy based nanocomposites for electrical energy storage effects of montmorillonite and barium titanate nanofillers, J. Appl. Phys. 108 (2010) 1–14 074116.

[4] N. Siddiqui, A. Bhardwaj, R. Hada, V.S. Yadav, D. Goyal, Synthesis, characterization and antimicrobial study of poly (methyl methacrylate)/Ag nanocomposites, Vacuum 153 (2018) 6–11.

[5] L. Ruan, X. Yao, Y. Chang, L. Zhou, G. Qin, X. Zhang, Properties and ApplicationsN of the β phase poly(vinylidene fluoride), Polymer 10 (3) (2018) 228.

[6] A.J. Lovinger, Ferroelectric polymers, Science 220 (1983) 1115–1121.

[7] J.B. Lando, H.G. Olf, A. Peterlin, Nuclear magnetic resonance and x-ray determination of the structure of poly(vinylidene fluoride), J. Polym. Sci. Part A- 1 4 (1966) 941–951.

[8] J. Scheinbeim, C. Nakafuku, B.A. Newman, K.D. Pae, High-pressure crystallization of poly(vinylidene fluoride), J. Appl. Phys. 50 (1979) 4399–4405.

[9] J.J. Wang, H.H. Li, J.C. Liu, Y.X. Duan, S.D. Jiang, S.K. Yan, On the $\alpha \rightarrow \beta$ transition of carbon-coated highly oriented PVDF ultrathin film induced by melt recrystallization, J. Am.Chem. SoC125 (2003) 1496–1497.

[10] G.T. Davis, K.Y. McKinney, M.G. Broadhurst, S.C. Roth, Electric-field-induced phase changes in poly(vinylidene fluoride), J. Appl. Phys. 49 (1978) 4998–5002.

[11] J. Zheng, A. He, J. Li, C.C. Han, Polymorphism control of poly(vinylidene fluoride) through electrospinning, Macromol. Rapid Commun. 28 (2007) 2159–2162.

[12] D. Mandal, S. Yoon, K.J. Kim, A novel nanogenerator based on PVDF nanofiber webs, ProCInt. Conf. Intelligent Textiles, Seoul, O- 11 (2010) 31–32.

[13] T. Furukawa, Ferroelectric properties of Vinylidene fluoride copolymers, Phase Transitions 18 (1989) 143–211.

[14] R. Sagar, M.S. Gaur, B.S. Bhadoria, Investigation of TSDC and dielectric modulus of PVDF–BaZrO3 nanocomposites thin film, Vacuum 156 (2018) 375–383.

[15] X. Huang, P. Jiang, L. Xie, Ferroelectric polymer/silver nanocomposites with high dielectric constant and high thermal conductivity, Appl. Phys. Lett. 95 (2009) 242901.

[16] H. Paik, Y.-Y. Choi, S. Hong, K. No, Effect of Ag nanoparticle concentration on the electrical and ferroelectric properties of Ag/P(VDF-TrFE) composite films, Sci. Rep. 5 (2015) 13209.

[17] K.S. Tan, W.C. Gan, T.S. Velayutham, W.H. Abd Majid, Pyroelectricity enhancement of PVDF nanocomposite thin films doped with ZnO nanoparticles, Smart Mater. Struct. 23 (2014) 125006.

[18] D. Mandal, K.J. Kim, J.S. Lee, Simple synthesis of palladium nanoparticles, β-phase formation, and the control of chain and dipole orientations in palladium-doped poly (vinylidene fluoride) thin films, Langmuir 28 (2012) 10310–10317.

[19] D. Mandal, K. Henkel, D. Schmeißer, The electroactive β-phase formation in poly (vinylidene fluoride) by gold nanoparticles doping, Mater. Lett. 73 (2012) 123–125.

[20] W. Wang, S. Zhang, L. Srisombat, T.R. Lee, R.C. Advincula, Gold-nanoparticle- and gold-nanoshell-induced polymorphism in poly(vinylidene fluoride), Macromol. Mater. Eng. 296 (2011) 178–184.

[21] D.Y. Kusuma, C.A. Nguyen, P.S. Lee, Enhanced ferroelectric switching characteristics of P(VDF-TrFE) for organic memory devices, J. Phys. Chem. B114 (2010) 13289–13293.

[22] Z. – M. Dang, J. – K. Yuan, S. – H. Yao, R. – J. Liao, Flexible nanodielectric materials with high permittivity for power energy storage, Adv. Mater. 25 (44) (2013) 6334–6365.

[23] Z. – M. Dang, J. – K. Yuan, J. – W. Zha, T. Zhou, S. – T. Li, G.-H. Hu, Fundamentals, processes and applications of high- permittivity polymer-matrix composites, Prog. Mater. Sci. 57 (2012) 660–723.

[24] P. Kim, N.M. Doss, J.,P. Tillotson, P.,J. Hotchkiss, M.J. Pan, S.R. Marder, J. Li, J.P. Calame, J.W. Perry, High energy density nanocomposites based on surface-modified BaTiO$_3$ and a ferroelectric polymer, ACS Nano 3.9 (2009) 2581–2592.

[25] E. Claudia, C. Fettkenhauer, J. Glenneberg, W. Münchgesang, C. Pientschke, T. HorstBeige, S.G. Ebbinghaus, BaTiO3 –P(VDF-HFP) nanocomposite dielectrics – influence of surface modification and dispersion additives, Mater. Sci. Eng. B 178 (13) (2013) 881–888.

[26] W. Li, L. Jiang, X. Zhang, Y. Shen, C.W. Nan, High-energy-density dielectric films based on polyvinylidene fluoride and aromatic polythiourea for capacitors, J. Mater. Chem. A2 (2014) 15803–15807.

[27] J. Gao, Y. Wang, Y. Liu, X. Hu, X. Ke, L. Zhong, Y. He, X. Ren, Enhancing dielectric permittivity for energy-storage devices through tricritical phenomenon, Sci. Rep. 7 (2017) 40916.

[28] C.W. Nan, Y. Shen, J. Ma, Physical properties of composites near percolation, Annu. Rev. Mater. Res. 131–151 (2010).

[29] J. Zhu, J. Shen, S. Guo, H.J. Sue, Confined distribution of conductive particles in polyvinylidene fluoride–based multilayered dielectrics: toward high permittivity and breakdown strength, Carbon 84 (2015) 355–364.

[30] W. Wang, S. Zhang, L. Srisombat, T. Lee, R. Advincula, Gold-nanoparticle and gold-nanoshell-induced polymorphism in poly(vinylidenefluoride), Macromol. Mater. Eng. 296 (2) (2011) 178–184.

[31] X.C. Chen, P.F. Green, Structure of thin film polymer/nanoparticle systems:polystyrene (PS) coated-Au nanoparticle/tetramethyl bisphenol-A polycarbonate mixtures (TMPC), Soft Matter 7 (2011) 1192–1198.

[32] N. Chen, L. Hong, Surface phase morphology and composition of the casting films of PVDF–PVP blend, Polymer 43 (4) (2002) 709,1429-1436.

[33] E.Yu Kaniukov, A.E. Shumskaya, M.D. Kutuzau, V.D. Bundyukova, D.V. Yakimchuk, D.B. Borgekov, M.A. Ibragimova, I.V. Korolkov, S.G. Giniyatova, A.L. Kozlovskiy, M.V. Zdorovets, Degradation mechanism and way of surface protection of nickel nanostructures, Mater. Chem. Phys. 223 (1) (2019) 88–97.

[34] A.L. Kozlovskiy, I.V. Korolkov, G. Kalkabay, M.A. Ibragimova, A.D. Ibrayeva, M.V. Zdorovets, V.S. Mikulich, D.V. Yakimchuk, A.E. Shumskaya, E. Yu Kaniukov, Comprehensive study of Ni nanotubes for bioapplications: from synthesis to payloads attaching, J. Nanomater. 9 (2017).

[35] R.S. Dahiya, D. Cattin, A. Adami, C. Collini, L. Barboni, M. Valle, IEEE Sens. J. 11 (2011) 3216–3226.

[36] B. Bera, M.D. Sarkar, Gold nanoparticle doped PVDF nanofiber preparation of concurrently harvesting light and Mechanical energy, IOSR J. of Appl. Phys. (IOSR-JAP) e-ISSN 9 (3) (2017) 2278–4861.

[37] D. Mandal, K. Henkel, D. Schmeißer, Comment on "Preparation and characterization of silver-poly(vinylidene fluoride) nanocomposites: formation of piezoelectric polymorph of poly(vinylidene fluoride), J. Phys. Chem. B 115 (2011) 10567–10569.

[38] B.S. Ince-Gunduz, R. Alpern, D. Amare, J. Crawford, B. Dolan, S. Jones, Impact of nanosilicates on poly(vinylidene fluoride) crystal polymorphism: Part 1. Melt-crystallization at high supercooling, Polymer 51 (2010) 1485–1493.

[39] S. Ramsundaram, S. Yoon, K.J. Kim, C. Park, J. Polym. Sci. B Polym. Phys. 46 (2008) 2173–2187.

[40] P. Martins, A. Lopes, S. Lanceros-Mendez, Electroactive phases of poly (vinylidene fluoride): determination, processing and applications, Prog. Polym. Sci. 39 (2014) 683–706.

[41] C. Malarkodi, R. Shanmugam Kuma, M. Vanaja, K. Paulkumar, G. Gnanajobitha, G. Annadurai, Eco-friendly synthesis and characterization of gold nanoparticles using Klebsiella pneumoniae Malarkodi, J. of Nanostruct. in Chemistr. 3 (2013) 30.

[42] P. Fakhria, H. Mahmoodb, B. Jaleha, A. Pegorettib, Improved electroactive phase content and dielectric properties of flexible PVDF nanocomposite films filled with Au- and Cu-doped graphene oxide hybrid nanofiller, Synth. Met. 220 (2016) 653–660.

[43] B. Mallick, T. Patel, R.C. Behera, S.N. Sarangi, S.N. Sahu, R.K. Choudhar, Microstrain analysis of proton irradiated PET microfiber, Nucl. Instrum. Methods Phys. Res., Sect. B 248 (2) (2006) 305–310.

[44] M. Madani, Structure optical and thermal decomposition characters of LDPE graft copolymers synthesized by gamma irradiation, Bull. Mater. Sci. 33 (1) (2010) 65–73.

[45] A. Vij, A.K. Chawla, R. Kumar, S.P. Lochab, R. Chandra, N. Singh, Effect of 120MeVAg 9 + ion beam irradiation on the structure and photoluminescence of SrS:Ce nanostructures, Phys. B Condens. Matter 405 (11) (2010) 2573–2576.

[46] P. Singh, R. Kumar, Influence of high-energy ion irradiation on the structural, optical, and chemical properties of polytetrafluoroethylene, Adv. Polym. Technol. 33 (3) (2014) 21410–21419.

[47] K.C. Kao, Dielectric Phenomena in Solids: with Emphasis on Physical Concepts of Electronic Processes, first ed., Elsevier Academic Press, London, 2004.

[48] A. Liu, H. Zhu, H. Sun, Y. Xu, Y.-Y. Noh, Solution processed metal oxide high-κ dielectrics for emerging transistors and circuits, Adv. Mater. 30 (33) (2018) 1706364.

[49] G.G. Raju, Dielectrics in Electric Fields, second ed., CRC press, New York, 2016.

[50] W.M. Steve, W. Yao, K. Berg, Space charge polarization measurements as a method to determine the temperature dependence of the number density of mobile cations in ion conducting glasses, Z. Phys. Chem. 223 (2009) 1379–1393.

[51] J. Lee, S. Lim, Polarization behavior of polyvinylidene fluoride films with the addition of reduced graphene oxide, J. of Indust. and Engineer. Chemist. 67 (25) (2018) 478–485.

[52] S.O. Kasap (Ed.), Principles of Electronic Materials and Devices, Mcgraw –Hill, 2006.

[53] H. Sun, H. Zhang, S. Liu, N. Ning, L. Zhang, M. Tian, Y. Wang, Interfacial polarization and dielectric properties of aligned carbonnanotubes/polymer composites:The role of molecular polarity, Compos. Sci. Technol. 154 (2018) 145–153.

[54] G. Zhang, D. Brannum, D. Dong, L. Tang, E. Allahyarov, S. Tang, K. Kodweis, J.-K. Lee, L. Zhu, Interfacial polarization-induced loss mechanisms in polypropylene/BaTiO3 nanocomposite dielectrics, Chem. Mater. 28 (13) (2016) 4646–4660.

[55] K. Lee, H. Kao, J. Parizi, S.S. Caruntu, G.T. Xu, Dielectric properties of barium titanate supramolecular nanocomposites, Nanoscale 6 (2014) 3526–3531.

[56] J. Mijovi, H. Lee, J. Kenny, J. Mays, Dynamics in polymer-silicate nanocomposites as studied by dielectric relaxation spectroscopy and dynamic mechanical spectroscopy, Macromolecules 39 (2006) 2172–2182.

[57] M. Arous, B.I. Amor, A. Kallel, Z. Fakhfakh, G. Perrier, Crystallinity and dielectric relaxations in semicrystalline poly (ether ether ketone), J. Phys. Chem. Solids 68 (2007) 1405–1414.

[58] C.C. Wang, J.F. Song, H.M. Bao, Q.D. Shen, C.Z. Yang, Enhancement of electrical properties of ferroelectric polymers by polyaniline nanofibers with controllable

conductivities, Adv. Funct. Mater. 18 (8) (2008) 1299–1306.

[59] P. Lunkenheimer, V. Bobnar, A.V. Pronin, A.I. Ritus, A.A. Volkov, A. Loidl, Phys. Rev. B Condens. Matter 66 (2002) 052105.

[60] E. Edwards Matthew, K.B. Ashok, K. Chilvery Ashwith, P. Guggilla, M. Curley, D. Mohan, Aggarwal pyroelectric properties of PVDF:MWCNT nanocomposite film for uncooled infrared detectors, Mater. Sci. Appl. 3 (2012) 851–855.

[61] K.S. Tan, W.C. Gan, T.S. Velayutham, W.H. Abd Majid, Pyroelectricity enhancement of PVDF nanocomposite thin films doped with ZnO nanoparticles Smart, Mater. Struct. 23 (2014) 125006–125011.

[62] T. Furukawa, Phase Transitions pyroelectric coefficient 18 (1989) 143–211.

[63] R. Capan, T.H. Richardson, D. Lacey, Pyroelectric figure of merit for a heterogeneous alternate layer Langmuir–Blodgett film system, Thin Solid Films 415 (2002) 236–241.

[64] L.L. Sun, O.K. Tan, W.G. Liu, X.F. Chen, W. Zhu, Comparison study on sol–gel Pb (Zr0.3Ti0.7)O3/PbTiO3 multilater thin films for pyroelectric infrared detectors, Microelectron. Eng. 66 (2003) 738–744.

[65] R. Wu, P. Du, W. Weng, G. Han, Pyroelectric properties of BST/PLT composite thick films with addition of xPbO-(1_x)B2O3 glass, Mater. Sci. Eng., B 130 (2006) 282–287.

[66] C. Wu, G. Cai, W. Luo, Q. Peng, X. Sun, W. Zhang, Enhancement of pyroelectric properties of composite thick films using Mn-doped PZT, Sens. Actuat. A-Phys. 199 (2013) 24–29.

[67] L. Jin, F. Li, S. Zhang, Decoding the fingerprint of ferroelectric loops: comprehension of the material properties and structures, J. Am. Ceram. Soc. 97 (2014) 1–27.

[68] R. Kumar, S. Singh, Giant electrocaloric and energy storage performance of [(K0.5Na0.5)NbO3](1 − x)-[LiSbO3]x nanocrystalline ceramics, Sci. Rep. 8 (2018) 3186.

[69] X. Hao, A review on the dielectric materials for high energy-storage application, J. Adv. Dielectr. 03 (2013) 1330001.

Hindustan College of Science and Technology
Farah-Mathura
(AICTE approved & affiliated to AKTU)

Project: II

Development of novel epoxy resin/graphene nanocomposite coating materials for aircraft structures

Sanctioned Agency:

(DRDO, New Delhi)

Sanctioned letter

Tele : 23007803

ARDB/01/1051902/M/I
Government of India,
Ministry of Defence,
Aeronautics R&D Board,
DRDO Bhawan, Rajaji Marg,
New Delhi-110 011

27th Feb 2019

To,
Director,
Hindustan College of Science and Technology,
Agra-Delhi NH#2, Farah,
Distt- Mathura–281122

GRANT-IN-AID SCHEME OF AERONAUTICS R&D BOARD

Under the powers vested in the Aeronautics R&D Board vide Govt. of India, Ministry of Defence letter No. Aero/4806/5/69/105/S/D(R&D) dated 12th Feb 1971 and in exercise of power delegated vide Sl No. 3.1 of GoI, MOD letter no DRDO/DFMM/PL/83226/M/01/1174/D(R&D) dated 28 Jun 2018. I am directed to convey the sanction of the Board for the following project for the year **2018-2019**.

2. TITLE OF THE PROJECT: **"Development of novel epoxy resin / graphene nanocomposite coating material for aircraft structures"**

PI : Dr MS Gaur
Co-PI : Dr RK Tiwari

SANCTION for the First year funds to be released during the year 2018-19 to the tune of **Rs. 5.26 lakhs** is accorded.

Total estimated funds for the project are **Rs 9.50 lakhs**. However, the same is subject to revision based on performance and review. The year-wise break-up is given below:-

HEAD	**Ist Year** (in lacs)	**IInd Year** (in lacs)	**IIIrd Year** (in lacs)
Staff Salary (01 PA @ 16000/-)	1.92	1.92	1.92
Equipment	2.70	0.00	0.00
Consumable	0.33	0.00	0.00
Contingency	0.15	0.06	0.05
Travel	0.05	0.05	0.00
Overhead	0.11	0.15	0.09
Total	**5.26**	**2.18**	**2.06**
Grand Total: Rs 9.50 lakhs (Nine Lakhs Fifty Thousand Only)			

3. The Deliverables of the project are:
   i. The electrochemical impedance, capacitance and corrosion test of nanocomposite material coated aluminum alloy.
   ii. The corrosion of aluminum alloy is expected to reduce by 30% using graphene as nanofillers in epoxy resin coating material.
   iii. Enhanced mechanical strength, weight reduction, improved barrier properties, and life time of aircraft directly.

. . .

Director
Hindustan College of
Science & Technology
FARAH (MATHURA)

4. Funds for subsequent year(s) will be released on satisfactory progress and submission of annual progress report by PI to the Panel and Sectt. and based on Panel recommendation with due approval of competent authority. Statement of accounts and utilization certificate duly certified by the executive financial authority of the Institution and audited by the competent audit authority is also required to be submitted along with the annual report. Excess expenditure, beyond the yearly sanction, unless authorized by AR&DB in writing, shall be the responsibility of the grantee institutions.

5. The duration of the project is **3 Years.** The date of receipt of the grant would be reckoned as the commencement date of the project which has to be intimated to this Sectt. without any ambiguity.

6. Grantee institute to open a savings bank account for the grant and refund the accrued interest to AR&DB. In case of common bank account held by the institute, the institute can reflect the accrued interest separately and refund the same to AR&DB.

7. The grantee institution shall incorporate necessary clause to provide reservation for SC & ST or OBC in posts and services for appointing project staff under grant-in-aid scheme.

8. On completion of the project unspent balance if any should be deposited through MRO at your end against AR&DB sanction project No. **"1051902"** to the PCDA (R&D), New Delhi A/c No.-4055000004. Thereafter, a copy of the MRO duly receipted may be sent to PCDA (R&D), West Block-V, RK Puram New Delhi-110066 under intimation to AR&DB Sett with a copy of MRO for necessary records.

9. A list of inventory of equipment purchased out of AR&DB grant shall be intimated year wise along with its cost and source of procurement to AR&DB Sectt. On completion of the project, the grantee institution would forward the consolidated list with request, if any, for retention of any equipment for another project of in-house R&D, with due recommendations of their executive authority and the concerned panel.

10. The grantee institutions shall not disclose any information under RTI ACT, 2005 as DRDO is placed under second schedule and is exempted from disclosure of information under Sec 24(i) of the Act except information pertaining to the allegation of corruption and Human Right Violation.

    (i) In case any application is received by the grantee institution for seeking information pertaining to DRDO project under RTI Act 2005, it may not be replied to directly and the same shall be transferred to CPIO, DRDO, HQ for necessary action and reply under sec (63) of the RTI Act at the following addresses:

    314 A, 'B' Block, RTI Cell, DRDO Bhawan, Rajaji Marg, New Delhi – 110011

11. Instruction and Conditions of Ownership of intellectual properties generated by this project is available in https://www.drdo.gov.in/drdo/boards/ardb/rules&grants_patents.htm . A copy of Govt letter is attached.

12. On completion of the projects, Closure Report along with copies of technical report for each Panel member and also one soft copy to Sectt. may be submitted within sixty days of completion of project along with Statement-2 (Statement of Expenditure) & Statement-3 (Utilisation Certificate) as per Annexure III of Grant-in-aids rules duly audited from the Audit Authority of Institution/organization signed in ink in duplicate.

13. PCDA (R&D), West Block V, RK Puram, New Delhi-110066 will make disbursement of money as sanctioned.

Director
Hindustan College of
Science & Technology
FARAH (MATHURA)

14. The expenditure will be debited to Major Head 2080 – Defence Services, R & D, Minor Head 004-Research/Research & Development and Code Head 852/02 (AR&DB Grant-in-aid) of Defence Services Estimates.

15. Contingent bill (in triplicate) duly completed and stamped along with ECS mandate (Bank A/C details) may please be forwarded to us within 30 days for countersignature and onward transmission to PCDA (R&D), West Block V, RK Puram, New Delhi-110066 for payment.

16. This is issued with the concurrence of IFA (R&D) New Delhi vide their UO No: IFA/R&D/New Delhi/1956/1457 dated 22.02.2019.

17. Sanction Code is MSRB/TM/ARDB/GIA/18-19/0105 dated 27 Feb 2019

(Dr Maitreyee Nanda)
Secretary, AR&DB

Copy to :-

(1) Principal CDA(R&D), West Block V, RK Puram, New Delhi-110066

(2) IFA (R&D), DRDO Bhawan

(3) Dy. Director of Audit, Defence Services, Southern Command, Pune – 411 001

(4) Principal Director of Audit, Air Force & Navy, `M' Block, N. Delhi-110 001

(5) Dr. Amol A Gokhale (Convenor TC)
(Former DS & Director,DMRL, Hyderabad)
Professor, Mechanical Engineering Department, IIT Bombay
Powai, Mumbai-400076

(6) Dr MS Gaur (PI), Prof,
Department of Physics, Hindustan College of Science and Technology,
Agra-Delhi NH#2, Farah, Distt- Mathura–281122

(7) Dr Rk Tiwari (Co-PI), Asso Prof,
Department of Physics, Hindustan College of Science and Technology,
Agra-Delhi NH#2, Farah, Distt- Mathura–281122

(8) Dr. Makarand Joshi Sc 'G'
Research & Development Establishment (Engrs)
Alandi Road, Dighi, Pune-411015

Control No: 105 (2018-2019)

Director
Hindustan College of
Science & Technology
FARAH (MATHURA)

Tele : 23007803

ARDB/01/1051902/M/I
Government of India,
Ministry of Defence,
Aeronautics R&D Board,
DRDO Bhawan, Rajaji Marg,
New Delhi-110 011

6th Jan 2021

To,

Director,
Hindustan College of Science and Technology,
Agra-Delhi NH#2, Farah,
Distt- Mathura–281122

<u>AR&DB SANCTIONED PROJECT NO. 1902</u>
<u>"Development of novel epoxy resin / grapheme nanocomposite coating material for aircraft structures"</u>

1. Further to the sanction letter No. ARDB/01/1051902/M/I dated 27th Feb 2019 under the power vested in the Aeronautics R&D Board Vide Govt. of India, Ministry of Defence letter No. Aero/4806/5/69/105/S/D(R&D) dated 12th Feb 1971 and in exercise of the power delegated vide Sl No. 3.1 of GoI, MoD letter No. DRDO/DFMM/PL/83226/M/01/1976/D(R&D) dated 18 Dec 2019 as amended from time to time, I am directed to convey the sanction of the Board for second year release of the subject project during FY **2020-2021**.
2. Fresh release of **Rs. 2,18,000 (Two Lakh eighteen thousand only)** for second year of the project is accorded to **Hindustan College of Science and Technology, Mathura.**
3. Unspent balance of 2019-20 may be utilized during the year 2020-21.
4. **Hindustan College of Science and Technology, Mathura** to maintain a saving bank account account and refund the accrued interest to AR&DB. In case of common account held by institute, the institute can reflect the interest accrued separately and refund the accrued interest.
5. So far (till 2019-20) a total sum of **Rs 5.26 lakhs** has been released to **Hindustan College of Science and Technology, Mathura** for the above project.
6. The total cost of the project is **Rs 9.50 lakhs.**
7. The expenditure will be debited to Major Head 2080 – Defence Services, R & D, Minor Head 004-Research/Research & Development and Code Head 852/02 (AR&DB Grant-in-aid) of Defence Services Estimates.
8. PCDA (R&D), West Block V, RK Puram, New Delhi-110066 will make disbursement of money as mentioned above.
9. Contingent bill (in triplicate) duly completed (signature of PI & HOD also required) and stamped, along with ECS mandate certificate may please be forwarded to this office for countersignature and onward transmission to PCDA (R&D), West Block V, RK Puram, New Delhi-110066.

Director
Hindustan College of
Science & Technology
FARAH (MATHURA)

Email: ardb.hqr@gov.in

ARDB/01/1051902/M/I
Government of India
Ministry of Defence
Aeronautics R&D Board
DRDO HQ Annexe,
Metacalfe House,
New Delhi-110054

29 Oct 2021

To,

Director,
Hindustan College of Science and Technology,
Agra-Delhi NH#2, Farah,
Distt- Mathura–281122

Release of third year grant of Project titled "Development of novel epoxy resin / graphene nanocomposite coating material for aircraft structures"

Further to the sanction letter No. ARDB/01/1051902/M/I dated 27 Feb 2019 and 06 Jan 2021 under the powers vested in the Aeronautics R&D Board vide Govt. of India, Ministry of Defence letter No. Aero/4806/5/69/105/S/D(R&D) dated 12th Feb 1971, and in exercise of power delegated vide DRDO/DFMM/PL/83226/M/01/1976/D(R&D) dated 18th Dec 2019 as amended from time to time, I am directed to convey sanction of release of third year grant, Rs. 1.65904 lakhs (one lakhs sixty five thousand nine hundred four rupees) for the subject project.

2. Unspent balance (Rs. 40,096) may be utilized during the year 2021-22.
3. Hindustan College of Science and Technology, Mathura to maintain a saving bank account and refund the accrued interest to PCDA. In case of common account held by institute, the institute can reflect the interest accrued separately and refund the accrued interest.
4. So far (till date) a total sum of Rs 7.44 lakhs has been released to Hindustan College of Science and Technology, Mathura for the subject project.
5. The total funds sanctioned for the subject project is Rs 9.50 lakhs.
6. The expenditure will be debited to Major Head 2080 - Defence Services, R & D, Minor Head 004–Research / Research & Development and Code Head 852/02 (AR&DB Grant-in-aid) of Defence Service's Estimates.
7. PCDA (R&D), West Block V, RK Puram, New Delhi-110066 will make disbursement of money as sanctioned.
8. Sanction Code is MSRB/TM/ARDB/GIA/21-22/95 dated 29.10.21

(Rekha Upadhyay)
Member Secretary, AR&DB

Copy to:

1. Principal CDA(R&D), West Block V, RK Puram, New Delhi-110066
2. IFA (R&D), DRDO Bhawan
3. Dy. Director of Audit, Defence Services, Southern Command, Pune – 411 001
4. Principal Director of Audit, Air Force & Navy, 'M' Block, N. Delhi-110 001

Director
Hindustan College of
Science & Technology
FARAH (MATHURA)

5. Dr. Amol A Gokhale (Chairman, Steering Committee), Professor, Mechanical Engineering Department, IIT Bombay, Powai, Mumbai-400076

6. Director, ADE, Bangalore-560075

7. Dr. Makarand Joshi Sc 'G', (Chairman Structure Panel)
Research & Development Establishment (Engrs)
Alandi Road, Dighi, Pune-411015

8. Dr MS Gaur (PI), Prof,
Department of Physics, Hindustan College of Science and Technology,
Agra-Delhi NH#2, Farah, Distt- Mathura–281122

9. Dr Rk Tiwari (Co-PI), Asso Prof,
Department of Physics, Hindustan College of Science and Technology,
Agra-Delhi NH#2, Farah, Distt- Mathura–281122

Control No. 95 (2021-22)

Director
Hindustan College of
Science & Technology
FARAH (MATHURA)

Ph : 011-2390 2743
Fax : 011-2390 2794

Email – ardb.hqr@gov.in

ARDB/01/1051902/M/I
Aeronautics R&D Board (AR&DB)
Govt. of India, Ministry of Defence
Room No-411, Old LASTEC Building
DRDO HQ Annexe, Metcalfe House,
Civil Lines, Delhi-110054

29 August 2022

To,

The Director,
Hindustan College of Science and Technology,
Agra-Delhi NH2, Farah,
Mathura–281122

PDC Extension with cost enhancement and release of remaining fund of Project titled "Development of novel epoxy resin / graphene nanocomposite coating material for aircraft structures"

Further to the sanction letter no ARDB/01/1051902/M/I dated 27 Feb 2019, 06 Jan 2021, 29 Oct 2021 and under the powers vested in the Aeronautics R&D Board vide Govt. of India, Ministry of Defence letter no. Aero/4806/5/69/105/S/D(R&D) dated 12th Feb 1971, and in exercise of power delegated vide Sl. No. 3.1 of DRDO/DFMM/PL/63226/M/01/1976/D(R&D) dated 10th Dec 2019 as amended from time to time, I am directed to convey sanction of CFA for **PDC Extension till 31st March 2023 with cost enhancement of Rs 2.0 lakhs and release of balance fund, Rs. 2.41096 lakhs** in the subject project.

2. The total funds sanctioned for the subject project is increased from Rs. 9.5 lakhs to Rs. 11.5 lakhs after cost enhancement of Rs. 2 lakhs. The revised break-up of funds is as follow:

HEAD	Funds (Rs. in Lakhs)
Staff Salary	6.99733
Equipment	2.7
Consumable	0.33
Contingency	0.41
Travel	0.26
Procured Services	0.4
Overhead	0.40267
Total	11.5

3. Unspent balance of FY 2021-22 may also be utilised in FY 2022-23.

4. Fresh release of Rs. 2.41096 lakhs for the subject project is accorded.

5. So far (till date) a total sum of Rs 9.08904 lakhs has been released to Hindustan College of Science and Technology, Mathura for the subject project.

6. Hindustan College of Science and Technology, Farah, Mathura to maintain a saving bank account and refund the accrued interest to AR&DB. In case of common account held by institute, the institute can reflect the interest accrued separately and refund the accrued interest.

Director
Hindustan College of
Science & Technology
FARAH (MATHURA)

To,

Director,
Hindustan College of Science and Technology,
Agra-Delhi NH#2, Farah,
Distt- Mathura--281122

AR&DB SANCTIONED PROJECT NO. 1902
"Development of novel epoxy resin / grapheme nanocomposite coating material for aircraft structures"

1. Further to the sanction letter No. ARDB/01/1051902/M/I dated 27th Feb 2019 under the power vested in the Aeronautics R&D Board Vide Govt. of India, Ministry of Defence letter No. Aero/48806/5/69/105/S/D(R&D) dated 12th Feb 1971 and in exercise of the power delegated vide SI No. 3.1 of GoI, MoD letter No. DRDO/DFMM/PL/83226/M/01/1976/D(R&D) dated 18 Dec 2019 as amended from time to time, I am directed to convey the sanction of the Board for second year release of the subject project during FY 2020-2021.
2. Fresh release of **Rs. 2,18,000 (Two Lakh eighteen thousand only)** for second year of the project is accorded to **Hindustan College of Science and Technology, Mathura.**
3. Unspent balance of 2019-20 may be utilized during the year 2020-21.
4. **Hindustan College of Science and Technology, Mathura** to maintain a saving bank account account and refund the accrued interest to AR&DB. In case of common account held by institute, the institute can reflect the interest accrued separately and refund the accrued interest.
5. So far (till 2019-20) a total sum of **Rs 5.26 lakhs** has been released to **Hindustan College of Science and Technology, Mathura** for the above project.
6. The total cost of the project is **Rs 9.50 lakhs.**
7. The expenditure will be debited to Major Head 2080 – Defence Services, R & D, Minor Head 004-Research/Research & Development and Code Head 852/02 (AR&DB Grant-in-aid) of Defence Services Estimates.
8. PCDA (R&D), West Block V, RK Puram, New Delhi-110066 will make disbursement of money as mentioned above.
9. Contingent bill (in triplicate) duly completed (signature of PI & HOD also required) and stamped, along with ECS mandate certificate may please be forwarded to this office for countersignature and onward transmission to PCDA (R&D), West Block V, RK Puram, New Delhi-110066.

Director
Hindustan College of
Science & Technology
FARAH (MATHURA)

Hindustan College of Science and Technology
Farah-Mathura
(AICTE approved & affiliated to AKTU)

Project: II

Development of novel epoxy resin/graphene nanocomposite coating materials for aircraft structures

Sanctioned Agency:

(DRDO, New Delhi)

Statement of Expenditure

√AUDITED/PROVISIONAL STATEMENT OF EXPENDUTURE ACCOUNTS

FOR THE FINANCIAL YEAR 2023-2024

(a) Title of the Project: “Development of novel epoxy resin/Graphene nanocomposites coating material for aircraft structure”
(b) Sanctioned letter no. & date: ARDB/01/1051902/M/I, 27.02.2019
(c) Principal Investigator : Dr. M. S. Gaur
(d) Date of Start of the Project: 08.08.2019
(e) Total Sanctioned cost of the Project: Rs. 9.50 Lakhs
(f) Grant received (Rs. Lakhs) in I yr 5.26 lakhs II yr 2.18 lakhs III yr .1.64904 IV Year: 2.41096
(g) Total Grants received so far: Rs. 11.5 Lakhs

S. No.	Sanctioned Heads	Funds Sanctioned for the year Rs. Lakhs	Funds released Rs. Lakhs	Carried forward from Previous year	Funds available (iv+v) Rs. Lakhs	Expenditure incurred during the FY Rs. Lakhs	Balance (vi-vii) Rs. Lakhs	Commitments Rs. Lakhs	Total expenditure (vii+ix) Rs. Lakhs
i	ii	iii	iv	v	vi	vii	viii	ix	x
(a)	Staff	0.00	0.00	0.16533	0.16533	0.16	0.00533	0.00	0.16
(b)	Equipment	0.00	0.00	0.01	0.01	0.00	0.01	0.00	0.00
(c)	Operation & Maint.	0.00	0.00	0.00	0.00	0.00	0.00	0.00	0.00
(d)	Consumable	0.0	0.0	0.00001	0.00001	0.0	0.00001	0.00	0.00
(e)	Travel	0.00	0.00	0.08336	0.08336	0.00	0.08336	0.00	0.00
(f)	Contingencies	0.00	0.00	0.06223	0.06223	0.00	0.06223	0.00	0.00
(g)	Research Consultant	0.00	0.00	0.00	0.00	0.00	0.00	0.00	0.00
(h)	Procured Service	0.00	0.00	0.16518	0.16518	0.00	0.16518	0.00	0.00
	Institutional over head	0.00	0.00	0.00	0.00	0.00	0.00	0.00	0.00
	Interest earned, if any								
	TOTAL	0.0	0.00	0.48611	0.48611	0.16	0.32611	0.00	0.16

Dr. M.S.Gaur
Name and Signature of
Principal Investigator
Date: 04.04.2023

Deepa Khanna and Associates
FRN-013795C
AGRA
Chartered Accountants

CA DEEPA KHANNA
M No. 403317 04.04.2023

Ishu Virakha
Name and Signature of
Accounts Officer
Date 04.04.2023

Director
Hindustan College of
Science & Technology
FARAH (MATHURA)

Signature of Administrative
Date 04.04.2023

Director
Hindustan College of
Science & Technology
FARAH (MATHURA)

√AUDITED/PROVISIONAL STATEMENT OF EXPENDUTURE ACCOUNTS

FOR THE FINANCIAL YEAR 2022-2023 (01.04.2022 to 31.03.2023)

(a) Title of the Project: "Development of novel epoxy resin/Graphene nanocomposites coating material for aircraft structure"
(b) Sanctioned letter no. & date: ARDB/01/1051902/M/I, 27.02.2019
(c) Principal Investigator : Dr. M. S. Gaur
(d) Date of Start of the Project: 08.08.2019
(e) Total Sanctioned cost of the Project: Rs. 9.50 Lakhs
(f) Grant received (Rs. Lakhs) in I yr 5.26 lakhs II yr 2.18 lakhs III yr .1.64904 IV Year: 2.41096
(g) Total Grants received so far: Rs. 11.5 Lakhs

S. No.	Sanctioned Heads	Funds Sanctioned for the year Rs. Lakhs	Funds released Rs. Lakhs	Carried forward from Previous year	Funds available (iv+v) Rs. Lakhs	Expenditure incurred during the FY Rs. Lakhs	Balance (vi-vii) Rs. Lakhs	Commitments Rs. Lakhs	Total expenditure (vii+ix) Rs. Lakhs
i	ii	iii	iv	v	vi	vii	viii	ix	x
(a)	Staff	1.23733	1.64829	0.43704	2.08533	1.92	0.16533	0.16	2.08
(b)	Equipment	0.00	0.00	0.01	0.01	0.00	0.01	0.00	0.00
(c)	Operation & Maint.	0.00	0.00	0.00	0.00	0.00	0.00	0.00	0.00
(d)	Consumable	0.0	0.00	0.05971	0.05971	0.05970	0.00001	0.00	0.05970
(e)	Travel	0.16	0.16	0.10	0.26	0.17664	0.08336	0.00	0.17664
(f)	Contingencies	0.15	0.15	0.17183	0.32183	0.2596	0.06223	0.00	0.2596
(g)	Research Consultant	0.00	0.00	0.00	0.00	0.00	0.00	0.00	0.00
(h)	Procured Service	0.40	0.40	0.00	0.40	0.23482	0.16518	0.00	0.23482
	Institutional over head	0.05267	0.05267	0.09	0.14267	0.14267	0.00	0.00	0.14267
	Interest earned, if any								Interest of Rs. 0.02669 lakhs
	TOTAL	2.0	2.41096	0.86858	3.27954	2.79343	0.48611	0.16	2.95343

Dr. M.S. Gaur 1/4/2023
Name and Signature of
Principal Investigator
Date: 01-04-2023

FRN-013795C
AGRA

CA Deepa Khanna.
M No 403317
01.04.2023

Ishu Vinahrung 1/4/23
Name and Signature of
Accounts Officer
Date 01/04/23

Director
Hindustan College of
Science & Technology
FARAH (MATHURA)

Signature of Administrative
Date 01/04/2023

Director
Hindustan College of
Science & Technology
FARAH (MATHURA)

Hindustan College of Science and Technology
Farah-Mathura
(AICTE approved & affiliated to AKTU)

Project: II

Development of novel epoxy resin/graphene nanocomposite coating materials for aircraft structures

Sanctioned Agency:

(DRDO, New Delhi)

Utilization Certificate

Hindustan College of Science & Technology

AICTE Approved • AKTU Affiliated • 5 NBA Accredited Courses

Agra-Delhi Highway (NH-2),
Farah, Distt. Mathura - 281 122
U.P. (India)
Tel : + 91-565-2763366,
+ 91-565-2763705 / 06
Fax : +91-565-2763364

DISCOVERING KNOWLEDGE

Auditated UC/SE 12.10.2021

To,

The Secretary
Aeronautics Research & Development Board (AR&DB),
DRDO Bhawan
AR&DB Secretariat,
Room No. 400A, DRDO HQrs, Ministry of Defence, Rajaji Marg, New Delhi -110011

Reference: Project no. 1902

Sub: Submission of audited UC/SE, interest deposited receipt, equipment details, manpower details, contingent bill, ECR form and project report

Reference: Project no. 1902

Sir,

I am submitting herewith the original said documents (UC/SE audited for FY 2020-2021) of above said project. The contingent bill (three copies) of III year grant is enclosed herewith for your kind perusal. Kindly release the III year grant and oblige.

Thanking you

With kind regards

Faithfully yours

12/10/2021

(Dr. M. S. Gaur)
Principal Investigator
Professor and Head
Department of Physics
Hindustan College of Science and Technology, Farah (Mathura) U P

Enclosures

(i) UC/SE (i.e. three audited copies) for F.Y 2020-2021 (ii) Interest deposited receipt(one copy) (iii) Equipment details (three copies), (iv) Manpower details (three copies), (v) Contingent bill (three copies), (vi) ECR form (three copies) and (vii) project report (three copies) (viii) Cancelled cheque (one)

Regd. Office : "SGI Tower", 500 Mtrs. from Bhagwan Talkies towards Agra-Mathura Highway (NH-2), Agra - 2
Phone : 0562-2522442, 2526758, Fax : 0562-2850274
Delhi Office : M-11, South Exth. II, New Delhi - 110 049. **Tel.**: +91-11-26262992/93/94,
visit us at : <www.hcst.in> <www.sgei.org>

SGi SHARDA GROUP OF INSTITUTIONS
Agra • Mathura • G. Noida

APPENDIX "F"

UTILIZATION CERTIFICATE

FOR THE FINANCIAL YEAR 2020-2021 (*From 01.04.2020 to 31.03.2021)*

1.	Title of the Project / Scheme	Development of novel epoxy resin/Graphene nanocomposites coating material for aircraft structure"
2.	Name of the Institution	Hindustan College of Science and Technology, Farah, Mathura-U.P.
3.	Principal Investigator	Dr. M. S. Gaur
4.	DRDO Letter No. and date of sanctioning the project Date of Start of the Project	ARDB/01/1051902/M/I, 27.02.2019 08.08.2019
5.	Head of account as given in the original sanction letter	**Pl. see Enclosure 1**
6.	Amount brought forward from the previous financial year quoting DRDO letter No. & date in which the authority to carry forward the said amount was given.	ARDB/01/105902/M/I dated 6th Jan 2021 Rs. 3.88215 lakh
7.	Amount received during the financial year (Please give no. and date of DRDO sanction letter for the amount)	Rs. 2.18 lakh
8.	Total amount that was available for expenditure (excluding commitments) during the financial year (SL. No 6 +7)	Rs. 6.06215 lakh
9.	Actual expenditure (excluding commitments) incurred during the financial this year	Rs. 4.72119 lakh
10.	Balance amount available	Rs. 1.34096 lakh
11.	Unspent balance refunded, if any) Please give details of Cheque No. etc.)	NA
12.	Amount allowed to be carried forward to this financial year	Rs. 1.34096 lakh

APPENDIX "F" (contd...)

UTILIZATION CERTIFICATE

FY 2020-2021(From 01.04.2020 to 31.03.2021)

Certified that sum of Rs. 2.18 lakhs sanctioned during the year 2020-2021 of grants-in-aid amount in favour of Director, Hindustan College of Science and Technology, Farah, Mathura U.P. DRDO letter No ARDB/01/1051902/M/I, 06.01.2021 and Rs. 3.88215 lakhs on account of unspent balance of the previous year, a sum of Rs. 4.72119 lakhs has been utilized for the purpose for which it was sanctioned and that the balance of Rs. 1.34096 lakhs will be refunded/adjusted toward the grants-in-aid payable during the 2021-2022.

Signature of Principal Investigator	Signature of Accounts/Finance Officer

2. Certified that I have satisfied myself that the conditions on which the grants-in-aid was sanctioned have been fulfilled/are being fulfilled and that I have exercised the following checks to see that the money was actually utilized for the purpose for which it was sanctioned.

Kinds of checks exercised.

1. Sanctioned head
2. Head-wise expenditure and bills of expenditure
3. Bank interest

Dr. R. K. Upadhyay
Director

Director
Hindustan College of
Science & Technology
FARAH (MATHURA)

Hindustan College of Science & Technology
AICTE Approved • AKTU Affiliated • 5 NBA Accredited Courses

Agra-Delhi Highway (NH-2),
Farah, Distt. Mathura - 281 122
U.P. (India)
Tel : + 91-565-2763366,
+ 91-565-2763705 / 06
Fax : +91-565-2763364

D I S C O V E R I N G K N O W L E D G E

Provisional UC/SE 12.10.2021

To,
The Secretary
Aeronautics Research & Development Board (AR&DB),
DRDO Bhawan
AR&DB Secretariat,
Room No. 400A, DRDO HQrs, Ministry of Defence, Rajaji Marg, New Delhi -110011

Reference: Project no. 1902

Sub: Submission of provisional UC/SE, interest deposited receipt and project report for FY 2021-2022

Reference: Project no. 1902

Sir,

I am submitting herewith the original said documents (UC/SE provisional from 1.04.2021 to 31.08.2021, interest deposited receipt and project report) of above said project. Kindly release the III year grant and oblige.

Thanking you

With kind regards

Faithfully yours

12/10/2021

(Dr. M. S. Gaur)
Principal Investigator
Professor and Head
Department of Physics
Hindustan College of Science and Technology, Farah (Mathura) U P

Encl. (i) UC/SE (i.e. three provisional copies) for FY 2020-2021
(ii) Interest deposited receipt
(iii) Report (three copies)

APPENDIX "F"

UTILIZATION CERTIFICATE

FOR THE FINANCIAL YEAR 202~~0~~1-202~~1~~2 *(From 01.04.2021 to 31.08.2021)*

1.	Title of the Project / Scheme	Development of novel epoxy resin/Graphene nanocomposites coating material for aircraft structure"
2.	Name of the Institution	Hindústan College of Science and Technology, Farah, Mathura-U.P.
3.	Principal Investigator	Dr. M. S. Gaur
4.	DRDO Letter No. and date of sanctioning the project Date of Start of the Project	ARDB/01/1051902/M/I, 27.02.2019 08.08.2019
5.	Head of account as given in the original sanction letter	**Pl. see Enclosure 1**
6.	Amount brought forward from the previous financial year quoting DRDO letter No. & date in which the authority to carry forward the said amount was given.	Rs. 1.34096 lakhs
7.	Amount received during the financial year (Please give no. and date of DRDO sanction letter for the amount)	0.00 lakhs
8.	Total amount that was available for expenditure (excluding commitments) during the financial year (SL. No 6 +7)	Rs. 1.34096 lakhs
9.	Actual expenditure (excluding commitments) incurred during the financial this year	Rs. 0.94 lakhs
10.	Balance amount available	Rs. 0.40096 lakhs
11.	Unspent balance refunded, if any) Please give details of Cheque No. etc.)	NA
12.	Amount allowed to be carried forward to this financial year	Rs. 0.40096 lakhs

APPENDIX "F" (contd...)

UTILIZATION CERTIFICATE

FY 2020-2021(From 01.04.2021 to 31.08.2021)

Certified that sum of Rs. 0.00 lakhs sanctioned during the year 2021-2022 of grants-in-aid amount in favour of Director, Hindustan College of Science and Technology, Farah, Mathura U.P. DRDO letter No´Nil and Rs. 1.34096 **lakhs** on account of unspent balance of the previous year, a sum of Rs. 0.94 lakhs has been utilized for the purpose for which it was sanctioned and that the balance of Rs. 0.40096 lakhs will be refunded/adjusted toward the grants-in-aid payable during the 2021-2022.

12/10/2021
Signature of
Principal Investigator

Signature of
Accounts/Finance Officer
Date. 12.10.2021

2. Certified that I have satisfied myself that the conditions on which the grants-in-aid was sanctioned have been fulfilled/are being fulfilled and that I have exercised the following checks to see that the money was actually utilized for the purpose for which it was sanctioned.

Kinds of checks exercised.

1. Sanctioned head
2. Head-wise expenditure and bills of expenditure
3. Bank interest

Dr. R. K. Upadhyay
Director

Director
Hindustan College o
Science & Technolog
FARAH (MATHURA)

Hindustan College of Science & Technology

AICTE Approved • AKTU Affiliated • 5 NBA Accredited Courses

Agra-Delhi Highway (NH-2),
Farah, Distt. Mathura - 281 122
U.P. (India)
Tel : + 91-565-2763366,
+ 91-565-2763705 / 06
Fax : +91-565-2763364

05.04.2023

To,

The Secretary
Aeronautics Research & Development Board (AR&DB),
DRDO Bhawan
AR&DB Secretariat,
Room No. 400A, DRDO HQrs, Ministry of Defence, Rajaji Marg, New Delhi -110011

Reference: Project no. 1902

Sub: Submission of audited UC/SE and interest deposited receipt report (three copies each) for FY 2022-2023

Reference: Project no. 1902

Sir,

I am submitting herewith the original said documents (UC/SE audited for FY 2022-2023) of above project for your kind perusal. The project completion report is submitted soon.

Thanking you

With kind regards

Faithfully yours

5/4/2023

(Dr. M. S. Gaur)
Principal Investigator
Professor and Head
Department of Physics
Hindustan College of Science and Technology, Farah (Mathura) U P

Enclosures
(i) UC/SE (i.e. three audited copies) for FY 2020-2021
(ii) Interest deposited receipt

DISCOVERING KNOWLEDGE

SGi
SHARDA GROUP OF INSTITUTIONS
Agra • Mathura • G. Noida

Regd. Office : "SGI Tower", 500 Mtrs. from Bhagwan Talkies towards Agra-Mathura Highway (NH-2), Agra - 2
Phone : 0562-2522442, 2526758, Fax : 0562-2850274
Delhi Office : M-11, South Exth. II, New Delhi - 110 049. Tel.: +91-11-26262992/93/94,
visit us at : <www.hcst.in> <www.sgei.org>

APPENDIX "F"

UTILIZATION CERTIFICATE

FOR THE FINANCIAL YEAR 2022-2023 (*From 01.04.2022 to 31.03.2023)*

1.	Title of the Project / Scheme	Development of novel epoxy resin/Graphene nanocomposites coating material for aircraft structure"
2.	Name of the Institution	Hindustan College of Science and Technology, Farah, Mathura-U.P.
3.	Principal Investigator	Dr. M. S. Gaur
4.	DRDO Letter No. and date of sanctioning the project Date of Start of the Project	ARDB/01/1051902/M/I, 27.02.2019 08.08.2019
5.	Head of account as given in the original sanction letter	Pl. see Enclosure 1
6.	Amount brought forward from the previous financial year quoting DRDO letter No. & date in which the authority to carry forward the said amount was given.	Rs. 0.86858 lakhs Letter no. ARDB/01/1051902/M/I, dated 29.08.2022
7.	Amount received during the financial year (Please give no. and date of DRDO sanction letter for the amount)	Rs. 2.41096 lakhs Letter no. ARDB/01/1051902/M/I, dated 29.08.2022
8.	Total amount that was available for expenditure (excluding commitments) during the financial year (SL. No 6 +7)	Rs. 3.27954 lakhs – Rs. 0.31 lakhs(commitment) = Rs. 2.96954 lakhs
9.	Actual expenditure (excluding commitments) incurred during the financial this year	Rs. 2.79343 lakhs
10.	Balance amount available	0.48611 Lakhs
11.	Unspent balance refunded, if any) Please give details of Cheque No. etc.)	NA
12.	Amount allowed to be carried forward to this financial year	0.48611 Lakhs

1/4/23

APPENDIX "F" (contd...)

UTILIZATION CERTIFICATE

FY 2022-2023 (From 01.04.2022 to 31.03.2023)

Certified that sum of Rs. 2.41096 lakhs sanctioned during the year 2022-2023 of grants-in-aid amount in favour of Director, Hindustan College of Science and Technology, Farah, Mathura U.P. DRDO letter No ARDB/01/1051902/M/I dated 29.08.2022 and received Rs. 2.41096 lakh and Rs. 0.86858 lakh on account of unspent balance of the previous year, a sum of Rs. 2.79343 lakhs has been utilized for the purpose for which it was sanctioned and that the balance of Rs. 0.48611 lakhs will be refunded/adjusted toward the grants-in-aid payable during the 2023-2024.

01/4/2023
Signature of
Principal Investigator

1/4/23
Signature of
Accounts/Finance Officer

2. Certified that I have satisfied myself that the conditions on which the grants-in-aid was sanctioned have been fulfilled/are being fulfilled and that I have exercised the following checks to see that the money was actually utilized for the purpose for which it was sanctioned.

Kinds of checks exercised.

1. Sanctioned head
2. Head-wise expenditure and bills of expenditure
3. Bank interest

Dr. R. K. Upadhyay
Director
Director
Hindustan College of
Science & Technology
FARAH (MATHURA)

Hindustan College of Science & Technology
AICTE Approved • AKTU Affiliated • 5 NBA Accredited Courses

Agra-Delhi Highway (NH-2),
Farah, Distt. Mathura - 281 12
U.P. (India)
Tel : + 91-565-2763366,
+ 91-565-2763705 / 06
Fax : +91-565-2763364

DISCOVERING KNOWLEDGE

6.4.2023

To,

The Secretary

Aeronautics Research & Development Board (AR&DB),

DRDO Bhawan

AR&DB Secretariat,

Room No. 400A, DRDO HQrs, Ministry of Defence, Rajaji Marg, New Delhi -110011

Reference: Project no. 1902

Sub: Submission of audited UC/SE and **unspent balance deposited receipt of Rs.0.32611 lakhs** (three copies each) for FY 2023-2024

Reference: Project no. 1902

Sir,

I am submitting herewith the original said documents (UC/SE audited for FY 2023-2024) of above project for your kind perusal.

Thanking you

With kind regards

Faithfully yours

6/4/2023

(Dr. M. S. Gaur)
Principal Investigator
Professor and Head
Department of Physics
Hindustan College of Science and Technology, Farah (Mathura) U P

Enclosures
(i) UC/SE (i.e. three audited copies) for FY 2023-2024
(ii) Unspent balance deposited receipt of Rs. 0.32611 lakhs

APPENDIX “F”

UTILIZATION CERTIFICATE

FOR THE FINANCIAL YEAR 2023-2024

1.	Title of the Project / Scheme	Development of novel epoxy resin/Graphene nanocomposites coating material for aircraft structure”
2.	Name of the Institution	Hindustan College of Science and Technology, Farah, Mathura-U.P.
3.	Principal Investigator	Dr. M. S. Gaur
4.	DRDO Letter No. and date of sanctioning the project Date of Start of the Project	ARDB/01/1051902/M/I, 27.02.2019 08.08.2019
5.	Head of account as given in the original sanction letter	PI. see Enclosure 1
6.	Amount brought forward from the previous financial year quoting DRDO letter No. & date in which the authority to carry forward the said amount was given.	Rs. 0.48611 lakhs
7.	Amount received during the financial year (Please give no. and date of DRDO sanction letter for the amount)	0.00 lakhs
8.	Total amount that was available for expenditure (excluding commitments) during the financial year (SL. No 6 +7)	Rs.0.48611 lakhs – 0.16 lakhs (committed amount) = 0.32611 lakhs
9.	Actual expenditure (excluding commitments) incurred during the financial this year	0.00 lakhs
10.	Balance amount available	0.32611 lakhs
11.	Unspent balance refunded, if any) Please give details of Cheque No. etc.)	Refunded back Rs. 0.32611 lakhs through e-MRO
12.	Amount allowed to be carried forward to this financial year	Nil

04/04/23

APPENDIX “F” (contd…)

UTILIZATION CERTIFICATE

FY 2023-2024

Certified that sum of Rs. 0.00 lakhs sanctioned during the year 2023-2024 of grants-in-aid amount in favour of Director, Hindustan College of Science and Technology, Farah, Mathura U.P. DRDO letter No nil and received Rs. 0.00 lakhs and Rs. 0.48611 lakhs on account of unspent balance of the previous year, a sum of Rs. 0.16 lakhs (i.e. committed amount of previous year) has been utilized for the purpose for which it was sanctioned and that the balance of Rs. 0.32611 lakhs will be refunded.

4/4/2023
Signature of
Principal Investigator

04/04/23
Signature of
Accounts/Finance Officer

2. Certified that I have satisfied myself that the conditions on which the grants-in-aid was sanctioned have been fulfilled/are being fulfilled and that I have exercised the following checks to see that the money was actually utilized for the purpose for which it was sanctioned.

Kinds of checks exercised.

1. Sanctioned head
2. Head-wise expenditure and bills of expenditure
3. Bank interest

Dr. R. K. Upadhyay
Director

Director
Hindustan College of
Science & Technology
FARAH (MATHURA)

Hindustan College of Science and Technology
Farah-Mathura
(AICTE approved & affiliated to AKTU)

Project: II

Development of novel epoxy resin/graphene nanocomposite coating materials for aircraft structures

Sanctioned Agency:

(DRDO, New Delhi)

Project Outcomes (Publications)

List of Publications

Entitled “Development of Novel Epoxy Resin/Grapheme Nano Composite Coating Material for Aircraft Structure”

Ministry of Defence, Aeronautics R & D Board, DRDO, New Delhi

S.No.	Name of the author	Title of the article	Name of the journal	Year of publication	Issue	Pages	Impact factor	ISSN No.	*Web link*
1	MS Gaur, Rajesh Kumar Raghav, Rohan Sagar, RK Tiwari	Investigation of anticorrosion properties of epoxy GO nanocomposites spin coated Aluminum Alloy 7075	Polymers and Polymer Composites	2022	11	8	2.12	0967-3911	https://doi.org/10.1177/09673911221106047
2	MS Gaur, Rajesh Kumar Raghav, Rohan Sagar, RK Tiwari	Investigation of Structural and Thermal Properties of Graphene Oxide Reinforced Epoxy Nanocomposites	ECS Journal of Solid State Science and Technology	2022	4	11	2.07	2162-8769	https://doi.org/10.1149/2162-8777/ac5eb0
3	Kohan Sagar, MS Gaur, Rajesh Kumar Raghav	Study of structural, thermal and piezoelectric properties of polyvinylidene fluoride–BaZrO3 nanocomposites	Journal of Thermal Analysis and Calorimetry (Springer)	2022	1	11	4.67	1388-6150	https://doi.org/10.1007/s10973-022-11302-x

①

Original Research Article

Polymers and
Polymer Composites

Polymers and Polymer Composites
Volume 30: 1–10

DOI: 10.1177/09673911221106047
journals.sagepub.com/home/ppc
SAGE

Investigation of anticorrosion properties of epoxy GO nanocomposites spin coated Aluminum Alloy 7075

Mulayam S Gaur, Rajesh K Raghav, Rohan Sagar and R.K. Tiwari

Abstract

The bisphenol A diglycidyl ether-polyaminoamide (epoxy resin)–graphene oxide (GO) nanocomposites have been prepared by chemical methods. The aim of this study is to produce epoxy –GO coatings on Aluminum Alloy 7075 and study the anticorrosion properties. Thin films have been characterized by scanning electron microscope – Energy Dispersive X-rays Spectroscopy (EDX) and Raman spectra. Raman spectra show the successful bonding of GO functional groups with epoxy. The composition of epoxy and GO is characterized by EDX. The Tafel plots were undertaken for analysis of corrosion of coating material. Therefore, the reduction of corrosion current of epoxy–GO nanocomposites coated Al alloy 7075 show its superior corrosion resistance properties. This is further confirmed by electrochemical impedance spectroscopy and potentiodynamic polarization. The very high value of low frequency impedance modulus (i.e. $10^{10}\ \Omega\ cm^2$) shows surprising anticorrosive effect on coating. The epoxy–GO spin coating in Al Alloy 7075 is significantly reduces the corrosion current density (I_{corr}) and corrosion rate due to anticorrosion properties of GO.

Keywords

Epoxy–graphene oxide, Nanocomposites, Raman, Corrosion, Scanning electron microscope-Energy Dispersive X-rays Spectroscopy

Received 11 August 2021; accepted 11 May 2022

Introduction

The nanoscale engineering produces nanostructured material, especially in polymers, the extraordinary properties could be achievable depending on selection of nanomaterials and its dispersion throughout the polymer matrix.[1–6] The presence of functional groups in polymeric materials can easily adsorb at the surface of metals. This property of polymers makes them efficient corrosion inhibitors.[7] Epoxy resins are very important class of thermosetting polymers that often exhibit high tensile strength and modulus, good corrosion resistance and good dimensional stability. The epoxy resins are the most important thermosetting materials used in various industrial applications such as in automobile, aerospace, and defense due to their excellent adhesion and mechanical properties.[8–10] The main drawback of nanoparticles in epoxy chain is the poor dispersibility, which restricted the potential application of nanocomposites in several cases.[11] Recently, it is reported that hardener cured epoxy with nano or micro structure enhances adhesion, anti-corrosion, viscoelastic and rheological properties.[12–25] The metallic nanofillers in epoxy matrix may hinder cross-linking reaction into epoxy chain reduces the corrosion resistance. Also metallic nanoparticles in epoxy matrix revealed the difference in adsorption potential due to change in curing characteristics[26–28], however, carbonaceous nanofiller like GO and Carbon Nano Tube (CNT) in epoxy are most promising candidate to enhance the mechanical properties, electrical properties and corrosion resistance is due to high surface area, high mechanical strength, low density and high thermal resistance.[29,30]

Chen et al. reported the sandwich-like structures of polydopamine and 8-hydroxyquinoline coated graphene oxide for excellent corrosion resistance of epoxy coatings.[31] Yankun Xie Chen et al. reported novel approach to fabricate polyacrylate

---

Department of Physics, Hindustan College of Science and Technology, Farah, Mathura, India, Affiliated to Dr. A.P.J. Abdul Kalam Technical University, Lucknow, U.P., India

Corresponding author:
Mulayam S Gaur, Department of Physics, Hindustan College of Science and Technology, Farah, Mathura, 281122, India, Affiliated to Dr. A.P.J. Abdul Kalam Technical University, Lucknow, U.P., India.
Email: mulayamgaur@rediffmail.com

modified graphene oxide for improving the corrosion resistance of epoxy coatings.[32] Mohammad et al reported the development of metal-organic framework (MOF) decorated graphene oxide nano-plateforms for anti-corrosion epoxy coatings.[33] These efforts develop a scientific knowledge to develop anticorrosion material. Ali et al reported that epoxy-polyamide nanocomposites coating with graphene oxide as cerium nanocontainer generating effective dual active/barrier corrosion protection.[34] The several publications have explored more attempts for the organic coating materials; however, these methods still have much room for improvement for the complex process steps, chemical modifiers, and therefore fail to satisfy the requirements of high efficiency, low cost and environment friendliness in industrial production. The novelty of this work is to present a method to coat uniform thin film of epoxy–GO nanocomposites on Al substrate to enhance anticorrosion properties as compare to other method. The spin coating method is most suitable for nanocomposites coatings as compare to other method. There are several advantages of spin coating over other methods such as (i) uniform coating thickness could be maintained, (ii) thickness of coating can be varied by varying the speed of spin coater, (iii) the solvent can be removed during the spinning process due to evaporation, (iii) strong adhesive coating and (iv) layer by layer coating. The main target of present work is to develop corrosion resistant novel coating method and material for aircraft aluminum. This objective could be achieved by applying Electrochemical impedance spectroscopy (EIS) and potentio-dynamic polarization techniques. Further, structural morphology of epoxy–GO thin film was studied by SEM and Raman to justify the compatibility of coating.

Experimental details

Materials

Epoxy resin, graphite flakes, curing agent (hardener) $KMnO_4$, H_2SO_4, H_3PO_4, HCl, H_2O_2, acetone, ethanol, and dimethylformamide were procured from Sigma Aldrich, India. The commercially available Aluminum Alloy 7075 (99% pure) sheet were procured from Mallinath Metals, Mumbai (India).

Preparation of graphene oxide

GO was prepared by modified Hummers method. In this method, a mixture of graphite powder (2 g), H_2SO_4 (50 mL) and H_3PO_4 (5.5 mL) were mixed and stirred for 2 h. During stirring, 5.5 g of $KMnO_4$ was slowly added into the solution. This mixture was stirred for 6 h until the solution became dark green. The more details of this method is reported in literature.[35] To reduce the excess of $KMnO_4$, 12 mL H_2O_2 and 80 mL of H_2O was dropped slowly and stirred for 15 min. The physical or chemical changes are occurred in exothermic reaction, they are generally accompanied by transfer of heat. 10 mL of hydrochloric acid (HCl) and 30 mL of deionized water (DIW) was added and centrifuged for 5 min at 4000 rpm for 30 min. The precipitate was washed with DI water, HCl and ethanol. The final precipitate was dissolved in DI water and sonicated for 1 h. The washed GO solution was dried using oven at 90 °C for 24 h to produce the powder of GO. The 80 mL of H_2O and 12 mL H_2O_2 was added to remove other impurity.

Preparation of epoxy/graphene oxide nanocomposites

The graphene oxide/epoxy nanocomposites thin films were prepared by sol gel method. The amounts of epoxy resins and curing agent were 70 and 30 parts by weight/weight ratio have been taken and stirred at room temperature for 20 min. For preparation of epoxy –GO solution, the GO of 0.4 wt.% were mixed slowly in previous solution and again stirred for the period of 20 minutes. The uniform viscous solution of epoxy and epoxy –GO have been prepared. The optically plane glass plates were immersed in epoxy solution and epoxy solution of different GO concentration at room temperature for about 10 minutes. The glass plates were gradually drawn out from solution and kept in vacuum oven at 50 °C overnight to remove the residual traces of solvents. The thin films were peeled off from the plates and again kept in vacuum over the period of 24 h to prevent them from impurity and moisture. Figure 1 shows the mechanism of chemical interaction/bonding of GO with epoxy resin. Mostly epoxy-based polymers are cross-structured polymers. The cross-linking of polymers is significantly affected the mechanical properties. The covalent bond based schematic epoxy network structure is shown in Figure 1 (represented by a solid black line in Figure 1(c)). The two active sites of epoxy resin are represented by rhombus E (Figure 1(a)) and the pentagon H (Figure 1(b)). Figure 1(b) shows the five active sites of curing agent. The formations of covalent bond are based on the sharing of electron between active sites and stabilize their potential energy. In this process four dots of hardener generates four covalent bond by cross-linking, but when GO was mixed, the last dot of pentagon connected with GO sheet functional group and make very strong cross-linking or very complex matrix, which is shown in Figure1(d). The mechanical strength of epoxy matrix could be increased in presence of GO. Further, Al 7075 of dimension 1×1 cm^2 is rotated at high speed in order to spread the coating materials by centrifugal force. The solvent from coating is removed during spinning process due to evaporation and keeping the coated samples at 50 °C in vacuum oven. The spin coating method is presented in Figure 2.

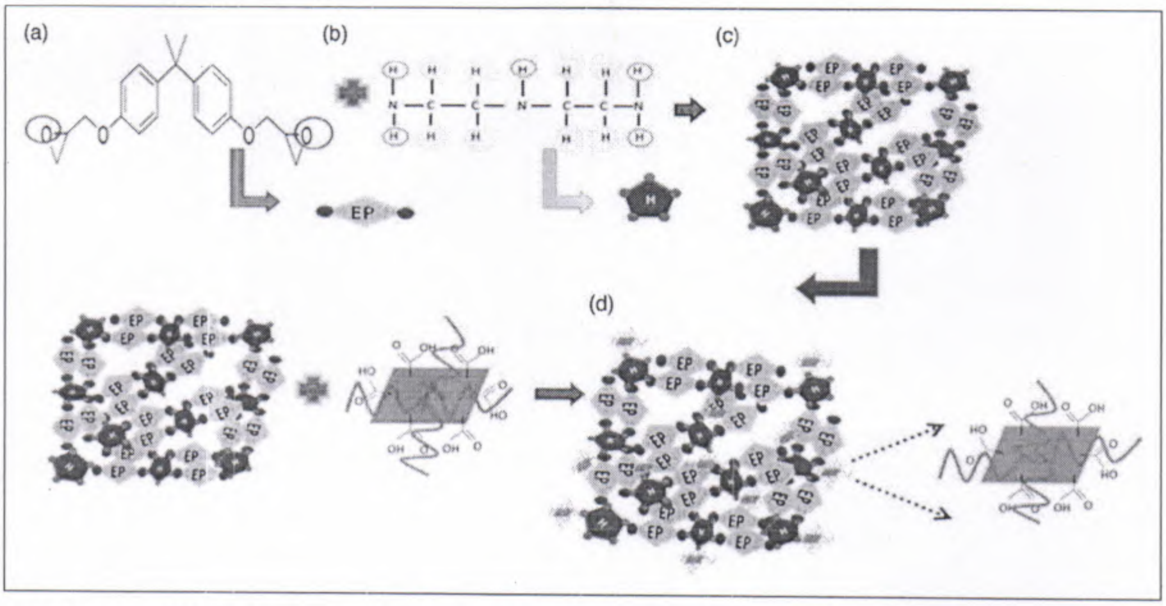

Figure 1. Mechanism of chemical interaction/bonding of GO with epoxy.

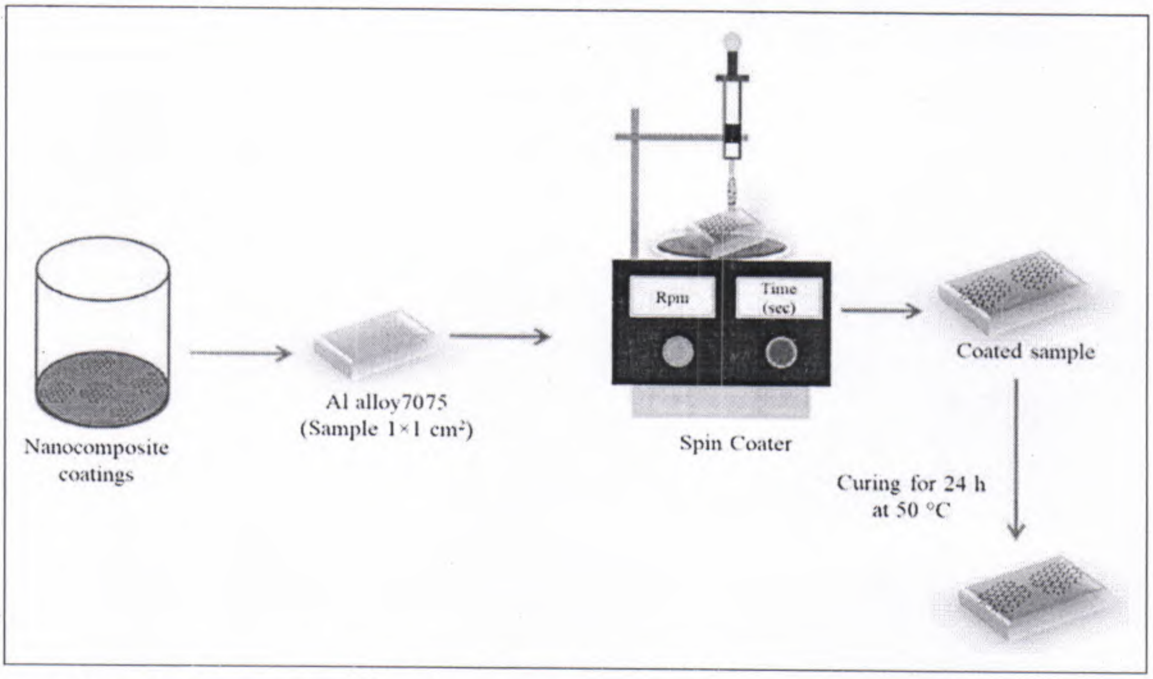

Figure 2. Spin coating of epoxy–GO in Al alloy 7075 sample.

Results and discussion

Scanning electron microscope–Energy Dispersive X-rays Spectroscopy analysis of epoxy/GO nanocomposites

The microstructure and their compositions of epoxy–GO nanocomposites were characterized by Scanning electron microscope (SEM)–Energy Dispersive X-rays Spectroscopy (EDX) (MIRA II LMH form TESCAN). Figures 3 and 4 show the SEM –EDX images of epoxy–GO nanocomposites. It has been observed that when concentration of GO increases, the dispersion of GO multilayers also increased, which is shown in Figure 3(b) and (c). It is well known that epoxy exhibits typically brittle fracture, however, epoxy –GO have gliding fracture. This shows that fault age was rough for the epoxy–GO nanocomposites. Thus, GO in epoxy matrix increases the toughness of the epoxy by preventing crack propagation. The strong interfacial bonding of GO with epoxy is due to influence of GO owned oxygen-containing groups. The oxidation potency of GO is high due to presence of the oxygen-containing (i.e., epoxide, C=O, hydroxyl) groups. The phytochemicals can be oxidized into quinone forms and, in this way, eliminate the oxygen-containing groups of GO.[36,37] This is an evidence that epoxy resin molecules are not only reduced the oxygen-containing groups, but also increase the GO interlayer d-spacing.[38]

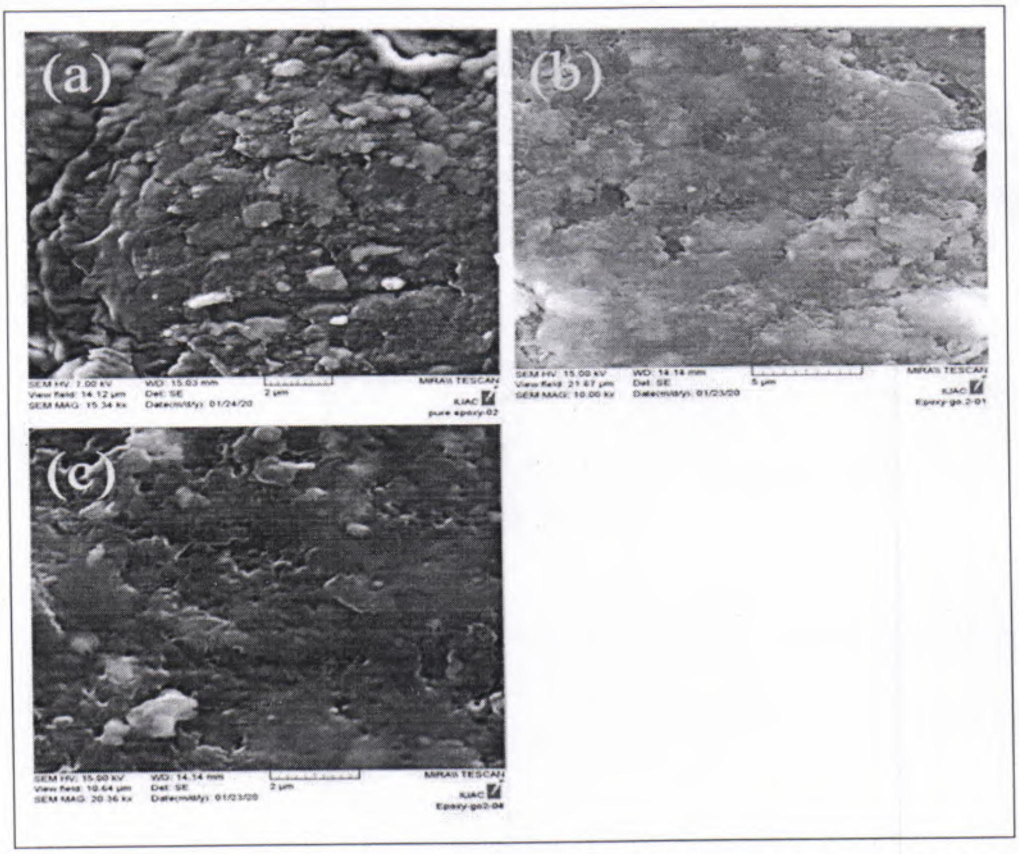

Figure 3. SEM images of nanocomposites with the varying amounts of GO (a) pure epoxy, (b) epoxy –0.2 wt.% GO and (c) epoxy –0.4 wt.% GO.

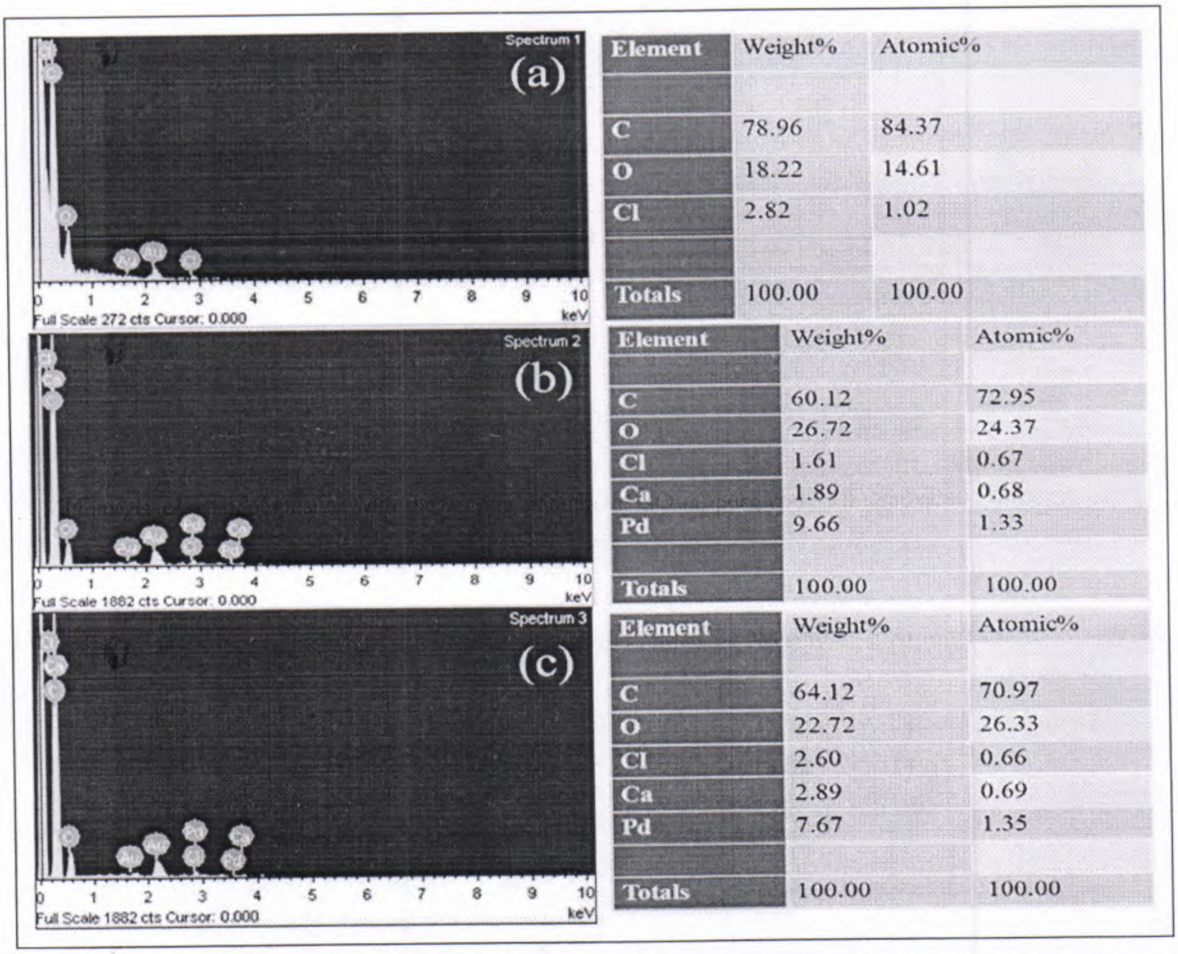

Element	Weight%	Atomic%
C	78.96	84.37
O	18.22	14.61
Cl	2.82	1.02
Totals	100.00	100.00

Element	Weight%	Atomic%
C	60.12	72.95
O	26.72	24.37
Cl	1.61	0.67
Ca	1.89	0.68
Pd	9.66	1.33
Totals	100.00	100.00

Element	Weight%	Atomic%
C	64.12	70.97
O	22.72	26.33
Cl	2.60	0.66
Ca	2.89	0.69
Pd	7.67	1.35
Totals	100.00	100.00

Figure 4. EDX analysis of nanocomposites with the varying amounts of GO (a) pure epoxy, (b) epoxy –0.2 wt.% GO and (c) epoxy –0.4 wt.% GO.

This suggests that strong adhesion exists between the epoxy and GO. At the same time, the orientation movement of molecular chain of polar groups in the epoxy–GO nanocomposites is restricted. EDX spectra of pure epoxy and epoxy –GO nanocomposites are shown in Figure 4. The EDX shows the presence of carbon, oxygen, chlorine, calcium, and palladium. The change in value of C, O and Cl indicates the occurrence of chemical reaction in pure epoxy and GO. This data attributed the successful preparation of nanocomposites. EDX presented the 66% carbon and 22% oxygen because of the fine grain graphite is oxidized from the surface and propagates gradually to the inner side. The graphene oxide in porous structure of epoxy reduces porosity. Thus, epoxy–GO coating in metal inhibited the effects between the protected metal and corrosive media.[39]

Raman spectra of epoxy resin- GO nanocomposites

Raman spectroscopy (Senterra, Bruker) is important technique to evaluate the structural changes in the prepared samples. Figure 5 shows the Raman spectra of pure epoxy and epoxy–GO (0.2 and 0.4 wt.%). As expected, the spectra of pure epoxy and epoxy–GO (0.2 & 0.4 wt. %) exhibits some characteristics peaks, which represents the groups present in GO, epoxy and epoxy –GO (0.2 and 0.4 wt.%) nanocomposites. Figure 5 shows the peaks at 75, 392, 606, 804, 997, 1097, 1304, 1378, 1545, 1592, 2065, 2528, 2852, 2874, 2922, and 3067 cm^{-1}.[40,41] The peak at 75 cm^{-1} could be ascribed to the lattice vibration or LA mode and 392 cm^{-1}describing the aliphatic chains (250-400 cm^{-1}) group and similarly at 606 cm^{-1}. This is corresponding to (CC) alicyclic aliphatic chain vibrations (600-1300 cm^{-1}). Other peak or band likes 804 cm^{-1} is indicating C-O-C (800-970 cm^{-1}) and 997 & 1097 cm^{-1} represents (CC) aromatic ring chain vibrations and (C-O-C) asymmetric group respectively.[42] The peak at 1304 cm^{-1} and 1408 cm^{-1} is corresponding to CH_3 group and N=N aromatic compounds. The peaks at 1615 and 1656 cm^{-1} is showing successful functionalization of GO.[43] The Raman spectra of pure GO displays two main peaks; the G band at 1592 cm^{-1} and D band at 1378 cm^{-1}, corresponding to the vibration of sp^2-bonded carbon atoms and sp^3 defects of disordered ones in the hexagonal graphitic layers.[44,45] The intensity ratio of D band against G band (I_D/I_G) represents the structural

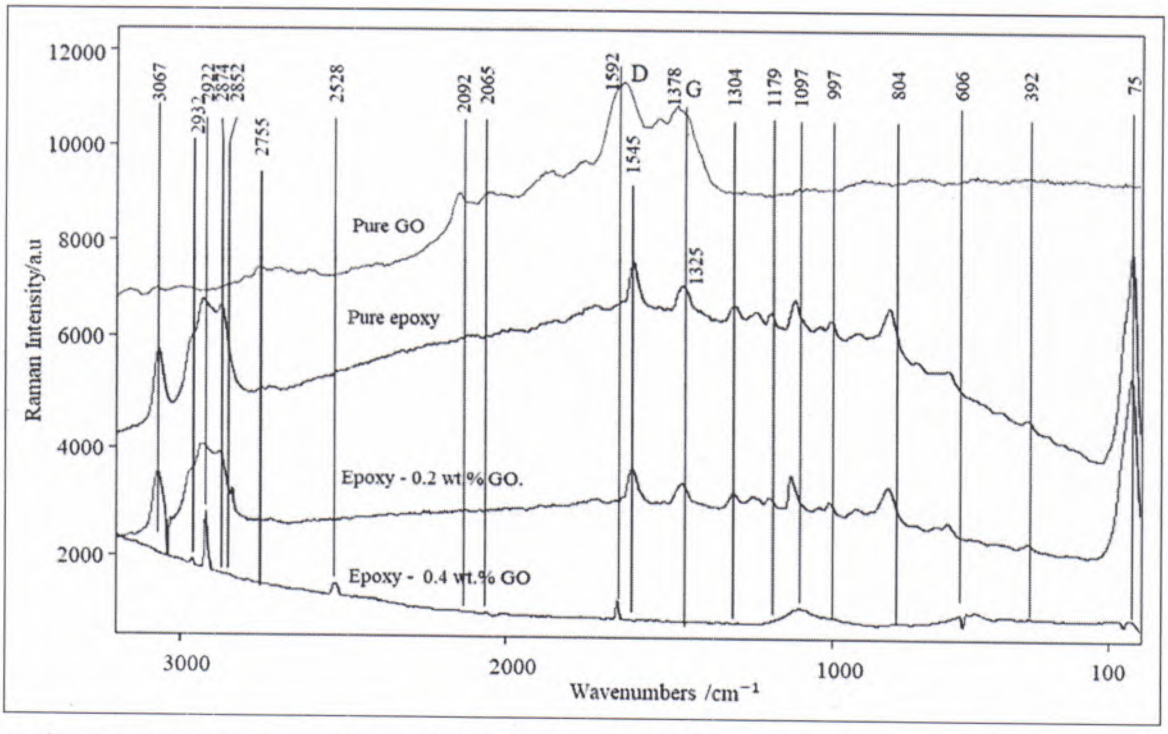

Figure 5. Raman spectra of nanocomposites with the varying amounts of GO in pure epoxy.

Table 1. Analysis of different peaks/bands in Raman spectra.

Sample	L A mode 10-200 cm^{-1}	(C-C) chains 250-400 cm^{-1}	(C-Br) Group 570-600 cm^{-1}	Benzene ring breathing at 992 cm^{-1}	(C=O) ketone Group at 1300-1600cm^{-1}	(C-H) 2800-3000 cm^{-1}	=C-H 3000-3100 cm^{-1}
Pure epoxy	75	392	606	997	1545	2852	3067
epoxy -0.2 wt.% GO	75	392	616	997	1325	2874	3068
epoxy -0.4 wt.% GO	75	397	621	997	1325	2922	3069

disorder degree of carbon material. The peaks at 2852, 2874, 2922 $\mathrm{cm^{-1}}$are indicating C-H group (i.e. ranging from 2800 to 3000 $\mathrm{cm^{-1}}$). However, peak at 3067 $\mathrm{cm^{-1}}$ is responsible for =C-H group. It has been observed that the some disturbance in the actual position of peaks (i. e. Table 1) attributed the presence of GO in epoxy resin composites.

Study of corrosion behavior

The corrosion properties were recorded by using Palmsan3 potentiostat system with microcode version 1.8. The corrosion resistance and barrier properties of epoxy–GO coatings were demonstrated in a solution of 3.0 wt.% NaCl at pH 5. The corrosion resistance of coating was performed in a salt cabinet. The epoxy/GO coated Al alloy (7075) samples of dimension $1 \times 1 \mathrm{cm^2}$ were immersed in sodium chloride solution of 3.5 wt.% for corrosion study. Throughout the test process, the three-electrode system, Ag/AgCl electrode as a reference, epoxy/epoxy nanocomposites coated Al alloy (7075) as active electrode and platinum as a counter electrode were used. The open circuit potential is an demonstration of polarization study of epoxy/GO coated Al alloy samples at pH 5. The OCP values were obtained for Al alloy (7075), pure epoxy coated Al alloy, epoxy–0.2 wt.% GO and epoxy–0.4 wt.% GO nanocomposites coatings as shown in Figure 6(a). It has been observed that epoxy–0.4 wt.% GO nanocomposites are more positive than other coatings. This shows that 0.4 wt.% of GO in epoxy favours the high corrosion resistance and suitability of material for commercial coating. The positive shift in OCP shows less corrosion, while negative shift of OCP suggests high corrosion of material.[46] The corrosion current density was determined by the method of Tafel extrapolation or by fitting the Butler-Volmer equation on a linear polarization measurement.

$$I = I_{corr}\left(e\frac{(2.303)(E-E_{corr})}{\beta_a}\right) - \left(e\frac{(-2.303)(E-E_{corr})}{\beta_c}\right) \tag{1}$$

where E, E_{corr} electrode potential, corrosion potential and β_a, β_c are the Tafel coefficients. The corrosion rates of the samples can be calculated from equation (2).

$$C_R = I_{corr} \cdot K \cdot \frac{Ew}{dA} \tag{2}$$

where E_W is equivalent weight in g $\mathrm{mol^{-1}}$, d is the density in grams $\mathrm{cm^{-3}}$, A is the sample area in $\mathrm{cm^2}$ of the sample and K is constant (3272 mm/(amp*cm*year)). The efficiency of coatings can be described as protection efficiency, expressed by following relation[32,47]:

$$\eta\% = \frac{l^0_{corr} - l_{corr}}{l^0_{corr}} \times 100 \tag{3}$$

where l^0_{corr} and l_{corr} are corrosion current density values of the Al alloy (7075) electrode samples and coated Al alloy. The Tafel polarization curves for Al alloy (7075), pure epoxy, epoxy–0.2 wt.% GO and epoxy–0.4 wt.% GO coated Al alloys (7075) are shown in Figure 6(b). The electrochemical parameters calculated from Tafel plots are presented in Table 2. The corrosion behavior of the epoxy–GO coatings in Al alloy 7075 was studied by measuring time dependent corrosion current at pH 5.[48] It has been observed that the corrosion current is much less for epoxy–GO coated Al alloy 7075 (i.e. Figure 6(a) and (b)). This shows that corrosion resistance is high for epoxy–GO coated Al alloy 7075. Epoxy–GO coated Al alloy 7075 possessed a

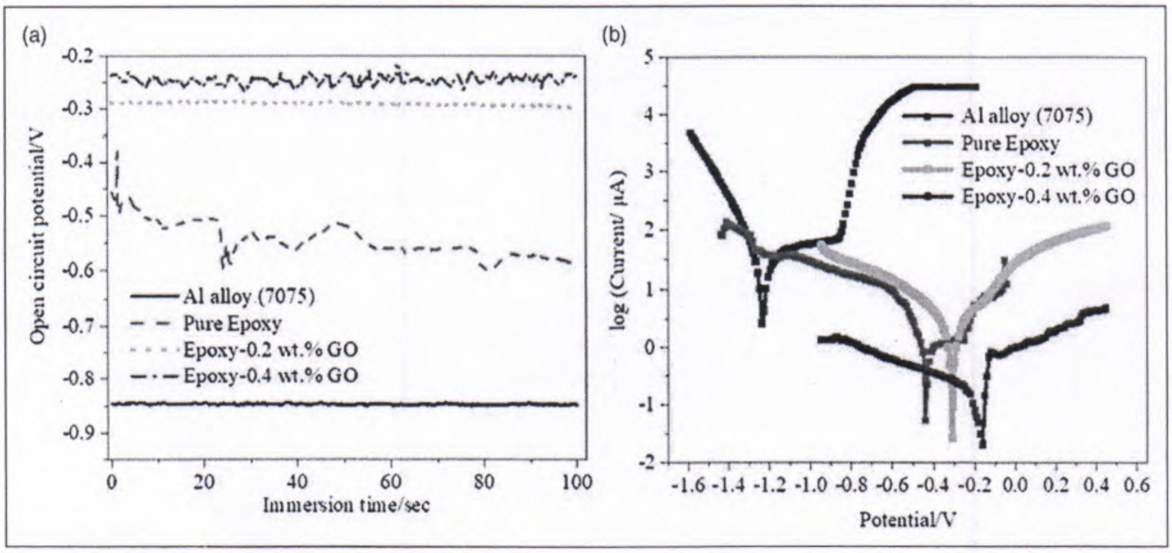

Figure 6. (a) Analysis of open circuit potential in uncoated and coated Al alloy with different concentration of GO in 3.5 wt% NaCl solution and (b) Tafel plots of Al alloy (7075), pure epoxy, epoxy–0.2 wt.% GO and epoxy–0.4 wt.% GO coated samples in 3.5 wt.% NaCl solution at pH 5.

Table 2. Tafel plot data of Al alloy (7075), pure epoxy, epoxy-0.2 wt.% GO and epoxy-0.4 wt.% GO coated samples.

Sample	E_{corr}/V	I_{corr}/A cm^{-2}	β_a(V/dec)	B_c(V/dec)	R_p/Ω	C_R/mm year^{-1}	η%
Al (7075)	−1.23	4.0×10^{-5}	0.095	0.317	1809	0.575	–
Pure epoxy	−0.486	3.5×10^{-6}	0.430	0.730	2.4×10^{4}	0.115	91.25%
epoxy -0.2 wt.%GO	−0.326	0.123×10^{-6}	1.126	0.360	9.64×10^{5}	0.004	99.69%
epoxy -0.4 wt.%GO	−0.280	5.72×10^{-12}	0.520	0.535	1.84×10^{10}	2.03×10^{-7}	99.99%

Note: Corrosion potential (E_{corr}), Tafel coefficients (β_a & β_c), corrosion rates (C_R), polarization resistance (R_p) and efficiency of coating (η%)

Table 3. Comparative studies of the current corrosion parameters with other work.

Sample	E_{corr}/V	I_{corr} /A cm^{-2}	β_a(V/dec)	B_c(V/dec)	η(%)	References
epoxy -0.4 wt.%GO	−0.280	5.72×10^{-12}	0.520	0.535	99.99	Present Work
PANI/GO(4:1)	−0.299	3.7×10^{-6}	0.004	0.007	95.88	[42]
GO@ZIF-8	−0.724	1.66×10^{-7}	0.070	0.123	79	[43]
MGel/GO-EP	−0.267	6.68×10^{-8}	4.446	5.090	99.2	[44]
RGO-PHSE-Zn	−0.637	3.1×10^{-6}	0.151	0.074	51	[45]
PDA-BN@f-Al_2O_3	−0.439	0.23×10^{-6}	0.238	0.186	98.05	[46]
E/PA-GO	−0.179	7.331×10^{-6}	0.140	-0.288	96.34	[37]

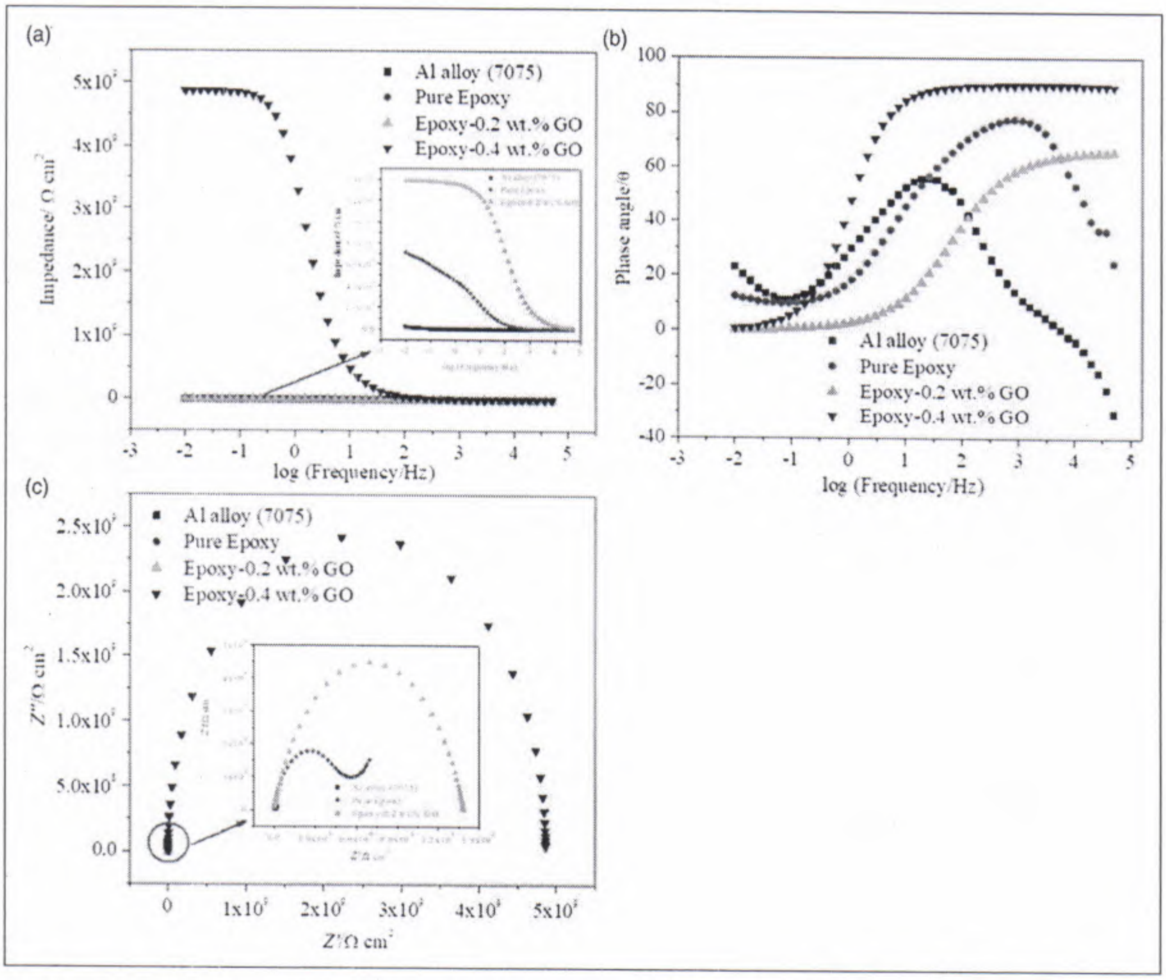

Figure 7. (a) and (b) Bode plots and, (c) Nyquist plots for Al alloy (7075), pure epoxy, epoxy–0.2 wt.% GO and epoxy–0.4 wt.% GO coated samples in 3.5 wt.% NaCl solution at pH 5.

lower corrosion current as compare to epoxy coated and uncoated sample.[49] These result are attributed that epoxy –GO coating effectively prevent the corrosion of Al alloy 7075 due to increase of corrosion resistance. However, epoxy and epoxy–0.2 wt.% GO coated Al alloy 7075 exhibited a slightly higher corrosion current density. The corrosion resistance of coated Al alloy 7075 increases in presence of graphene oxide due to high corrosion resistance of coating. The barrier properties of the present study were compared with other work and tabulated in Table 3.[46,50–53] These results have potential of efficient

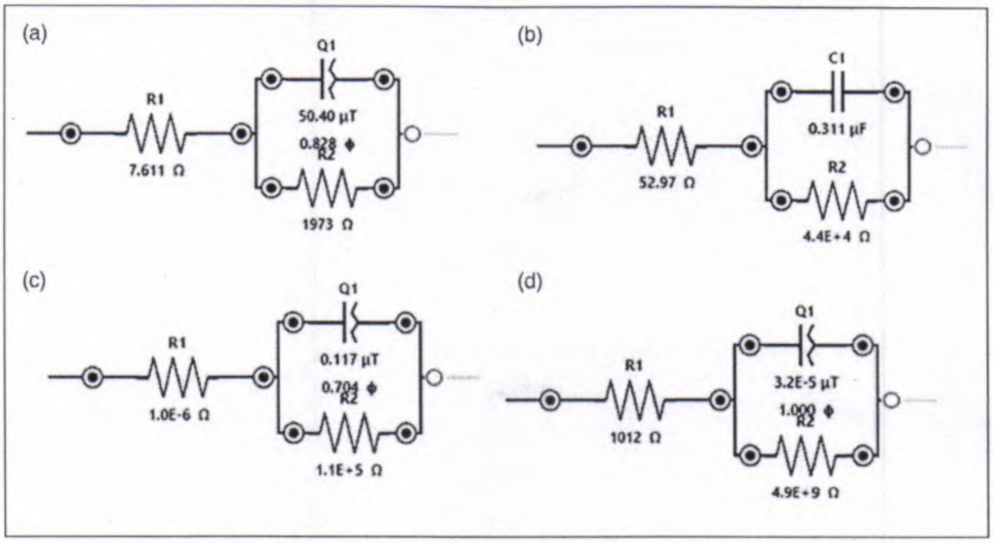

Figure 8. Equivalent circuit diagram of Al alloy (7075), pure epoxy, epoxy–0.2 wt.% GO and epoxy–0.4 wt.% GO coated samples in 3.5 wt.% NaCl solution at pH 5.

anticorrosion nature of epoxy–GO nanocomposites coating by spin coating method, which can prevent aluminum substrate from environmental corrosion media.

Electrochemical impedance measurement

Electrochemical impedance spectroscopy is an effective approach to decide the corrosion safety performance of coatings. Sinusoidal amplitude of 20 mV among the frequency varies from 0.01 to 50 kHz. The Bode and Nyquist plots for corrosion study are shown in Figure 7(a) and (b). It has been observed that impedance value of epoxy–0.4 wt.% GO coated sample is rather high (0.86×10^{10} Ω. cm^2) as compare to other coating concentration of GO with epoxy. This indicates the improvement in low frequency impedance modulus as compare to previously published data.[32] The Bode plots are an evidence for anticorrosion performance of epoxy–GO coating in Al Alloy 7075 by spin coating method at the level of lower frequency. The corrosion cell in surface of metal alloy will stop the corrosion reaction in presence of GO due to good dispersion and proper alignment in the epoxy matrix. The high aspect ratio and large surface area make longer diffusion pathway for permeation of corrosion agent. It has been observed that the lower concentration (0.2 wt.%) of GO do not block the pores and the defects in matrix are remains the same. The value of phase angle at higher frequency (0.01 Hz) in Bode Plot (Figure 7) also represents the comparison of coating material. In principle, corrosion resistance is high for higher value of phase angle. The pattern of phase angle plot is similar to Bode plot. It is observed that epoxy coating exhibit small value of phase angle as compare to epoxy–GO coating. Its value decreases with time in a particular salt. The barrier properties of epoxy–GO (0.4 wt.%) of coated sample was carried out in NaCl solution. It has been observed that barrier properties are maintained without much degradation of coating. Figure 8 shows the appropriate equivalent circuit for EIS study. The equivalent circuit is well agreed with EIS data.

Conclusions

The structural morphology of epoxy are significantly changed by cross-linking of GO with side groups of epoxy as demonstrated by Raman spectra. The SEM–EDX demonstrate the influence of GO in epoxy resin and its compositional analysis. The epoxy–GO coating is also acted as good barrier for the defects and microspores in the coating and provides excellent barrier property for oxygen, water and other corrosive medium to diffuse into the coating. Tafel results indicates the lower corrosion current density (i.e. 5.72×10^{-12} A cm^2) and higher corrosion protection efficiency (i.e. 99.99%) with corrosion rate of 2.03×10^{-7} mm/year for epoxy–0.4 wt.% GO nanocomposites coating as compare to epoxy and epoxy −0.2 wt.% GO coating. The low frequency impedance modulus of GO in epoxy coating of Al alloy 7075 was 10^{10} Ω cm^2. The anticorrosion properties of epoxy increases due to enhancement of hydrophobicity and adhesion strength by incorporation of GO in epoxy matrix. This study provided a new coating material for corrosion prevention of aluminum alloy. Successful alignment of the composite cover on the aluminum alloy surface has been critical in improving the aluminum structures and extending its service life in the aviation area and these nanocomposites can be used in other applications.

Acknowledgements

Acknowledgements Financial assistance from Aeronautics Research & Development Board, DRDO Bhawan, New Delhi-110011, India (Letter no. ARDB/01 11051902l/M/l), is gratefully acknowledged). We are also thankful to Director IUAC, New Delhi for providing characterization facilities.

Declaration of conflicting interests

The authors declared no potential conflicts of interest with respect to the research, authorship, and/or publication of this article.

Funding

The author(s) disclosed receipt of the following financial support for the research, authorship, and/or publication of this article: This work was supported by Aeronautics Research and Development Board and grand id ARDB/01 110519021/M/I.

ORCID iD

Mulayam S Gaur https://orcid.org/0000-0002-9335-8233

Supplemental Material

Supplemental material for this article is available online.

References

1. Vertuccioa L, Guadagnoa L, Iannuzzod G, et al. Smart coatings of epoxy based CNTs designed to meet practical expectations in aeronautics. *Composit Part B* 2018; 147: 42–46.
2. Schulte K and Baron C. Load and failure analyses of CFRP laminates by means of electrical resistivity measurements. *Composit Sci Technol* 1989; 36: 63–76.
3. Weber I and Schwartz P. Monitoring bending fatigue in carbon-fibre/epoxy composite strands: a comparison between mechanical and resistance techniques. *Composit Sci Technol* 2001; 61: 849–853.
4. Kupke M, Schulte K and Schüler R. Non-destructive testing of FRP by d.c. and a.c. electrical methods. *Composit Sci Technol* 2001; 61: 837–847.
5. Schueler R, Joshi SP and Schulte K. Damage detection in CFRP by electrical conductivity mapping. *Composit Sci Technol* 2001; 61: 921–930.
6. Zahed A. Epoxy in nanotechnology: a short review. *Prog Org Coat* 2019; 132: 445–448.
7. Dagdag O, Harfi E, Safi Z, et al. Fabrication on designing of a macromolecular epoxy resin as anti-corrosive coating material for electrocatalytically deposited cadmium on 15CDV6 steel in 3% NaCl solution. *J Mater Res Technol* 2020; 9: 5549–5563.
8. Salgin B, Terryn H and Rohwerder M. Scanning kelvin probe study of (oxyhydr) oxide surface of Aluminum Alloy. *J Phys Chem C* 2013; 117: 1805–1811.
9. Tomić M, Stanković N, Pavlović VB, et al. Polyamidoamine as a clay modifier and curing agent in preparation of epoxy nanocomposites. *Prog Org Coat* 2019; 131: 311–321.
10. Haddadi SA, Kohlan TB, Momeni S, et al. Synthesis and application of mesoporous carbon nanospheres containing walnut extract for fabrication of active protective epoxy coatings. *Prog Org Coat* 2019; 133: 206–219.
11. Zhang X, Peng H, Limmack A, et al. Viscoelastic damping behaviour of cup stacked carbon nanotube modified epoxy nanocomposites with tailored interfacial condition and re-agglomeration. *Composit Sci Technol* 2014; 105: 66–72.
12. Bifulco A, Tescione F, Branda F, et al. Effects of post cure treatment in the glass transformation range on the structure and fire behavior of in situ generated silica/epoxy hybrids. *J Sol-Gel Sci Technol* 2018; 87: 156–169.
13. Higuchi C, Horvath D, Yoshizawa K, et al. Prediction of the glass-transition temperatures of linear homo/heteropolymers and cross-linked epoxy resins. *ACS App Poly* 2019; 1: 1430–1442.
14. Nonahal M, Saeb MR, Jafari SH, et al. Design, preparation, and characterization of fast cure epoxy/amine-functionalized graphene oxide nanocomposites. *Poly Composit* 2018; 39: 2016–2027.
15. Jouyandeh M, Jazani OM, Navarchian AH, et al. Surface engineering of nanoparticles with macromolecules for epoxy curing: development of superreactive nitrogen-rich nanosilica through surface chemistry manipulation. *App Sur Sci* 2018; 447: 152–154.
16. Ghaffari M, Saeb MR, Ramezanzadeh B, et al. Demonstration of epoxy/carbon steel interfacial delamination behavior: electrochemical impedance and X-ray spectroscopic analyses. *Corros Sci* 2016; 102: 326–337.
17. Bahlakeh G, Ramezanzadeh B, Terryn H, et al. Corrosion protection properties and interfacial adhesion mechanism of an epoxy/polyamide coating applied on the steel surface decorated with cerium oxide nanofilm: complementary experimental, molecular dynamics (MD) and first principle quantum mechanics (QM) simulation methods. *App Surf Sci* 2017; 419: 650–669.
18. Saeb MR, Bakhshandeh E, Heinrich G, et al. Cure kinetics of epoxy nanocomposites affected by MWCNTs functionalization: a review. *Sci World J* 2019; 2013: 14.
19. Saeb MR, Najafi F, Bakhshandeh E, et al. Highly curable epoxy/MWCNTs nanocomposites: An effective approach to functionalization of carbon nanotubes. *Chem Eng J* 2015; 259: 117–125.
20. Sari MG, Saeb MR, Shabanian M, et al. Epoxy/starch-modified nano-zinc oxide transparent nanocomposite coatings: a showcase of superior curing behavior. *Prog Org Coat* 2018; 115: 143–150.
21. Keramatinia M, Najafi F and Saeb MR. Synthesis and viscoelastic properties of acrylated hyperbranched polyamidoamine UV-curable coatings with variable microstructures. *Prog Org Coat* 2017; 113: 151–159.
22. Sari MG, Vahabi H, Saeb MR, et al. An attempt to mechanistically explain the viscoelastic behavior of transparent epoxy/starch-modified ZnOnanocomposite coatings. *Prog Org Coat* 2018; 119: 171–182.
23. Puglia D, Rastin H, Formela K, et al. Cure kinetics of epoxy/MWCNTs Nanocomposites: Isothermal calorimetric and rheological analyses. *Prog Org Coat* 2017; 108: 75–83.
24. Saeb MR, Rastin H, Formela K, et al. Cure kinetics of epoxy/MWCNTs nanocomposites: Nonisothermal calorimetric and rheokinetic techniques. *J Appl Poly Sci* 2017; 134: 45221.

25. Kaffashi B, Kaveh A, Jazani OM, et al. Improving rheological properties of covalently MWCNT/epoxy nanocomposites via surface re-modification. *Poly Bull* 2012; 68: 2187–2197.
26. Yarahmadi E, Didehban K, Sari MG, et al. Development and curing potential of epoxy/starch-functionalized graphene oxide nanocomposite coatings. *Prog Org Coat* 2018; 119: 194–202.
27. Jouyandeh M, Paran SMR, Jannesari A, et al. Protocol for nonisothermal cure analysis of thermoset composites. *Prog Org Coat* 2019; 131: 333–339.
28. Hong SG and Tsai JS. Adsorption and curing behaviors of the epoxy/aminoamine system in the presence of metal oxides. *J Therm Anal Calorim* 2001; 63: 31–46.
29. Choi WJ, Powell RL and Kim DS. Curing behavior and properties of epoxy nanocomposites with amine functionalized multiwall carbon nanotubes. *Poly Compos* 2009; 30: 415–421.
30. Wang Q, Song C and Lin W. Study of the exfoliation process of epoxy–clay nanocomposites by different curing agents. *J App Poly Sci* 2003; 90: 511–517.
31. Yanning C, Baohui R, Shuiying G, et al. The sandwich-like structures of polydopamine and 8-hydroxyquinoline coated graphene oxide for excellent corrosion resistance of epoxy coatings. *J of Coll and Inter Sci* 2020; 565: 436–448.
32. Yankun X, Chunhua L, Weiqu L, et al. A novel approach to fabricate polyacrylate modified graphene oxide for improving the corrosion resistance of epoxy coatings. *Coll and Sur A* 2020; 595: 124627.
33. Mohammad R, Bahram R, Mohammad M, et al. Development of metal-organic framework (MOF) decorated graphene oxide nanoplatforms for anti-corrosion epoxy coatings. *Carbon* 2020; 161: 231–251.
34. Ali A, Reza N and Bahram R. Epoxy-polyamide nanocomposite coating with graphene oxide as cerium nanocontainer generating effective dual active/barrier corrosion protection. *Composit Part B* 2019; 172: 363–375.
35. Paulchamy B, Arthi G and Lignesh BD. A simple approach to stepwise synthesis of graphene oxide nanomaterial. *J of Nanomedi & Nanotechno* 2015; 6: 1–4.
36. Thakur S and Karak N. Green reduction of graphene oxide by aqueous phytoextracts. *Carb* 2012; 50: 5331–5339.
37. Fern´andez-Merino MJ, Guardia L, Paredes JI, et al. Solís-Fern´andez P and Martínez-Alonso AVitamin C is an ideal substitute for hydrazine in the reduction of graphene oxide suspensions. *J Phys Chem C* 2010; 114: 6426–6432.
38. Ramezanzadeh Ghasem B, Bahram R, et al. Construction of an epoxy composite with excellent thermal/mechanical properties using graphene oxide nanosheets reduced/functionalized by Tamarindus indiaca extract/zinc ions; detailed experimental and DFT-D computer modeling explorations. *Resul Phy* 2020; 19: 103400.
39. Jouyandeh M, Yarahmadi E, Ganjali MR, et al. Cure kinetics of epoxy/graphene oxide (GO) nanocomposites: Effect of starch functionalization of GO nanosheets. *Prog in organ Coatin* 2019; 136: 105217.
40. Wang W, Wang C, Yue X, et al. Raman spectroscopy and resistance-temperature studies of functionalized multiwalled carbon nanotubes/epoxy resin composite film. *Microelectr Eng* 2019; 214: 50–54.
41. Qiyuan G, Kang G, Weihong T, et al. Rapid decomposition of epoxy resins via raman spectrometry in combination with machine learning algorithms. *J Bio resour Bio prod* 2019; 4: 130–134.
42. Venkatesan P, Thamotharan S, Percino MJ, et al. Intramolecular resonance assisted N–H···O=C hydrogen bond and weak noncovalent interactions in two asymmetrically substituted geminal amido-esters: crystal structures and quantum chemical exploration. *J Mole Stru* 2021; 1246: 131210.
43. Galpaya D, Wang M, George G, et al. Preparation of graphene oxide/epoxy nanocomposites with significantly improved mechanical properties. *J App Phy* 2014; 116: 053518.
44. Qiu Y, Liu J, Yang H, et al. Graphene oxide -stimulated acoustic attenuating performance of Tungsten based Epoxy films. *J Mater Chem C* 2015; 10: 1039–10855.
45. Tian W, Gao Q, Tan Y, et al. Bio-inspired beehivelike hierarchical nanoporous carbon derived from bamboo-based industrial byproduct as a high performance supercapacitor electrode material. *J Mater Chem A* 2015; 3: 5656–5664.
46. Pengying W, Nie Z, Fugang Q, et al. Synthesis of PDA-BN@f-Al_2O_3 hybrid for nanocomposite epoxy coating with superior corrosion protective properties. *Prog in org coatin* 2020; 146: 105713.
47. Guiyu Z, Xiaokun C and Zhanhu G. Poly (vinyl butyral)/Graphene oxide/poly (methylhydrosiloxane) nanocomposite coating for improved aluminum alloy anticorrosion. *Poly* 2019; 172: 115–122.
48. Tianhao G, Zhao W, Yanlin H, et al. Design alternate epoxy-reduced graphene oxide/epoxy-zinc multilayer coatings for achieving long-term corrosion resistance for Cu. *Mater and Desin* 2020; 186: 108299.
49. Jeffrey R and Melchers RE. Atmospheric and immersion corrosion of steel alloyed with aluminium. *Corros eng Sci technol* 2020; 10: 1–10.
50. Yanga N, Yang T, Lid W, et al. Polydopamine modified polyaniline-graphene oxide composite for enhancement of corrosion resistance. *J Hazardous Mater* 2019; 377: 142–151.
51. Fang Y, Xia L, Jian RK, et al. Mechanically strong and flame-retardant epoxy resins with anti-corrosion performance. *Composit Part B* 2020; 193: 108019.
52. Rajithaa K, Madhusudhana M, Mohanan A, et al. Evaluation of anti-corrosion performance of modified gelatin-graphene oxide nanocomposite dispersed in epoxy coating on mild steel in saline media. *Collid and surf A* 2020; 587: 124341.
53. Raman M, Mohammad R, Bahram R, et al. Graphene oxide nanoplatforms reduction by green plant-sourced organic compounds for construction of an active anti-corrosion coating; experimental/electronic-scale DFT-D modeling studies. *Chem Eng J* 2020; 397: 125433.

Funding

The author(s) disclosed receipt of the following financial support for the research, authorship, and/or publication of this article: This work was supported by Aeronautics Research and Development Board and grand id ARDB/01 11051902l/M/I.

ORCID iD

Mulayam S Gaur https://orcid.org/0000-0002-9335-8233

Supplemental Material

Supplemental material for this article is available online.

References

1. Vertuccioa L, Guadagnoa L, Iannuzzod G, et al. Smart coatings of epoxy based CNTs designed to meet practical expectations in aeronautics. *Composit Part B* 2018; 147: 42–46.
2. Schulte K and Baron C. Load and failure analyses of CFRP laminates by means of electrical resistivity measurements. *Composit Sci Technol* 1989; 36: 63–76.
3. Weber I and Schwartz P. Monitoring bending fatigue in carbon-fibre/epoxy composite strands: a comparison between mechanical and resistance techniques. *Composit Sci Technol* 2001; 61: 849–853.
4. Kupke M, Schulte K and Schüler R. Non-destructive testing of FRP by d.c. and a.c. electrical methods. *Composit Sci Technol* 2001; 61: 837–847.
5. Schueler R, Joshi SP and Schulte K. Damage detection in CFRP by electrical conductivity mapping. *Composit Sci Technol* 2001; 61: 921–930.
6. Zahed A. Epoxy in nanotechnology: a short review. *Prog Org Coat* 2019; 132: 445–448.
7. Dagdag O, Harfi E, Safi Z, et al. Fabrication on designing of a macromolecular epoxy resin as anti-corrosive coating material for electrocatalytically deposited cadmium on 15CDV6 steel in 3% NaCl solution. *J Mater Res Technol* 2020; 9: 5549–5563.
8. Salgin B, Terryn H and Rohwerder M. Scanning kelvin probe study of (oxyhydr) oxide surface of Aluminum Alloy. *J Phys Chem C* 2013; 117: 1805–1811.
9. Tomić M, Stanković N, Pavlović VB, et al. Polyamidoamine as a clay modifier and curing agent in preparation of epoxy nanocomposites. *Prog Org Coat* 2019; 131: 311–321.
10. Haddadi SA, Kohlan TB, Momeni S, et al. Synthesis and application of mesoporous carbon nanospheres containing walnut extract for fabrication of active protective epoxy coatings. *Prog Org Coat* 2019; 133: 206–219.
11. Zhang X, Peng H, Limmack A, et al. Viscoelastic damping behaviour of cup stacked carbon nanotube modified epoxy nanocomposites with tailored interfacial condition and re-agglomeration. *Composit Sci Technol* 2014; 105: 66–72.
12. Bifulco A, Tescione F, Branda F, et al. Effects of post cure treatment in the glass transformation range on the structure and fire behavior of in situ generated silica/epoxy hybrids. *J Sol-Gel Sci Technol* 2018; 87: 156–169.
13. Higuchi C, Horvath D, Yoshizawa K, et al. Prediction of the glass-transition temperatures of linear homo/heteropolymers and cross-linked epoxy resins. *ACS App Poly* 2019; 1: 1430–1442.
14. Nonahal M, Saeb MR, Jafari SH, et al. Design, preparation, and characterization of fast cure epoxy/amine-functionalized graphene oxide nanocomposites. *Poly Composit* 2018; 39: 2016–2027.
15. Jouyandeh M, Jazani OM, Navarchian AH, et al. Surface engineering of nanoparticles with macromolecules for epoxy curing: development of superreactive nitrogen-rich nanosilica through surface chemistry manipulation. *App Sur Sci* 2018; 447: 152–154.
16. Ghaffari M, Saeb MR, Ramezanzadeh B, et al. Demonstration of epoxy/carbon steel interfacial delamination behavior: electrochemical impedance and X-ray spectroscopic analyses. *Corros Sci* 2016; 102: 326–337.
17. Bahlakeh G, Ramezanzadeh B, Terryn H, et al. Corrosion protection properties and interfacial adhesion mechanism of an epoxy/polyamide coating applied on the steel surface decorated with cerium oxide nanofilm: complementary experimental, molecular dynamics (MD) and first principle quantum mechanics (QM) simulation methods. *App Surf Sci* 2017; 419: 650–669.
18. Saeb MR, Bakhshandeh E, Heinrich G, et al. Cure kinetics of epoxy nanocomposites affected by MWCNTs functionalization: a review. *Sci World J* 2019; 2013: 14.
19. Saeb MR, Najafi F, Bakhshandeh E, et al. Highly curable epoxy/MWCNTs nanocomposites: An effective approach to functionalization of carbon nanotubes. *Chem Eng J* 2015; 259: 117–125.
20. Sari MG, Saeb MR, Shabanian M, et al. Epoxy/starch-modified nano-zinc oxide transparent nanocomposite coatings: a showcase of superior curing behavior. *Prog Org Coat* 2018; 115: 143–150.
21. Keramatinia M, Najafi F and Saeb MR. Synthesis and viscoelastic properties of acrylated hyperbranched polyamidoamine UV-curable coatings with variable microstructures. *Prog Org Coat* 2017; 113: 151–159.
22. Sari MG, Vahabi H, Saeb MR, et al. An attempt to mechanistically explain the viscoelastic behavior of transparent epoxy/starch-modified ZnOnanocomposite coatings. *Prog Org Coat* 2018; 119: 171–182.
23. Puglia D, Rastin H, Formela K, et al. Cure kinetics of epoxy/MWCNTs Nanocomposites: Isothermal calorimetric and rheological analyses. *Prog Org Coat* 2017; 108: 75–83.
24. Saeb MR, Rastin H, Formela K, et al. Cure kinetics of epoxy/MWCNTs nanocomposites: Nonisothermal calorimetric and rheokinetic techniques. *J Appl Poly Sci* 2017; 134: 45221.

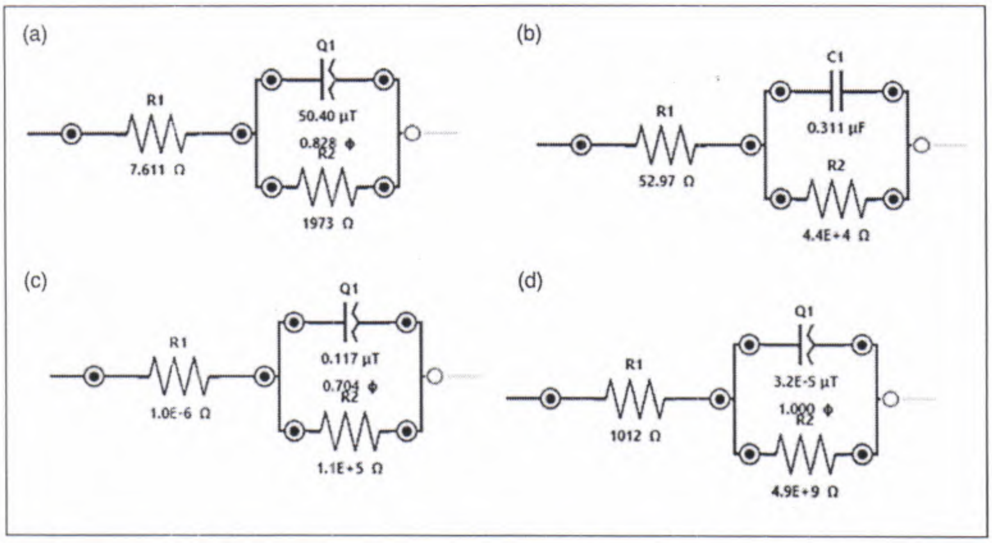

Figure 8. Equivalent circuit diagram of Al alloy (7075), pure epoxy, epoxy–0.2 wt.% GO and epoxy–0.4 wt.% GO coated samples in 3.5 wt.% NaCl solution at pH 5.

anticorrosion nature of epoxy–GO nanocomposites coating by spin coating method, which can prevent aluminum substrate from environmental corrosion media.

Electrochemical impedance measurement

Electrochemical impedance spectroscopy is an effective approach to decide the corrosion safety performance of coatings. Sinusoidal amplitude of 20 mV among the frequency varies from 0.01 to 50 kHz. The Bode and Nyquist plots for corrosion study are shown in Figure 7(a) and (b). It has been observed that impedance value of epoxy–0.4 wt.% GO coated sample is rather high (0.86×10^{10} Ω. cm^2) as compare to other coating concentration of GO with epoxy. This indicates the improvement in low frequency impedance modulus as compare to previously published data.[32] The Bode plots are an evidence for anticorrosion performance of epoxy–GO coating in Al Alloy 7075 by spin coating method at the level of lower frequency. The corrosion cell in surface of metal alloy will stop the corrosion reaction in presence of GO due to good dispersion and proper alignment in the epoxy matrix. The high aspect ratio and large surface area make longer diffusion pathway for permeation of corrosion agent. It has been observed that the lower concentration (0.2 wt.%) of GO do not block the pores and the defects in matrix are remains the same. The value of phase angle at higher frequency (0.01 Hz) in Bode Plot (Figure 7) also represents the comparison of coating material. In principle, corrosion resistance is high for higher value of phase angle. The pattern of phase angle plot is similar to Bode plot. It is observed that epoxy coating exhibit small value of phase angle as compare to epoxy–GO coating. Its value decreases with time in a particular salt. The barrier properties of epoxy–GO (0.4 wt.%) of coated sample was carried out in NaCl solution. It has been observed that barrier properties are maintained without much degradation of coating. Figure 8 shows the appropriate equivalent circuit for EIS study. The equivalent circuit is well agreed with EIS data.

Conclusions

The structural morphology of epoxy are significantly changed by cross-linking of GO with side groups of epoxy as demonstrated by Raman spectra. The SEM–EDX demonstrate the influence of GO in epoxy resin and its compositional analysis. The epoxy–GO coating is also acted as good barrier for the defects and microspores in the coating and provides excellent barrier property for oxygen, water and other corrosive medium to diffuse into the coating. Tafel results indicates the lower corrosion current density (i.e. 5.72×10^{-12} A cm^2) and higher corrosion protection efficiency (i.e. 99.99%) with corrosion rate of 2.03×10^{-7} mm/year for epoxy–0.4 wt.% GO nanocomposites coating as compare to epoxy and epoxy –0.2 wt.% GO coating. The low frequency impedance modulus of GO in epoxy coating of Al alloy 7075 was 10^{10} Ω cm^2. The anticorrosion properties of epoxy increases due to enhancement of hydrophobicity and adhesion strength by incorporation of GO in epoxy matrix. This study provided a new coating material for corrosion prevention of aluminum alloy. Successful alignment of the composite cover on the aluminum alloy surface has been critical in improving the aluminum structures and extending its service life in the aviation area and these nanocomposites can be used in other applications.

Acknowledgements

Acknowledgements Financial assistance from Aeronautics Research & Development Board, DRDO Bhawan, New Delhi-110011, India (Letter no. ARDB/01 11051902l/M/I), is gratefully acknowledged). We are also thankful to Director IUAC, New Delhi for providing characterization facilities.

Declaration of conflicting interests

The authors declared no potential conflicts of interest with respect to the research, authorship, and/or publication of this article.

②

ECS Journal of Solid State Science and Technology, 2022 **11** 041007
2162-8777/2022/11(4)/041007/8/$40.00 © 2022 The Electrochemical Society ("ECS"). Published on behalf of ECS by IOP Publishing Limited

Investigation of Structural and Thermal Properties of Graphene Oxide Reinforced Epoxy Nanocomposites

M. S. Gaur,[z] Rajesh Kumar Raghav, Rohan Sagar, and R. K. Tiwari

Department of Physics, Hindustan College of Science and Technology, Farah, Mathura, U.P 281122, India Affiliated to Dr. A.P.J. Abdul Kalama Technical University, Lucknow, Uttar Pradesh 226031, India

The nanocomposites thin film was prepared by adding exfoliated GO in epoxy-hardner solution in different weight ratio. We investigate the thermal and surface properties of epoxy-graphene oxide (GO) nanocomposites using differential scanning calorimetry (DSC), fourier transform infrared spectroscopy (FTIR), atomic force microscopy (AFM) and contact angle measurement method. AFM and contact angle results are supporting that graphene oxide provides the best reinforcement in epoxy. AFM is investigated the dispersion of GO and structural morphology process of epoxy nanocomposites. The FTIR results show that exfoliated GO of two-dimensional (2D) shape favors the hardening process of the epoxy matrix, increasing its reaction rate by observing an epoxy stretching frequency at 907 cm^{-1}. The GO modified with amino group of epoxy lead to the increase of crosslinking density. FTIR absorption peak in 1700–1500 cm^{-1} regions is due to amino group. This attributes the significant increase of glass transition temperature of epoxy/GO nanocomposites . The contact angle and surface roughness increases with increase in concentration of GO in epoxy shows roughness induced hydrophobic surface. The solid surface energy was calculated by contact angle favors the good dispersion of GO in epoxy matrix.

[DOI: 10.1149/2162-8777/ac5eb0]

Manuscript submitted January 27, 2022; revised manuscript received March 8, 2022. Published April 12, 2022.

Recently, polymer nanocomposites have attracted much attention of researchers due to their multifunctional properties. The carbonaceous nanomaterials (i.e. carbon nanotubes, carbon nanofibers and graphene oxides) as a filler in polymer matrix is an developing area of research. For example carbonaceous nanofiller have shown significant improvement in optical, mechanical, electrical, and thermal properties of polymers as compared to unfilled polymers.[1–3] Now a day the polymer nanocomposites materials of lightweight, high toughness, high stiffness is a requirement of automotive and aerospace industries.

Presently, nano scale materials have wide range of applications in industries due to their extraordinary structural properties. However, currently researchers are looking for dimensional improvement of the material properties, which is most suitable in the field of nanoscience and nanotechnology. In this concern, discovery of graphene played key role for development of nanotechnology.[4] Graphene is a two dimensional carbon nanosheet and thinnest material of universe with unlimited potential of applications. It exhibits high thermal conductivity, high electrical conductivity, and superior optical and mechanical properties.[5,6]

The effectiveness of polymer nanocomposites is depends on chemical and physical interaction of nanofiller with polymer. The nonuniform dispersion is caused by poor adhesive forces between nanofiller and polymer which causes the formation of defects centre and agglomeration of nanofiller. The uniform dispersion could be achieved by increasing adhesion force between nanofiller and polymer due to surface functionalization of nanofiller. However, strong bonding between polymer and nanofiller is useful for thermal, mechanical, coating and many other applications. The uniform dispersion of nanofiller is the main challenge of preparation of nanocomposites. In order to minimize this effect, the surface of carbonaceous nanomaterials must be functionalized by amino or carboxyl groups.[7,8]

Recently, researchers focused on synthesis method of graphene and processing method of graphene polymer nanocomposites to ensure the modification in properties.[9,10] Currently, other form of graphene such graphene oxide, reduced graphene oxide and graphene dots in polymer matrix shown outstanding properties. Previously, a lot of researches were undertaken on incorporation of nanoparticles in polymer matrix.[11–14] However, in recent year there are considerable interest on incorporation of graphene and graphene oxide in polymer matrix is due to high level of dispersion in polar solvent, better compatibility and dispersibility in various matrixes as compared to CNTs. The uniform dispersion of nanofillers indicates large reinforced surface area. This ultimately affects the polymer chain and finally properties of polymer.[15]

The epoxy has highly cross linked matrix with undesirable brittleness and stiffness lead to spontaneous failure. To maintain the thermo-mechanical properties of epoxy is a challenge, and therefore this is an area of potential research.[16] The existing problem of epoxy may be solved by formation of nanostructure using novel nanofiller like graphene oxide.

Atomic force microscopy (AFM) is an important technique to characterize the structure and surface morphology of polymer nanocomposites by means of three-dimensional (3D) topographic images of high resolution.[17,18] In present study AFM is applied to study the distribution of GO in epoxy matrix. This also investigate the ability of GO to create self-assembled structures embedded in the polymer matrix due to interfacial interaction between polymer and GO. The chemistry of interfacial interaction of GO with epoxy improve the performance of nanocomposites.[19] The study of surface energy, wettability and adhesion of low surface energy materials is possible by measuring the contact angle using simple method like sessile drop method instead of expensive method.

The hydrophobicity of nanocomposites with respect to water is very important parameter for coating application. This property of nanocomposites is evaluated by measuring contact angle. The graphene and graphene oxide are hydrophobic due to high density carbon atoms and large value of roughness.[20,21] Epoxy resins are of particular interest in structural composite applications because they provide a unique balance between chemical and mechanical properties. Epoxy has excellent chemical resistance and heat resistance. Now a day many researchers are working on nanocomposites because nanocomposites show many applications. Therefore, this work shows many applications such as glass transition temperature of epoxy containing GO has been increased and which is responsible for enhanced chemical, mechanical and thermal properties. The moisture is the serious issue of several metals for their useful applications. This could be understood in terms of hydrophobicity by measuring contact angle.[22,23] The effect of GO on hydrophobocity of epoxy needs a lot of research to attain superhydrophobicity. The thermal properties of epoxy-carbon black composite shows better thermal stability as compared to pure epoxy matrix.[24,25]

Experimental

Materials.—Graphite flakes (Molecular weight 12.01 g mol^{-1} and particle size <44 micron) powder, epoxy resin (Bisphenol-A

---

[z] E-mail: mulayamgaur@rediffmail.com

diglycidyl ether with molecular weight 340.41 g mol^{-1} and density 1.16 g ml^{-1}), curing agent (polyamide as a Hardener), acetone, ethanol, and Dimethylformamide (DMF) were procured from Merck (Sigma Aldrich). The polyamide consists of reaction product of polyfunctional amine and dimmer fatty acid. It is also having at least two cyclic rings. Each one is having at least two amine group separated from each other. These properties of polyamide compositions favour for use as hardner of epoxy resin formulation.

Preparation of graphene oxide.—The synthesis of graphene oxide was carried out by oxidative treatment of graphite using the method developed by Brodie, Hummers and Staudenmaeir[26] due to its simplicity and several advantages over the other methods. In this method, a mixture of graphite powder (2 g), H_2SO_4 (50 ml) and H_3PO_4 (5.5 ml) were mixed and stirred for several minutes. During stirring, 5.5 g of $KMnO_4$ was slowly added into the solution. This mixture was stirred for 6 h until the solution became dark green. To reduce the excess of $KMnO_4$, 12 ml H_2O_2 and 80 ml of H_2O was dropped slowly and stirred for 15 min. The exothermic reaction was occurred and let it to cool down. 10 ml of hydrochloric acid (HCl) and 30 ml of deionized water (DIW) was added and centrifuged for 5 min at 4000 rpm for 30 min. The precipitate was washed with DI water, HCl and ethanol. The final precipitate was dissolved in DI water and sonicated for 1 h. The washed GO solution was dried using oven at 90 °C for 24 h to produce the powder of GO. The 80 ml of H_2 O and 12 ml H_2 O_2 was added to remove other impurities.

Preparation of epoxy/graphene oxide nanocomposites.—Thin films of pure epoxy and epoxy/GO nanocomposites were prepared on a glass substrate by spin-coating method of an aqueous solution prepared from epoxy resin, hardener and GO. After mixing of epoxy and hardener in ratio of 70:30, the solution was stirrer for 2 h and mixed with GO followed by sonication of 3 h. The epoxy-GO solution was used for thin film preparation by spin coating method. First of all spinning time (i.e. 60 s), speed (i.e. 1500 rpm) and temperature (i.e. 30 °C) of spin coater was fixed before casting of film. The film has been taken for curing and put into oven for 24 h at NTP.

Characterization methods.—FTIR spectroscopy has been successfully used for quantitative determination of functional groups in polymer samples.[27,28] The epoxy and epoxy-GO nanocomposites samples were characterized by FTIR (OPUS-Bruker Vertex 70) in the range 500–3000 cm^{-1}. In this technique different absorption bands are assigned to different crystalline, chemical bonds, polymer microstructure, chain conformation and etc., consequently it is useful in thin film studies. The KBr plates must be thoroughly cleaned by ethanol after each run to prevent contamination of future samples.

AFM allows accurate and non-destructive measurements of the topography AFM images for all samples in the contact mode. AFM is investigate the properties of sample surface at the level of high resolution[29] in air, liquids or ultrahigh vacuum. The samples were characterized by Atomic Force microscope (Model no, NTMDT, Solver-PRO) in tapping mode. Atomic Force Microscopy (AFM) is a high-resolution non-optical imaging technique first demonstrated by Binnig, Quate and Gerber.[30] Since then it has developed into a powerful measurement tool for surface analysis. The knowledge of the surface topography at nanometric resolution made possible to probe surfaces. The versatility of this technique allows meticulous observations and evaluations of the textural and morphological characteristics of the sample, showing better facilities than other microscopic methods. AFM scanned the surface in 3D and the analysis of images allow the determination of the average height of the particles, the average roughness and the power spectra density gives the periodicity in the arrangement of particles.[31]

The contact angle formed between the solid thin film and water/glycerin was measured by sessile drop method[32,33] with respect to polar liquid. In this method the angle is determined from the tangent made to the drop curvature at the base. Contact edges are ordinarily indicated in degrees, the test liquid utilized as a part of the estimations must be expressed, for its surface pressure will influence the edge (Young's equations).

The epoxy–GO nanocomposites samples were cut into small pieces and were kept in aluminum pans. The samples were weighed in a microbalance. The weight of the free nanocomposites sample piece (pure epoxy, epoxy-GO (0.2%) and epoxy-GO (0.4%)) used for the DSC measurements varied from 1.5 to 3.8 mg. Alumina was taken as reference material.[34] DSC technique has been proved to be a vital tool in producing phase diagrams for various chemical systems and phase transition in the various systems and it also has the ability to determine transition temperatures and enthalpies.[35] DSC analysis does not require large samples, numerous control or extensive method involvement make it more advantageous. DSC was run with heating rate of 10 °C min^{-1} with the accuracy of ±2 °C.

Results and Discussion

FTIR spectra of epoxy-GO nanocomposites.—FTIR spectra of pure epoxy and epoxy-GO (0.2 and 0.4%) nanocomposites are shown in Fig. 1. Absorption bands of FTIR spectra were found at

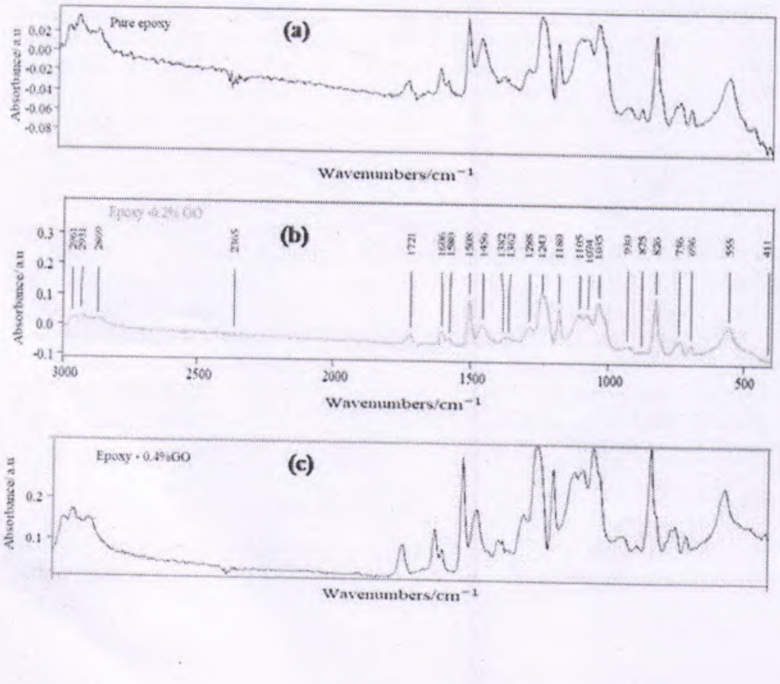

Figure 1. FTIR spectra of nanocomposites with the varying amounts of GO, pure epoxy, epoxy – 0.2%GO and epoxy –0.4% GO nanocomposites.

1606, 1721, 2931, 2961 cm^{-1}, which represents several groups in epoxy resin. 1606 cm^{-1} could be described to the C=C stretching mode of unconjugated olefins shows weak absorption peak at 1660–1640 cm^{-1}, however, vinyl absorb at 1640 cm^{-1}. The C=C stretching band of vinyl could be ascribed to the band frequency as a doublet resulting from absorption of rotational isomers, five—membered ring lactams appeared near 1750–1700 cm^{-1}. The peaks at 2935 and 3000 cm^{-1} appeared because of the presence of C-H stretch from methyl or methylene group in this region. A broad moderately intense band between 3000–2500 cm^{-1} and 2931−2961 cm^{-1} could be ascribed due to =C–H stretch for which these sharp bands of weak to medium intensities are present.

For epoxy-GO(0.2%) thin films, the FTIR absorption bands found at positions of 930, 1243, 1580, and 1721 cm^{-1}, which represent the several groups in epoxy resin.[36] The first peak of epoxy -GO (0.2%) is observed at 930 cm^{-1}, which is below the 1000 cm^{-1}, therefore, this region is very useful in identifying the type of substitution on the aromatic rings but here 930 cm^{-1} is near to 970–960 cm^{-1}, which indicate the appearance of cis and trans alkenes. The peak at 1243 cm^{-1} could be ascribed for primary alcohols and 1580 cm^{-1} represent the appearance of primary and secondary amides and a few lactams near (1650–1515 cm^{-1}). The last band of this composition at 1730cm^{-1} is ascribed to saturated ketone groups near 1715 cm^{-1}. For epoxy-GO (0.4%) thin films, the FTIR absorption spectra show the bands at 736, 1243, 1580 and 1721 cm^{-1}. These bands are responsible for several groups, which are present in epoxy-GO nano composites. The first peak similar to epoxy -GO(0.2%), which is below the 1000 cm^{-1}, therefore, this region is very useful in identifying the type of substitution on the aromatic rings. A strong band at 770–730 cm^{-1} shows monosubstitution. The band at 1243 cm^{-1} could be ascribed for primary alcohols and band at 1580 cm^{-1} represent the appearance of primary and secondary amides and a few lactams near 1650–1515 cm^{-1}. The last band of this composition 1721cm^{-1} is ascribed to saturated ketone groups near 1715 cm^{-1}. These all bands are same to epoxy -GO (0.2%). Table I represents the presence of different main functional groups in structure of epoxy resin and epoxy nanocomposites. Here we conclude that the absorption bands of GO changed due to mixing of epoxy resin, which is 1721 cm^{-1}, 1615 cm^{-1}, and 1074 cm^{-1} as shown in Fig. 1. In epoxy matrix some bands have been shifted due to presence of GO that indicate dispersion of GO in epoxy resin.

Atomic force microscopy (AFM) of epoxy-GO nanocomposites.—The two dimensional AFM surface profile of epoxy and epoxy nanocomposites are shown in Fig. 2. The AFM image of pure epoxy (i.e. Fig. 2a) represent smooth surface as compare to nanocomposites. Figure 3 show the three dimensional AFM images. These images shows the hills and valley of micro-scale dimensions in presence of GO in epoxy matrix. The modified surface structure of epoxy in presence of GO is owing to some short of agglomeration of GO. This surface structure is responsible for increase of nanocomposites surface roughness (i.e. Table II). The oxygen containing groups of GO increases the d-spacing allow to interact with epoxy matrix.[37]

The pure epoxy shows a poor surface roughness parameter ($R_q = 0.70$ nm and $R_a = 0.52$ nm), whereas, for epoxy -GO nanocomposites $R_q = 5.6$ nm -14.3 nm and $R_a = 3.6$ nm to 10.2 nm. It is clear that the dispersion of GO in epoxy matrix is subjected to interfacial interaction of epoxy with functional groups of GO. The R_q is the root mean square average of height deviation taken from the mean image data plane. The R_a is determined by taking arithmetic average of the absolute values of the surface height deviations measured from the mean plane and shows surface roughness of samples. The higher surface roughness *(R_a)* of epoxy is due to mixing of GO. After mixing of GO, large quantities of GO is attached to epoxy (Figs. 2 and 3) leads to the highest roughness. The roughness describes the disordered in surface of nanocomposites. The large value of roughness is good for mechanical interlocking with metal substrate. The grain size refers to the size of single crystal inside a matrix. The AFM parameters are summarized in Table II. The entropy of any system or material represents its regularity. The positive entropy means material is influenced by increasing disorders, however, negative entropy means material is ordered as observed in present case and its value is summarized in Table II. The negative value of entropy itself represents the epoxy -Go structure gets a regular array in long range.

Meaurement of contact angle of epoxy-GO nanocomposites.—It has been observed that the contact angle of pure epoxy is less than epoxy-GO nanocomposites. This means that epoxy-GO nanocomposites are more hydrophobic in the presence of these liquids. Consequently, the wettability decreased in their presence. The wettability is the tendency of a fluid to spread or adhere to a solid surface as defined by Anderson.[38,39] The wettability of solid surface relative to liquid depends on the nature of the bonding force. There are two categories of solid surface wetting (i) physical wetting and (ii) chemical wetting. The contact angle formed between liquid and solid is the measurement of physical wetting. Equation 1 represents the Young's equation of energy, which attributes the contact angle of the liquid on the solid surface:[40,41]

$$\gamma_s = \gamma_{SL} + \gamma_L \operatorname{Cos}\theta \qquad [1]$$

where γ is called the free surface energy and the subscripts *"S"* and *"L"* indicate the solid and liquid, respectively. However, chemical wetting is caused by chemical substance like surfactant that increases the spreading and penetrating properties of a liquid by lowering its surface tension.

The lower value of contact angle corresponds to (i.e. < 90°) high wettability, while larger value (>90°) of contact angle corresponds to low wettability.[42]

The wettability of thin film is directly related to surface energy. They are supplementary to each other. The effective surface energy between liquid and solid is equal to difference of surface energy of liquid and solid. The tendency of liquid molecules takes a lower energy state when moves in solid surface because solid exert the force towards liquid. We have noted that the epoxy -GO environment with water and glycerin attains the region of low surface energy as shown in Table III.

We can explain our results on the basis of following phenomenons:

i. Surface energy (Table III) attributed by solid and liquid. The water and glycerin in surface of epoxy/epoxy -GO nanocomposites gives the different characteristic. They react differently when contacted with surface of nanocomposites as compare to pure epoxy film. It is well known that epoxy and GO have highly polar character. This suggests that both the characteristics are overlapped and justify the adhesion of water or repulsiveness of water.

ii. The other phenomenon is probably occurring is the roughness of the sample. In this case, when water exposed to chosen liquid, the contact angle increases or decreases. It is depend on role of roughness. It is depend on type of wetting that can be homogeneous or heterogeneous. It is reported that homogeneous wetting attributed the greater roughness and greater the wetability, however, heterogeneous wetting offers the lower roughness and decrease the wetability. This theory also justifies our results of heterogeneous matrix (i.e. epoxy −GO nanocomposites). When nanocomposites thin film is in contact with water/glycerin, the behavior is heterogeneous wetting. In this case entire surface is not wet by liquid. This expels the air between the liquid and roughness of the surface. This is the reason of high value of contact angle for epoxy nanocomposites.

iii. The contact angles of the epoxy nanocomposites films measured the surface energy of the solid films, which can be

Table I. Analysis of different peaks/bands in FTIR spectra.

Sample	(C–CL) 550–800 cm^{-1}	(C–O–C) 800–970 cm^{-1}	(C=S) 1000–1250 cm^{-1}	(C=O) 1610–1680 cm^{-1}	>C=O 1710–1745 cm^{-1}	(C–H) 2800–3000 cm^{-1}
Pure epoxy	550	830	1034	1580	1720	2839
	555	835	1074	1606		2850
Epoxy −0.2%GO	555	875	1180	1615	1721	2869
			1105			2931
Epoxy −0.4%GO	555	930	1240	1620	1721	2950
		934	1243			2970
		941				

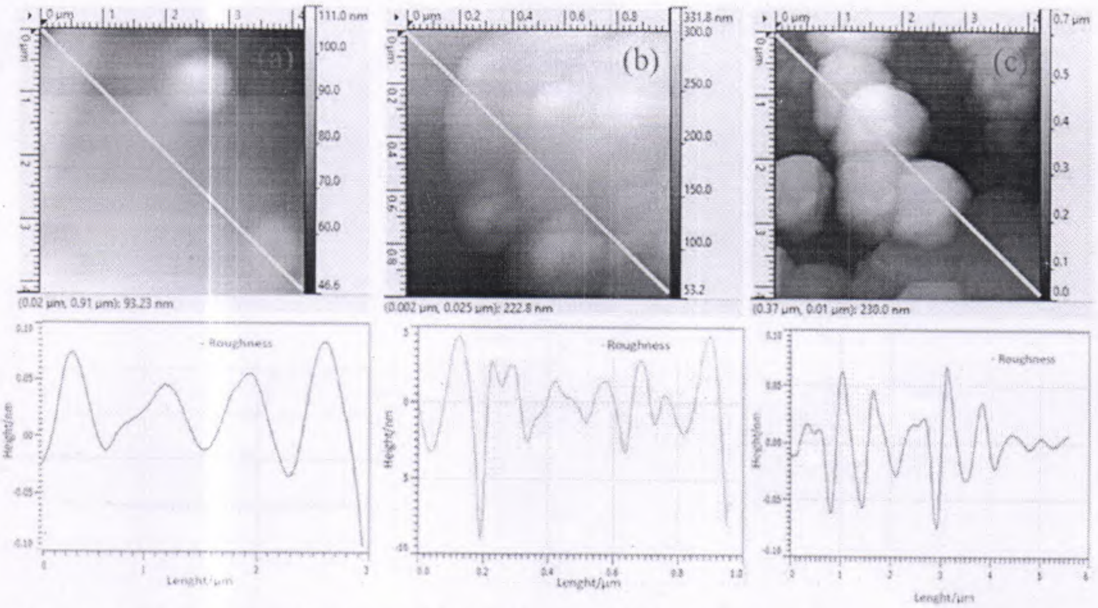

igure 2. AFM 2D-images of (a) Pure epoxy, (b) Epoxy–0.2%GO and (c) Epoxy −0.4%GO nanocomposite.

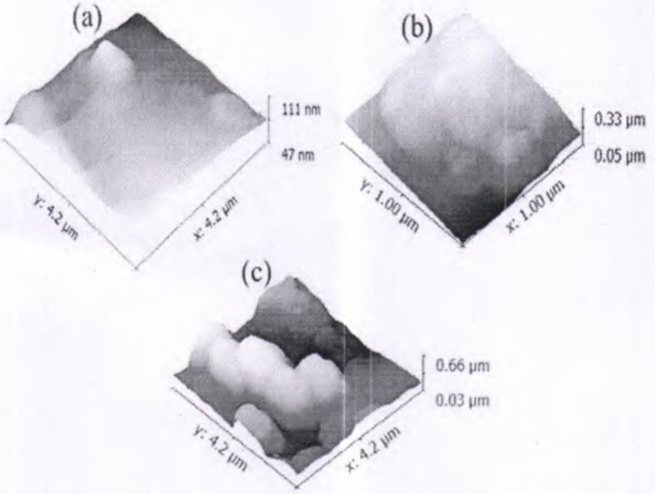

igure 3. AFM 3D-images of (a) Pure epoxy, (b) Epoxy–0.2%GO and c) Epoxy −0.4%GO nanocomposite.

calculated by Zisman method. The surface energy of three samples viz., water and glycerin are 31.36, 14.17 and 12.72, mJ m^{-2} corresponding to contact angles as shown in Fig. 4. The surface energy is related to force of adhesion, which is directly related to adhesive bonding and work of adhesion, therefore, the contact angle increases then surface energy will decrease. If contact angle is more than 90° then it shows hydrophobic properties,[43,44] which is good for coatings. In our results, we have observed hydrophobic properties due to contact angle value more than 90°. The surface free energy and interfacial tension for the epoxy nanocomposites are given in Table III. Hence, the increase of contact angle of epoxy -GO nanocomposite concludes the superior anti-corrosive properties.

Differential scanning calorimetry (DSC).—Figure 5 represents the DSC of pure epoxy, epoxy -GO (0.2%) and epoxy -GO (0.4%) in exothermic mode with the heating rate of 10 °C min^{-1} under the nitrogen medium, It has been observed that glass transition temperature (T_g) rises from 73.29 °C to 109.49 °C and 111.16 for 0.2%GO and 0.4%GO in epoxy matrix, which is much higher than the previously reported work.

Table II. AFM parameters of pure epoxy and epoxy-GO nanocomposites.

Sample	Roughness Average(R_a)/nm	Roughness R_{ms}(R_q)/nm	(R_a/R_q)/nm	Grain Size/nm	Entropy
Pure epoxy	0.52	0.70	1.36	5.51	−17.87
Epoxy −0.2%GO	3.6	5.6	1.6	96.76	−14.82
Epoxy −0.4%GO	10.2	14.3	1.40	149.8	−14.48

Table III. Contact angle (θ), work of adhesion (W_A) and surface energy (γs) of nanocomposites.

Samples	θ		W_A/mJ m^{-2}		γs/mJ m^{-2}
	Water	Glycerine	Water	Glycerine	
Pure epoxy	68	72	95.29	87.15	31.36
Epoxy −0.2%GO	92	98	62.66	61.18	14.77
Epoxy −0.4%GO	96	101	94.08	58.90	12.72

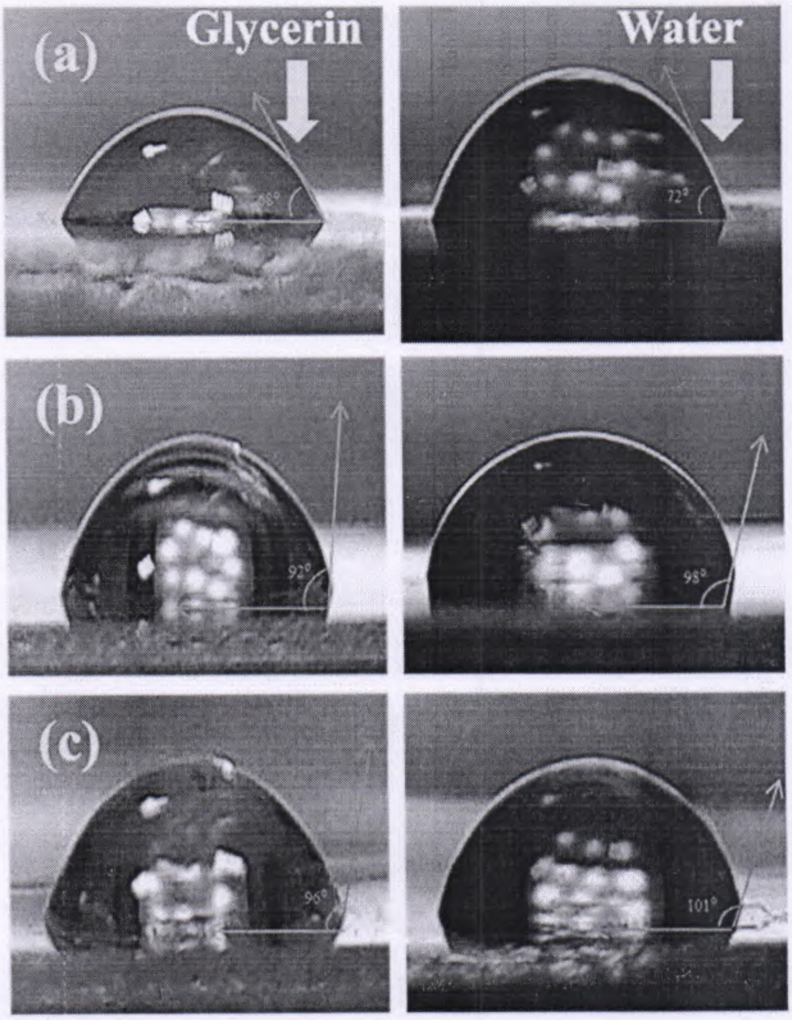

Figure 4. Contact angle images of nanocomposites with the varying amounts of GO (a) Pure epoxy, (b) Epoxy-0.2%GO and (c) Epoxy −0.4%GO nanocomposite.

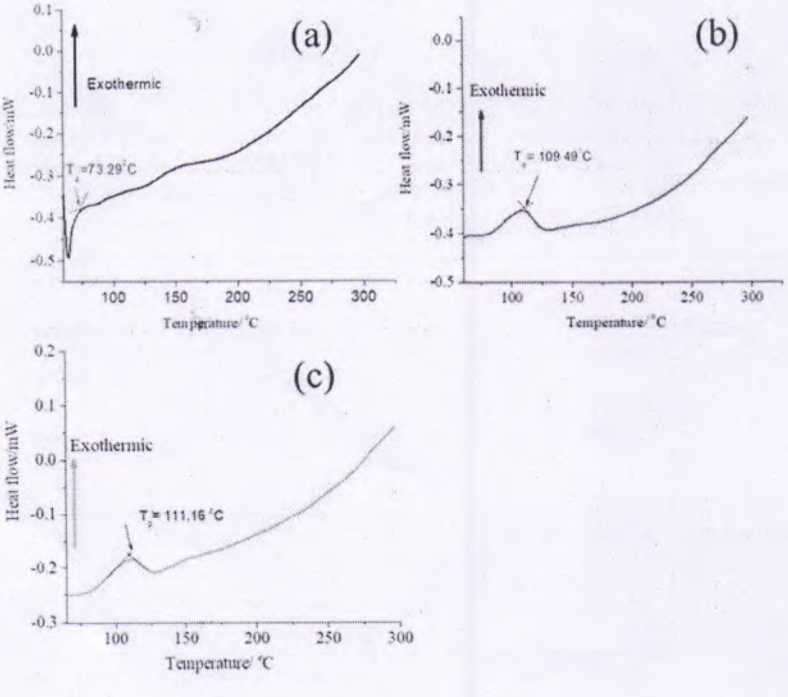

Figure 5. DSC of (a) Pure epoxy, (b) Epoxy-0.2%GO and (c) Epoxy −0.4%GO nanocomposite.

The exothermic peak in epoxy - GO nanocomposites is appeared at higher temperature as shown in Figs. 5b and 5c. This confirm the steric hindrance effect, which is occurred by addition of GO in epoxy matrix. The high surface area of GO in epoxy matrix could hinder the chain mobility.[45] Therefore, GO in epoxy matrix increases the segmental motion range and consequently increases

Table IV. DSC results of pure epoxy and epoxy -GO nanocomposites.

Samples	Tg/°C	ΔH_m/J g^{-1}	ΔH_C/J g^{-1}	Cp/J kg^{-1} K^{-1}	X/%
Pure epoxy	73.29	6.80	47.04	1621.51	53.12
Epoxy–0.2% GO	109.49	5.82	49.28	1643.91	28.50
Epoxy–0.4% GO	111.16	5.26	51.52	1775.74	25.90

T_g, glass transition temperature, ΔH_m, heat of fusion, ΔH_centhalpy of crystallization, C_p specific heat capacity and X, mass fraction crystallinity

the glass transition temperature. It is reported that the graphene nanofillers have general tendency to increases glass transition temperature of material.[46] It is well known that the properties of epoxy nanocomposites are depends on dispersion and interfacial bonding of nanofiller with epoxy matrix. The addition of plasticizers in polymer matrix is the traditional way to improve the toughness, however, they deteriorates the thermal properties. Fortunately, CNT and GO are not only improve the toughness but also improve the thermal properties. As glass transition temperature is an important property of an adhesive. It shows the mechanical properties of an adhesive, which are affected by the degree of cross-linking during the curing process. This study present the curing behavior and glass transition temperature of epoxy based adhesive reinforced with GO. The following may be the possible reason for improving T_g of epoxy:

i. Ultrahigh surface of GO as well as strong interface with epoxy. Therefore, interfacing of GO in epoxy matrix hinder the chain mobility.
ii. Possibly GO can react with epoxy matrix and form the chemical cross linking. The effective interaction of GO with epoxy resulting higher cross linking density. Generally, the higher value of cross linking density favours to increase of glass transition temperature of nanocomposites adhesive.[47–49]

The above two reason are responsible for enhancing the glass transition temperature of epoxy. The high T_g value of epoxy -GO nanocomposites suggest high strength of adhesives and high stiffness. This property is important for use of material in coating applications. The energy releases (i.e. enthalpy) pre and post melting of sample is the measure of ΔH_m and ΔH_c respectively. We can observe that melting enthalpy (ΔH_c) increases in presence of GO and consequently percentage crystallinity of epoxy-Go nanocomposite decreases (i.e. Table IV). This shows that the deformation of epoxy -Go nanocomposite at or near melting temperature is due to the destruction of crystalline structure of pure epoxy.

Conclusions

We report the effect of GO on structural and thermal properties of epoxy based composites. The results provide an evidence for modification of structure morphology, surface roughness, contact angle and thermal properties. The presented methods are efficient for the preparation of high performance epoxy-GO nanocomposites. The structural alteration of epoxy is caused by local changes at surface and cross linking of GO with epoxy structure as observed by FTIR and AFM. AFM images describes the contrast between epoxy, GO and interphases. The intermolecular interaction between components of epoxy and GO has been demonstrated by detailed analysis of OH band in nanocomposite samples. The functional group of GO (i.e., hydroxyl, epoxide, carbonyl and carboxyl) is attached with epoxy. These functional groups are responsible to improve the interfacial bonding between GO and the epoxy matrix. These groups are observed by FTIR. This interfacial bonding is responsible for enhanced corrosion resistance and thermal stability. DSC results demonstrate the exothermic epoxy resin curing reactions and formation of amino and hydroxyl group by incorporation of GO of high surface area in epoxy matrix, which increases the T_g of pure epoxy. Present findings are considered for future study of application based system such as anti-corrosive, anti-bacterial, antifouling and mechanical properties of epoxy-GO nanocomposites.

Acknowledgments

Acknowledgements Financial assistance from Aeronautics R&D Board, DRDO New Delhi-110 011 India (Letter no. ARDB/01 11051902l/M/l), is gratefully acknowledged). We are also thankful to Director IUAC, New Delhi for providing characterization facilities.

ORCID

M. S. Gaur https://orcid.org/0000-0002-9335-8233
Rohan Sagar https://orcid.org/0000-0002-9787-0138

References

1. B. Yongfeng, X. Meijuan, L. Hongyu, G. Kaixiong, Z. Yanhu, C. Beibei, M. Chunying, H. Xijun, and F. Yonghong, "Fabrication of low friction and wear carbon/epoxy nanocomposites using the confinement and self-lubricating function of carbon nanocage fillers." *Appl. Surf. Sci.*, **538**, 148109 (2020).
2. M. Raimondo, L. Guadagno, V. Speranza, L. Bonnaud, P. Dubois, and K. Lafdi, "Multifunctional graphene/POSS epoxy resin tailored for aircraft lightning strike protection." *Compos. Part B Eng.*, **140**, 44 (2018).
3. M. Raimondo, L. Guadagno, L. Vertuccio, C. Naddeo, G. Barra, G. Spinelli, P. Lamberti, V. Tucci, and K. Lafdi, "Electrical conductivity of carbon nanofiber reinforced resins: potentiality of tunneling atomic force microscopy (TUNA) technique." *Compos. Part B Eng.*, **143**, 148 (2018).
4. K. Tapas, B. Sambhu, Y. Dahu, H. K. Nam, B. Saswata, and H. L. Joong, (2010), (2010)"Recent advances in graphene based polymer composites." *Prog. Poly. Sci.*, **35**, 1350.
5. A. Ashery, M. A. Moussa, and G. M. Turky, "Synthesis, characterization and electrical properties of conducting nanoparticles of graphene oxide." *Materil. Proceed.*, **44**, 3017 (2021).
6. I. Rabia, M. J. Badrul, and A. Waqas, "An overview of industrial scalable production of graphene oxide and analytical approaches for synthesis and characterization." *J. Mater. Resear. Tech.*, **9**, 11587 (2020).
7. N. Golnaz, M. M. Mahmoud, and S. F. Masoud, "Reinforcement of polymer nanocomposites by α-graphyne nanotubes: a multiscale simulation." *Comput. Mater. Sci.*, **194**, 110431 (2021).
8. V. D. Punetha, S. Rana, H. J. Yooc, A. Chaurasia, and J. W. Choc, "Functionalization of carbon nanomaterials for advanced polymer nanocomposites: a comparison study between CNT and grapheme." *Prog. Poly. Sci.*, **67**, 1 (2017).
9. K. Duan, F. Wang, S. Liu, H. Yujin, and X. Wang, "New insights into interface interactions of CNT-reinforced epoxy nanocomposites." *Compos. Sci. tech.*, **204**, 108638 (2021).
10. M. He-nan and W. Xiao-gong, "Use of in situ polymerization in the preparation of graphene/polymer nanocomposites." *New Carb. Mater.*, **35**, 336 (2020).
11. N. Saravanan, R. Rajasekar, S. Mahalakshmi, K. T. Sathish, K. K. Sasi, and S. Sahoo, "Graphene and modified graphene-based polymer nanocomposites—a review." *J. Reinfor. Plast. Compos.*, **33**, 1158 (2014).
12. R. Mohammad, R. Bahram, M. Mohammad, and B. Ghasem, "Development of metal-organic framework (MOF) decorated graphene oxide nanoplatforms for anti-corrosion epoxy coatings." *Carb.*, **161**, 231 (2020).
13. L. Zhi-Jin, W. Fa-Shan, L. Yu-Chia, S. Zhong-En, and Y. Yuan-Hsiang, "Flexible epoxy graphene thermoset with excellent weather and corrosion resistance." *Prog. Org. Coat.*, **151**, 106052 (2021).
14. A. Taylor, *Adhesives with Nanoparticles in Handbook of Adhesion Technology* (Springer, Heidelberg, Berlin) 1437 (2011).
15. K. Virat, K. Vanish, and A. B. Suneev, "Mechanical properties of aluminium-graphene/carbon nanotubes (CNTs) metal matrix composites: advancement, opportunities and perspective." *Mater. Resea. Bull.*, **138**, 111224 (2021).
16. R. Sheikh, A. Sufyan, K. Antonios, and E. Ahmed, "Development of new graphene/epoxy nanocomposites and study of cure kinetics.Thermal and mechanical properties." *Thermochim. Acta*, **694**, 178785 (2020).
17. S. Saeed, J. Wim, Z. Ali, T. Zahra, and N. Mohammadreza, "Fabrication and evaluation of silica aerogel-epoxy nanocomposites: fracture and toughening mechanisms." *Theor. App. Frac. Mech.*, **94**, 154 (2018).
18. R. N. Maria, G. Liberata, N. Carlo, V. Luigi, and R. Marialuigia, "Graphene/epoxy resins: rheological behavior and morphological analysis by atomic force microscopy (AFM)." *Mater. Today: Proceed.*, **34**, 160 (2021).

19. S. Adriana, E. L. Gabriela, T. Bogdan, and L. Simona, "Silver nanoparticles/polyvinyl alcohol film: studies of thermal characterization, AFM and corrosion protection by electrodeposition on 304L stainless steel." *J. Therm. Analy. Calorim.*, **20**, 10444 (2021).
20. A. K. Pathak, H. Garg, M. Singh, T. Yokozeki, and S. R. Dhakate, "Enhanced interfacial properties of graphene oxide incorporated carbon fiber reinforced epoxy nanocomposite: a systematic thermal properties investigation." *J. Poly. Resea.*, **26**, 1668 (2019).
21. R. Kamalon, N. Kikkeri, M. Shetty, M. Avvadukkam, and M. Ambale, "Evaluation of anti-corrosion performance of modified gelatin-graphene oxide nanocomposite dispersed in epoxy coating on mild steel in saline media." *Colloi. Surf. A.*, **587**, 124341 (2020).
22. M. Lichun, S. Guojun, Z. XieChen, Z. Shaofeng, L. Yaqing, and L. Zhang, "Attaching SiO_2 nanoparticles to GO sheets via amino-terminated hyperbranched polymer for epoxy composites: Extraordinary improvement in thermal and mechanical properties." *Euro. Poly. J.*, **157**, 110677 (2021).
23. A. Bhanu, P. Vijayan, S. Thomas, J. K. Parameswaranpillai, D. Puglia, S. Siengchin, and A. Manohar, "Fabrication of water-resistant epoxy nanocomposite with improved dynamic mechanical properties and balanced thermal and dimensional stability: Study on dual role of graphene oxide nanosheets and barium oxide microparticles." *Colloi. Surf. A: Physicochem. Engin. Asp.*, **617**, 126405 (2021).
24. S. Mansour, "Study of thermal stabilization for polystyrene/carbon nanocomposites via TG/DSC techniques." *J. Therm. Anal. Calorim.*, **12**, 1 (2012).
25. A. Sen and S. Kumar, "Coir-fiber-based fire retardant nano filler for epoxy composites." *J. Therm. Anal. Calorim.*, **101**, 265 (2010).
26. N. I. Zaaba, K. L. Foo, U. Hashim, S. J. Tan, W. WenLiu, and C. H. Voon, "Synthesis of graphene oxide using modified hummers method: solvent influence." *Proce. Eng.*, **184**, 469 (2017).
27. A. R. S. Annappa, S. Basavarajappa, and P. D. Shivaramu, "Spectral characterization of morphological structure of organomodified montmorillonite clay-based epoxy nanocomposite." *Inter. J. Poly. Analy. Character.*, **26**, 471 (2021).
28. S. A. Haddadi, E. Mehmandar, H. Jabari, S. A. Ramazani, R. Mohammadkhani, N. Yan, and M. Arjmand, "Zinc-doped silica/polyaniline core/shell nanoparticles towards corrosion protection epoxy nanocomposite coatings." *Compos. Part B: Eng.*, **212**, 108713 (2021).
29. G. Binnig, C. F. Quate, and C. Gerber, *Atomic Force Microscope. Phys. Rev. Lett.*, **56**, 930 (1986).
30. R. Howland and B. Lisa, "A practical guideto scanning probe Microsco." (1997), https://1lib.in/g/Howland%20Rebecca.
31. O. Marti, B. Drake, and P. K. Hansma, "Atomic force microscopy of liquid-covered surfaces: atomic resolution images." *Appl. Phys. Lett.*, **51**, 484 (1987).
32. M. A. Duchesne and R. W. Hughes, "Slag density and surface tension measurements by the constrained sessile drop method." *Fuel.*, **188**, 173 (2017).
33. F. K. Skinner, Y. Rotenberg, and A. W. Neumann, "Contact angle measurements from the contact diameter of sessile drops by means of a modified axisymmetric drop shape analysis." *J. Colloid. Interf. Sci.*, **130**, 25 (1989).
34. J. McHugh, P. Fideu, A. Herrmann, and W. Stark, "Determination and review of specific heat capacity measurements during isothermal cure of an epoxy using TM-DSC and standard DSC techniques." *Poly. Test.*, **29**, 759 (2010).
35. C. K. Tziamtzi and K. Chrissafis, "Optimization of a commercial epoxy curing cycle via DSC data kinetics modelling and TTT plot construction." *Poly.*, **230**, 124091 (2021).
36. Q. Liu, X. Bao, S. Deng, and X. Cai, "The investigation of methyl phenyl silicone resin/epoxy resin using epoxy-polysiloxane as compatibilizer." *J. Therm. Anal. Calorim.*, **118**, 247 (2014).
37. D. H. Ali-Asgari, S. Mazinani, D. Zaarei, M. Kalaee, H. Jabari, and N. Sedaghat, "Thermal and morphological characteristics of solution blended epoxy/NBR compound." *J. Therm. Anal. Calorim.*, **114**, 185 (2013).
38. R. Sagar, M. S. Gaur, and B. S. Bhadoria, "Investigation of TSDC and dielectric modulus of PVDF–$BaZrO_3$ nanocomposites thin film." *Vacu.*, **156**, 375 (2018).
39. J. Park, D. Kim, and C. Lee, "Contact angle control of sessile drops on a tensioned web." *App. Surf. Sci.*, **437**, 329 (2018).
40. M. Boris, "Smart hydrophobic and soilrepellent protective composite coatings for textiles and leather." *Smar. Comp. Coat. Memb.*, **1**, 261 (2016).
41. W. Alnoush, A. Sayed, T. I. Solling, and N. Alyafei, "Impact of calcite surface roughness in wettability assessment: Interferometry and atomic force microscopy analysis." *J Petrol. Sci. Eng.*, **203**, 108679 (2021).
42. D. N. Rao, "Measurements of dynamic contact angles in solid–liquid–liquid systems at elevated pressures and temperatures." *Colloi. Surf. A: Physicochem.*, **206**, 1 (2002).
43. R. M. Shanker, I. Ahmed, P. A. Bourassa, and K. V. Carola, "An *in vitro* technique for measuring contact angles on the corneal surface and its application to evaluate corneal wetting properties of water soluble polymers." *Intern. J. Pharmac. Eng. Asp.*, **206**, 203 (1995).
44. S. Lu, J. Robert, E. Pugh, and Forssber, "Hydrophobic flocculation and hydrophobic aggregation separation (HAS)." *Interf. Separ. Partic.*, **20**, 415 (2005).
45. H. Ribeiro, W. M. Silva, M. T. F. Rodrigues, J. C. Neves, R. Paniago, C. Fantini, and G. G. Silva, "Multifunctional nanocomposites based on tetraethelenepentamine modified graphene oxide/epoxy." *J. Mater. Sci.*, **48**, 7883 (2013).
46. B. Tianjiao, W. Zhiyong, Z. Yan, W. Yan, and Y. Xiaosu, "Improving tribological performance of epoxy composite by reinforcing with polyetheramine functionalized graphene oxide." *J. Mater. Resear. Tech.*, **12**, 1516 (2021).
47. I. Zaman, B. Manshoor, A. Khalid, Q. Meng, and S. Araby, "Influence of interface on epoxy/clay nanocomposites: mechanical and thermal dynamic properties." *J. Mater. Sci.*, **49**, 5856 (2014).
48. B. B. Johnson, A. J. Kinloch, R. D. Mohammed, A. C. Taylor, and S. Sprenger, "Toughening mechanisms of nanoparticle-modified epoxy polymers." *Poly.*, **48**, 530 (2007).
49. T. Sun, H. Fan, X. Liu, and Z. Wu, "Sandwich-structured graphene oxide@poly (aminophenol-formaldehyde) sheets for improved mechanical and thermal properties of epoxy resin." *Compos. Sci. Tech.*, **207**, 108671 (2021).

Journal of Thermal Analysis and Calorimetry
https://doi.org/10.1007/s10973-022-11302-x

Study of structural, thermal and piezoelectric properties of polyvinylidene fluoride –$BaZrO_3$ nanocomposites

Rohan Sagar[1] · **M. S. Gaur**[1] · **Rajesh Kumar Raghav**[1]

Received: 7 June 2021 / Accepted: 1 March 2022

Abstract

The thin film of nanocomposites was prepared by solution casting methods and characterized by UV–Vis spectra, Raman spectra and scanning electron microscopy (SEM). The optical band gap was determined by Tau plots. The band gap of PVDF was determined with and without $BaZrO_3$ nanoparticles. It could be seen that the band gap decreases from 4.98 to 3.32 eV in the presence of $BaZrO_3$ nanoparticles in PVDF matrix. The Raman study identifies the interacting species with PVDF due to structural change by the addition of $BaZrO_3$ nanoparticles. This helps to understand the potential of new nanocomposites. The structural changes were analyzed by crystallinity, nature of bonds, phase transition from G to B-phase, etc. SEM images represent the change in spherulitic morphology of PVDF by incorporation of $BaZrO_3$ nanoparticles. SEM images are presented the aggregation of $BaZrO_3$ nanoparticles in PVDF matrix causes the generation of larger particles in PVDF chain. DSC supports the crystallization of PVDF nanocomposites upon heating due to the rearrangement of PVDF structure in the presence of $BaZrO_3$ nanoparticles. It is observed that $BaZrO_3$ nanoparticles enrich the structural, thermal and piezoelectric properties due to the change in spherulitic morphology, which creates a large number of micro- to nano-sized pores, increases the β-phase content of the PVDF.

Keywords PVDF · $BaZrO_3$ · Raman · SEM · Piezoelectric · DSC

Introduction

There are potential applications of polyvinylidene fluoride (PVDF) nanocomposites in the area of optoelectronics and piezoelectric devices [1–3]. PVDF is one of the first flexible and efficient electromechanical materials. The polar nature is due to the positive charge on hydrogen and the negative charge in fluorine atoms. PVDF is an excellent piezoelectric polymer gaining importance amongst various polymers [4–8].

The previous studies proved that the PVDF is one of the most electroactive polymers mainly due to the presence of β- and γ-phases. The role of β- and γ-phases promoted its applications in the field of sensors, energy storage devices, etc. Moreover, its easy processing can improve the structural, electrical and mechanical properties [9–16]. The increase of β-phase in PVDF is subjected to the processing conditions. The solution casting, spin coating, and bland technique are the most important processing methods. It has been observed that the incorporation of inorganic nanoparticles is one of the strategic parts to improve the functional properties of polymers. Currently, nanofiller like ceramic nanoparticles are popular to improve the β-phase. There are some of the important nanofillers (i.e., CuO, NiO, Pt, $BaZrO_3$, $BaTiO_3$, etc.) that are considered to enhance β-phase of PVDF [17–24].

The combinations of polymers and ceramic nanofillers have received significant attention due to their excellent properties, which are suitable for flexible electronic devices such as embedded capacitors system, multilayer capacitors, field-effect transistors, piezo and pyroelectric sensors [25]. There are five crystalline phases of PVDF. Out of these, only electroactive β-phase is highly demanded because it exhibits a high dipole moment. This makes the polymer of high dielectric constant, high piezo and pyroelectric coefficients [26].

✉ M. S. Gaur
mulayamgaur@rediffmail.com

[1] Department of Physics, Hindustan College of Science and Technology, Farah, Mathura, U.P 281122, India affiliated to Dr. A.P.J. Abdul Kalama Technical University, Lucknow, U.P 226031, India

Barium zirconate is a ferroelectric ceramic material that possesses outstanding electroactive properties [27, 28]. Its crystalline structure is fcc type. Its structure consists of tetravalent ions at the centre of the cube and divalent ions at the top corner. However, O^{2-} ions are placed at the centre of each face.

The -OH groups of $BaZrO_3$ nanoparticles, as mixed with PVDF, provide strong hydrogen bonding sites and increase the electroactive β-phase. There are several questions regarding piezoelectric, dielectric, thermal properties, etc., of these nanocomposites that are unanswered. Understanding of the microscopic mechanisms of polarization reversal in PVDF nanocomposites is a critical issue amongst researchers.

The wide variety of PVDF nanocomposites have been developed with improved thermal, mechanical, and excellent barrier properties [29–31]. However, developing the PVDF nanocomposites for prolonged service at high temperatures is still a challenge.

The melting temperature of PVDF of different phases is in the range of 167–172 °C. The DSC is used to determine several parameters of material such as glass transition temperature, melting temperature, percentage crystallinity, and other thermal properties; however, it is unable to distinguish different phases of PVDF clearly. For this purpose FTIR, X-ray and Raman spectra are used [32–37].

Currently, nanocomposites play a very important role in the field of flexible electronic industries due to the simple architecting of nanofiller in the polymer matrix and their uncommon properties. The less number of publications of PVDF-$BaZrO_3$ nanocomposites have been found in literature. Therefore, in this work, the possibility of preparing $BaZrO_3$ embedded PVDF with different concentrations is demonstrated. In the present work, the optical, structural, electroactive and thermal properties of PVDF-$BaZrO_3$ nanocomposites were studied by UV–Vis spectroscopy, Raman spectroscopy and SEM–EDX spectra, P-E loop and DSC techniques. This research would help us better understand the effect of $BaZrO_3$ on the structure and properties of PVDF nanocomposites.

Experimental

Materials

PVDF was procured from Redox (India). The 64.03 and 1.78 g cm^{-3} are molecular weight and molecular density of PVDF. The N, N, dimethylformamide (DMF) was procured from Merck India Ltd. The barium zirconate ($BaZrO_3$) nanoparticles of size less than 100 nm were procured from Sigma Aldrich. All materials are used as obtained without any further processing for the preparation of nanocomposites. The material properties are presented in Table 1.

Table 1 Properties of PVDF and $BaZrO_3$ nanoparticles

Material	Density/g cm^{-3}	Particle size/nm	Specific surface area/ m^2g^{-1}	Purity/%
PVDF	1.78	100	3.76–6.61	99
$BaZrO_3$	5.96	25–50	3.5–11.2	98

Method

In this method, the PVDF is dissolved in N, N, dimethylformamide (DMF). The $BaZrO_3$ nanoparticles have higher chemical compatibility with PVDF due to the existence of hydroxyl groups onto the surface of $BaZrO_3$ nanoparticles. The $BaZrO_3$ solution in DMF was undergone a thorough stirring process followed by sonication of 5 min. $BaZrO_3$ solution was added drop by drop in PVDF solution. More details of sample preparation is reported in our earlier work [38, 39]. Figure 1 shows the different steps followed for the preparation of nanocomposites thin film.

Characterization

The UV–Vis spectra were recorded by Hitachi—4150 spectrophotometer. Aluminium electrodes on thin-film for piezoelectric measurement were prepared by using a vacuum coating unit (Model no, VEQCO Delhi, India). The morphology and phase images were recorded by using SEM–EDX (Model no, MIRA II LMH from TESCAN). The polarization–electric field (P-E) loops were recorded at 100 Hz using the ferroelectric test system (Marine India). Raman spectroscopy was recorded using Renishaw Invia Mirco Raman setup. Differential Scanning Calorimetry (DSC) was recorded using Differential Scanning Calorimetry (DSC); model Q20; (TA Instruments, USA). The d_{33} coefficient of the poled thin film was measured by piezo test (PM100).

Results and discussion

UV–Vis spectra

UV–Vis spectroscopy is an important tool to provide the information on bond structure and optical band gap of materials. The molecular band theory of material describes the promotion of an electron from the ground state (i.e. π, σ, and n- orbits) to higher energy states by absorption of ultraviolet and visible radiation [40].

Figure 2 shows the absorbance of PVDF and PVDF-$BaZrO_3$ nanocomposites with different wavelengths. It

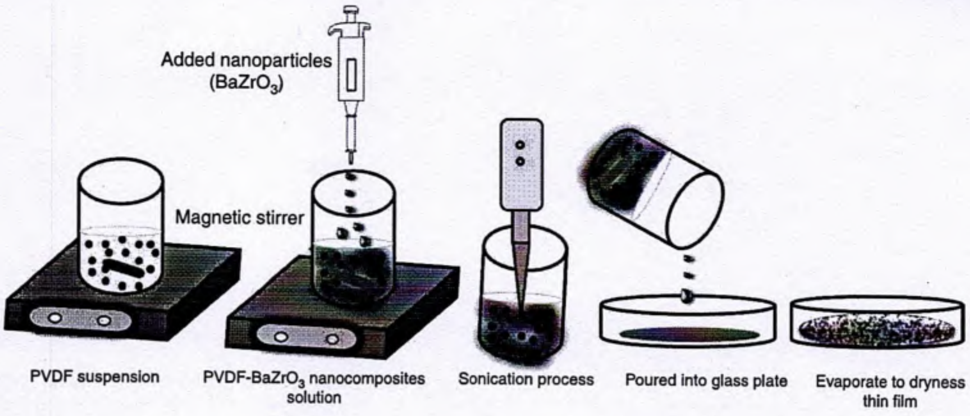

Fig. 1 Preparation of nanocomposites thin film by solution casting method

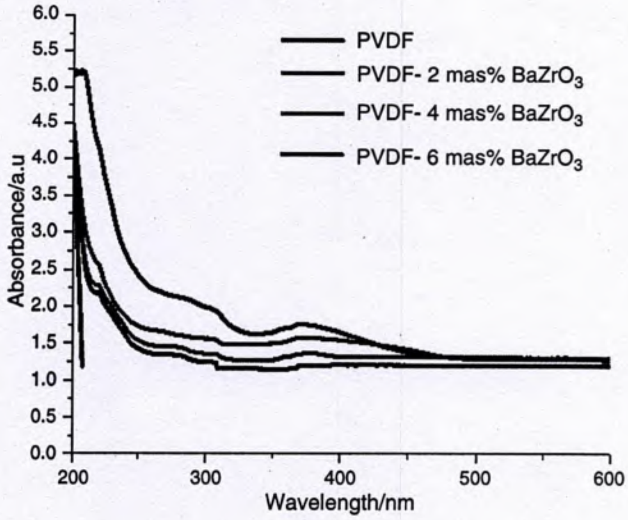

Fig. 2 UV–Vis absorption spectra of **a** PVDF, **b** PVDF-2mass% $BaZrO_3$, **c** PVDF-4mass% $BaZrO_3$, and **d** PVDF -6mass% $BaZrO_3$ nanocomposites

has been observed that the absorbance of PVDF increases with the increasing concentration of $BaZrO_3$ nanoparticles. This may be due to the many defects formed in the chemical structure of PVDF by the addition of $BaZrO_3$. In general, the physical properties of nanoparticles such as particle size, roughness, dispersion, nano-interfaces in polymer affect the absorbance of polymer nanocomposites. The very high absorbance of PVDF nanocomposites in the UV region indicates its interest in UV shielding applications [41].

The absorption edge of PVDF at around 219 nm was shifted to 273, 307 and 366 nm for 2, 4 and 6mass% of $BaZrO_3$ nanoparticles. Generally, in polymer matrix attributed the change in molecular configuration as discussed in literature [42].

Optical band gap E_g was calculated by Tauc,s expression [43, 44]:

$$E = h\nu = \frac{hc}{\lambda} \tag{1}$$

$$(\alpha h\nu)^{\mathrm{m}} = B\left(h\nu - E_{\mathrm{g}}\right) \tag{2}$$

where λ represents the maximum wavelength (nm), h is a plank constant, c is the speed of light, α is the absorption coefficient, hν is the photon energy, B is a constant, E_g is the band gap of the material, and the exponent m depends on the type of the transition. The m may be equal to ½ and 2 corresponding to the allowed indirect, allowed direct, forbidden direct, and forbidden indirect transition, respectively [45]. Figure 3a, b shows the variation of $(\alpha h\nu)^{1/2}$ with hν. The band energy gap was calculated by using the method as reported in literature [46, 47].

The direct and indirect optical band gap of PVDF and PVDF nanocomposites are shown in Fig. 3a, b. The direct and indirect optical band gaps of the PVDF- 6mass% $BaZrO_3$ are calculated to be 3.40 and 3.33 eV, respectively. It is comparatively higher than other combinations of $BaZrO_3$ in PVDF. This behavior of PVDF is agreed with our earlier work [48].

PVDF- 6mass% $BaZrO_3$ nanoparticles filled nanocomposites show the highest intensity of UV absorption with maximum width for the absorption window. This can be related to the formation of an interpenetrating network (IPN). This type of network cannot be separated unless chemical bonds are broken. The formation of IPN offers better possibilities for getting extended regions of π^* conjugation, which influences the optical properties significantly.

Raman spectroscopy

Raman spectroscopy is used to sense atomic and molecular motions of organic and inorganic materials at any wavelength except the wavelength of the incident electromagnetic radiation. In polymer nanocomposites, the shift of the Raman line is subjected to the concentration of nanofiller [49, 50].

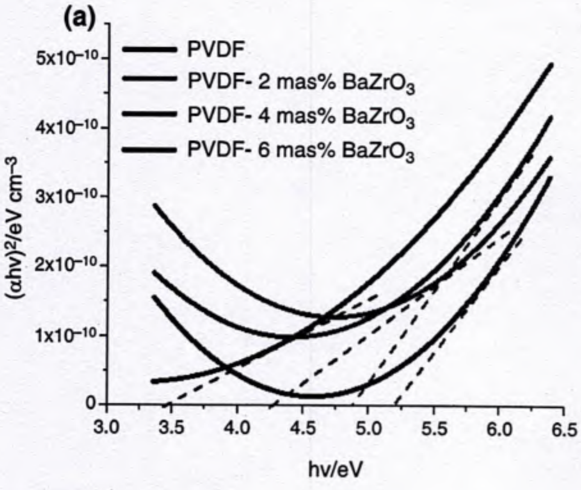

Fig. 3 Plots for **a** Direct optical band gap and **b** Indirect optical band gap for polymer nanocomposite

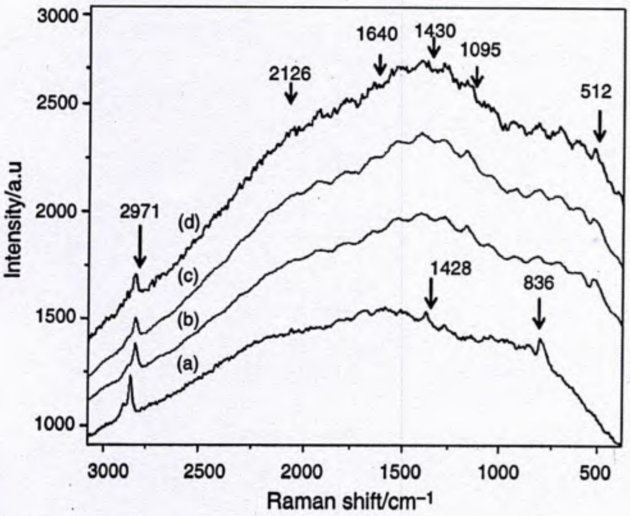

Fig. 4 Micro Raman spectra of **a** PVDF, **b** PVDF-2mass% $BaZrO_3$, **c** PVDF-4mass% $BaZrO_3$, and **d** PVDF -6mass% $BaZrO_3$ nanocomposites

Raman spectra confirm the stretching of the polymer matrix in the presence of nanofiller by means of Raman shift. The Raman shift is related to changes in various vibrations and molecular motions of the polymer-based nanocomposites. The Raman band located at 838 cm^{-1} originates from combined CF_2 bending and CCC skeletal out- of-phase vibrations. It is expected that this band would be sensitive to the loading with $BaZrO_3$ due to skeletal vibrations. Figure 4 shows the Raman spectra in the range of 500 to 3000 cm^{-1} at room temperature with the 532 nm laser line for PVDF and PVDF nanocomposites. In contrast, the PVDF vibration bands exhibited β-phase peaks located at 512, 838, and 1277 cm^{-1} caused by CF_2 vibration. The bands at 512 cm^{-1} attributed to CF_2 bending vibration and higher intensity band at 834 cm^{-1} due to out-of-phase combination of CH_2 rocking and CF_2 stretching mode. The intensity of peak increases with increase in nanoparticles concentration. The shift of Raman spectra of PVDF and nanocomposites with $BaZrO_3$ (i.e. 2, 4 and 6mass%) are shown in Fig. 4b–d. The spectra present from 1542 to 1756 cm^{-1} for G band assigned to the in-plane vibration, from 1334 to 1428 cm^{-1} for D band is activated by the presence of disorder in carbon systems and some Raman bands are located at 2126 to 2971 cm^{-1} called the *G′* band [51–53]. The assignment of bands in Raman spectra of PVDF and nanocomposites are presented in Table 2. The change in position of Raman band of polymer nanocomposites indicates two domains. First domain is compressive strain and second is the expansion domain. It has been observed that by increasing the concentration of $BaZrO_3$, the position of band shifted downwards, suggesting a positive strain resulted in the crowding of nanofillers above the elastic capabilities of the matrix. The band located at 2980 cm^{-1} is shifted downward for PVDF nanocomposites. This band is connected to crystalline domains of PVDF. This means that the contribution of elongational strain becomes visible. This experimental result suggests that the band recorded at 2988 cm^{-1} is corresponding to the crystalline domain of PVDF. The amorphous phase of PVDF accommodates the nanoparticles. The possible electrostatic interaction of oxygen contents of $BaZrO_3$ and partially charged CH_2 group of PVDF nucleates and form high electroactive *β*-phase induces polymeric chain to orient in all-trans (TTTT) conformation structure [54–56].

Scanning electron microscopy (SEM)

The SEM micrograph (Fig. 5) of PVDF and PVDF-$BaZrO_3$ nanocomposites provides the information of spherulites and dispersion of $BaZrO_3$ nanoparticles in the polymer matrix.

Table 2 Analysis of different peaks/bands in Raman spectra of PVDF and PVDF-BaZrO$_3$ nanocomposites samples

Samples	Peaks/bands				
	CF$_2$ modes β-phase in500-950/cm^{-1}	CF$_2$ Symmetric/ Asymmetric stretch in1000-1300/cm^{-1}	CH$_2$, D-Band in1300-1500/cm^{-1}	G-Band in1500-1900/cm^{-1}	G′-Band in2000-3000/ cm^{-1}
PVDF	512 659 836 915	1004 1107 1191 1277	1339 1430	1642 1740	2545 2969
PVDF-2mass% BaZrO$_3$	728 834	1108 1190	1334 1438 1641	1542, 1743 1862	2116 2969
PVDF-4mass% BaZrO$_3$	834 950	1105 1207	1341, 1431, 1643	1746 1869	2120 2483
PVDF-6mass% BaZrO$_3$	832 838	1000 1033 1206	1326, 1428, 1640	1756 1855	2126 2971

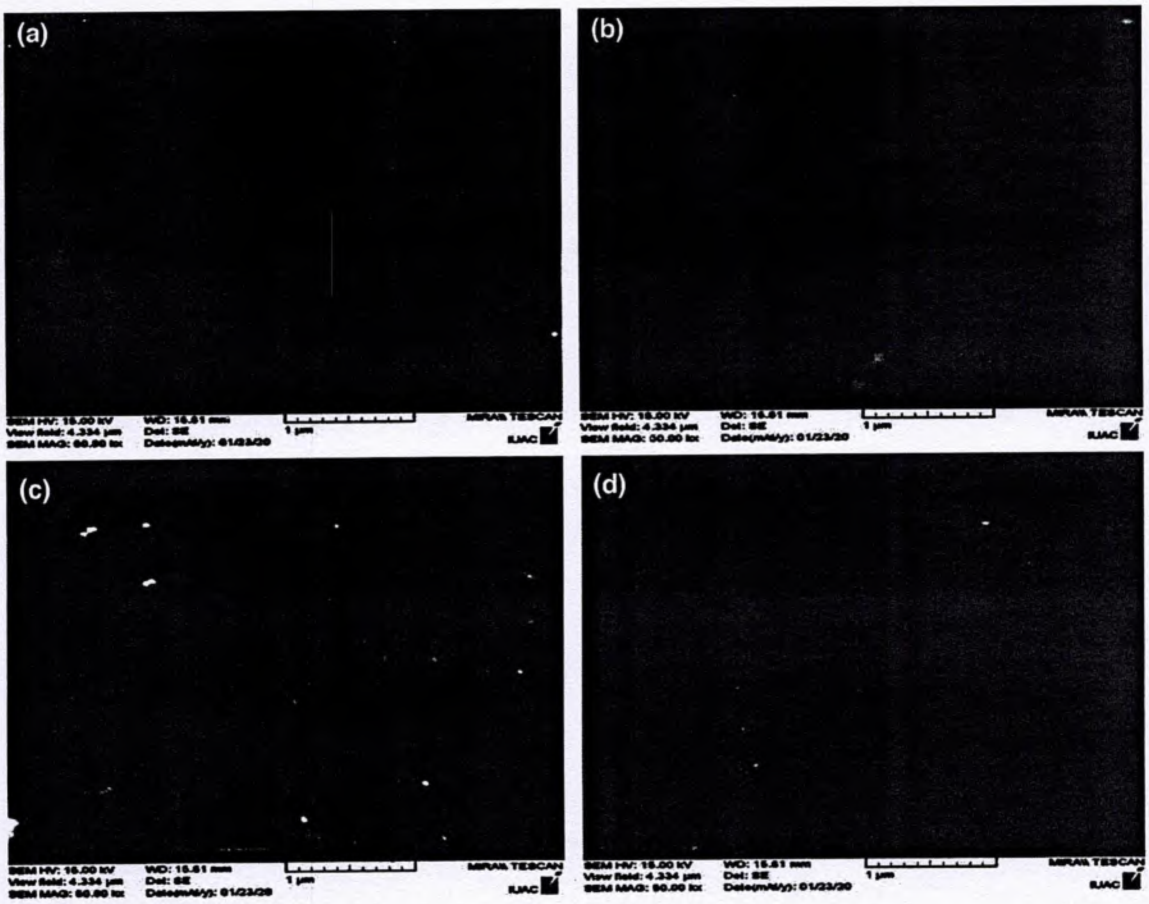

Fig. 5 SEM images of **a** PVDF, **b** PVDF-2mass% BaZrO$_3$, **c** PVDF-4mass% BaZrO$_3$, and **d** PVDF -6mass% BaZrO$_3$ nanocomposites

The SEM image of PVDF shows the well-defined structure of spherulites for which the polymer chains are self-connected into a continuous network along with some scattered pores. The SEM image of nanocomposites reflects that the spherulites are merging with each other and pores are disappearing with increasing concentration of BaZrO$_3$. We could understand from these results that BaZrO$_3$ nanoparticles acted as a nucleation agent leading to close interaction or

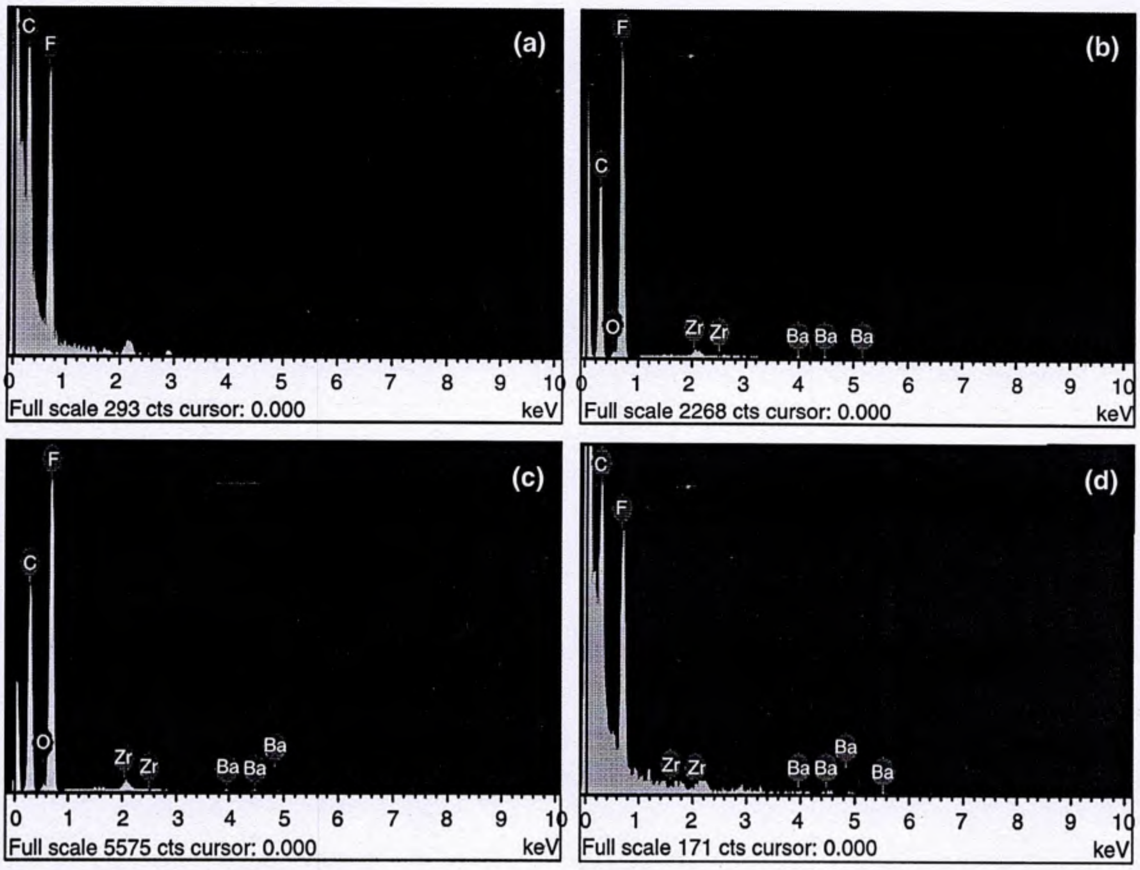

Fig. 6 SEM–EDX spectra of **a** PVDF, **b** PVDF-2mass% $BaZrO_3$, **c** PVDF-4mass% $BaZrO_3$, and **d** PVDF-6mass% $BaZrO_3$ nanocomposites

growth of spherulites in PVDF matrix. The bright spots in PVDF-$BaZrO_3$ nanocomposites show the aggregated region of nanoparticles and the faded part reflects the homogeneous distribution of nanoparticles. The dispersion of nanoparticles is supported by the interaction of oxygen contents of $BaZrO_3$ with the hydrogen bond of PVDF. Also, the surface charge of $BaZrO_3$ nanoparticles helps to smooth the orientation of molecular chain due to the formation of induced dipoles [57, 58]. The formation of nano-crystalline regions of $BaZrO_3$ in PVDF matrix led to a significant improvement in piezoelectric and thermal properties of PVDF.

The EDX spectra (i.e. Figure 6b) are showing the presence of barium, zirconium, oxygen, gold, carbon, and fluorine. The elements Ba, Zr, O, C, and F were originating from the PVDF structure due to the presence of $BaZrO_3$. The presence of gold is due to the coating material of samples was ignored. Each component in nanocomposites samples shows the characteristics peak and peak height is the measurement of percentage concentration of components in PVDF matrix. These results clearly indicate the successful formation of nanocomposites.

Hysteresis *P-E* loops

The charge generation capability of PVDF-$BaZrO_3$ nanocomposites was studied by using polarization–electric field

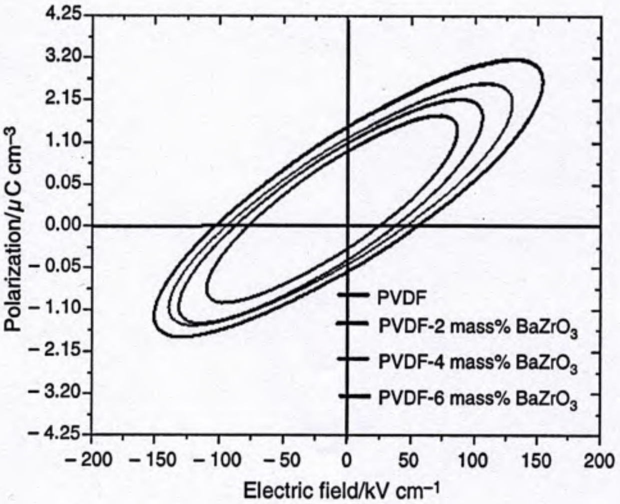

Fig. 7 Electric field dependent polarizations (P–E loop) at 100 Hz for PVDF and PVDF-$BaZrO_3$ nanocomposites at room temperature

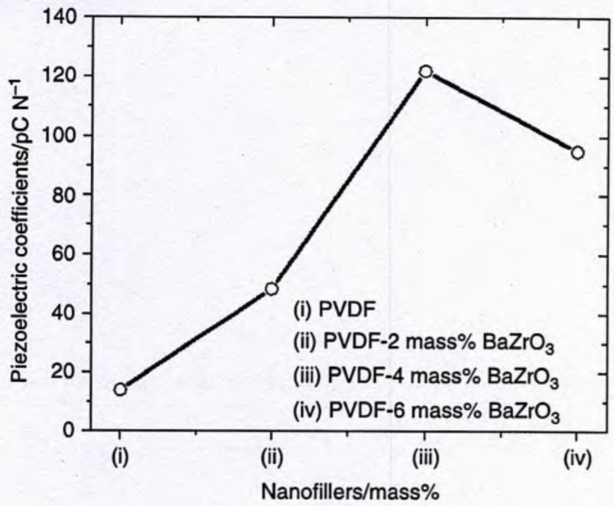

Fig. 8 Piezoelectric coefficient d_{33} for PVDF and PVDF-$BaZrO_3$ nanocomposites at room temperature

(P-E) loop. The P-E loops were recorded for PVDF and PVDF-$BaZrO_3$ nanocomposites with polarization electric field of 200 kV cm^{-1} at room temperature under a frequency of 100 Hz (i.e. Figure 7).

The polarization parameter (i.e. remnant polarization, coercive field, etc.) of PVDF nanocomposites attain a higher value as compared to pure PVDF. For example, the P_r value of PVDF is 1.13 μC cm^{-2}, and P_r value PVDF nanocomposites with 6mass% of $BaZrO_3$ is 3.25 μC cm^{-2}. This change itself demonstrates the enhancement of energy density and dielectric permittivity of PVDF nanocomposites [59]. This is due to the fact that the β-phase is dominated in the structure of PVDF by the addition of $BaZrO_3$. The area of the curve represents the charge storage ability of the material. It could be observed that area of the P-E loop for PVDF nanocomposites is higher than pure PVDF. The P_r value of PVDF nanocomposites attributed charge accumulation at the interface, which facilitates the heterogeneous polarization. The $BaZrO_3$ in PVDF matrix enhances the remnant polarization and coercive field. Therefore, it is reasonable to understand that $BaZrO_3$ nanoparticles are responsible for increasing polarization response as well as charge generation capability of PVDF.

Piezoelectric properties

It is found that d_{33} coefficient of PVDF nanocomposites with 6mass% of $BaZrO_3$ is less than 4mass% of $BaZrO_3$ (Fig. 8). This is due to the fact that the higher concentrations of nanofillers have tendency of agglomeration in polymer matrix leading to poor electrochemical coupling. The modifications of piezoelectric properties are completely caused by the improvement of β-phase in PVDF, which is verified from Raman spectra [38, 59, 60]. The poling field and surface of PVDF are perpendicular to each other during polarization. This arrangement orients the molecular dipoles along the direction of field. This perturbation will dynamically change the position of nuclei and the electrons, which will favor the formation of more and more dipoles. As a result, the opposite facing poles inside the PVDF cancel each other and fixed charges appear on the surface. If V is the applied voltage and d is the thickness of the film. If the thin film is assumed to be behave like a parallel plate capacitor, then d_{33} coefficient will be [61];

$$d_{33} = -\alpha\, CV/F \qquad (3)$$

where α is a calibration factor associated with the specimen to be tested. If α is determined a priori via a finite element analysis, C is the capacitance and F is the finite applied force. The capacitance of PVDF nanocomposites enhances many times by the addition of $BaZrO_3$ nanoparticles as reported in our earlier work [38]. This is the origin of increasing piezoelectric coefficients of PVDF.

Differential scanning calorimetry (DSC)

The melting behavior of the polymeric samples and the degree of crystallinity were investigated by differential scanning calorimetry (DSC). Figure 9 shows the DSC of PVDF, PVDF- 2mass% $BaZrO_3$, PVDF- 4mass% $BaZrO_3$, and PVDF- 6mass% $BaZrO_3$ in endothermic mode with the heating rate of 10 °C min^{-1} under the nitrogen medium. Figure 9a–d shows the DSC of β-phase PVDF and nanocomposites with different mass% of $BaZrO_3$. It has been observed that melting temperature (T_m) at 143.04, 140.40, 139.81, and 138.32 °C for PVDF and PVDF nanocomposites samples of different $BaZrO_3$ concentrations.

Figure 9 shows an endothermic peak followed by enthalpy relaxation upon heating. The broad relaxation peak is owing to heating-dependent crystallization. It is noted that the melting peak gives the crystalline and noncrystalline behavior of the material in terms of sharp and broad shape. The enthalpy (ΔH_c) value for nanocomposites is larger as compared to pure samples. That means crystallinity of samples increases in presence of nanofiller. These results are supported by literature [62, 63] and summarized in Table 3. Apart from this, the rearrangement of the molecular chain took place during heating resulting in the shifting of glass transition temperature from amorphous region to crystalline region [64].

The effect of $BaZrO_3$ on glass transition temperature (T_g) can be explained by the enthalpy interaction between the polymer and nanoparticles. The enthalpy of crystallization (ΔH_c) of PVDF increases with increasing concentration of $BaZrO_3$ nanoparticles. Either an increase or decrease in (T_g) can be induced depending on the specific

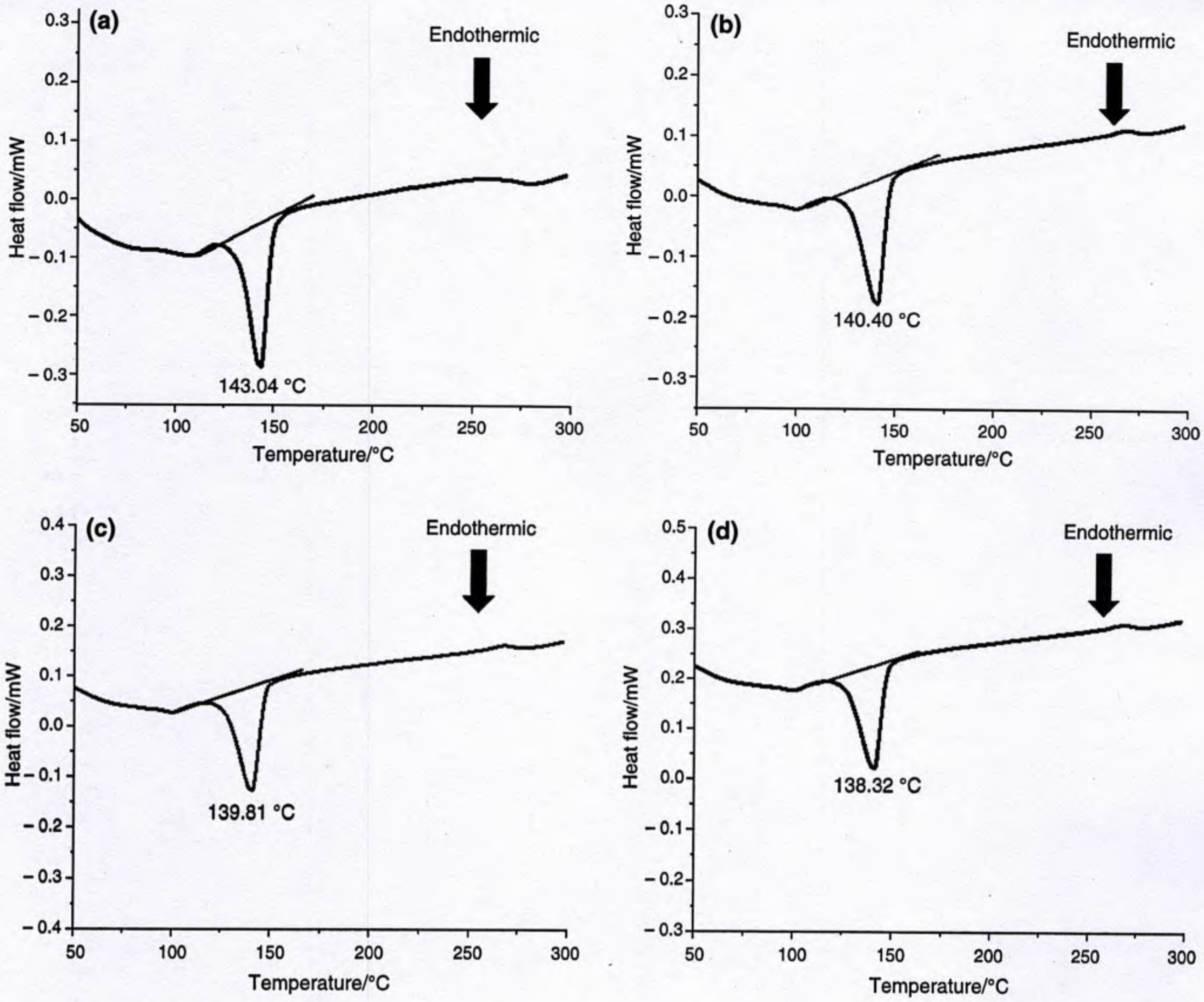

Fig. 9 DSC of **a** PVDF, **b** PVDF-2mass% $BaZrO_3$, **c** PVDF-4mass% $BaZrO_3$, and **d** PVDF-6mass% $BaZrO_3$ nanocomposites

Table 3 DSC parameters of PVDF and PVDF-$BaZrO_3$ nanocomposites samples

Samples	T_m /°C	ΔH_m /J g^{-1}	ΔH_C /J g^{-1}	C_p/J kg^{-1} K^{-1}	X/%
PVDF	143.04	16.59	38.24	1244.55	40.21
PVDF-2mass%$BaZrO_3$	140.40	15.16	40.58	1256.69	45.92
PVDF-4mass%$BaZrO_3$	139.81	12.58	45.71	1332.12	46.58
PVDF-6mass%$BaZrO_3$	138.32	10.44	67.36	1419.56	47.09

T_m, melting temperature, ΔH_m heat of fusion, ΔH_C enthalpy of crystallization, C_p specific capacitance and *X*, mass fraction crystallinity

capacitance (C_p) interaction [65, 66]. The percentage crystallinity of polymeric samples is based on the mass fraction crystallinity *(X%)*, crystallization enthalpy/heat release of crystallization *(ΔH_c)* under DSC scans, which is obtained from the following relations [67–70]:

$$\Delta H_c = kA/M \tag{4}$$

$$X(\%) = \frac{\Delta H_m}{M \Delta H_{100\%,\text{crystalline}}} \times 100\% \tag{5}$$

where k is the instrument constant, which is found to be 1.12; A is the area under the crystallization peak and M is the mass of the sample and $\Delta H_{100\%,\ \mathrm{crystalline}}$ is the heating enthalpy of fusion of pure crystalline PVDF, which is reported to be 104.6 J g^{-1} [71, 72] and ΔH_m melting peak temperature of the polymeric samples. The results are presented in Table 3.

$BaZrO_3$ nanoparticles in PVDF matrix modified the crystalline structure due to the formation of more and more β phases. This means the polymer chain interweaves with nanofillers and forms nucleolus. The polymer nucleation may become a multi-stage process due to the involvement of a wide range of relaxation processes. The $BaZrO_3$ in PVDF matrix modified the crystallization and polarization behavior of PVDF by means of nucleation effect and crystal growth. The possibility of molecular stacking of PVDF molecules cannot ignore. The molecular stacking increases the crystallization rate, and finally, crystallinity. Since the crystallization process is time-dependent, lower cooling rates give the macromolecular chains enough time-to-change conformation. This led to the less energetic arrangement and formation of crystallites at higher temperatures. This mechanism is consistent with the work reported in literature [73, 74].

Conclusions

In addition of $BaZrO_3$ nanoparticles in the PVDF matrix enhances the β-phase by nucleation process. We conclude that electrochemical interaction and nucleation effect in PVDF nanocomposites is the driving force of electroactive and thermal properties. The formation of nanocomposites enhances the charge generation capability and d_{33} coefficient. As a result, the area of the P-E loop increases with the increasing concentration of $BaZrO_3$ nanoparticles. It showed the improvement of piezoelectric properties explores the possible applications in the field of biomedical, robotics, membrane, and sensor. The results of the DSC showed the notable improvements in glass transition temperature, enthalpy, melting point, crystallinity, etc., by incorporation of $BaTiO_3$ nanoparticles in PVDF matrix. The main reason of improvement is the interaction between nanoparticles surfaces and PVDF chains may reform the crystalline structure of PVDF. The enthalpy is considered to support the crystallization and nucleation effect.

Acknowledgements Financial assistance from Aeronautics R&D Board, DRDO New Delhi-110 011 India (Letter no. ARDB/01 11051902l/M/l), is gratefully acknowledged). We are also thankful to Director IUAC, New Delhi for providing characterization facilities. One of the authors Rohan Sagar acknowledges the University Grant Commission (UGC), New Delhi (India) for a providing research fellowship (RGNF-2017-18-SC-UTT-29088).

Declarations

Conflict of interest No potential conflict of interest was reported by the authors.

References

1. Kim M-S, Ahn H-R, Lee S, Kim C, Kim Y-J. A dome-shaped piezoelectric tactile sensor arrays fabricated by an air inflation technique. Sens Actuators A Phys. 2014;212:151–8.
2. Beringer LT, Xu X, Shih W, Shih WH, Schauer CL. Optimization of an electrospun PVDF-TrFe fiber sensor platform for biological applications. Sens Actuators A. 2015;222:293–300.
3. Mei H, Wang R, Feng J, Xia Y, Zhang T. A flexible pressure-sensitive array based on soft substrate. Sens Actuators A. 2015;222:80–6.
4. Cho Y, Park JB, Kim BS, Lee J, Hong WK, Park IK, Jang JE, Sohn JI, Cha S, Kim JM. Enhanced energy harvesting based on surface morphology engineering of P(VDF-TrFE) film. Nano Energy. 2015;16:524–32.
5. Zampetti E, Macagnano A. Flexible piezoelectric transducer based on electrospun PVDF nanofibers for sensing applications. Procedia Eng. 2014;87:1509–12.
6. Bayramol DV, Soin N, Shah T, Siores E, Matsouka D, Vassiliadis S. Energy harvesting smart textiles. Blacksburg: Springer; 2017.
7. Lang C, Fang J, Shao H, Ding X, Lin T. High-sensitivity acoustic sensors from nanofibre webs. Nat Commun. 2016;7:11108.
8. Priya S, Song HC, Zhou Y, Varghese R. A review on piezoelectric energy harvesting: materials, methods, and circuits. J Energy Harvest Syst. 2017;4:3.
9. Chen C, Bai Z, Cao Y, Dong M, Jiang K, Zhou Y. Enhanced piezoelectric performance of $BiCl_3$/PVDF nanofibers-based nanogenerators. Compos Sci Technol. 2020;192:108100.
10. Singh V, Singh B. Fabrication of PVDF-transition metal dichalcogenides based flexible piezoelectric nanogenerator for energy harvesting applications. Mater Today Proc. 2020;28:282–5.
11. Song L, Huang Q, Huang Y, Bi R, Xiao C. An electro-thermal braid-reinforced PVDF hollow fiber membrane for vacuum membrane distillation. J Membr Sci. 2019;591:117359.
12. Al-Osaimi J, Al-Hosiny N, Abdallah S, Badawi A. Characterization of optical, thermal and electrical properties of SWCNTs/PMMA nanocomposite films. Iran Polym J Engl Ed. 2014;23:437–43.
13. Badawi A, Ahmed EM, Mostafa NY, Alomairy SE. Enhancement of the optical and mechanical properties of chitosan using Fe_2O_3 nanoparticles. J Mater Sci Mater Electron. 2017;28:10877–84.
14. Badawi A, Alharthi SS, Mostafa NY, Althobaiti MG, Altalhi T. Effect of carbon quantum dots on the optical and electrical properties of polyvinylidene fluoride polymer for optoelectronic applications. Appl Phys A. 2019;125:858.
15. Indolia AP, Gaur MS. Investigation of structural and thermal characteristics of PVDF/ZnO nanocomposites. J Therm Anal Calorim. 2012;113(2):821–30.
16. Suma GR, Subramani NK, Shilpa KN, Sachhidananda S, Satyanarayana SV. Effect of $Ce_{0.5}Zr_{0.5}O_2$ nano fillers on structural and optical behaviors of poly(vinyl alcohol). J Mater Sci Mater Electron. 2017;28:10707–14.
17. Bai Y, Cheng ZY, Zhang QM. High-dielectric-constant ceramic-powder polymer composites. Appl Phys Lett. 2000;76:3804.
18. Arbatti M, Shan X, Cheng ZY. Ceramic–polymer composites with high dielectric constant. Adv Mater. 2007;19:1369–72.
19. Khatun F, Thakur P, Hoque NA, Kool A, Roy S, Biswas P, Bagchi B, Das S. In situ synthesized electroactive and large dielectric

BaF_2/PVDF nanocomposite film for superior and highly durable self-charged hybrid photo-power cell. Energy Convers Manag. 2018;171:1083–92.

20. Dutta B, Kar E, Bose N, Mukherjee S. Significant enhancement of the electroactive β-phase of PVDF by incorporating hydrothermally synthesized copper oxide nanoparticles. RSC Adv. 2015;5:105422–34.
21. Dutta B, Kar E, Bose N, Mukherjee S. Smart, lightweight, flexible NiO/poly(vinylidene flouride) nanocomposites film with significantly enhanced dielectric, piezoelectric and EMI shielding properties. J Polym Res. 2017;24:220.
22. Yu S, Zheng W, Yu W, Zhang Y, Jiang Q, Zhao Z. Formation mechanism of β- phase in PVDF/CNT composite prepared by the sonication method. Macromolecules. 2009;42:8870–4.
23. Gaur MS, Singh PK, Ali A, Singh R. Thermally stimulated discharge current (TSDC) characteristics in β-phase PVDF–BaTiO3 nanocomposites. J Therm Anal Calorim. 2014;117(3):1407–17.
24. Kar E, Bose N, Das S, Mukherjee N, Mukherjee S. Temperature dependent dielectric properties of self-standing and flexible poly(vinylidene fluoride) films infused with Er^{3+} doped GeO_2 and SiO_2 nanoparticles. J Appl Polym Sci. 2016;133:44016.
25. Mohanty HS, Kumar A, Kulriya PK, Thomas R, Pradhan DK. Dielectric/ferroelectric properties of ferroelectric ceramic dispersed poly (vinylidene fluoride) with enhanced β-phase formation. Mater Chem Phys. 2019;230:221–30.
26. Uchino K. Advanced piezoelectric materials: science and technology. Philadelphia: Wood head Publishing; 2010.
27. Cai E, Liu Q, Zhou S, Zhu Y, Xue A. Structure, piezoelectric, dielectric and ferroelectric properties of lead-free (1–x)($Ba_{0.85}$ $Ca_{0.15}$)($Ti_{0.93}$ $Zr_{0.07}$)O3–x($Bi_{0.5}$ $K_{0.5}$)TiO_3 ceramics. J Alloys Compd. 2017;726:1168–78.
28. Mayeen A, Kala MS, Sunija S, Rouxel D, Bhowmik RN, Thomas S, Kalarikkal N. Flexible dopamine-functionalized $BaTiO_3$/ $BaTiZrO_3$/$BaZrO_3$-PVDF ferroelectric nanofibers for electrical energy storage. J Alloys Compd. 2020;837:155492.
29. Huaying L, Hern K. Thermal degradation and kinetic analysis of PVDF/modified MMT nanocomposite membranes. Desalination. 2008;234:9–15.
30. Bertini F, Canetti M, Audisio G, Costa G, Falqui L. Characterization and thermal degradation of propylene-montmorillonite nanocomposites. Polym Degrad Stab. 2006;91:600–5.
31. Dobkowski Z. Thermal analysis techniques for characterization of polymer materials. Polym Degrad Stab. 2006;91:488–93.
32. Lopes A, Costa CM, Tavares C, Neves I, Lanceros MS. Nucleation of the electroactive phase and enhancement of the optical transparency in low filler content poly(vinylidene)/clay nanocomposites. J Phys Chem C. 2011;115:18076–82.
33. Martins P, Lopes A, Lanceros MS. Electroactive phases of poly(vinylidene fluoride): determination, processing and applications. Prog Polym Sci. 2014;39:683–706.
34. Sajkiewicz P, Wasiak A, Gocłowski Z. Phase transitions during stretching of poly(vinylidene fluoride). Eur Polym. 1999;35:423–9.
35. Huang Li X, Yang C, Cheng Y. Thermal reaction properties of aluminum/copper (II) oxide/poly(vinylidene fluoride) nanocomposite. J Therm Anal Calorim. 2015;124(2):899–907.
36. Boccaccio T, Bottino A, Capannelli G, Piaggio P. Characterization of PVDF membranes by vibrational spectroscopy. J Membr Sci. 2002;210:315–29.
37. Imamura R, Silva A, Gregorio R. Phase transformation induced in poly(vinylidene fluoride) by stretching. J Appl Polym Sci. 2008;110:3242–6.
38. Sagar R, Gaur SS, Gaur MS. Effect of $BaZrO_3$ nanoparticles on pyroelectric properties of polyvinylidene fluoride (PVDF). J Ther Anal Calorim. 2016;128:1235–9.
39. Sagar R, Gaur MS, Rogachev AA. Piezoelectric and pyroelectric properties of ceramic nanoparticles-based nanostructured PVDF/ PVC blend nanocomposites. J Therm Analys Calorim. 2020. https://doi.org/10.1007/s10973-020-09979-z.
40. Kumar R, Ali SA, Mahur AK, Virk HS, Singh F, Khan SA, Avasthi DK, Prasad R. Study of optical band gap and carbonaceous clusters in swift heavy ion irradiated polymers with UV–vis spectroscopy science direct. Nucl Instrum Meth Phys Res B. 2008;266:1788–92.
41. Kim H, Baik DH, Gyu Y. Structures, electrical, and dielectric properties of PVDF-based nanocomposite films reinforced with neat multi-walled carbon nanotube. Macromol Res. 2012;20:920–7.
42. Guirguis OW, Manel TH. Optical study of poly (vinyl alcohol)/hydroxypropyl methylcellulose blends. J Mater Sci. 2011;46:5775–89.
43. Tsai FC, Chang CC, Liu LC, Chen WC, Jenekhe SA. New thiophene-linked conjugated poly(azomethine)s: theoretical electronic structure. Synthes Prop Macrmol. 2005;38:1958.
44. Baig U, Gondal MA, Ilyas AM, Sanagi MM. Band gap engineered polymeric-inorganic nanocomposite catalysts: synthesis, isothermal stability, photocatalytic activity and photovoltaic performance. J Mater Sci Technol. 2017;33:547–57.
45. Ibrahim S, Ahmad R, Joha MR. Conductivity and optical studies of plasticized solid polymer electrolytes doped with carbon nanotube. J Chemilumi. 2012;132:147–52.
46. Ammar AH, Farag AAM, Abo-Ghazala MS. Influence of Sb addition on the structural and optical characteristics of thermally vacuum evaporated Sb x Se 1–x thin films. J Alloy Compd. 2017;694:752–60.
47. Kumar R, Singh P. UV–visible and infrared spectroscopic studies of Li3+ and C5+ irradiated PADC polymer. Result Phys. 2013;3:122–8.
48. Miodyńska M, Bajorowicz B, Mazierski P, Lisowski W, Klimczuk T, Winiarski MJ. Preparation and photocatalytic properties of $BaZrO_3$ and $SrZrO_3$ modified with Cu_2 O/Bi_2O_3 quantum dots. Solid State Sci. 2017;74:13–23.
49. Anagnostopoulos G, Androulidakis C, Koukaras E, Tsoukleri GN. Stress transfer mechanisms at the submicron level for graphene/ polymer systems. Appl Mater Interface. 2015;7:4216–23.
50. Colomban P. Understanding the nano—and macromechanical behaviour, the failure and fatigue mechanisms of advanced and natural polymer fibres by Raman/IR microspectrometry. Adv Nat Sci Nanosci Nanotechnol. 2013;4:13001.
51. Lovinger AJ. Ferroelectric polymers. Science. 1983;220:1115–21.
52. Lando JB, Peterlin A. Nuclear magnetic resonance and x-ray determination of the structure of poly(vinylidene fluoride). J Poly Sci Part A. 1966;4:941–51.
53. Scheinbeim J, Nakafuku C, Pae KD. High-pressure crystallization of poly(vinylidene fluoride). J Appl Phy. 1979;50:4399–405.
54. Chen S, Yao K, Tay FEH, Liow CL. Ferroelectric poly(vinylidene fluoride) thin films on Si substrate with the β phase promoted by hydrated magnesium nitrate. J Appl Phys. 2007;102:104108.
55. Lopes AC, Costa CM, Tavares CJ. Nucleation of the electroactive γ phase and enhancement of the optical transparency in low filler content Poly(vinylidene)/Clay Nanocomposites. J Phys Chem C. 2011;115:18076–82.
56. Gomes J, Nunes JS, Sencadas V. Influence of the β-phase content and degree of crystallinity on the piezo- and ferroelectric properties of poly(vinylidene fluoride). Smart Mater Struct. 2010;19:65010–65010.
57. Rahul N, Somasekhara RT. Self-powered flexible piezoelectric nanogenerator made of poly (vinylidene fluoride)/Zirconium oxide nanocomposites. Mater Res Express. 2019;6:115330.
58. Mohanty HS, Kumar A, Kulriya PK, Thomas R, Pradhan DK. Dielectric/ferroelectric properties of ferroelectric ceramic

dispersed poly (vinylidene fluoride) with enhanced β-phase formation. Mater Chem Phys. 2019;230:221–30.

59. Elashmawi IS, Gaabour L. Raman, morphology and electrical behavior of nanocomposites based on PEO/PVDF with multi-walled carbon nanotubes. Result Phys. 2015;5:105–10.
60. Lederle F, Härter C, Beuermann S. Inducing *β* phase crystallinity of PVDF homopolymer, blends and block copolymers by anti-solvent crystallization. J Fluor Chem. 2020;12:109510–22.
61. Qing G, Cao GZ, Shen Y. Measurements of piezoelectric coefficient d_{33} of lead zirconate titanate thin films using a mini force hammer. J Vib Acoust. 2013;135:011003–11.
62. You Y, Huang X, Pu Z, Jia K, Liu X. Enhanced crystallinity, mechanical and dielectric properties of biphenyl polyarylene ether nitriles by unidirectional hot-stretching. J Polym Res. 2015;22:221.
63. You Y, Wei R, Yang R, Yang W, Hua X, Liu X. Crystallization behaviors of polyarylene ether nitrile filled in multi-walled carbon nanotubes. RSC Adv. 2016;6:70877–83.
64. Du YouY, X, Mao H, Tang X, Wei R, Liu X. Synergistic enhancement ofmechanical, crystalline and dielectric properties of polyarylene ether nitrile-based nanocomposites by unidirectional hot stretching-quenching. Polym Int. 2017;66:1151–8.
65. Agarwal H, Yadav S, Jaiswar G. Effect of nanoclay and barium sulfate nanoparticles on the thermal and morphological properties of polyvinylidene fluoride nanocomposites. J Therm Anal Calorim. 2017;129(3):1471–9.
66. Kao KC. Dielectric phenomena in. Solids1st ed. San Diego: Elsevier Academic Press,; 2004. p. 579.
67. Wang TT, Herbert JM, Glass AM. The applications of ferroelectric polymers. 1st ed. New York: Blackie; 1988.
68. Lines M, Glass A. Principles and applications of ferroelectrics and related materials. Oxford: Oxford Clarendon Press; 1977.
69. Dang DM, Zhou T, Yao SH. Advanced calcium copper titanate/polyimide functional hybrid films with high dielectric permittivity. Adv Mater. 2009;21:2077–82.
70. Prakash BS, Varma KBR. Dielectric behavior of CCTO/epoxy and Al-CCTO/epoxy composites. Compos Sci Tech. 2007;67:2363–8.
71. Srivastava A, Maiti P, Parkash O. Mechanical and dielectric properties of $CaCu_3Ti_4O_{12}$ and La doped $CaCu_3Ti_4O_{12}$ poly(vinylidene fluoride) composites. Compos Sci Tech. 2014;93:83–9.
72. Srivastava A, Jana KK, Parkash O. Mechanical and dielectric behaviour of $CaCu_3Ti_4O_{12}$ and Nb doped $CaCu_3Ti_4O_{12}$ poly(vinylidene fluoride) composites. J Compos. 2014;52:769379–89.
73. Sajkiewicz P, Wasiak A. Phase transitions during stretching of poly (vinylidene fluoride). Eur Polym. 1999;35:423–9.
74. Neidh FM, Beaume F. Structural evolution of PVDF during storage or annealing. Polymer. 2004;45:1679–88.

Hindustan College of Science and Technology
Farah-Mathura
(AICTE approved & affiliated to AKTU)

Project: III

Development of test methods for control of heavy metals in water for environmental monitoring and prevention of health risks

Sanctioned Agency:

(DST New Delhi)

Sanctioned letter

Government of India
Ministry of Science and Technology
Department of Science & Technology
(International Bilateral Cooperation Division)

Technology Bhavan, New Mehraulli Road
New Delhi-110016
Date: 13.08.2019

DST/INT/RUS/RSF/P-28/G

ORDER

Subject: Implementation of **Indo-Russian** Joint project entitled: "**Development of test methods for control of heavy metals in water for environmental monitoring and prevention of health risks**" Coordinated by **Prof. Mulayam Singh Gaur**, Hindustan College of Science and Technology-Farah, Mathura - regarding.

Sanction of the President is hereby accorded for incurring an expenditure not exceeding **Rs. 31,81,672/- (Rupees Thirty One Lakh Eighty One Thousand Six Hundred Seventy Two Only)** for implementation of the Indo-Russian joint project entitled "Development of test methods for control of heavy metals in water for environmental monitoring and prevention of health risks" Coordinated **Prof. Mulayam Singh Gaur**, Hindustan College of Science and Technology-Farah, Mathura with the Russian partner **Dr. Anna N. Berlina**, Russian Academy of Sciences, Moscow, Russia for a total duration of Two years from the date of issue of the Sanction Order. The detailed breakup of the grant for General as well as Capital Components are given below:-

General Component	:	**Rs. 31,81,672/-**
Capital Component	:	Rs. **7,50,000/-**

2. As per the terms and conditions, agreed by both side, under the project the sending side will bear all the cost related to the International air travel, medical insurance, visa charges, accommodation and local travels of the visiting scientist. The break-up of approved expenditure is as indicated below :

Item of Expenditure	**Amount**		
	First year	**Second year**	**Total**
1. **Equipment** (UV-Visspectrophotometer)	Rs. 7,50,000	Nil	Rs. 7,50,000
2. **Consumables**	Rs. 1,00,000	Rs 1,00,000	Rs 2,00,000
3. **Contingency**	Rs 50,000	Rs 50,000	Rs 1,00,000
4. **Exchange Visits** (two visits each year, as calculated in para 3 below) For visit of Indian scientists to Russia	Rs. 5,76,400	Rs. 5,76,400	Rs 11,52,800
5. (i) JRF – 1. @ Rs. 31,000 pm + 8% HRA	Rs. 4,01,760	Rs.4,01,760	Rs. 8,03,520
Year wise Cost	18,78,160/-	11,28,160/-	30,06,320/-
Overhead on 1, 2 & 4 @ 10%	1,25,176/-	50,176/-	1,75,352/-
Total year wise cost	20,03,336/-	11,78,336/-	31,81,672/-
Grand Total	Rs. 31,81,672/-		

Director
Hindustan College of
Science & Technology
FARAH (MATHURA)

3. Sanction of the President is hereby accorded for release of 1st instalment amounting of **Rs. 12,53,336/- (Rupees Twelve Lakh Fifty-Three Thousand Three Hundred Thirty-Six Only)** to the grantee Institute. The amount of grant will drawn by the Drawing and Disbursing Officer, DST and will be disbursed to **Hindustan College of Science and Technology-Farah, Mathura.** The bank details for electronic transfer of funds through RTGS are given below:-

Account Holders name/ designation	Hindustan College of Science and Technology, Mathura
Name of Bank	Punjab National Bank
Bank Account Number	1841002100004382
IFSC Code	PUNB0184100
E-Mail	mulayamgaur@rediffmail.com

Condition for placing of grant amount :

4. The grantee organisation will maintain separate audited account for the project and the entire amount of grant will be kept in an interest bearing account. For Grants released during F.Y. 2017-18 and onwards, all interests and other earnings against released Grant shall be remitted to Consolidated Fund of India (through Non-Tax Receipt Portal (NTRP), i.e. www.bharatkosh.gov.in), immediately after finalisation of accounts, as it shall not be adjusted towards future release of Grant. A certificate to this effect shall have to be submitted along with Statement of Expenditure / Utilisation Certificate for considering subsequent release of Grant/ Closure of Project accounts.

Conditions for submission of SE/UC and Progress report:

5. (a) the grantee organisation will furnish to the Department of Science & Technology, financial year wise Utilization Certificate (UC) in the proforma prescribed as per GFR 2017 and audited statement of expenditure (SE) along with up to date progress report at the end of each financial year duly reflecting the interest earned / accrued on the grants received under the project. This is also subject to the condition of submission of the final statement of expenditure, utilization certificate and project completion report within one year from the scheduled date of completion of the project.

(b) While submitting Utilisation Certificate/Statement of Expenditure, the organization has to ensure submission of supporting documentary evidences with regard to purchase of equipment/capital assets as per the provisions of GFR 2017. Subsequent release of grants under the project shall be considered only on receipt of the said documents.

(c) a transparent procurement procedure in line with the Provisions of General Financial Rules 2017 will be followed by the Institute/ Organisation under the appropriate rules of the grantee 2organization while procuring capital assets sanctioned for the above mentioned project and a certificate to this effect will be submitted by the Grantee 2organization immediately on receipt of the grant;

6. The grantee organisation will have to enter & upload the Utilization Certificate in the PFMS portal besides sending it in physical form to this Division. The subsequent/final instalment will be released only after confirmation of the acceptance of the UC by the Division and entry of previous Utilization Certificate in the PFMS.

7. In the event grant has been released under capital head through separate sanction order under the same project for purchase of equipment(s), separate SE/UC has to be furnished for the released Capital head grant.

Conditions of Assets (if any) :

8.(a) DST reserves sole rights on the assets created out of grants. Assets acquired wholly or substantially out of government grants (except those declared as obsolete and unserviceable or condemned in accordance with the procedure laid down in GFR 2017), shall not be disposed of without obtaining the prior approval of DST.

Director
Hindustan College of
Science & Technology
FARAH (MATHURA)

(b) The equipment/instrument shall have to be purchased within twelve months from the date of release of the capital grant. Fresh permission shall have to be sought from DST, in the event, the Institute fails to purchase the equipment/instrument within the prescribed period of twelve months from the date of release of sanctioned amount.

(c) As per the Rule of GFR 2017, it is mandatory for the grantee organization to purchase the equipment through the Government e-Marketplace (GeM), to the extant available there as the project involves government funding.

Conditions for International Visits :

9. All project related visits to be undertaken by the Scientists from either side in connection with the implementation of the project shall require prior approval from this Department separately on a case to case basis before any expenditure is incurred in this regard.

10. As per MoF instructions, it has been decided that in all cases of air travel, both domestic and international, where the Government of India bears the cost of air passage, the officials concerned may travel only by Air India. For travel to stations not connected by Air India, the officials may travel by Air India to the hub/point closest to their eventual destination, beyond which they may utilize the services of another airline which should also preferable be an alliance partner of Air India. Tickets are to be booked in terms of guidelines issued under DoE OM No. 19024/22/2017-E.IV dated 19th July, 2017

Other Conditions:

11. GI should also follow Rule 230(17) of GFR, 2017 concerning reservation of SC/ST/OBC, if applicable.

12. The account of the grantee organisation shall be open to inspection by the sanctioning authority and audit (both by C&AG of India and Internal Audit by the Principal Accounts Office of the DST), whenever the organisation is called upon to do so, as laid down under Rule 236(1) of General Financial Rules 2017.

13. Due acknowledgement of technical support / financial assistance resulting from this project grant should mandatorily be highlighted by the grantee organisation in bold letters in all publications / media releases as well as in the opening paragraphs of their Annual Reports during and after the completion of the project.

14. In case the scheme provides for payment of honorarium / remuneration / fellowship / scholarship to the PI, a para may suitably be incorporated in the DSO to the effect that "PI is not drawing any emoluments/ salary/ fellowship from any other project either supported by DST or by any other funding agency.

15. **Failure to comply with the terms and conditions of the sanction order will entail full refund with interest in terms of Rule 231 (2) of GFR 2017.**

16. The expenditure involved is debitable to Demand No.86, Department of Science & Technology for the year 2019-20:

3425	:	Other Scientific Research (Major Head)
60	:	Others
60.798	:	International Cooperation (Minor Head)
14	:	Research & Development
14.00.31	:	Grants-in-aid General for the year 2019-20 (**Previous** : ICD-3425.60.798.12.00.31)

17. This sanction order being 1st instalment for implementation of this project, no SE/UC is due from the grantee institution against this project.

18. This issues with the concurrence of IFD vide their concurrence Dy. No. **C/2165/IFD 2019-20 dated 13.08.2019.**

Director
Hindustan College of
Science & Technology
FARAH (MATHURA)

19. As per Rule 234 of GFR 2017, this sanction has been entered at S. No 219...in the register of grants maintained in the Division.

(Rajiv Kumar)
Scientist 'E'

To,

The Pay & Accounts Officer,
Department of Science & Technology,
New Delhi-110016

Copy to:

1. Office of the Principal Director of Audit, AGCR Bldg., IP Estate, New Delhi-110002
2. Cash Section (3 copies), DST
3. I.F. Division/Accounts Section, DST
4. Sanction Folder
5. Project File.
6. **Prof. Mulayam Singh Gaur,** Hindustan College of Science and Technology-Farah, Mathura
7. **Director / Registrar,** Hindustan College of Science and Technology-Farah, Mathura
8. **Finance Officer,** Hindustan College of Science and Technology-Farah, Mathura
9. **Unique Id of VO/NGO : UP/2017/0116810**

(Rajiv Kumar)
Scientist 'E'

Annexure – I

Break up of expenditure on each visit of Indian Scientists visiting collaborative institute is calculated broadly as below: (All conversion US $ 1= Rs. 70)

1) International Fare Delhi – Moscow - Delhi i. by excursion economy class	Rs. 80,000
2) Medical Insurance (Silver Class)	Rs. 4,000
3) Domestic Travel related to visit (Mathura-Delhi-Back)	Rs. 10,000
4) Visa Fee (as per actual)	Rs. 8,000
5) Accommodation in Moscow @US $ 125 14 days	Rs. 1,22,500
6) Cash Allowance @ US $ 40 for 14 days	Rs. 39,200
7) Transport Allowance @ Us $ 25 for 14 days	Rs. 24,500
Total	**Rs. 2,88,200/-**

(Rajiv Kumar)
Scientist 'E'

Director
Hindustan College of
Science & Technology
FARAH (MATHURA)

Government of India
Ministry of Science and Technology
Department of Science & Technology
(International Bilateral Cooperation Division)

Technology Bhavan, New Mehraulli Road
New Delhi-110016
Date: 13-08-19

DST/INT/RUS/RSF/P-28/C

ORDER

Subject: Implementation of Indo-Russian Joint project entitled: **"Development of test methods for control of heavy metals in water for environmental monitoring and prevention of health risks"** Coordinated by **Prof. Mulayam Singh Gaur,** Hindustan College of Science and Technology-Farah, Mathura - regarding.

In continuation to this Department's sanction order of even number dated 13-08-19. Sanction of the President is also accorded to the release of an amount of **Rs. 7,50,000/- (Rupees Seven Lakh Fifty Thousand Only)** to **Hindustan College of Science and Technology-Farah, Mathura** for purchase of equipment. The organization should utilize the released funds for procurement during the first year for implementation of the said project during 2019-20.

2. This is being a new project to this organization; there is no question of getting UC/SE's for the earlier grant of the aforesaid proposal.

3. The expenditure involved is debitable to Demand No.86, Department of Science & Technology for the year 2019-20:

3425 : Other Scientific Research (Major Head)
60 : Others
60.798 : International Cooperation (Minor Head)
14 : S & T Cooperation with Other countries
14.00.35 : Grants Creation of Capital Assets during the current financial year 2019-20
(Previous : ICD-3425.60.798.12.00.35)

4. An amount of **Rs. 7,50,000/- (Rupees Seven Lakh Fifty Thousand Only)** will be disbursed by means of electronic transfer (E-transfer) in favour Hindustan College of Science and Technology-Farah, Mathura as indicated below:-

Account Holders name/ designation	Hindustan College of Science and Technology, Mathura
Name of Bank	Punjab National Bank
Bank Account Number	1841002100004382
IFSC Code	PUNB0184100
E-Mail	mulayamgaur@rediffmail.com

5. As per rule 211 (i) of GFR the accounts of project shall be open to inspection by sanctioning authority/ audit whenever the institute is called upon to do so.

6. Grant-in-aid will be utilized for scientific research only.

Director
Hindustan College of
Science & Technology
FARAH (MATHURA)

7. Assets acquired wholly or substantially out of government grants except those declared as obsolete and unserviceable or condemned in accordance with the procedure laid down in GFR's shall not be disposed of without obtaining the prior approval of DST.

8. Grant released are proprietary in nature and DST reserves proprietary rights on the assts created out of grants.

9. As per the Rule of GFR 2017, it is mandatory for the grantee organization to purchase the equipment through the Government e-Marketplace (GeM), to the extant available there as the project involves government funding.

10. This sanction is subject to submission of Utilization Certificate (UC) and audited statement of expenditure (SE) along with up to date progress report at the end of each financial year for the grants already received under the project and seeking specific approval of this Department for carry forward of under the project. It may please be noted that the agencies will have to enter and upload the UCs in PFMS portal besides sending it in physical form as per instructions attached.

11. The grantee organisation will maintain separate audited account for the project and the entire amount of grant will be kept in an interest bearing account. For Grants released during F.Y. 2017-18 and onwards, all interest or other earnings against Grant shall be remitted to the Consolidated Fund of India (through Non-Tax Receipt Portal (NTRP), i.e. www.bharatkosh.gov.in), immediately after finalization of the accounts, as it shall not be allowed to be adjusted against future releases of grant. **A certificate to this effect shall have to be submitted along with Statement of Expenditure / Utilisation Certificate for considering subsequent release of Grant/ closure of Project accounts.**

12. The grant sanctioned/ released is for the specific project sanctioned and portion of the grant. which the grantee fails to utilize for the purpose for which the grant is sanctioned will be recovered along with the penal interest of 10% per annum.

13. In the event of the grantee failing to comply with the conditions or committing breach of the conditions of the bond the authorized signatories to the bond and all the members of the Executive committee shall be jointly and severally liable to refund to the President of India, the whole or a part of the grant with interest at 10% per annum thereon or the sum specified in the bond.

14. This sanction order being 1st instalment for implementation of this project, no SE/UC is due from the grantee institution against this project.

15. This issues with the concurrence of IFD vide their concurrence Dy. No. **C/2166/IFD 2019-20 dated 13.08.2019.**

16. As per Rule 234 of GFR 2017, this sanction has been entered at S. No. ..10....in the register of grants maintained in the Division.

Director
Hindustan College of
Science & Technology
FARAH (MATHURA)

(Rajiv Kumar)
Scientist 'E'

To,

The Pay & Accounts Officer,
Department of Science & Technology,
New Delhi-110016

Copy to:

1. Office of the Principal Director of Audit, AGCR Bldg., IP Estate, New Delhi-110002
2. Cash Section (3 copies), DST
3. I.F. Division/Accounts Section, DST
4. **Prof. Mulayam Singh Gaur**, Hindustan College of Science and Technology-Farah, Mathura
5. Accounts officer, Hindustan College of Science and Technology-Farah, Mathura
6. Director / Registrar, Hindustan College of Science and Technology-Farah, Mathura
7. Sanction Folder
8. Project File.

(Rajiv Kumar)
Scientist 'E'

Director
Hindustan College of
Science & Technology
FARAH (MATHURA)

Hindustan College of Science and Technology
Farah-Mathura
(AICTE approved & affiliated to AKTU)

Project: III

Development of test methods for control of heavy metals in water for environmental monitoring and prevention of health risks

Sanctioned Agency:

(DST New Delhi)

Statement of Expenditure

Annexure-II

REQUEST FOR ANNUAL INSTALMENT WITH UP-TO-DATE STATEMENT OF EXPENDITURE

1. **Sanction Order No. and date:** DST/INT/RUS/P-28/C dated 13.08.2019
2. **Total Project Cost** : Development of test methods for control of heavy metals in water for environmental monitoring and prevention of health risk
3. **Revised Project Cost (if applicable)** : NA
4. Date of Commencement : 13.08.2019
5. Statement of Expenditure :
(Month wise expenditure incurred during current financial year)

Month & Year	Expenditure incurred/ Committed
01.04.2021 to 11.02.2022	Nil

6. Grant received in each year:

a. 1st Year : Rs. 7,50,000/-
b. 2nd Year : NA
c. 3rd Year : NA
d. Interest, if any: Rs. 13,393/- (FY 2019-20) + Rs.24,897/-(FY 2020-2021) + Rs. 23,364/- (FY 2021-2022) /- = Rs.61,654/- (Deposited)
e. Total (a+b+c+d): Rs. 8, 11,654/-

Statement of Expenditure

(to be submitted financial year wise i.e. DOS* to 31st March of that financial year say 2021-2022, (01.04.2021 to 11.02.2022)

Sr. No. (I)	Sanctioned Heads (II)	Funds Allocated (indicate sanctioned or revised) (III)	Expenditure Incurred Ist Year (*DOS to 31st March next year) (IV)	Expenditure Incurred IInd Year (1st April to 31st March next year) (V)	Expenditure Incurred IIIrd Year and so on (1st April to 31st March next year) (VI)	Total Expenditure IV+V+VI (VII)	Balance as on (date) (VIII) = III-(IV+V+VI)	Requirement of Funds up to 31st March next year	Remarks (if any)
1.	Equipments	Rs. 7,50,000/-	Nil	Nil	Nil	Nil	Rs. 7,50,000/-	Nil	
2	Interest Earned	Rs. 23,364/- FY(2021-22)							Rs. 23,364/- Refunded
3.	Total	Rs.7,50,000/-	Nil	Nil	Nil	Nil	Rs. 7, 50,000/-	Nil	Rs.7,50,000/- refunded back

Dr. M.S. Gaur

Name and Signature of Principal Investigator:
Date: 20.04.2022

Per Hindustan [illegible]

03/04/2022
Account Officer

Account officer (with seal)
PAWAN KUMAR GOYAL

Signature of Competent financial authority:
Date: CA Deepa Khanna.
M.No. 403317
FRN-013795C
21/04/2022

*DOS-Date of start of project

Note:Expenditure under the sanctioned heads, at any point of time, should not exceed funds allocated under that head, without prior approval of DST i.e. Figures in Column (VIII) should not exceed corresponding figures in Column (II).

1.Utilisation Certificate (Annexure III) for each financial year ending 31st March has to be enclosed along with request for carry forward permission to the next year.

Annexure-II

REQUEST FOR ANNUAL INSTALMENT WITH UP-TO-DATE STATEMENT OF EXPENDITURE

1. **Sanction Order No. and date:** DST/INT/RUS/P-28/G dated 13.08.2019
2. **Total Project Cost** : Development of test methods for control of heavy metals in water for environmental monitoring and prevention of health risk
3. **Revised Project Cost (if applicable)** : NA
4. Date of Commencement : 13.08.2019
5. Statement of Expenditure :
(Month wise expenditure incurred during current financial year)

Month & Year	Expenditure incurred/ Committed
01.04.20201to 11.02.2022	Rs.5,21,734/-

6. Grant received in each year:
a. 1st Year : Rs. 12,53,336/-
b. 2nd Year : Nil
c. 3rd Year : NA
d. Interest, if any: Rs. 21,808/- (FY 2019-20) + Rs 33,541 (FY 2020-2021) + Rs. 16,664/-(FY 2021-22) = Rs. 72,013/- (Deposited)
e. Total (a+b+c+d): Rs. 13,25.349/-

For Hindustan College of Science & Technology

Account Officer

Statement of Expenditure

(to be submitted financial year wise i.e. DOS* to 31st March of that financial year say 2021-2022 **(01.04.2021 to 11.02.2022)**

Sr. No. (I)	Sanctioned Heads (II)	Funds Allocated (indicate sanctioned or revised) (III)	Expenditure Incurred: Ist Year (*DOS to 31st March next year) (IV)	IInd Year (1st April to 31st March next year) (V)	IIIrd Year and so on (1st April to 31st March next year) (VI)	Total Expenditure IV+V+VI (VII)	Balance as on (date) (VIII) = III-(IV+V+VI)	Requirement of Funds up to 31st March next year	Remarks (if any)
1.	Consumables	Rs. 2,00000/-	Nil	Rs. 82,616/-	Nil	Rs. 82,616/-	Rs. 1,17,384/-	Nil	
	Contingency	Rs. 100000/-	Rs. 42,862/-	Rs. 25,305/-	Rs.24,617/-	Rs. 92,784/-	Rs. 7,216/-	Nil	
2.	Exchange Visit	Rs. 11,52,800/-	Nil	Nil	Nil	Nil	Rs. 11,52,800/-	Nil	
3	Manpower	Rs. 8,03,520/-	Rs. 32,364/-	Rs. 401760/-	Rs.3,68,280/	Rs. 8,02,404/-	Rs. 1,116/-	Nil	
3.	Overhead	Rs.1,75,352/-	Rs. 19,703/-	Nil	Rs.1,28, 837/-	Rs. 1,48,540/-	Rs. 26,812/-	Nil	
6	Interest Earned	Rs.16,664/- (FY 2021-22)							Rs.16,664/ Refunded
7.	Total	Rs. 24,31,672/-	Rs. 94,929/-	Rs.5,09681/-	Rs. 5,21,734/-	Rs. 11.26,344/-	Rs.13,05328 /-	Nil	Rs.1,26,992/- Refunded back

Name and Signature of Principal Investigator: Dr. Goyal
Date: 20.04.2022

Account officer (with seal)
(Pawan Kumar Goyal)
20/04/2022

Signature of Competent financial authority:
Date: CA Deepa Khanna
M.No. 403317
FRN-013795C
21/04/2022

*DOS-Date of start of project

Note:Expenditure under the sanctioned heads, at any point of time, should not exceed funds allocated under that head, without prior approval of DST i.e. Figures in Column (VIII) should not exceed corresponding figures in Column (II).

1.Utilisation Certificate (Annexure III) for each financial year ending 31st March has to be enclosed along with request for carry forward permission to the next year.

Hindustan College of Science and Technology
Farah-Mathura
(AICTE approved & affiliated to AKTU)

Project: III

Development of test methods for control of heavy metals in water for environmental monitoring and prevention of health risks

Sanctioned Agency:

(DST New Delhi)

Utilization Certificate

Annexure-III

UTILISATION CERTIFICATE (2 COPIES) FOR THE FINANCIAL YEAR – (ENDING 31ST MARCH)

1. **Title of the Project/ Scheme:** "Development of test methods for control of heavy metals in water for environmental monitoring and prevention of health risk"
2. **Name of the Institution:** Hindustan College of Science & Technology, Farah, Mathura-281122.
3. **Principal Investigator:** Dr. M. S. Gaur, Professor, Department of Physics
4. **Department of Science & Technology sanction order No & Date sanctioning the project:** DST/INT/RUS/RSF/ P-28/C dated 13.08.2019
5. **Head of account as given in the original sanction order:**

S. No.	Budget Head	Original sanction Amount (in Rs.)
1.	Equipment	7,50,000/-
Total		7,50,000/-

6. **Amount brought forward from the previous Financial year quoting DST letter no and date in which authority to carry forward the said amount was given :**
    - i. Amount: 7,50,000/-
    - ii. Letter No : DST/INT/RUS/RSF/ P-28/C
    - iii. Date : 03.02.2021
7. **Amount received during the financial year (Please give DST letter/order no and date):**
    - i. Amount : Nil
    - ii. Letter No. : Nil
    - iii. Date : Nil
8. **Interest earned:** Rs.23,364/- *(Deposited in Bharatkosh)*
9. **Total amount that was available for expenditure (excluding commitments) during the financial year (Sr. No. 6+7+8):** Rs. 7,73,364/-
10. **Actual Expenditure (excluding commitments) Incurred during the financial year (upto 31st March):** Rs. Nil
11. **Balance amount available at the end of the financial year:** Rs. 7, 50,000/-
12. **Unspent balance refunded, if any (please give details of cheque no etc.) :** Rs.7,50,000/- Deposited in BharatKosh
13. **Amount to be carried forward to the next financial year (if applicable):**
    - i. Amount :
    - ii. Letter No
    - iii. Date

UTILISATION CERTIFICATE

Certified that out of Rs. 7,50,000 /- of grants-in-aid sanctioned during the year 2019-2020 in favour of The Director, HCST, Farah, Mathura under this Ministry/ Department letter/ order No. DST/INT/RUS/P-28/C dated 13.08.2019 and Rs. Nil on account of unspent balance of the previous year, a sum of Rs.Nil has been utilised for the purpose of project for which it was sanctioned and that the balance of Rs. 7,50,000 /- is available for FY 2020-2021, a sum of Rs.Nil has been utilised for the purpose of project for which it was sanctioned and that the balance of Rs. 7,50,000 /-remaining will be adjusted towards the grants-in-aid payable during the FY 2021-2022, a sum of Rs.Nil has been utilised for the purpose of project for which it was sanctioned and that the balance of Rs. 7,50,000 /- is refunded back.

For Hindustan College of Science & Technology

Account Officer

Signature of PI   Signature of Director   Accounts Officer of the Institute

Date 05.04.2022   Date 05.04.2022   Date 05/04/2022

(To be filled in by DST)

Certify that I have satisfied that the conditions on which the grants-in-aid was sanctioned have been fulfilled/ are being fulfilled and that I have exercised the following checks to see that the money was actually utilized for the purpose for which it was sanctioned:-

Kinds of checks exercised.

1.
2.
3.
4.
5.

Signature:____________
Designation:____________
Date:____________

Annexure-III

UTILISATION CERTIFICATE (2 COPIES)
FOR THE FINANCIAL YEAR – (ENDING 31ST MARCH)

1. **Title of the Project/ Scheme:** "Development of test methods for control of heavy metals in water for environmental monitoring and prevention of health risk"
2. **Name of the Institution:** Hindustan College of Science & Technology, Farah, Mathura-281122.
3. **Principal Investigator:** Dr. M. S. Gaur, Professor, Department of Physics
4. **Department of Science & Technology sanction order No & Date sanctioning the project:** DST/INT/RUS/RSF/ P-28/G dated 13.08.2019
5. **Head of account as given in the original sanction order:**

S. No.	Budget Head	Original sanction Amount (in Rs.)
1.	Consumable	200000/-
2.	Contingency	100000/-
3.	Exchange visit	11,52,800/-
4	Manpower	8,03,520/-
5	Overhead	1,75,352
Total		24,31,672/-

6. **Amount brought forward from the previous Financial year quoting DST letter no and date in which authority to carry forward the said amount was given :**
   - i. Amount: 6,48,726/- available for FY 2021-22
   - ii. Letter No :
   - iii. Date :
7. **Amount received during the financial year (Please give DST letter/order no and date):**
   - i. Amount : Nil
   - ii. Letter No. : Nil
   - iii. Date : Nil
8. **Interest earned:** Rs. 16,664/- *(Deposited in Bharatkosh)*

9. **Total amount that was available for expenditure (excluding commitments) during the financial year (Sr. No. 6+7+8):** Rs. 6,48,726/- +Rs.16,664 (deposited)

10. **Actual Expenditure (excluding commitments) Incurred during the financial year (upto 31st March):** Rs. 5,21,734/-
11. **Balance amount available at the end of the financial year:** Rs. 1,26,992/-

12. **Unspent balance refunded, if any (please give details of cheque no etc.) :** 1,26,992/- deposited in BharatKosh
13. **Amount to be carried forward to the next financial year (if applicable):** NA
    - i. Amount :
    - ii. Letter No
    - iii. Date

Hindustan College of Science and Technology
Farah-Mathura
(AICTE approved & affiliated to AKTU)

Project: III

Development of test methods for control of heavy metals in water for environmental monitoring and prevention of health risks

Sanctioned Agency:

(DST New Delhi)

Project Outcomes (Publications)

List of Publications (Joint Project)

Entitled "Development of test methods for control of heavy metals in water for environmental monitoring and prevention of health risks"

Department of Science and Technology, New Delhi - Russian Academy of Sciences, Moscow, Russia

S.No.	Name of the author	Title of the article	Name of the journal	Year of publication	Issue	Pages	Impact factor	ISSN No.	*Web link*
1	Mamta Kushwah, Reetu Yadav, Mulayam Singh Gaur & Anna Nikolaevna Berlina	Copper nanoparticles-catalys ed reduction of methylene blue and high-sensitive chemiluminescence	International Journal of Environmental Analytical Chemistry	2021	4		1.7	0306-7319	https://doi.org/10.1080/03067319.2021.1893706
2	Reetu Yadav, Anna N Berlina, Anatoly V Zherdev, MS Gaur, BB Dzantiev	Rapid and selective electrochemical detection of pb 2 ions using aptamer-conjugated alloy nanoparticles,	SN Applied Sciences	2020	12	11	2.11	2523-3971	https://doi.org/10.1007/s42452-020-03840-6
3	Anna N. Berlina , Nadezhda S. Komova , Anatoly V. Zherdev , Mulayam S. Gaur and Boris B. Dzantiev	Colorimetric technique for antimony detection based on the use of gold nanoparticles conjugated with poly-A oligonucleotidenal	Applied Science	2019	9	13	2.6	2454-6194	https://doi.org/10.3390/app9224782

HINDUSTAN COLLEGE OF SCIENCE & TECHNOLOGY FARAH (MATHURA)

INTERNATIONAL JOURNAL OF ENVIRONMENTAL ANALYTICAL CHEMISTRY
https://doi.org/10.1080/03067319.2021.1893706

Taylor & Francis
Taylor & Francis Group

ARTICLE

Copper nanoparticles-catalysed reduction of methylene blue and high-sensitive chemiluminescence detection of mercury

Mamta Kushwah[a], Reetu Yadav[a], Mulayam Singh Gaur[a] and Anna Nikolaevna Berlina[b]

[a]Department of Physics, Hindustan College of Science and Technology, Mathura, UP, India; Affiliated to Department of Biotechnology, APJ Abdul Kalam Technical University, Lucknow, UP, India; [b]A.N. Bach Institute of Biochemistry, Research Center of Biotechnology of the Russian Academy of Sciences, Moscow, Russia

ABSTRACT

Mercury contamination is a significant public health and environmental problem; thus, detection of Hg^{2+} at sensitive levels is very important for environmental protection. In this study, we report a noble green synthesis of copper nanoparticles (CuNPs) using *Aegle marmelos* fruit peel extract, characterising their catalytic properties for reduction of methylene blue (MB) and sensitive chemiluminescence (CL) detection of Hg^{2+} ions based on this reaction. The transformation of MB dye in the presence of sodium borohydride ($NaBH_4$) was analysed by UV-visible spectroscopy, and kinetics of pseudo first order were found. Changes of CL were used for determination of Hg^{2+} in the presence of ethylenediamine. Interestingly, the formation of the ethylenediamine-CuNPs-Hg^{2+} complex increases the rate of H_2O_2-Luminol catalysis and the corresponding CL growth. The given effect was applied to determine the Hg^{2+} concentration in real water. The linear range of the calibration curve was from 0.01 pM to 1.0 pM of Hg^{2+}, and 0.0062 pM was the detection limit. The assay selectivity was confirmed using other toxic metallic ions. The proposed approach may be qualified as cost effective, eco-friendly, sensitive and selective.

ARTICLE HISTORY
Received 30 November 2020
Accepted 11 February 2021

KEYWORDS
Green synthesis; copper nanoparticles; methylene blue; chemiluminescence sensor; mercury detection

1. Introduction

Mercury (II), a highly toxic heavy metal released from both natural and anthropogenic sources, can cause serious damage to environmental safety and human health [1], including serious problems to the central nervous system and abnormal functioning in the brain, kidneys and bones [2]. The World Health Organization (WHO) recommended that the upper limit of mercury in drinking water should not be more than 6 ppb. Therefore, researchers aim to develop new, more sensitive techniques for the detection of Hg^{2+}. Several analytical methods have been established for Hg^{2+} detection, including colorimetry [3,4], fluorimetry [5], electrochemical sensors [1], atomic absorption spectrometry [6] and chemiluminescence (CL) [7,8].

CONTACT Mulayam Singh Gaur ✉ mulayamgaur@rediffmail.com

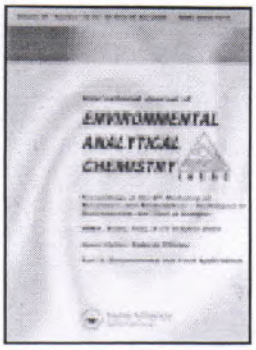

International Journal of Environmental Analytical Chemistry

ISSN: (Print) (Online) Journal homepage: https://www.tandfonline.com/loi/geac20

Copper nanoparticles-catalysed reduction of methylene blue and high-sensitive chemiluminescence detection of mercury

Mamta Kushwah, Reetu Yadav, Mulayam Singh Gaur & Anna Nikolaevna Berlina

To cite this article: Mamta Kushwah, Reetu Yadav, Mulayam Singh Gaur & Anna Nikolaevna Berlina (2021): Copper nanoparticles-catalysed reduction of methylene blue and high-sensitive chemiluminescence detection of mercury, International Journal of Environmental Analytical Chemistry, DOI: 10.1080/03067319.2021.1893706

To link to this article: https://doi.org/10.1080/03067319.2021.1893706

The synthesis of nanoparticles by chemical and physical methods is expansive, involves toxic chemicals and is not environmentally friendly. To overcome these problems, the biosynthesis of nanoparticles is important because it is easy to process, cost-effective and environmentally friendly. *Aegle marmelos* is a medicinal plant found in India that has many therapeutic properties. Different metal nanoparticles have been synthesised by *Aegle marmelos* plant extract. *Aegle marmelos* contains bioactive compounds like phenolics, alkaloids, pectins, flavonoids, tannins, coumarins, carotenoids and terpenoids. Due to this, *Aegle marmelos* plant extract can be used as a reducing or capping agent and as fuel [9–11]. For example, metal hexacyanoferrate nanoparticles were prepared using *Aegle marmelos* extract for decomposition of toxic dyes [12]. Green synthesis of nickel oxide nanoparticles was also realised using *Aegle marmelos* leaf extract.

The *Aegle marmelos* peel extract could be considered a useful reducing and capping agent for the synthesis of CuNPs. Many articles reported that CuNPs are suitable for degradation of various organic compounds and in wastewater treatment [13–18]. Sinha el al. reported 96% degradation of methylene blue (MB) by CuNPs synthesised using Labeorohita [19]. Similarly, Sebia et al. mentioned MB degradation by CuNPs synthesised using Nerium oleander [20].

Chemiluminescence is an advanced, highly sensitive analytical technique. Its advantages include a wide calibration range; no interference from background scattering light; the use of simple, cheap instruments and versatility for the analysis of a wide variety of analytes [3,21–23]. Xu et al. reported copper nanoclusters for Hg^{2+} detection using the CL technique; Cu nanoclusters can enhance the CL signal from the luminol–H_2O_2 system in an alkaline medium for assays of environmental water samples [24].

Uzu et al. reported high catalytic activity of new copper complex II for luminol in chemiluminescence. In the presence of ascorbic acid in an aqueous environment, new copper complex II reduced dissolved O_2 and oxidised the luminol with H_2O_2 to produce efficient CL signals [25,26]. The nanoparticle-based CL method has been used for mercuric ion detection. For example, Shengcai et al. demonstrated a method with a limit of detection (LOD) of 50 pM of mercuric ions; in this method, AuNPs triggered luminol-$AgNO_3$ and thymine-Hg^{2+}-thymine (T-Hg^{2+}-T) coordination bonds that enhance the CL reaction [27]. Most of the articles for Hg^{2+} detection are aptamer based. Hence, they are very sensitive but they are very costly, low selflife and not easy to handle the experiment.

Herein, we have developed a novel method using copper nanoparticles as a catalysing agent to amplify the CL signal for the detection of heavy metals. In this article, we have used ethylenediamine, luminol, H_2O_2 and CuNPs. Hg^{2+} can bind with the amino group of ethylenediamine, and free nanoparticles (NPs) enhance the CL signals [28]. Ethylenediamine has the ability to quench CuNPs/Hg^{2+}. It was assumed that the amino groups of ethylenediamine would capture CuNPs. CuNPs do not catalyse the luminol-H_2O_2; rather, they turn off the CL signals. However, in the presence of $Hg^{2+,}$ strong CL signals are created by the CuNPs-based catalysis. The schematic diagram (scheme 1) shows two variants. Firstly, in the absence of Hg^{2+}, CL signals are quenched by ethylenediamine. Secondly, in the presence of Hg^{2+}, CL signals are recovered and enhanced due to the specific binding of Hg^{2+} to the amino groups of ethylenediamine.

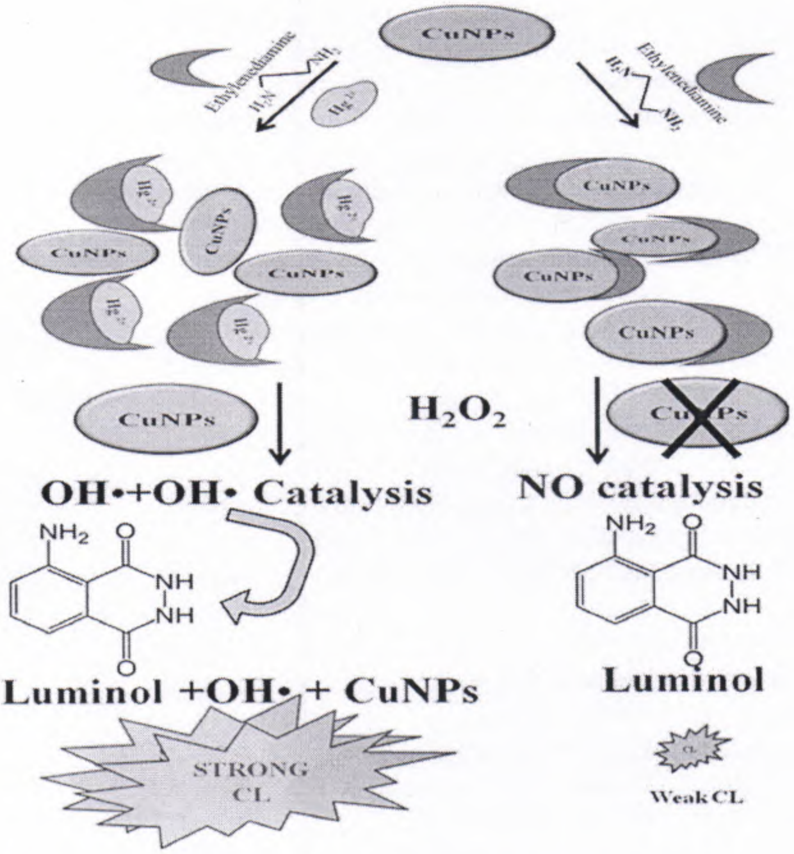

Scheme 1. Chemiluminescent detection of Hg^{2+} by CuNPs with ethylenediamine.

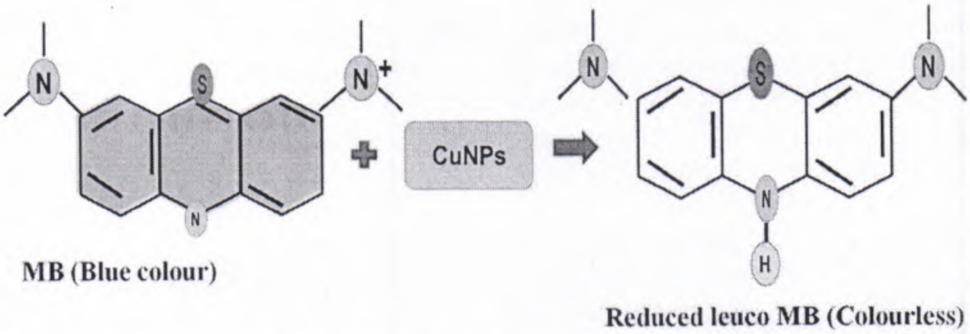

Scheme 2. Mechanism of MB reduction using CuNPs as catalyst.

This paper presents the green synthesis, characterisation, catalytic activity and Hg^{2+} detection ability of CuNPs.

2. Materials and methods

2.1. Materials

Ultrapuremili-Q water (18.2 MΩ cm^{-1}) was used throughout the study. Copper sulphate, MB, $Hg(NO_3)_2$ and luminol were purchased from Sigma Aldrich. Ethylenediamine, H_2O_2-, K_2HPO_4, KH_2PO_4 and metal salts including NiCl, LiCl, $CaCl_2$, $MgCl_2$, $MnCl_2$, $BaCl_2$, $CoCl_2$, $FeCl_2$, $FeCl_3$ and $CrCl_3$were of analytical reagent grade.

Then, 0.0177 g luminol were dissolved in 10 mL of 0.1 M NaOH for the preparation of luminol (10^{-2} M) stock in ice-cold conditions. Ethylenediamine stock solution (1 M) was prepared in 2 M HCl. A buffer solution of 40 mM K_2HPO_4-KH_2PO_4, pH 8.0, was prepared from stock solutions of salts.

2.2. Extract preparation by hard shell of A. marmelos fruit peel

The peel of the *A. marmelos* fruit was removed, dried at room temperature, washed by running water and then by distilled water, cut into small pieces and dried in an incubator at 37°C for 3–4 weeks. A fine powder was prepared by grinding small pieces of the peel. 10 gm of powder were dissolved in 200 mL of ethanol:water (1:1) and kept at 50°C for 10 min in a magnetic stirrer. The extract was filtered by Whatman filter paper-1 and stored at 2–8°C for further use.

2.3. Synthesis and characterisation of CuNPs

The CuNPs were obtained by green synthesis using *Aegle marmelos* fruit peel extract. The freshly prepared *Aegle marmelos* fruit peel extract (100 mL) was mixed with 50 mL of copper sulphate solution of 0.1 M under continuous stirring at 80°C for 1 h. A colour change was observed, indicating synthesis of CuNPs. The 52.4 mg/L of CuNPs were calculated.

CuNPs were characterised by UV-Visible spectra ranges from 200 to 800 nm by using a Varian CARY 300 UV-Vis spectrophotometer. The size, shape and crystallinity of nanoparticles were determined by Transmission Electron Microscopy (Jeol, Japan) and X-ray diffractometer (PANalyticalX'pert PRO, Netherlands). Stability of CuNPs was determined by performing zeta potential (ZEECOM ZC-3000, Japan). The FTIR spectra peak shift was used to determine the functional group of molecules by performing FTIR spectroscopy (Bruker-Tensor 27, Germany). A digital pH metre (CIRONIX) was used for pH measurements, and CL registration was recorded by a multifunctional microplate luminometer (Wellkang, UK).

2.4. Catalysis of MB dye using CuNPs

The catalytic activity of CuNPs was studied for the reduction of MB. $NaBH_4$ was used as an electron mediator. Initially, 5 mL of MB (1 mM) were taken into an Erlenmeyer flask. Then and 2.5 mL of $NaBH_4$ (10 mM) and 1 ml of CuNPs (0.1, 1.0 and 10 mg/mL) were added to the obtained solution. The final volume of the solution was maintained at 10 mL by adding distilled water. Finally, the solution was stirred for 1 min. The UV-Vis spectra were recorded at each 5 min interval. The kinetic study of MB reduction was analysed during experiment 10 mg/mL CuNPs was used and observe the result in respect to the time dependent manner,change in absorption maxima.

2.5. Hg^{2+} detection by chemiluminescence assay

CL assays were performed for the detection of Hg^{2+} in the presence of CuNPs. 100 µL ethylenediamine (6.9 µM) was mixed with 100 µL of a different concentration of Hg^{2+} and incubated for 15 min. Conjugation of ethylenediamine to the Hg^{2+} is facilitated during incubation. Then 1 mL CuNPs (63.8x 10^{-6} mg/ml) was added, reacting at room temperature for 5 min. Next, 50 µL of the reaction mixture was transferred to a well in the 96-well microplate and mixed with 100 µL of 50 µM H_2O_2. Finally, 100 µL of 5 mM luminol was injected into the well. The CL intensity was recorded by the microplate reader at 600 ms intervals. Each sample was tested three times parallelly.

2.6. Collection and characterisation of real water samples

The Real water samples were collected from Delhi, Agra and Gwalior (local area). Samples were stored in plastic bottles at 4°C. Before Hg^{2+} detection, they were boiled for 10 min to remove chlorine and filtered by Whatman filter paper. Samples were then diluted 10 times and used without any pre-treatment. Three concentrations (1.0, 0.50 and 0.05 pM) of Hg^{2+} were used to spike the treated water sample. Each sample was tested three times; relative standard deviation (RSD) and recovery were calculated.

3. Results and discussion

3.1. Green synthesis of CuNPs and characterisation

CuNPs were prepared by reduction of $CuSO_4$ salt using *Aegle marmelos* fruit peel extract. Copper (II) sulphate in distilled water will dissociate into copper and sulphate. The copper ion is responsible for the blue colour of $CuSO_4$. The ion was reduced into copper nuclei by a reducing agent (i.e. *A. marmelos* fruit peel extract). Green synthesis of CuNPs increases the nucleation reaction rate. The growing nuclei were capped and stabilised by a reducing agent such as phenolic compound, reducing sugar, etc.In the course of this process the brown colour of the colloidal CuNPs solution is formed.

The synthesised CuNPs were initially characterised by colour. The brown colour originated due to the formation of copper ions (Cu^{+}) into copper free radicals (Cu^{o}) by the active component of reducing agents (Figure 1 [a-b]). The excitation of the Surface Plasmon Resonance (SPR) of CuNPs creates a dark brown colour. Green-synthesised CuNPs were confirmed by UV-Visible spectra. The UV-Vis peak was observed at 685 nm. The spectra formed a band of metallic nanoparticles by SPR. SPR is generated by excitation of the free electrons of CuNPs by incident light and the absorption of light by nanoparticles responsible for absorption band formation. The CuNPs show a bathochromic shift (lower energy and lower frequency) in the visible range.

Morphology, size and shape of the synthesised CuNPs were determined by transmission electron microscopy (TEM), as shown in Figure 2 (a-b). The CuNPs were found to be spherical, without any aggregation, and the average particle size was 6–8 nm. This is in

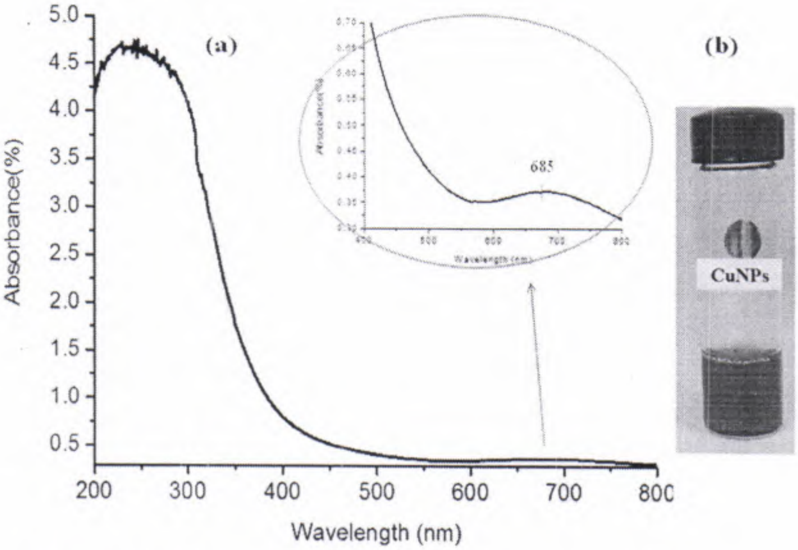

Figure 1. (a) UV-Visible spectra and (b) colour image of green synthesised CuNPs.

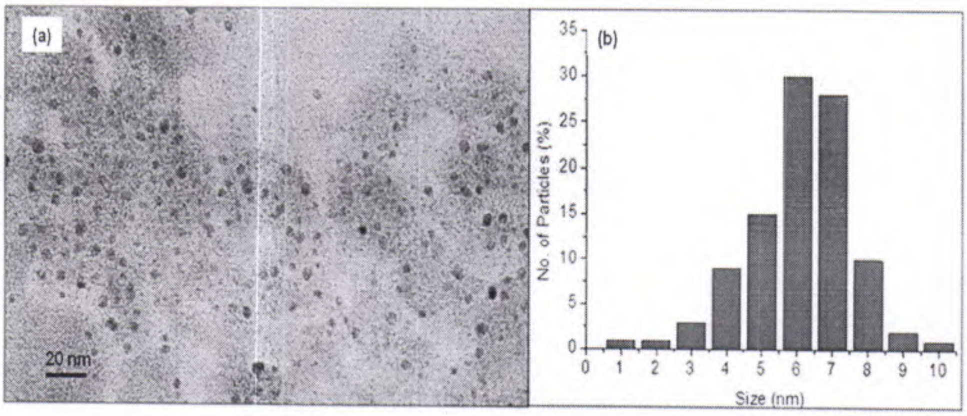

Figure 2. (a) TEM and (b) particle size distribution graph of CuNPs.

agreement with the size calculated from X-Ray Powder Diffraction (XRD) analysis. The particle distribution is illustrated in Figure 2 (b), which shows that the majority of particles ranged from 6 to 7 nm, and the mean diameter of the particles was found to be 20 nm.

XRD analysis revealed the 2θ position of the diffraction pattern of CuNPs (Figure 3). XRD patterns were obtained at 36.7°, 44.6°, 55.9° and 73.5°, and the hkl indexed were (1 1 0), (1 1 1), (2 1 1) and (2 2 0), respectively. These hkl index values are very similar to those reported in JCPDS file no. 04–0836 for CuNPs [29]. Table 1 summarises the parameters of XRD. The d-spacing analysis and lattice parameter (a) were calculated using the following relations:

$$2d \sin\theta = n\lambda \tag{1}$$

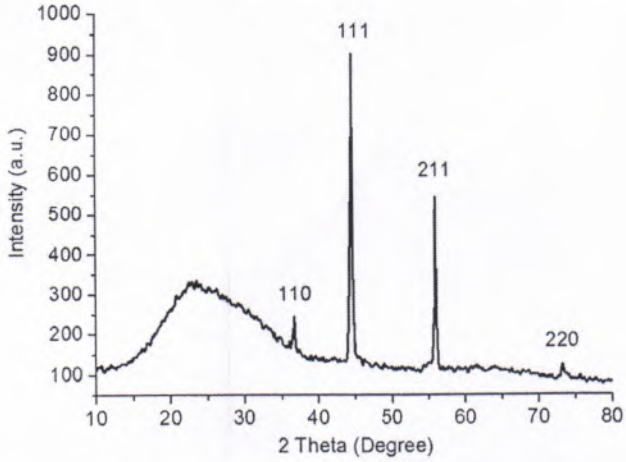

Figure 3. XRD spectra of CuNPs.

Table 1. XRD parameters of CuNPs.

S.No.	2θ position	θ	d(Å)	h k l	a (nm)
1	36.7	18.3	2.315	1 1 1	0.891
2	44.6	22.3	2.151	2 1 1	1.523
3	55.9	27.9	1.608	2 2 0	1.891
4	73.5	36.7	1.311	2 2 2	2.081

where λ = 0.15418 nm for Cu Kα, d is the inter planar spacing between atoms, and n is an integer (in this particular case, n = 1).

$$\frac{1}{d^2} = \frac{(h^2) + (k^2) + (l^2)}{a} \qquad (2)$$

The result of XRD analysis confirms that the green-synthesised CuNPs is face centred cubic (FCC) and crystalline in nature.

FTIR spectra describes the functional group of CuNPs shown in Figure 4. The peak at 3398 cm^{-1} overlaps with O–H stretching and the alcohol group. The sharp absorption peak at 2959 cm^{-1} is assigned to C–H stretching. The peak at 1624 cm^{-1} overlaps with N-H bending. The peak at 1372 cm^{-1} overlaps with C-H stretching. The sharp absorption peak at 1099 cm^{-1} is assigned to C–O stretching, and the peak at 755.8 cm^{-1} (alcohol group) overlaps with C-Cl strong stretching of alkyl halide. The peaks of CuNPs and aqueous extract also exhibited at 755.8 and 759.6 cm^{-1}, which overlaps with the C-Cl strong stretching of alkyl halide. Therefore, the phenolic compounds present in the extract have high affinity to bind towards CuNPs and help in the stabilisation of CuNPs. Thus, the phenolic compounds assist in the formation of CuNPs and also prevent possible aggregation.

The zeta potential determines the stability of CuNPs. Figure 5 shows the histogram of zeta potential data at pH 7.0. The average value of the zeta potential was −15 mV, which indicates moderate stability of nanoparticles. The values of the zeta potential showed the extent of electrostatic repulsion between all the adjacent, like-charged particles in

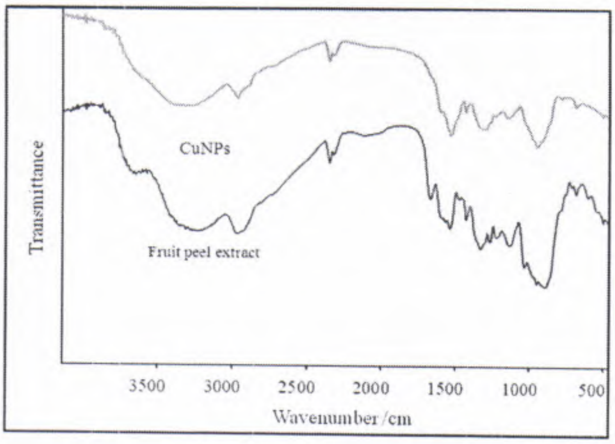

Figure 4. FTIR spectra of CuNPs and *Aegle marmelos* fruit peel extract.

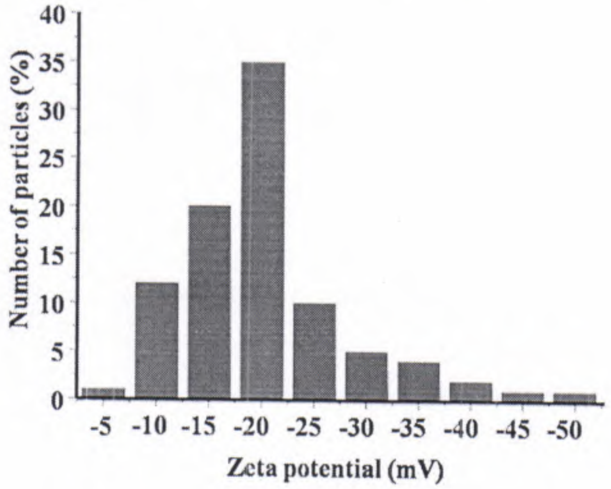

Figure 5. Zeta potential of CuNPs.

a dispersion medium. In the nanoscale parameter, molecules and particles showed more negative or more positive values of zeta potential, reflecting their stability.

3.2. *Catalytic properties of CuNPs*

The reduction of MB in the presence of NPs has been studied by several researchers [30–32]. Catalytic activity of NPs depends on such parameters as size, shape, monodispersity and surface coating [33]. Oxidised MB has a blue colour; after reduction, it is converted to colourless leucomethylene blue [34,35]. The relative absorbance peaks were at 664 and 614 nm, as shown in Figure 6(a) . The absorption peak at 664 nm is related to n-π^* transition of electrons. For effective catalysis, CuNPs should be located between donor and acceptor – $NaBH_4$ and MB, respectively. This is due to the electron relay effect, in which the CuNPs act as a relay of electron mediators between $NaBH_4$ and MB during

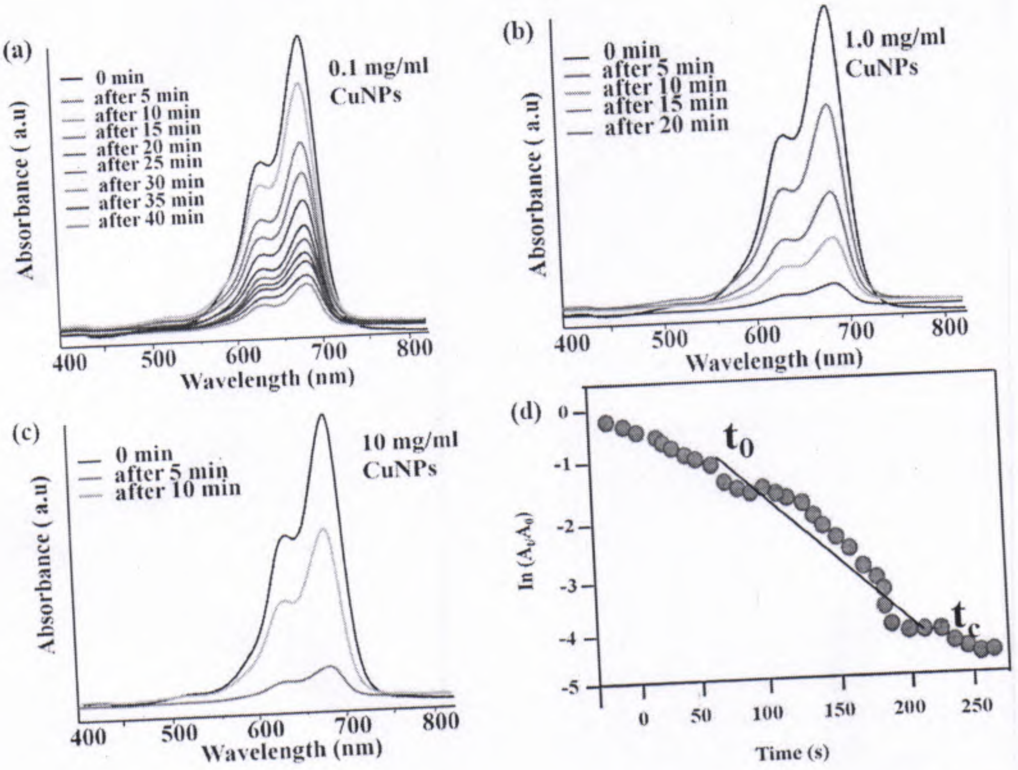

Figure 6. MB reduction by CuNPs. Three concentrations of CuNPs were used for transformation of 1 mM MB: (a) 0.1 mg/ml, (b) 1.0 mg/ml, (c) 10 mg/ml; (d) Kinetic study of MB catalysis in the presence of CuNPs.

catalysis [36]. The NaBH$_4$ releases H$_{\text{(hydrogen)}}$, and the CuNPs absorb H$_{\text{(hydrogen)}}$ and release electrons, reducing MB.

Figure 6 (a-c) shows MB reduction using different concentrations of CuNPs. Here, effective results were found at 10 mg/mL CuNPs for a reduction of 1 mM MB dyes in 10 min. This result was much higher than the other two CuNP concentrations. Here, these results are also more significant than previous findings, Sinha et al. and Sebiea et al. found MB (1 mM) dye was reduced by 10 mg/mL CuNPs after 135 min and 30 min, respectively [20,37].

3.3. *Kinetic study of MB catalysis*

Figure 6 (d) demonstrates the kinetic study of dye reduction, where t$_0$ is initiation time and t$_c$ is the end time of the reaction. The initiation period indicates the activation of CuNPs for dye reduction. NaBH$_4$ had no role in the initiation of the reaction; instead, it enhanced the reduction via electron donation and acceptance, and CuNPs initiated the reaction with the dye. After initiation of the reaction, the absorbance decreased in respect to the time due to the decolourization of the MB solution. It is known that absorbance is directly proportional to the concentration. The absorbance intensity (A$_t$/A$_0$) decreases as the dye concentration (C_t/C_0) is reduced during catalysis. The kinetic reaction is described by a pseudo first-order equation:

$$(A_t/A_0) = -kt, \tag{3}$$

where k = rate constant, t = reaction time, and A_t and A_0 = the absorbance of dye at time t and time 0, respectively.

The slope of the plot indicates that the rate is constant. This study has explained the mechanism of dye reduction in the presence of $NaBH_4$ and suggested that CuNPs are an efficient catalyst for MB reduction.

3.4. Inhibition effect of ethylenediamine on the luminol-H_2O_2-CuNPs CL reaction

Xu *et al* [24] reported that CuNPs enhance the CL reaction between luminol and H_2O_2. The CuNPs may facilitate the formation of OH•+ OH• radicals, which further react with luminol, converting it to luminol radicals: (L^{-}) and $O_2^{\cdot}$. The radicals will further react with each other, causing high light emission due to the formation of 3-aminophthalate. Hu et al. reported significant peroxidise-like activity of CuNPs interacting with the O–O bond of H_2O_2 and broken up into $[OH]_2$ radicals [38].

We speculate that ethylenediamine shows the inhibition effect of CuNPs on catalytic activity due to several factors. Firstly, incubation of the CuNPs with ethylenediamine resulted in two types of interactions: (i) the amino groups of ethylenediamine interact with the outer surface of the CuNPs through coordination bonding of the Cu atom (with N lone pair) [39]; and (ii) the amino groups of ethylenediamine are protonated at 8 pH, generating electrostatic interactions between CuNPs and ethylenediamine [40]. According to Xu et al., the CuNPs are responsible for the enhancement of CL signals: that the luminol radicals and O_2 radicals are generated from luminol-H_2O_2 in the presence of CuNPs [24]. Figure 7 (a) shows the effect of ethylenediamine on luminol-H_2O_2-CuNPs. Hence, we assume that ethylenediamine binds with CuNPs, decreasing the concentration of free CuNPs and inhibiting the luminol-H_2O_2-CuNPs complex. The result showed the maximum inhibition effect (96.95%) of 6.90 μM ethylenediamine on CuNPs, creating a decrease in CL intensity (see in Scheme 1).

3.5. Hg^{2+} detection via CL method

It has been reported that Hg^{2+} has a high affinity for ethylenediamine due to strong interaction with ethylenediamine amino groups [41]. Catalytic activity of CuNPs is enhanced in the presence of Hg^{2+}. The amino groups of ethylenediamine bind with Hg^{2+}, recovering the catalytic activity of CuNPs, and subsequently enhance CL intensity. In contrast, in the absence of Hg^{2+}, catalytic activity of CuNPs is inhibited (Scheme 1). This is confirmed by the experiments shown in Figure 7 (b). These experiments were based on a luminol-H_2O_2 system and performed under various parameters:

(i) H_2O_2 (50 μM) and luminol (5 mM) gives a very weak CL signal (shown in Curve [d] of Figure 7 [b]).

(ii) When 63.8×10^{-6} mg/ml of the CuNPs were added, we obtained a fast and intense CL signal – 100% in Curve (a) in Figure 7 (b).

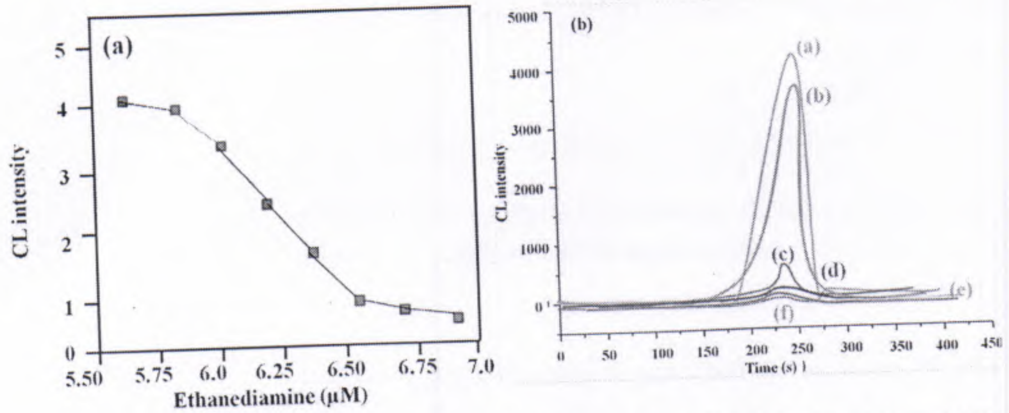

Figure 7. (a) Effect of ethylenediamine on the CL intensity of luminal-H_2O_2-CuNPs system. (b) The kinetic curves of CL intensity under different conditions: a) luminol+ H_2O_2 + CuNPs; b) luminol+H_2O_2+ CuNPs+ethylenenediamine+Hg^{2+}; c) luminol+H_2O_2+ CuNPs + ethylenedi-amine; d) luminol+H_2O_2; e) luminol+H_2O_2+ Hg^{2+}; f) luminol+H_2O_2 + ethylenediamine+Hg^{2+}; Experiment conditions: ethylenediamine, 6.9 μM; CuNPs, 63.8 × 10^{-6} mg/ml; H_2O_2, 50 μM; luminol, 5 mM; Hg^{2+}, 1 pM.

(iii) When we added 6.9 μM of ethylenediamine to the last reaction solution, we observed decreased CL; see Curve (c) in Figure 7 (b).

(iv) When we pre-incubated the ethylenediamine with 1 pM Hg^{2+} for 15 min, we observed dramatically enhanced CL, as shown in Curve (b) in Figure 7 (b).

CL signal recovery was up to 94.44%. The control was prepared with a Hg^{2+} and ethylenediamine mixture. The result of the control experiment shows no enhancement in CL intensity in Curves (e) and (f) in Figure 7 (b). The blank sample curve is the same as the control curves (e and f). The above investigation shows the enhancement effect in the presence of luminol-H_2O_2-CuNPs and ethylenediamine. However, CL intensity was decreased in the absence of Hg^{2+}. According to this investigation, the concentration of Hg^{2+} in water samples can be determined.

3.6. Optimisation of the assay

Hg^{2+} ion detection via the CL method is highly dependent on the concentration of ethylenediamine, performance of CuNPs, H_2O_2 and luminol. These materials' concentration and performance were optimised systematically (see Figure 8).

Ethylenediamine has a quenching effect on CL for luminol-H_2O_2-CuNPs. But in the presence of Hg^{2+}, ethylenediamine binds to it and recovers CL intensity. CuNPs concentration was fixed at 63.8 × 10^{-6} mg/ml, and the concentration of ethylenediamine was increased. The 6.9 μM ethylenediamine caused higher CL intensity (Figure 8 [a]). Concentrations of H_2O_2 ranging from 0.0–6.0 mM were used to study the effect of H_2O_2 on the CL (Figure 8 [b]). Concentrations of more than 3.0 mM decreased the CL intensity. Figure 8 (c) shows the effect of the luminol concentration. Increased concentrations of luminol enhanced the CL in the presence of H_2O_2 and CuNPs. The highest intensity of the CL was demonstrated with the use of 5 mM of luminol.

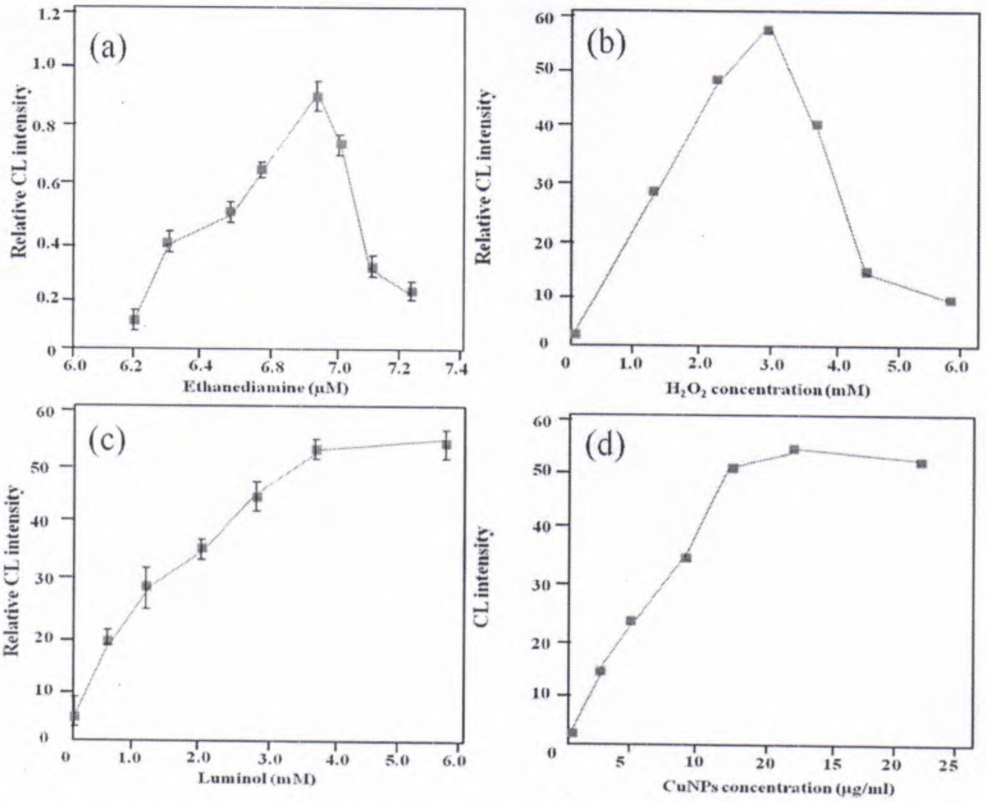

Figure 8. Optimisation of concentrations for (a) ethylenediamine, (b) H_2O_2, (c) luminol, (d) CuNPs. Experiment conditions: (A) luminol, 0.5 mM; H_2O_2, 10 μM. (B) ethylenediamine, 6.9 μM; luminol, 0.5 mM. (C) ethylenediamine, 6.9 μM; H_2O_2, 50 μM. (D) ethylenediamine, 6.9 μM; luminol, 5 mM; H_2O_2, 50 μM.

Finally, the effects of CuNPs were investigated in the absence of Hg^{2+} (Figure 8 [d]) and in the presence of Hg^{2+} (Figure 7 [b], Curve [a]). The CL intensity increases slowly, due to the saturation concentration of CuNPs (18–20 mg/mL) with ethylenediamine. When we enhanced the concentration to more than 20 mg/mL, the CL signal reached maximum intensity (Figure 8 [d]).

3.7. *Quantitative analysis of Hg^{2+}*

The quantitative assays of Hg^{2+} were realised. Figure 9 (a) shows the calibration plot for Hg^{2+} concentrations from 0 to 1.20 pM. The calibration curve indicated good linearity between relative CL intensity and the Hg^{2+} concentration logarithm. The linear range from 0.01 pM to 1.0 pM had a correlation coefficient of 0.9951. The LOD was 0.0062 pM. This method has higher sensitivity than other methods and materials (Table 2). To evaluate the reproducibility of the method, five repetitive observations of 1.2 pM Hg^{2+} were performed under optimum conditions. The standard deviation was found to be 1.25%, indicating that the present method shows good reproducibility.

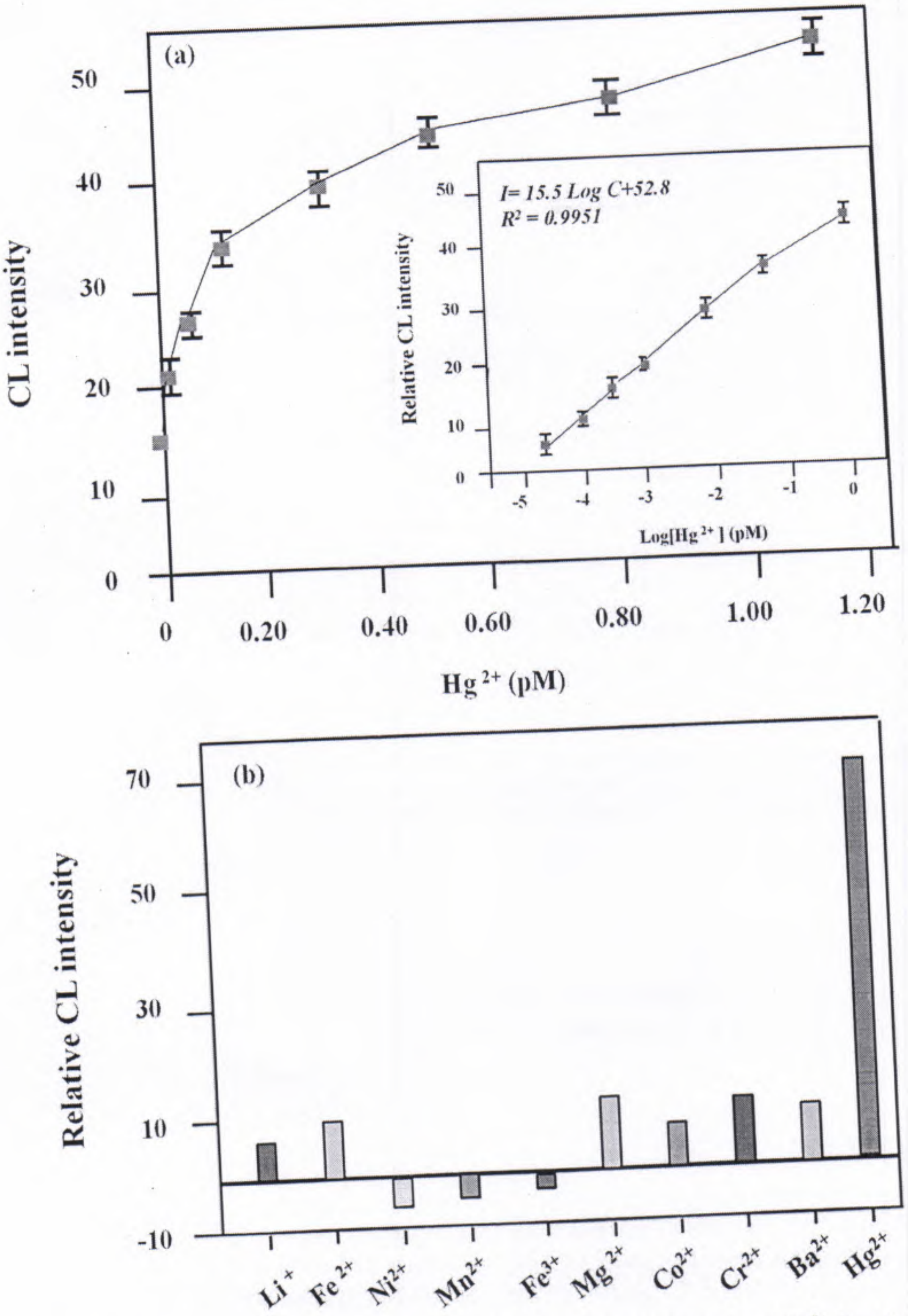

Figure 9. Calibration plot (a) and selectivity (b) of the CL system for the detection of Hg^{2+}. Experiment conditions: ethylenediamine, 6.6 µM; CuNPs, **63.8×10^{-6} mg/ml**; luminol, 5 mM; H_2O_2, 50 µM.

Table 2. Comparison of the assay performance with previously developed methods.

Methods	Analyte	Nanoparticles	LOD	Linear range	Reference
Colorimetric method		Magnetic beads	5 nM	10–200 nM	[42]
	Hg^{2+}	*Durio zibethinus* extract AgNPs	0.1 μM	0–33 μM	[32]
		CuNPs	0.11 μM	0–75 μM	[43]
FL	**Hg**$^{2+}$	Nitrogen-doped carbon dots	0.23 μM	0–25 μM	[44]
	Hg^{2+}	Ag nanoclusters	10 nM	10 nM- 5 μM	[45]
CL	**Hg**$^{2+}$	Phenyleneethynylene, nanoporous silver	1pM	20 nM- 0.5 μM	[46]
		Level free (aptamer)	**50 pM (0.01 ppb)**	**0.01 to 1000 ng/mL**	[27]
	Hg^{2+}	Graphene oxide	2 nM	~0-100 nM	[47]
		AuNPs	**0.54 fM**	**1 fM to 1 pM**	[28]
	Hg^{2+}	CuNPs	0.0062 pM	0.01–1.0 pM	This work

Table 3. Detection results for Hg^{2+} in real water samples.

Sample	Added amount (pM)	Found amount (pM)	RSD (%)	Recovery (%)
Delhi (NCR, India)				
1	1.00	1.050	2.5	105
2	0.50	0.510	1.6	101
3	0.05	0.046	1.9	97
Agra (U.P, India)				
1	1.00	1.091	1.7	110
2	0.50	0.480	2.1	98
3	0.05	0.056	1.0	103
Gwalior (M.P., India)				
1	1.00	0.982	1.9	95
2	0.50	0.525	2.0	103
3	0.05	0.051	2.2	101

The selectivity of the assay to Hg^{2+} was compared with some other toxic metallic ions, including Li^{+}, Fe^{2+}, Ni^{2+}, Mn^{2+}, Fe^{3+}, Mg^{2+}, Co^{2+}, Cr^{3+}, and Ba^{2+}. The concentrations of the interfering toxic metallic ions were 100 times higher then the concentration of Hg^{2+} (1.2 pM).

In this experiment, the much higher concentrations of alternate ions showed very negligible signals, similar to a blank sample. However, Hg^{2+} showed a remarkable signal (Figure 9 [b]). These results demonstrate the high selectivity of the assay and indicate that the metallic ions we tested will not interfere with the determination of Hg^{2+} in real samples.

3.8. Detection of Hg^{2+} in areal water sample

Here we tested real water samples. The CL method was used to evaluate Hg^{2+} in real water samples by applying the standard addition method. Evidently, the recovery percentage (%) of the sensor measurement showed 95–110%, and the relative standard deviation percentage (RSD %) was obtained in the range of 1.0–2.5% (Table 3). The results demonstrated that the CL method for Hg^{2+} detection in real water samples are environmentally friendly and cost effective.

4. Conclusions

The CuNPs were successfully synthesised by the green method using *Aegle marmelos* fruit peel extract. The CuNPs were found to be monodisperse, with a spherical shape. The CuNPs exhibited high catalytic activity for MB reduction. The CL intensity enhancement method for Hg^{2+} detection was realised using luminol-H_2O_2-CuNPs. We conclude that the CL signal may be attributed to the conjugation of Hg^{2+} with the amino groups of ethylenediamine, leading to the recovery of the catalytic activity of the CuNPs. The CL method showed a detection limit of 0.0062 pM for Hg^{2+}. The study of other ions shows that the assay is highly sensitive to Hg^{2+} ions. This method can quantitatively detect Hg^{2+} ions in drinking water within the acceptable recovery range of 92–113%. Overall, the experimental outcomes suggest that CuNPs are an excellent catalyst for the reduction of MB and the increase of CL signals. The obtained results indicate the feasibility and sensitivity of the method, which that may be considered as a tool for testing environmental samples

Acknowledgments

The Russian author thanks the Russian Science Foundation for its financial support (project no. 19-44-02020).

Disclosure statement

There is not any conflict of interest.

Funding

This work was supported by the Department of Science and Technology (DST), Government of India, New Delhi, under the DST-RSF joint project [project no. DST/INT/RUS/RSF/P-28/G].

ORCID

Mamta Kushwah http://orcid.org/0000-0002-1252-9716
Mulayam Singh Gaur http://orcid.org/0000-0002-9335-8233
Anna Nikolaevna Berlina http://orcid.org/0000-0002-3761-7472

References

[1] C.T. Driscoll, R.P. Mason, H.M. Chan, D.J. Jacob and N. Pirrone, Environ. Sci. Technol. **47**, 4967 (2013). doi:10.1021/es305071v.

[2] J. Anish, N. Jain, H. Joshi and S. Prasad, J. Sci. Ind. Res. 647 (2008). http://hdl.handle.net/123456789/1862.

[3] T. Li, E. Wang and S. Dong, Anal. Chem. **82**, 1515 (2010). doi:10.1021/ac902638v.

[4] E. Priyadarshini and N. Pradhan, Sens. Actuators B Chem. **238**, 888 (2017). doi:10.1016/j.snb.2016.06.081.

[5] J. Zang, C. Li, K. Zhou, H. Dong, B. Chen, F. Wang and G. Zhao, Anal. Chem. **88**, 10275 (2016). doi:10.1021/acs.analchem.6b03011.

[6] O. US EPA, *EPA Method 7473 (SW-846): Mercury in Solids and Solutions by Thermal Decomposition, Amalgamation, and Atomic Absorption Spectrophotometry* (2019). https://www.epa.gov/esam/epa-method-7473-sw-846-mercury-solids-and-solutions-thermal-decomposition-amalgamation-and.

[7] M.S. Gaur, R. Yadav, A.N. Berlina, A.V. Zherdev and B.B. Dzantiev, J. Exp. Nanosci. **11**, 1372 (2016). doi:10.1080/17458080.2016.1227096.

[8] A.V. Gribas and I.Y. Sakharov, Anal Lett **51**, 1280 (2018). doi:10.1080/00032719.2017.1378229.

[9] P. Maity, D. Hansda, U. Bandyopadhyay and D.K. Mishra, Indian J. Exp. Biol. **47**, 849 (2009). http://hdl.handle.net/123456789/6527.

[10] H.N. Murthy, M.A. Bhat and D. Dalawai, in Bioactive Compounds of Bael (Aegle Marmelos (L.) Correa), *Bioactive Compounds in Underutilized Fruits and Nuts*, edited by H. N. Murthy and V. A. Bapat (Springer International Publishing, Cham, 2019), pp. 1. doi:10.1007/978-3-030-06120-3_35-1

[11] M. Kushwah, S. Bhadauria, K.P. Singh and M.S. Gaur, Anal. Chem. Lett. **9**, 329 (2019). doi:10.1080/22297928.2019.1626279.

[12] V. Jassal, U. Shanker and B.S. Kaith, Hindawi 1 (2016). https://www.hindawi.com/journals/scientifica/2016/2715026/.

[13] S. Otari, R. Patil, N. Nadaf, S. Ghosh and S. Pawar, Environ. Sci. Pollut. Res. Int. **21**, (2013). doi:10.1007/s11356-013-1764-0

[14] P. Zhang, Y. Sui, C. Wang, Y. Wang, G. Cui, C. Wang, B. Liu and B. Zou, Nanoscale **6**, 5343 (2014). doi:10.1039/C4NR00412D.

[15] M. Tang, S. Zhang, X. Li, X. Pang and H. Qiu, Mater Chem Phys **148**, 639 (2014). doi:10.1016/j.matchemphys.2014.08.029.

[16] J. Tang, Z. Shi, R.M. Berry and K.C. Tam, Ind. Eng. Chem. Res. **54**, 3299 (2015). doi:10.1021/acs.iecr.5b00177.

[17] B.K. Ghosh, S. Hazra, B. Naik and N.N. Ghosh, Powder Technol. **269**, 371 (2015). doi:10.1016/j.powtec.2014.09.027

[18] B. Baruah, RSC Adv. **6**, 5016 (2016). doi:10.1039/C5RA20059H.

[19] T. Sinha and M. Ahmaruzzaman, Environ. Sci. Pollut. Res. Int. **22**, 20092 (2015). doi:10.1007/s11356-015-5223-y.

[20] N. Sebeia, M. Jabli and A. Ghith, Inorg. Chem. Commun. **105**, 36 (2019). doi:10.1016/j.inoche.2019.04.023.

[21] Y. Su, H. Chen, Z. Wang and Y. Lv, Appl. Spectrosc. Rev. **42**, 139 (2007). doi:10.1080/05704920601184275.

[22] B. Wang, M. Chen, H. Zhang, W. Wen, X. Zhang and S. Wang, Microchim Acta. **184**, 3189 (2017). doi:10.1007/s00604-017-2270-8.

[23] Z. Zhang, J. Lai, K. Wu, X. Huang, S. Guo, L. Zhang and J. Liu, Talanta **180**, 260 (2018). doi:10.1016/j.talanta.2017.12.024.

[24] S. Xu, F. Chen, M. Deng and Y. Sui, RSC Adv. **4**, 15664 (2014). doi:10.1039/C4RA00516C.

[25] T. Uzu and S. Sasaki, Org. Lett. **9**, 4383 (2007). doi:10.1021/ol702002e.

[26] T. Khajvand, R. Akhoondi, M.J. Chaichi, E. Rezaee and H. Golchoubian, J. Photochem. Photobiol. A Chem. **282**, 9 (2014). doi:10.1016/j.jphotochem.2014.02.011.

[27] S. Cai, K. Lao, C. Lau and J. Lu, Anal. Chem. **83**, 9702 (2011). doi:10.1021/ac202789q.

[28] M. Wang, Y. Kong, Y. Li, Y. Huang and A. Fan, Anal. Methods **11**, 1317 (2019). doi:10.1039/C8AY02815J.

[29] Z.I. Ali, O.A. Ghazy, G. Meligi, H.H. Saleh and M. Bekhit, J. Inorg. Organomet. Polym. **28**, 1195 (2018). doi:10.1007/s10904-018-0780-4.

[30] A. Ma, Y. Xie, J. Xu, H. Zeng and H. Xu, Chem. Commun. **51**, 1469 (2015). doi:10.1039/C4CC08489F.

[31] R. Begum, J. Najeeb, A. Sattar, K. Naseem, A. Irfan, A. Al-sehemi and Z. Farooqi, Rev. Chem. Eng. 2019. doi:10.1515/revce-2018-0047

[32] M. Sengan, D. Veeramuthu and A. Veerappan, Mater. Res. Bull. **100**, 386 (2018). doi:10.1016/j.materresbull.2017.12.038.

[33] M. Kaushik and A. Moores, Green Chem. **18**, 622 (2016). doi:10.1039/C5GC02500A.

[34] M.A. Rauf, M.A. Meetani, A. Khaleel and A. Ahmed, Chem. Eng. J. **157**, 373 (2010). doi:10.1016/j.cej.2009.11.017.
[35] I. Laoufi, M.-C. Saint-Lager, R. Lazzari, J. Jupille, O. Robach, S. Garaudée, G. Cabailh, P. Dolle, H. Cruguel and A. Bailly, J. Phys. Chem. C **115**, 4673 (2011). doi:10.1021/jp1110554.
[36] M. Kushwah, M.S. Gaur, A.N. Berlina and K. Arora, Mater. Res. Express **6**, 116561 (2019). doi:10.1088/2053-1591/ab485e.
[37] T. Sinha and M. Ahmaruzzaman, Environ. Sci. Pollut. Res. **22**, 20092 (2015). doi:10.1007/s11356-015-5223-y.
[38] L. Hu, Y. Yuan, L. Zhang, J. Zhao, S. Majeed and G. Xu, Anal. Chim. Acta **762**, 83 (2013). doi:10.1016/j.aca.2012.11.056.
[39] J. Sharma, Z. Jiang, A. Bhutani, P. Behera and D.P. Shoemaker, Cryst. Eng. Comm. **21**, 2718 (2019). doi:10.1039/C8CE02188K.
[40] M.P. Sooraj, A.S. Nair, S.C. Pillai, S.J. Hinder and B. Mathew, Arabian J. Chem. **13**, 2483 (2020). doi:10.1016/j.arabjc.2018.06.002.
[41] Z. Yan, M.-F. Yuen, L. Hu, P. Sun and C.-S. Lee, RSC Adv. **4**, 48373 (2014). doi:10.1039/C4RA07930B.
[42] X. Huang, Y. Hao, H. Wu, Q. Guo, L. Guo, J. Wang, L. Zhong, T. Lin, F. Fu and G. Chen, Sens. Actuators B Chem. **191**, 600 (2014). doi:10.1016/j.snb.2013.10.025.
[43] M. Sengan and A. Veerappan, Microchem. J. **148**, (2019). doi:10.1016/j.microc.2019.04.049.
[44] R. Zhang and W. Chen, Biosens. Bioelectron. **55**, 83 (2014). doi:10.1016/j.bios.2013.11.074.
[45] C. Guo and J. Irudayaraj, Anal. Chem. **83**, 2883 (2011). doi:10.1021/ac1032403.
[46] F. Liu, S. Wang, M. Zhang, Y. Wang, S. Ge, J. Yu and M. Yan, Microchim Acta. **181**, 663 (2014). doi:10.1007/s00604-014-1171-3.
[47] Y. Tian, Y. Wang, Y. Xu, Y. Liu, D. Li and C. Fan. Sci. China Chem. **58**, 514 (2015). Background Reduction. *Sci. China Chem.* 2015, *58*(3), 514–518. doi:10.1007/s11426-014-5258-9

Research Article

Rapid and selective electrochemical detection of pb^{2+} ions using aptamer-conjugated alloy nanoparticles

Reetu Yadav[1,2] · Anna N. Berlina[3] · Anatoly V. Zherdev[3] · M. S. Gaur[1] · B. B. Dzantiev[3]

Received: 8 July 2020 / Accepted: 4 November 2020 / Published online: 25 November 2020

Abstract

Heavy metals are an important class of technogenic toxicants that pollute rivers and underground water. Here we proposed the use of electrochemical methods using silver (Ag)–gold (Au) alloy nanoparticle (NP)–aptamer-modified glassy carbon electrode (GCE) for the detection of lead ions (Pb^{2+}). Alloy Ag–Au NPs were electrodeposited on the electrode using the potentiostatic double-pulse method. The NPs were characterized by high-resolution transmission electron microscopy, which revealed that the average NP size was 44 nm. The binding of Pb^{2+} induced conformational changes of the aptamer and corresponding modulation of electrochemical signals. As a result, we were able to detect Pb^{2+} with a straight slope of 0.01–10 µg/L with limits of detection (LOD) of 0.03×10^{-2} µg/L for CV, DPV and 0.04×10^{-2} µg/L for EIS. The minimum detectable Pb^{2+} concentration was calculated to be 0.8 µM.

Graphic abstract

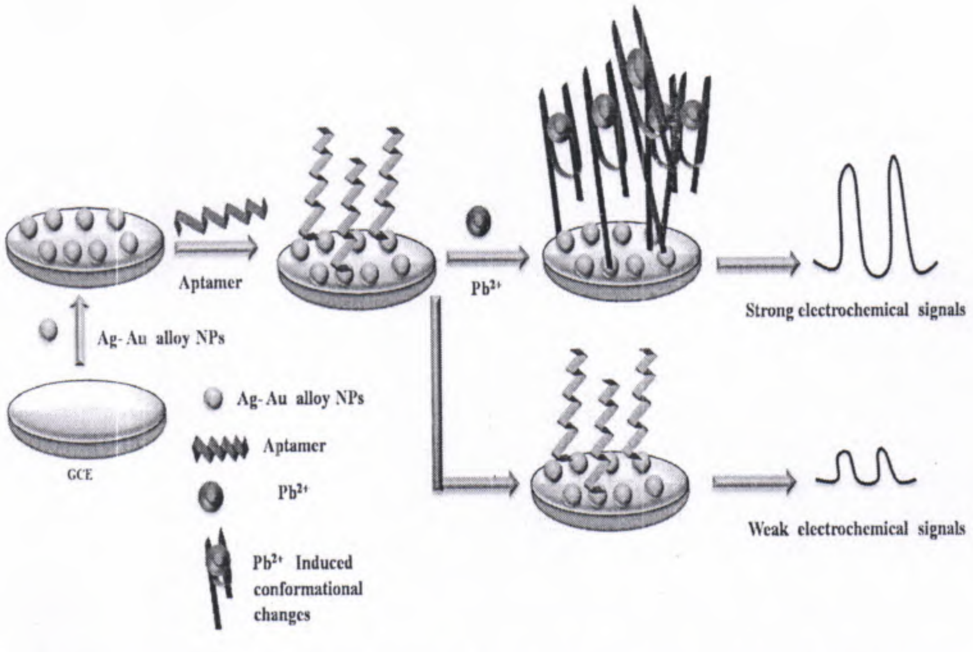

✉ M. S. Gaur, mulayamgaur@rediffmail.com | [1]Shri Anand Swaroop Interdisciplinary Research Laboratory, Hindustan College of Science and Technology (Affiliated To Dr. A. P. J. Abdul Kalam Technical University), Farah, Mathura, Uttar Pradesh 281122, India. [2]Microbiology Research Laboratory, Department of Botany, R.B.S. College, Agra, Uttar Pradesh 282005, India. [3]Division of ligand receptor interaction, Laboratory of Immunobiochemistry, A. N. Bach Institute of Biochemistry, Research Center of Biotechnology of Russian Academy of Sciences, Leninsky Prospect 33, Moscow, Russia 119071.

SN Applied Sciences (2020) 2:2077 | https://doi.org/10.1007/s42452-020-03840-6

Keywords Alloy ag-au NPs · Cyclic voltammetry · Differential pulse voltammetry · Electrochemical impedance spectroscopy

1 Introduction

The analysis of heavy metals at very low levels in drinking water has become a globally high-priority area of research [1, 2]. Metal quantification at the microgram and nanogram level in water was a challenging assignment before the development of such systems as flameless atomic absorption spectrophotometry and differential pulse anodic stripping. These methods can measure the total metal contents in a sample. However, assessing the bioavailable concentration of heavy metals in a more convenient way remains a great challenge. The scientific community has turned its attention towards nanobiosensor research to overcome this challenge.

In general, metal nanoparticles (NPs) exhibit very good conductivity and catalytic properties. These two features make them appropriate to improve the electron exchange between redox-active groups in biomolecules and electrode surfaces. Metal NPs can also act as catalysts, promoting electrochemical reactions. Recently, there have been some reports on the evaluation of the application of nanoparticles to electrochemical biosensors [3–6].

Recently, alloy, core–shell nanoparticles and biametallic nanostrucrued material played important role for design of electrochemical biosensor because of their excellent optical, magnetic, and catalytic properties. They offer better sensing properties as compare to single nanometallic material [7–9].The conjugation of metal particles Pb^{2+} with bioreceptors, for example, proteins, antibodies, or nucleic acids, can increase the selectivity and lower the limit of detection (LOD) of nanobiosensors [10, 11].

The reasons for selecting silver (Ag) and gold (Au) to develop bimetallic NPs are (i) a metal of a higher valency can dissolve in one with lower valency (i. e. valency of Ag and Au are 1 and 3, respectively) [12] and (ii) the tunability of bimetallic NPs means they show potential applications in biosensors, drug delivery, and cell labeling [13, 14]. Recently, several developments were aimed at the detection of lead ions (Pb^{2+}) in water [15–19]. For example, Shen et al. [20]. Constructed an electrochemical biosensor using an Au NP–oligonucleotide-modified glassy carbon electrode (GCE) for detection of Pb^{2+} in water. The electrode achieved a low LOD of 1 nM. However, electron flow prompted direct oxidation of nucleotides, which resulted in incorrect estimation of Pb^{2+} levels. Currently, biosensors have constraints regarding strength, reaction time, and precision, so their further development is required.

Different DNAzyme-based biosensors have been produced for detection of Pb^{2+}, including ones designed detection of Pb^{2+} and including those designed for colorimetric electrochemical and fluorescence detection [21–25]. These sensors do not require complicated pretreatment, costly delivery of samples to central research facilities with a long turnaround time, or rather complex laboratory techniques. However, the LODs of conventional sensors are not satisfactory. Thus, the development of a high sensitivity nanobiosensor for Pb^{2+} in water with good stability and low LOD is still desired.

The novelty of present work is that Ag-Au modified electrode possesses excellent biocompatibility with a variety of biomolecules, such as aptamers, antibodies, enzymes, DNA, cells, and proteins [26].

Aptamers are short, single-stranded oligonucleotides (DNA or RNA) that bind to targets with high affinity and specificity by folding into tertiary structures as compare to traditional nucleic acids. A combinational selection process called systematic evolution of ligands by exponential enrichment (SELEX). The SELEX is process used to select aptamer from large oligonucleotide library. There are several advantages in using aptamers instead of enymes/antibodies, including having the ability to be modified chemically, chemical stability, and flexibility for being used in biosensors [27].

An aptamer contains various groups that can interact with metal particles, such as exocyclic keto, ribose hydroxyl, ring nitrogen, and negatively charged phosphate-based groups [28]. For example, the N_7 atoms of purines can directly bind to bases and indirectly bind to phosphate groups. These binding sites of aptamers are responsible for their ability to sense metal ions. A literature survey revealed that electrochemistry is a useful technology for studying bimolecular interactions based on ligand binding interaction-induced changes in electrode properties.

The many metals are known to be of specific physiological function to life systems [29]. These metals show preference for certain types of ligands. The most common types of ligands are the amino acids, especially cysteine and the porphyrins. The main function of the porphyrins is to bind metal atoms which act as centres for significant electrochemical or biochemical events. Electrochemical reduction or oxidation occurs at the surface of ligand modified electrode for detection heavy metals is reported by many researcher [30].

The nanobiosensor has great potential for on-site detection of multiple heavy metals. The nanotechnology provides the solution of challenges faced by traditional techniques. The nanobiosensor could able to improve the sensitivity, limit of detection, selectivity, and reproducibility. Nanoparticle-modified electrodes have higher surface area to volume ratio, improved electron transfer rate, increased mass-transport rate, less solution resistance, and higher signal-to-noise ratio [31–33]. The nanoparticle-aptamer modified glassy carbon electrode significantly reduces the memory effect, foreign ions, detection limit and sensitivity of nanobiosensor [34, 35]. For example, the Au NP-modified glassy carbon electrode significantly lowered the LOD toward Hg^{2+} and As^{3+} and its sensitivity is much higher than other sensor [36, 37]. Recently, bimetallic nanoparticles are applied for modification of surface of GCE and showed excellent results for detection of heavy metals using different bioreceptors due to higher electroactive surface area.

The objective of the present work is to detect Pb^{2+} in drinking water by cyclic voltammetry (CV), differential pulse voltammetry (DPV), and electrochemical impedance spectroscopy (EIS) using a GCE modified with Au–Ag alloy NPs and an aptamer.

2 Materials and methods

2.1 Materials and reagents

Silver nitrate ($AgNO_3$) and chloroauric acid were purchased from Sigma-Aldrich (India). An aqueous solution of Pb^{2+} (1 g/L) was purchased and used as a stock solution. (Thiol-C6 GGGTGGGTGGGTGG) was obtained from Sigma-Aldrich. G-quadruplex electrochemical biosensors have received particular attention, since the electrochemical response is particularly sensitive to the DNA structural changes from single-stranded, double-stranded, or hairpin into a G-quadruplex configuration. Furthermore, the development of an increased number of G-quadruplex aptamers that combine the G-quadruplex stiffness and self-assembling versatility with the aptamer high specificity of binding to a variety of molecular targets allowed the construction of biosensors with increased selectivity and sensitivity [38]. The stock solution of aptamer sequence Thiol-C6-GGGTGG GTGGGTGG (40 mg/L) in phosphate buffered saline (PBS, pH = 7.4) was kept at − 20 °C. All experiments were performed at room temperature using Milli-Q water with a conductivity of less than 1 µg/L mho and pH of 5.6. Detection of Pb^{2+} from the real water samples was carried out with the help of CV, DPV and EIS methods. The optimization experiments are shown in Fig. 1. (a) Optimization) pH value (b) Optimization of aptamer different concentration for sensing of Pb^{2+} (c) time on the stability of (Ag–Au) NP–aptamer-modified GCE.

2.2 Apparatus

A Palmsan3 potentiostat system with microcode version 1.8 was used to conduct CV, DPV, and EIS measurements. The size and shape of the synthesized NPs were characterized by high-resolution transmission electron microscopy (HRTEM) using a Techani G230S electron microscope (TWIN Company FEI).

2.3 Synthesis and characterization of the bimetallic alloy NPs

Solutions of $AgNO_3$ and chloroauric acid at 1:3 volume ratio were mixed in a flask and purged with nitrogen gas continuous 10 min. To prevent the photochemical reaction of $AgNO_3$, the flask was completely covered with black cloth during the reaction. The solution was stirred for 10 min using a magnetic stirrer. Deposition of bimetallic alloy NPs on the GCE was conducted in 0.1 M $NaNO_3$ solution by differential pulse voltammetry (DPV) [39]. In this experiment the potential range from 0 to + 800 mV was selected using sweep rate of 100 m Vs^{-1} for 20 cycles.

2.4 Surface modification and characterization of the modified GCE

The surface modification of the GCE disk working electrodes was polished with 0.05 µm silver powder. The experiment was carried out in aqueous media in the potential range from 0 to + 800 mV using a sweep rate of 100 m Vs^{-1} for 20 cycles. The thiolated aptamer (3 µg/L) was pipetted onto the GCE modified with Au–Ag NPs and then incubated overnight at 25 °C in 100% humidity. After flushing with 10 mM PBS (pH 7.4), the electrode was washed with Milli Q water to rinse away nonspecific adsorption sites. The modified electrode was used for direct detection of Pb^{2+} in real-life water samples.

2.5 Electrochemical detection of Pb^{2+}

The interaction of Pb^{2+} with the modified electrode was measured in terms of oxidation and reduction peak currents, the peak current in CV, and DPV and peak value in EIS measurements. All responses were measured until saturation of the sensor signal. The electrochemical reactions of Pb^{2+} in Milli Q water and environmental water tests were recorded in 0.1 M citrate solution (pH 6). For each experiment, a fresh electrode was prepared.

2.6 Recovery tests and assay of real water samples

Real water samples were collected from the Agra ground water, Mathura ground water, Chambal river water, Gwalior

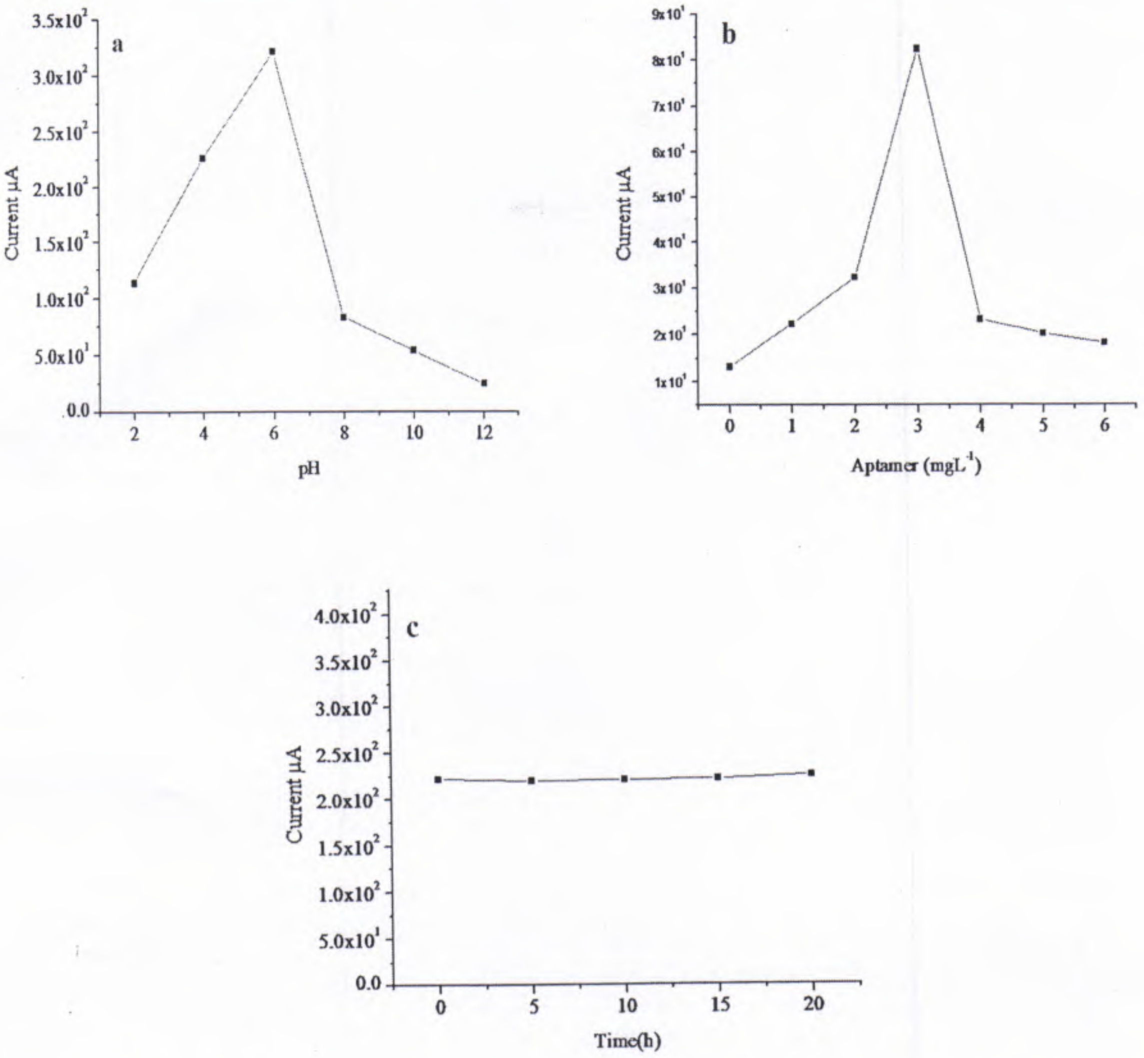

Fig. 1 **a** Optimization of pH value **b** Optimization of aptamer different concentration for sensing of Pb^{2+} **c** time on the stability of (Ag–Au) NP–aptamer-modified GCE

water, Delhi Ground water and Meerut ground water (north region of India). Each sample was collected in plastic tubes and kept frozen at − 20 °C prior to analysis. Before the electrochemical experiments, all the water samples were heated at 25 °C and centrifuged 15 min at 8500 rpm to remove denaturated high molecular organic compounds. The supernatant was filtered through 0.22 µm filter Millex GP by Millipore. The prepared water samples were tested by Atomic absorption spectroscopy (AAS) method to estimate Pb^{2+} concentration. The present value Pb^{2+} in all water samples are presented in Table 1.

3 Results and discussion

3.1 TEM studies of native and modified NPs

HRTEM was used to investigate the structure, morphology, and size distribution of the Ag-Au bimetallic NPs and their binding with the aptamer. Figure 2a shows an HRTEM image of the spherical NPs, which are homogeneously dispersed with an average size of 44 nm. The NPs were physically conjugated with the aptamer. Figure 2b shows the diameter of NPs increases when bound with aptamer and Pb^{2+}.

Table 1 Determination of Pb^{2+} in real water samples by CV, DPV, and EIS

Sample	Present (μg/L)	Added (μg/L)	CV cycle found (μg/L)	Recovery (%)	DPV Found (μg/L)	Recovery (%)	EIS Found (μg/L)	Recovery (%)
Milli-Q waterwater	0	0.1	0.096	96	0.093	93	0.107	107
		0.5	0.49	98	0.48	96	0.49	98
Agra water	167	0.1	166.9	93	166.9	99	166.9	94
		0.5	166.5	94	166.4	102	166.5	97
Mathura water	321	0.1	320.8	102	320.9	93	320.9	99
		0.5	320.5	97	320.4	106	320.4	105
Chambal water	623	0.1	622.9	92	622.9	98	622.9	93
		0.5	622.5	95	622.5	92	622.5	99
Gwalior water	123	0.1	122.9	98	122.9	95	122.9	92
		0.5	122.5	94	122.5	98	122.5	99
Delhi water	350	0.1	349.9	93	349.9	96	349.8	102
		0.5	349.5	96	349.5	95	349.5	96
Meerut water	231	0.1	230.9	92	230.9	92	230.9	92
		0.5	230.5	97	230.4	103	230.5	94

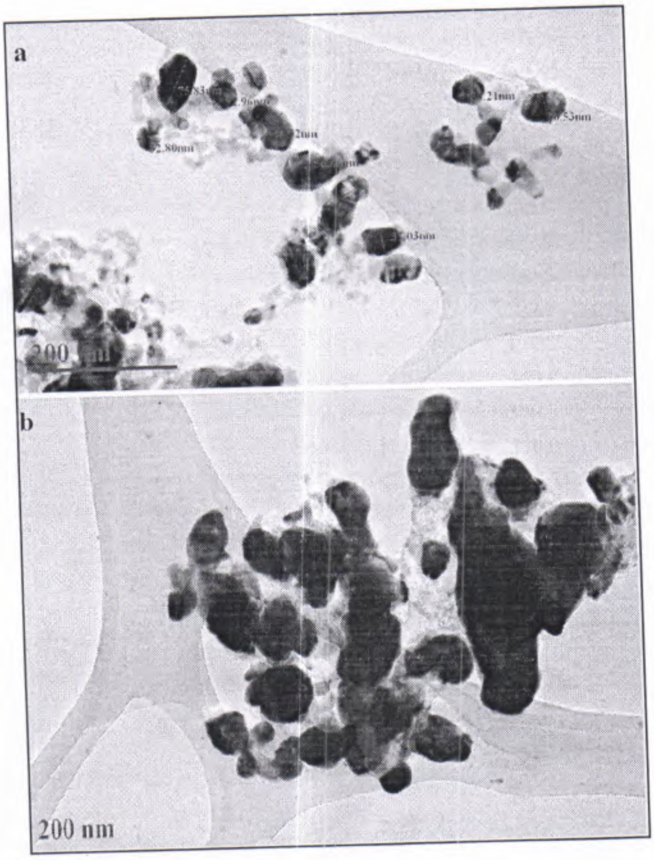

Fig. 2 **a** HRTEM image of bimetallic alloy (Ag–Au) NPs without aptamer. **b** TEM image of NPs with aptamer and bound Pb^{2+}

3.2 Molecular mechanism of the modified electrode action

A schematic diagram of the interaction of Pb^{2+} with the Ag-Au NP–aptamer-modified GCE is shown in Fig. 3. The electronic configurations of Ag and Au are $4d^{10}5s^1$ and $6s^1$, respectively, so they both have their valence electron in s^1. The oxidation potentials of Ag and Au are − 0.799 and − 1.50 V vs SHE, respectively. Ag and Au can easily form alloys because of their similar atomic radii. In addition, Ag and Au both easily lose an electron, resulting in favorable electrochemical properties and endowing sensors with high sensitivity and selectivity. The electrostatic attractive force between the bimetallic NPs and GCE aided the uniform deposition of NPs. More details of the Pb^{2+}–aptamer interaction can be found elsewhere [40–45].

The overall reaction and its standard cell potential at 25 °C and 1atmoshperic pressure for the reaction involving the galvanic cell in which Pb metal is oxidized to 1 M Pb ion and a half-cell consisting of an silver electrode in 1 M. This could be taken relative to standard hydrogen electrode (SHE). The reduction of $Pb^{2+}{}_{(aq)}$ to $Pb_{(s)}$ is a straight transfer of two electrons shown in Eq. (3.1):

$$Pb^{2+} + 2e^{-} \leftrightarrow Pb(s) \tag{3.1}$$

Differential pulse voltammetry markedly increased the signal-to-noise ratio for lead deposition and better allowed detection of low levels of lead in the solution and its corresponding binding with modified electrode

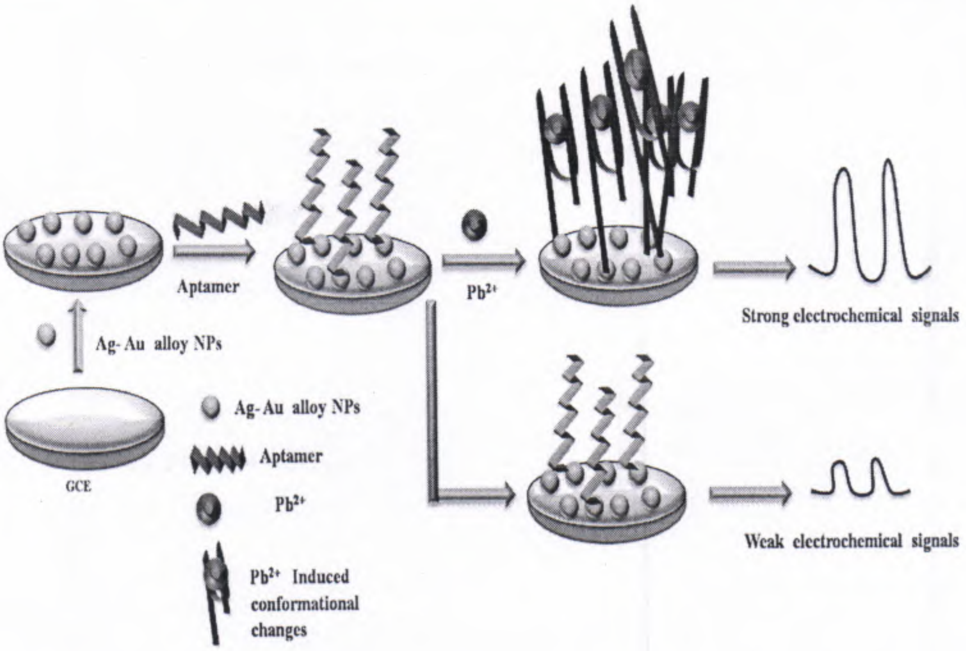

Fig. 3 Schematic illustration of the alloy (Ag–Au) NP–aptamer-modified GCE for Pb^{2+} detection

because it successfully minimized the double layer capacitive current [46].

The Ag–Au bimetallic NPs have an electronic polarity as a result of the 5s^1 electron of Ag and 6s^1 electron of Au. This polarity attracts the charged aptamer and promotes a loading platform for the attachment of the aptamer on the surface of the GCE. This process formed a large number of binding sites for metal ions for electrochemical detection. These binding sites help to increase the sensitivity and stability of the electrode and lower its LOD for metal ions. In the present case, Pb^{2+} bind negatively charged oxygen atoms of the phosphate backbone and with selected groups of nucleobases (e.g., N_7 and O_6 of guanine) to form $Pb(OH)^+$ [47].

In the aptamer, the electrostatic repulsion between the phosphate groups is responsible for its conformation. This repulsion is alleviated by binding of Pb^{2+}, which leads to a change of aptamer structure. The binding of Pb^{2+} with phosphate groups in the G-quadruplex aptamer showed different electrochemical responses due to the different labeling positions and G-quadruplex structures. G-quadruplex secondary structures (G_4) are formed in nucleic acids by sequences that are rich in guanine. They are helical structures containing guanine tetrads that can form from one, two or four strands.

3.3 Detection of Pb^{2+} by CV

The modified electrode was used to investigate redox processes, reaction intermediates, quantitative analyte determination, and the stability of reaction products. Three electrode system (i.e. modified GCE as a working electrode, pt as a counter electrode and Ag/AgCl as a reference electrode) have been used for detection of Pb^{2+} in water. The varying potential was applied to the modified GCE in both forward and reverse directions at 0.05 s.

In this process, the change in the measured current upon exposure of the electrode in different concentrations of Pb^{2+} has been monitored. The CV response of the electrode to different concentrations of Pb^{2+} in Milli Q water and real water samples is shown in Fig. 4a. The peak current increases gradually as the concentration of Pb^{2+} increases. The calibration plot in Fig. 4b revealed the good linear relationship between its electrochemical response (i.e., current) and Pb^{2+} concentrations ranging from 0.10 to 10 μg/L, with a coefficient of determination of 0.97. The LOD for Pb^{2+} was found to be 0.03×10^{-2} μg/L by CV. Good recoveries of Pb^{2+} from different water samples of between 100 and 105% were obtained (Table 1).

3.4 Detection of Pb^{2+} by DPV

In the DPV method, the potential is scanned with a series of pulses. The electrochemical current is estimated at two points for each pulse; one is before the pulse and the other is toward the end of a pulse. These two points are used to measure the decay of the charging current. The difference of potential between these two points was determined and plotted against the base potential for different concentrations of Pb^{2+} (Fig. 5a). The DPV calibration plot in Fig. 5b showed a linear relationship between charging current for different Pb^{2+} concentrations ranging from 0.10 to 10 μg/L with a coefficient of determination of 0.97. The scan rate

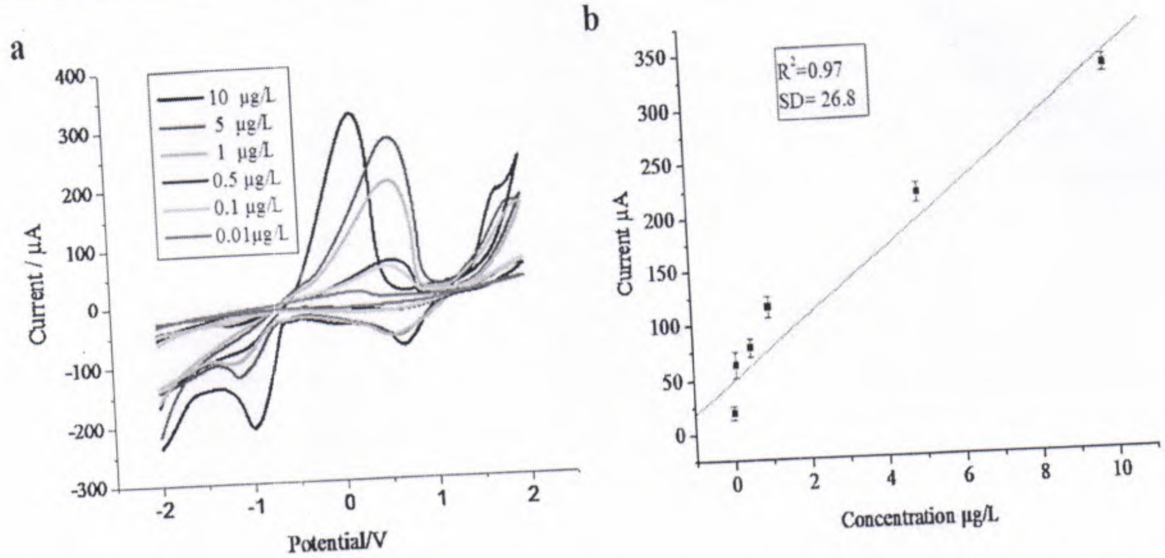

Fig. 4 Cyclic voltammetry measurements showing Pb^{2+} detection by the modified electrode: **a** Cyclic voltammetry measurements showing Pb^{2+} detection by the modified electrode and **b** calibration plot of cyclic voltammetry measurements showing Pb^{2+} detection by the modified electrode

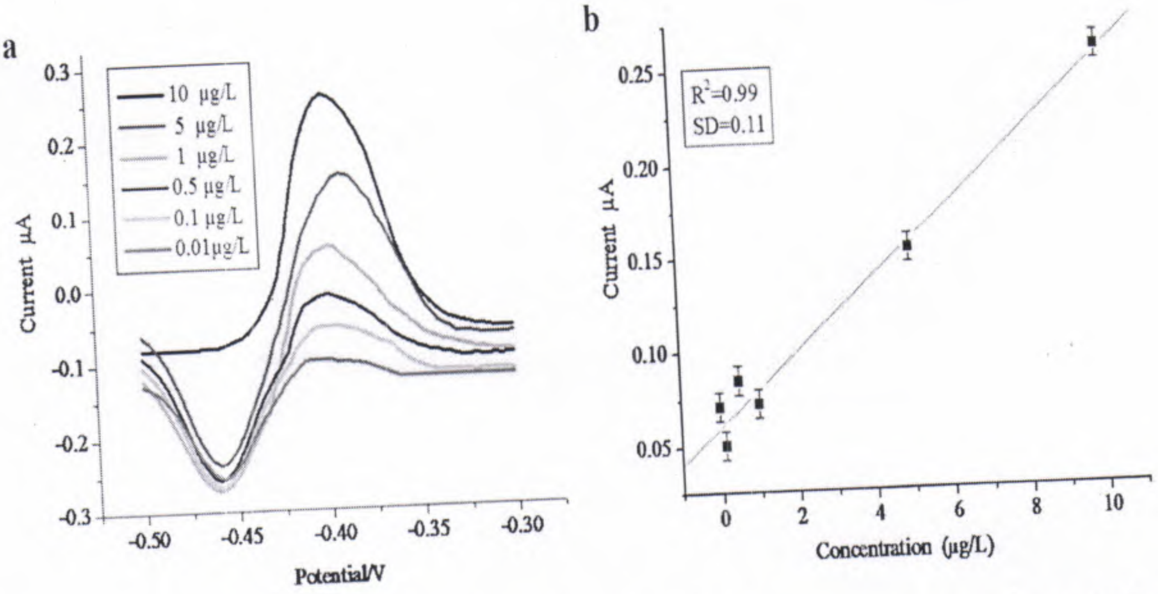

Fig. 5 DPV measurements showing Pb^{2+} detection by the modified electrode: **a** DPV measurements showing Pb^{2+} detection by the modified electrode and **b** calibration plot of DPV measurements showing Pb^{2+} detection by the modified electrode

was 50 mVs. All experiments were carried out at 25 °C. This result shows that the charging current is functions of Pb^{2+} concentration and pulse potential. The LOD for Pb^{2+} for the modified electrode in DPV measurements calculated from the calibration plot in Fig. 5b was 0.03×10^{-2} µg/L. The recoveries for this method ranged from 92 to 106% (Table 1).

3.5 Detection of Pb^{2+} by EIS

EIS measurements provided the change in impedance of the modified electrode at different concentrations of Pb^{2+}. The semicircle part of the Cole–Cole plot in Fig. 6a shows the electron transfer resistance in the higher frequency region, whereas the linear region corresponds to that of the diffusion-limited process. The diameter of the semicircle part increased with Pb^{2+} concentration. This result indicates that the electron transfer resistance increased because Pb^{2+} hindered the access to the redox probe at the modified electrode surface, reflecting the change in the interfacial charge-transfer resistance (R_{ct}) of the aptamer-conjugated bimetallic Ag–Au NP-modified GCE. R_{ct} is an important parameter to achieve a low LOD for Pb^{2+}. The calibration plot obtained from the EIS data is presented in Fig. 6b. We have measure the height of high peak in Fig. 6a at the scan rate was 50 mV s. The calibration plot is a straight line that implies that the impedance increases with the concentration of Pb^{2+} in the water samples. A proportional relationship was achieved between R_{ct} and Pb^{2+} concentration in the range of 0.01–1 μg/L with a coefficient of determination of 0.97. The LOD was calculated to be 0.04 μg/L based on 3 s per slope, where S is the standard deviation of a blank sample measured ten times. The recoveries (Table 1) for real-life water samples ranged from 92 to 107%, indicating the suitability of the modified GCE for detection of Pb^{2+}.

3.6 Analytical parameters

Analytical parameters such as coefficient of determination, LOD, and LOQ were evaluated from calibration plot [48]. Linear calibration plots were obtained over the concentration range from 0.01 to 10 μg/L using ten standard solutions and three replicates per standard. The linearity of standard curves obtained for CV, DPV, and EIS

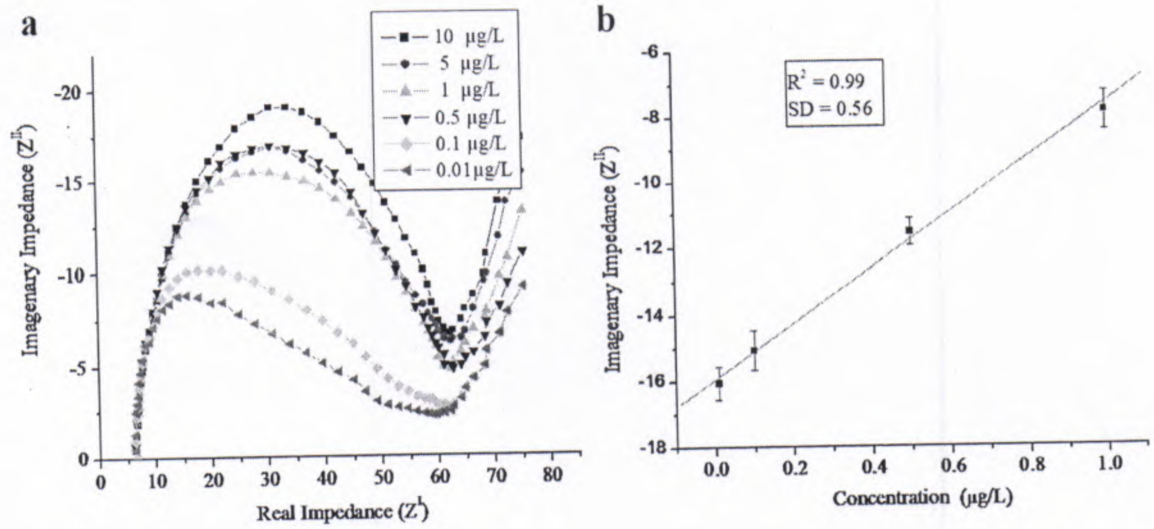

Fig. 6 **a** Electrochemical impedance spectroscopy (EIS) measurements showing Pb^{2+} detection by the modified electrode and **b** calibration plot of EIS measurements showing Pb^{2+}detection by the modified electrode

Table 2 Analytical parameters using the peak area in pb^{2+}

Calibration plot and analytical parameters using the peak area in Pb^{2+}			
Using the peak area	Cyclic voltametry	DPV	EIS
coefficient of determination (r^2)	0.97	0.99	0.99
LOD (μg/L)	0.03×10^{-2}	0.03×10^{-2}	0.002×10^{-2}
LQD (μg/L)	0.09×10^{-2}	0.1×10^{-2}	0.006×10^{-2}

Table 3 Limits of detection (LOD) of different sensor systems for Pb^{2+}

S.N	Species	Detection method	LOD (μg/L)	Linear range (μg/L)	Refs
1	Pb(II)	Electrochemical	1.05	0–100	[45]
2	Pb(II)	Electro-chemiluminescence	0.011	0.25–1.0	[46]
3	Pb(II)	DLS detection	0.035	0.1–1.0	[47]
4	Pb(II)	Photoelectrochemical	0.1	0.5–20	[48]
5	Pb(II)	Photoelectrochemical	0.05	0.1–50	[49]
6	Pb(II)	Present work	0.03×10^{-2}	0.1–10	

measurements was confirmed by their high r^2 values, as shown in Table 2. This conversion is a purely statistical that allows for the direct comparison of the results with standard values. The units of a standard deviation are identical to the base units of the data from which the standard deviation was calculated. Table 3 lists the LODs of different sensor systems for Pb^{2+} and demonstrates competitive advantages of the proposed nanobiosensor as compared with the existing ones.

3.7 Selectivity and interference studies

The effects of interfering elements on Pb^{2+} detection by the modified GCE were evaluated. The response of the modified electrode was recorded in Pb^{2+} solutions containing other ions. In this experiment, Cd^{2+}, Cr^{3+}, Na^+, K^+, Ni^{2+}, Fe^{2+}, Fe^{3+}, Zn^{2+}, and Cu^{2+} were chosen as interfering ions to investigate the selectivity of the modified electrode. The results demonstrated that the intensities of signals from these interfering elements were very small compared with those for Pb^{2+}. However, Cd^{2+} interfered slightly with Pb^{2+} detection.

3.8 Reproducibility and storage stability

The reproducibility of the response of the modified GCE was evaluated by comparing the anodic behavior in CV, DPV and EIS. The current in DPV was 0.069 µA and the imaginary part of impedance in EIS was 8.78 for 0.01 µg/L Pb^{2+} solution under the optimized conditions. The relative standard deviation (RSD) calculated from the calibration plot drawn from the electrochemical techniques was around 0.98% for the modified electrode, revealing that the electrode possessed good reproducibility. The storage stability of the modified electrode was investigated by repeated DPV and EIS measurements of a solution containing Pb^{2+}. The electrode was stored at 4 °C and used for 20 days consecutively. DPV and EIS measurements were conducted under the same experimental conditions each day. The results displayed an RSD of 0.5%. Therefore, the modified GCE showed good storage stability and reproducibility.

4 DNA conformational changes improve the interaction between lead (Pb^{2+}) and aptamer

Pb^{2+} induced G-quadruplex (G4) complex have high sensitivity and selectivity (because of its smallest diameter of Pb^{2+} 130 pm) as compared with other heavy metal ions [49]. Pb^{2+} induced aptamer conformational changes from random coil to G-quadruplex (G4) with Ag–Au alloy nanoparticles. This means that structural changes of aptamer, when Pb^{2+} attached with it. Or coil structure attain the quadruplex structure with alloy nanoparticles after binding of Pb^{2+} ions. Pb^{2+} induced aptamer conformational changes from random coil to G-quadruplex (G4) with Ag-Au alloy nanoparticles.

On the surface of modified electrode aptamer was self assembled by hybridizing with the G- rich and forming aptamer double helix structure. The Pb^{2+}-induced G-rich DNA aptamer duplex is formed by addition of Pb^{2+}, which is unwinds and forms a stabilizing G-quadruplex. Overall, Ag-Au alloy and aptamer modified GC electrode offer good charge transport capacity and large surface area which make sensor highly unique and highly sensitive and selective.

5 Conclusions

An Ag-Au alloy NPs aptamer-modified GCE with good storage stability and reproducibility was developed and used for detection of Pb^{2+} in real water samples without effects from interfering metal ions. The modified electrode contained numerous binding sites for Pb^{2+} because of the bimetallic NPs conjugated with an aptamer on the GCE surface. The interaction between Pb^{2+} and aptamer confirm the formation of G quadruplex structures by enhancement of electrochemical signal with concentration of Pb^{2+}. Therefore, Pb^{2+} diffused around the aptamer because of the strong electrostatic interactions between these materials and bound to the phosphate backbone, which stabilized the aptamer. The use of an aptamer and bimetallic NPs markedly enhanced the sensitivity of the GCE to around ten times that of a bimetallic NP-modified GCE without aptamer. The modified GCE has potential to contribute to new sensing applications in the field of nanobiosensor research. The developed nanobiosensor is rapid among all the existing techniques, due to its ease of use, high sensitivity and responsiveness.

Acknowledgements This work was supported by the Department of Science and Technology (DST), Government of India, New Delhi under the DST-RSF joint project (i.e. project no. DST/INT/RUS/RSF/P-28/G). The Russian authors thank to financial support of Russian Science Foundation (project # 19-44-02020). We also thank Natasha Lundin, PhD, from Edanz Group (www.edanzediting.com/ac) for editing a draft of this manuscript.

Compliance with ethical standards

Conflict of interest The authors declare that they have no known competing financial interests or personal relationships that could have appeared to influence the work reported in this paper.

References

1. He ZL, Yang XE, Stoffella PJ (2005) Trace elements in agroecosystems and impacts on the environment. J Trace Elem Med Biol 19:125–140. https://doi.org/10.1016/j.jtemb.2005.02.010
2. Ogwok P, Bamuwamye M, Apili G, Hatoho JM (2014) Health risk posted by lead, copper and iron via consumption of organs meats in Kampala city (Uganda). J Environ Pollut Hum Health 2:69–73. https://doi.org/10.12691/jephh-2-3-3
3. Teresa AP, Santos R (2014) Sensor and biosensor based on magnetic nanoparticles. TrAC Trends Anal Chem 62:28–36. https://doi.org/10.1016/j.trac.2014.06.016
4. Xiaobo L, Dumitrescu E, Reescu S (2015) Electrochemical biosensors for real time monitoring of reactive oxygen and nitrogen species. ACS Symp Ser 1200(13):301–327. https://doi.org/10.1021/bk-2015-1200.ch013
5. Luo X, Morrin A, Killard AJ, Smyth MR, (2006) Application of nanoparticles in electrochemical sensors and biosensors. Electroanalysis 18:319–326. https://doi.org/10.1002/elan.200503415
6. Shevchenko GP, Zhuravkov VA, Shishko GV (2019) A one-pot synthesis of colloidal Ag–Au nanoparticles with controlled composition. SN Appl Sci 1:1192–1198. https://doi.org/10.1007/s42452-019-1143-7
7. Li W, Kuai W, Qin LQ, Geng B (2013) Ag-Au bimetallic nanostructures:co-reduction synthesis and their component-dependent performance for enzyme free H_2O_2 sensing. J Mater Chem A 1:7111–7117. https://doi.org/10.1039/C3TA00106G
8. Liu S, Zhang C, Yuan L, Bao J, Tu W, Han M, Dai Z (2013) Component controlled synthesis of small sized Pd-Ag bimetallic alloy nanocrystals and their application in a non enzymatic glucose biosensors. Part Syst Charact 30:549–556. https://doi.org/10.1002/ppsc.201200150
9. Yan J, Liu S, Zhang Z, He G, Zhou P, Liang H, Tian L, Zhou X, Jiang H (2013) Simultaneous electrochemical detection of ascorbic acid, dopamine and uric acid based on graphene anchored with Pd-Ptnanoparticles. Coll Surf B Biointerf 111(392):407. https://doi.org/10.1016/j.colsurfb.2013.06.030
10. Mingxian L, Fenglin T, Zhengli Y, Jing X, Xiupei Y (2019) Recent progress on Gold nanocluster based fluorescent probe for environmental analysis and biological sensing. J Anal Meth in Chem 2019:1–10. https://doi.org/10.1155/2019/1095148
11. Zhou Y, Tang L, Zeng G, Zhang C, Zhang Y, Xie X (2016) Current progress in biosensors for heavy metal ions based on DNAzymes/DNA molecules functionalized nanostructures: a review Sens Actuat B. Chemistry 223:280–294. https://doi.org/10.1016/j.snb.2015.09.090
12. Tabatabaei S (2011) Synthesis and Characterization of Two Component Alloy Nanoparticles. Doctoral Dissertation. Rice University Electronic Theses and Dissertations. https://scholarship.rice.edu/handle/1911/70466
13. Chavali SM,Nikolova PM (2019) Metal oxide nanoparticles and their applications in nanotechnology. SN Appl Sci 1:607–637. https://doi.org/10.1007/s42452-019-0592-3
14. Qiu G, Ng SP, Wu CML (2018) Bimetallic Au-Ag alloy nanoislands for highly sensitive localized surface plasmon resonance biosensing. Sens Actuat B Chem 265:459–467. https://doi.org/10.1016/j.snb.2018.03.066
15. Ilangovan R, Daniel D, Krastanov A, Zachariah C, Elizabeth R (2014) Enzyme based biosensors for heavy metal ion determination. Biotechnol Equip 20:184–189. https://doi.org/10.1080/13102818.2006.10817330
16. Bagal KD, Karve MS, Kakade B, Pillai VK (2008) Invertase inhibition based electrochemical sensor for the detection of heavy metal ions in aqueous system: application of ultra-microelectrode to enhance sucrose biosensor's sensitivity. Biosens Bioelectron 24:657–664. https://doi.org/10.1016/j.bios.2008.06.027
17. Berlina AN, Sharma AK, Zherdev AV, Gaur MS, Dzantievs BB (2015) Colorimetric determination of lead using gold nanoparticles. Anal Lett 48:766–782. https://doi.org/10.1080/00032719.2014.961641
18. Kang W, Pei X, Rusinek CA, Bange A, Haynes EN, Heinemanand WR, Papautsky I (2017) Determination of lead with a copper-based electrochemical sensor. Anal Chem 89:3345–3352. https://doi.org/10.1021/acs.analchem.6b03894
19. Geca I, Korolczuk M (2017) Anodic stripping voltammetry following double deposition and stripping steps: application of a new approach in the course of lead ion determination. Talanta 171:321–326. https://doi.org/10.1016/j.talanta.2017.05.008
20. Shen L, Chen Z, Li Y, He S, Xie S, Xu X, Liang Z, Meng X, Li Q, Zhu Z, Li M, XC L, Shao Y, (2008) Electrochemical DNAzyme sensor for Lead based on amplification of DNA-Au bio-bar codes. Anal Chem 80:6323–6328. https://doi.org/10.1021/ac800601y
21. Sun H, Li X, Li Y, Fanand L, Kraatz HB (2013) A novel colorimetric potassium sensor based on the substitution of lead from G-quadruplex. Analyst 138:856–862. https://doi.org/10.1039/C2AN36564B
22. Wang Z, Lee JH, Lu Y (2008) Label-free colorimetric detection of Lead ions with a nanomolar detection limit and tunable dynamic range by using gold nanoparticles and DNAzyme. Adv Mater 20:3263–3267. https://doi.org/10.1002/adma.200703181
23. Wang L, Wen Y, Li L, Yang X, Jia N, Li W, Liu G (2018) Sensitive and label-free electrochemical lead ion biosensor based on a DNAzyme triggered G-quadruplex/hemin conformation. Biosens Bioelectron 115:91–96. https://doi.org/10.1016/j.bios.2018.04.054
24. Xiao Y, Roweand A, Plaxco K (2007) Electrochemical detection of parts-per-billion lead via an electrode-bound DNAzyme assembly. J Am Chem Soc 129:262–263. https://doi.org/10.1021/ja067278x
25. Wang XY, Niu CG, Guo LJ, Hu LY, Wu SQ, Zeng GM, Li F (2017) A Fluorescence sensor for Lead (II) Ions determination based on label-free gold nanoparticles (Gnps)-Dnazyme using time-gated mode in aqueous solution. J Fluoresc 27:643–649. https://doi.org/10.1007/s10895-016-1993-y
26. Guo Y, Li J, Zhang X, Tang Y (2015) A sensitive biosensor with a DNAzyme for Lead(II) detection based on fluorescence turn-on. Analyst 140:4642–4647. https://doi.org/10.1039/C5AN00677E
27. Salehnia F, Hosseini M, Ganjali MR (2017) A fluorometric aptamer based assay for cytochrome C using fluorescent graphitic carbon nitride nanosheets. Microchim Acta 184:2130–2136. https://doi.org/10.1007/s00604-017-2130-6
28. Xiang Y, Tong A, Lu Y (2009) A basic site-containing DNAzyme and aptamer for label-free fluorescent detection of pb^{2+} and adenosine with high sensitivity, selectivity and tunable dynamic range. J Am Chem Soc 131:15352–15357. https://doi.org/10.1021/ja905854a
29. Zhou W, Runjhun S, Liu J (2017) Metal sensing by DNA. Chem Rev 117:8272–8325. https://doi.org/10.1021/acs.chemrev.7b00063
30. March G, Nguyen TD, Piro B (2015) Modified electrode used for electrochemical detection of metal ions in environmental analysis. Biosensors 5:241–275. https://doi.org/10.3390/bios5020241
31. Zhang B, Wei C (2018) Highly sensitive and selective detection of Pb^{2+} using a turn on fluorescent aptamer DNA silver nanoclusters. Sensors 15:125–130. https://doi.org/10.1016/j.talanta.2018.01.061
32. Khoshbin Z, Housaindokht MR, Izadyar M, Bozorgmehr MR, Verdian A (2019) The investigation of the G-quadruplux aptamer

selectivity to Pb^{2+} ion: a joint molecular dynamics simulation and density functional theory study. J Biomol Struct Dyn 18:1–17. https://doi.org/10.1080/07391102.2019.1664933

33. Rassaei L, Marken F, Sillanpaa M, Amiriand M, Cirtiu C (2011) Nanoparticles in electrochemical sensors for environmental monitoring. Trends Anal Chem 30:1704–1715. https://doi.org/10.1016/j.trac.2011.05.009
34. Oyama M (2010) Recent nanoarchitecture in metal nanoparticles-modified electrode for electroanalysis. Anal Sci 26:1–12. https://doi.org/10.2116/analsci.26.1
35. Aragayand G, Merkoci A (2012) Nanomaterials application in electrochemical detection of heavy metals. Electrochim Acta 84:49–61. https://doi.org/10.1016/j.electacta.2012.04.044
36. Khairy M, Choudry NA, Ouasti M, Kampouris DK, Kadaraand RO, Banks CE (2010) Gold nanoparticles ensembles allow mechanistic insights into electrochemical processes. Chem Phys Chem 11:875–879. https://doi.org/10.1002/cphc.200900825
37. Majid E, Hrapovic S, Liu Y, Keith B, Luong JH (2006) Electrochemical determination of arsenite using a gold nanoparticle modified glassy carbon electrode and flow analysis. Anal Chem 78:762–769. https://doi.org/10.1021/ac0513562
38. Lee GJ, Kim CK, Lee MK, Rhee CK (2010) Simultaneous voltammetric determination of Zn, Cd and Pb at bismuth nanopowder electrodes with various particle size distributions. Electroanal Int J Devot Fundam Pract Asp Electroanal 22:530–535. https://doi.org/10.1002/elan.200900356
39. Brown RS, Dewanand JC, Klug A (1985) Crysallographic and biochemical investigation of the lead(II) catalyzed hydrolysis of yeast phenylalanine IRNA. Biochemistry 24:4785–4801. https://doi.org/10.1021/bi00339a012
40. Liu ZG, Huang XL (2014) Voltammetric determination of inorganic arsenic. TrAC Trends Anal Chem 60:25–35. https://doi.org/10.1016/j.trac.2014.04.014
41. Maria A, Paquim C, Eritja R, Oliveira B (2018) Electrochemical and AFM characterization of G-quadruplex electrochemical biosensors and applications. J Nucl Acids 2018:1–20. https://doi.org/10.1155/2018/5307106
42. Janegitz BC, Silva TA, Wong A, Ribovski L, Vicentini FC, Taboada MDPS, Fihlo OF (2017) The application of graphene for in vitro and in vivo electrochemical biosensing. Biosens Bioelectron 89:224–233. https://doi.org/10.1016/j.bios.2016.03.026
43. Yang D, Liu X, Zhou Y, Luo L, Zhang Y, Huang A, Mao Q, Chen X, Tang L (2017) Aptamer based biosensors for detection of Lead(II) ion: a review. Anal Methods 9:1976–1990. https://doi.org/10.1039/C7AY00477J
44. Farzin L, Shamsipur M, Sheibani S (2017) A review: Aptamer-based analytical strategies using the nanomaterials for environmental and human monitoring of toxic heavy metals. Talanta 174:619–627. https://doi.org/10.1016/j.talanta.2017.06.066
45. Shen L, Chen Z, Li HY, He SL, Xie BS, Xu DX, Liang WZ, Meng X, Li Q, Zhu WZ, Li XM, Le CX, Shao HY (2008) Elochemical DNAzyme sensor for lead based on amplification of DNA-Au bio bar code. Anal Chem 80:6323–6328. https://doi.org/10.1021/ac800601y
46. Zhu X, Lin Z, Chen L, Qiu B, Chen G (2009) A sensitive and specific electrochemiluminescent sensor for lead based on DNAzyme. Chen NG Chem Commun 40:6050–6052. https://doi.org/10.1039/B911191C
47. Gutiérrez-Sama S, Bazin D, Robert M, Amiet F (2019) Experimental determination of limits of detection for volatile organic compounds inambient air measured by automatic gas chromatograph and comparison with reference methods. In: Brisson M (ed) Detection limits in air quality and environmental measurements. ASTM International, West Conshohocken, PA, pp 134–145. https://doi.org/10.1520/STP161820180076
48. Zhu C, Yang G, Li H, Du D, Lin Y (2015) Electrochemical sensors and biosensors based on nanomaterials and nanostructures. Anal Chem 87:230–249. https://doi.org/10.1021/ac5039863
49. Karlene FV, Jaime S, Valerie MO, Edwin QO, Beatriz A, David A, Castilla C, Jorge VA, Marvin BJ, Eduardo MRAJN (2018) Aptamer-based impedimetric assay of arsenite in water. Interf Prop Perform ACS Omega 3:1437–1444. https://doi.org/10.1021/acsomega.7b01710

Article

Colorimetric Technique for Antimony Detection Based on the Use of Gold Nanoparticles Conjugated with Poly-A Oligonucleotide

Anna N. Berlina[1], Nadezhda S. Komova[1], Anatoly V. Zherdev[1], Mulayam S. Gaur[2], Boris B. Dzantiev[1,]*

[1] A.N. Bach Institute of Biochemistry, Research Center of Biotechnology of the Russian Academy of Sciences, Leninsky prospect 33, Moscow 119071, Russia
[2] Department of Physics, Hindustan College of Science and Technology, Farah, Distt.: Mathura U.P., 281122, India
* Correspondence: dzantiev@inbi.ras.ru, boris.dzantiev@mail.ru. Tel.: +7-495-954-31-42

Abstract: A simple and rapid positive–negative colorimetric approach to determine the presence of antimony ions based on the use of gold nanoparticles conjugated with oligonucleotide (poly-A sequence) is developed. Colorimetric measurements reveal that the aggregates of modified gold nanoparticles were afforded after adding antimony ions, thus changing the solution color from pink to blue. The results of aptamer's interaction on the gold nanoparticle surface with target analyte can be detected either by photometry or by the naked eye. The realized assay provides rapid (2 min), sensitive (detection limit 10 ng/mL), specific, and precise (variation coefficient less than 3.8%) detection of antimony (III) in drinking water.

Keywords: heavy metal analyses; gold nanoparticles; oligonucleotide; antimony; color change.

Graphical abstract

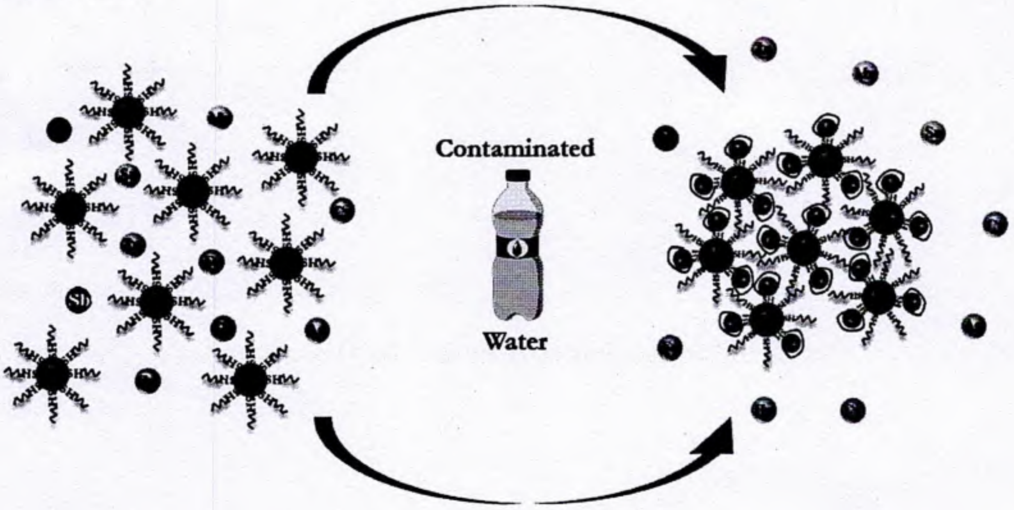

---

1. Introduction

Heavy metals are a class of highly toxic pollutants that can affect human health and the environment. Antimony pollution is of increasing interest because of its wide use in various industries including semiconducting [1]. Normally, antimony occurs in different forms in environmental water as a result of the oxidation of sulfide minerals and dissolution by water [2]. Its biological function, permissible levels, and mechanisms of interaction with biological materials remain poorly understood. To answer these questions, Filella et al. showed its binding by iron oxide phases [3]. In this case, compounds of antimony have a valency of 5. Due to rock disruptions and increased consumption by industry, antimony can be easily emitted into the environment [4]. Antimony basically occurs as Sb_2S_3 and Sb_2O_3 compounds [3]. Sb^{3+} is more toxic than Sb^{5+}, and Sb can form bonds with methylated and other organic compounds [5].

The importance of antimony detection is confirmed by the fact that the U.S. Environmental Protection Agency (EPA) regards it a priority pollutant and the Council of the European Communities [6] established the maximum permissible concentration of antimony in waters at 0.01 mg/L. However, the task of widespread monitoring of antimony is not yet solved. High-performance liquid chromatography [7], electrothermal atomic absorption spectrometry [8-10], atomic fluorescence spectroscopy [8], anodic stripping voltammetry [11,12], and multi-syringe flow injection analysis with hydride generation-atomic fluorescence detection [13] are currently the main methods for Sb3+ detection. However, the listed approaches require expensive equipment and high qualification of workers, and can be implemented only in limited quantity of laboratories.

Currently, a range of easy and cheap colorimetric techniques has been proposed to determine the presence of antimony [7,14-17]. The first technique was based on antimony hydride generation and its detection by UV-spectrophotometry [7]. Various indicator dyes, such as pyrogallol red [15], pyridine-2,6-dicarboxylic acid [18], brilliant green, malachite green and crystal violet [16, 19], and bromopyrogallol red [16], are traditionally used for these assays. These dyes are used due to their property of form colored complexes with target antimony ions [15,] with followed assessment of absorbance. The developed colorimetric techniques are based on complexation of antimony with organic molecules allowing the colored product to be detected spectrophotometrically.

Alternatively, the colorimetric approaches based on modified gold nanoparticles (GNPs) are widely applied due to their unique optical properties [20]. Aggregation of GNPs modified with receptor molecules after the addition of metal ions can change the original color of GNPs from red to blue [21-23]. However, selective induction of the aggregation should be based on specific recognition of the target metal ion. Increasing the selectivity of this method can be achieved by modifying the GNPs' surface using an aptamer poly-A oligonucleotide (PAO). Aptamers are oligonucleotide receptors that can react with the target molecule with high affinity and selectivity. A number of aptamers have been used to detect heavy metal ions [24], such as Hg^{2+} [25], Pb^{2+} [26], Cd^{2+} [27], Ag^{+} [28], and As^{3+} [29]. The majority of these solutions are based on a heterogeneous interaction on solid surfaces and therefore require additional equipment to detect induced changes [30]. Carrying out the reaction in a homogeneous medium with visually observed changes is an undoubted advantage. Aggregation of aptamer-modified GNPs after adding target analyte allowed rapid color change. To the best of our knowledge, there has been no research on aptamer application for Sb^{3+} detection. The study presents the first homogeneous colorimetric Sb^{3+} н assay based on aptamer-modified GNPs.

2. Materials and Methods

2.1. Chemicals

The aqueous solutions of Sb^{3+}, Zn^{2+}, Fe^{3+}, Cu^{2+}, Ag^{+}, and Sn^{4+} were obtained from LLC "Center of standardization of samples and high-purity substances" (2K-1, St. Petersburg, Russia) and used as stock solutions. Gold chloride was supplied by Fluka (St. Louis, MO, USA). Sodium citrate, tris(hydroxymethyl)aminomethane (Tris) and bovine serum albumin were purchased from Sigma-Aldrich (St. Louis, MO, USA). The (SH-C_6)AA-AAA-AAA-AA oligonucleotide was synthesized by Syntol (Moscow, Russia). Milli-Q water filtered with the use of a Millipore machine (Millipore, Bedford, MA; 18.5 MΩ · cm at 22 °C) and applied to prepare all the solutions in this study.

2.2. Instruments and Measurements

The shaker Intelli-Mixer (ELMI, Riga, Latvia) was used for conjugate synthesis. Absorption spectra of GNPs and their conjugates with PAO were measured by Biochrom Libra S80 spectrophotometer (Biochrom, Cambridge, UK). The morphology of GNPs was characterized by transmission electron microscopy (TEM) using microscope model JEM CX-100 (Jeol, Japan). Dynamic light scattering (DLS) measurements were implemented using a Malvern Zetasizer Nano (Malvern, UK).

2.3. Preparation of Gold Nanoparticles

The 30mn spherical GNPs were synthesized by citrate reduction of HAuCl$_4$ solution based on [31] with modifications. A quantity of 1.5 mL of 1% sodium citrate was rapidly added to 97.5 mL of boiling deionized water containing 0.2 mL of 5% HAuCl$_4$ solution and kept boiling for 25 min. Then, the mixture was cooled to room temperature and stored at 4–6 °C in liquid form. The concentration of synthesized GNPs was 1,66169E^{+11} particles in 1 mL of sol.

2.4. Preparation of poly-A Oligonucleotide Immobilized GNPs

Although freshly prepared gold nanoparticles can be stored at least 3 months without loss of stability, it is preferable to conjugate them with proteins or oligonucleotide sequences within two weeks of the synthesis. The conjugation technique was based on [32] with modifications. The pH of the obtained GNPs was adjusted to 8.5 using 1 M NaOH. Then, 30 µl of PAO solution (with the initial concentration of 100 µM) was added to 1 mL of GNPs. After 10 hours incubation at room temperature (RT) under stirring with the Intelli-Mixer, 30 µl of 100 mM phosphate buffer (pH 7.5) containing 700 mM NaCl was added drop-by-drop and left stirring for 24 h under the same conditions. Then, 10 µl of 10% BSA (water solution) was added to stabilize the conjugate and left for 1 hour at RT. The obtained GNPs–PAO conjugate was purified from unreacted oligonucleotides by 3-fold centrifugation at 9500 g and +4 °C for 15 min. The supernatant contained an excess amount of oligonucleotide, stabilizing protein was removed, and the resulting pellet was re-dispersed in 25 mM Tris-HCl buffer (pH 7.8) with 300 mM NaCl and stored at +4 °C in liquid form. Conjugates are stable 1 year after the synthesis.

2.5. Characterization of Native Gold Nanoparticles and poly-A Oligonucleotide Immobilized GNPs

The characterization of native and modified gold nanoparticles was provided by TEM and DLS. Native and conjugated nanoparticles suspensions were applied to 300-mesh grids (Pelco International, Redding, CA, USA) coated with a support film of polyvinyl formal deposited from chloroform. A JEM CX-100 electron microscope (JEOL, Tokyo, Japan) operating at 80 kV was used to obtain the microphotographs. The digital images were analyzed using Image Tool software (University of Texas Health Science Center, San Antonio, TX, USA). To analyze nanoparticles, 7 µL of suspension with optical density 1.0 was dropped on the grid surface.

Dynamic light scattering of gold nanoparticles–aptamer conjugate and freshly synthesized gold nanoparticles was provided using a Malvern Zetasizer Nano (Malvern, UK). Statistical data processing was performed using the software Malvern software version 7.11 (Malvern, UK). Size determination of native particles and conjugates was performed in the range from 0.3 nm to 10 µm using NIBS technology. For this purpose, 200 µL Milli-Q water was mixed with 10 µL of native/conjugated gold nanoparticles and transferred to the tube for DLS technique. GNP–PAOs and GNPs were analyzed in a mixture of water containing antimony in the same way.

2.6. Colorimetric Assay of Antimony

The detection of Sb^{3+} was performed at RT. Various concentrations (0.5–1000 ng/mL) of Sb^{3+} were prepared using serial dilution of the stock solution. A quantity of 2.5 µl of GNP–PAO solution was added to 50 µl of the Sb^{3+} solutions. The color change and the absorbance at 620 nm were measured immediately and the result obtained after 2 min (due to the speed of scanning).

To determine the assay's selectivity, it was applied to solutions of other ions, including alkali (Na^{+}, K^{+}, Li^{+}, and Cs^{+}), earth alkali (Mg^{2+}, Ca^{2+}, Sr^{2+}, and Ba^{2+}), transition (Mo^{2+}, Mn^{2+}, Fe^{3+}, Co^{2+}, Ag^{+}, Cd^{2+}, Cu^{2+}, Zn^{2+}, Hg^{2+}, Ni^{2+}, and Cr^{3+}), and post-transition (Al^{3+}, Sn^{4+}, and Pb^{2+}) metals; metalloids (As^{3+} and Sb^{3+}); and lanthanides (La^{3+}). Some anions were also tested as they are often present in environmental and mineral waters (Cl^{-}, NO$_3^{-}$, and SO$_4^{2-}$).

The tested drinking water samples were purchased from the local market and analyzed in the same way. These samples were spiked with antimony (III) stock solution to make positive samples for analysis with known ion concentrations.

3. Results and Discussion

3.1. Principle of Antimony Detection

To determine the presence of Sb^{3+} ions, the thiolated PAO was conjugated with GNPs via the strong Au-S bond. In the absence of Sb^{3+} ions, the PAO-modified GNPs dispersed well in the solution due to their stability. Some authors suppose that the aptamers stabilizing GNPs are in the coil state before meeting a target [33]. When added Sb^{3+} binds specifically with the aptamer, the PAO–GNP switches from a dispersed state to an aggregated state with a substantial change in the absorption spectra (Figure 1).

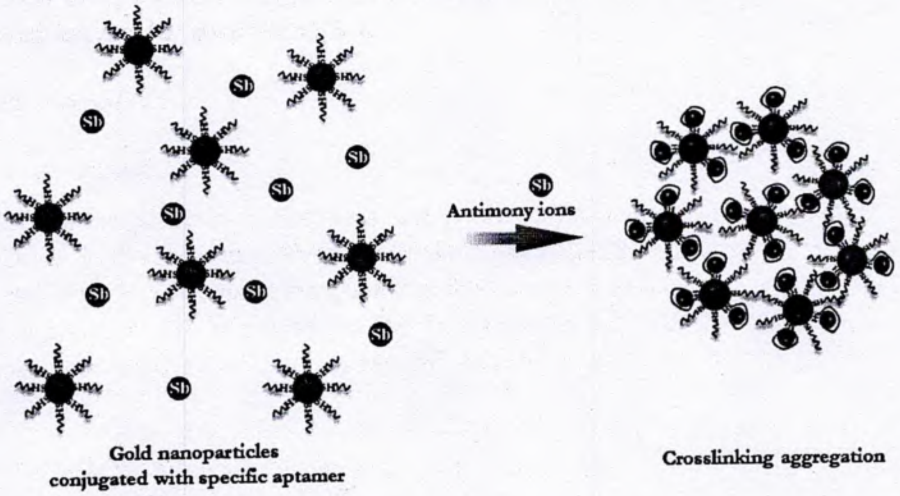

Figure 1. Principle of colorimetric determination of Sb^{3+} based on aggregation of modified gold nanoparticles (GNPs).

The poly-A sequence was used because of its particular reaction with ions as revealed in preliminary results. The interactions of poly-A oligonucleotide with a variety of ions (Hg^{2+}, Pb^{2+}, As^{3+}, Sr^{+}, Cd^{2+}, Ba^{2+}, Co^{2+}, and Mo^{2+}) as standard solutions and salts $MgSO_4$, NH_4VO_3, CsCl, Li_2SO_4, Na_3VO_4, $CrCl_3$, $Bi(OH)_2NO_3$, Na_2WO_4, $(CH_3COO)_2Ni$, $CaCl_2$, and $La(NO_3)_3$ of chemical purity dissolved in 0.1 M HNO_3 were tested. The technique used for choosing a target for selective analysis is described in Materials and Methods. GNPs, modified with poly-A DNA, were mixed with solutions of the ions of interest and changes in optical density were measured. Observed color changes indicated the sensitivity of the chosen oligonucleotide to the detected ions. The experiments revealed a high specificity with respect to Sb^{3+} at a low concentration (10 ng/mL). The simple and quick interaction achieved with the use of GNPs modified with PAO also provided optimal sensitivity in ion determination. A complete list of ion interactions with the oligonucleotide sequence is presented below in Section 3.4.

3.2. Characterization of PAO–GNPs Conjugate

Conjugation of GNPs was provided with the use of 3 μM of PAO. This concentration was chosen in accordance with our previous study [21] to stabilize GNPs. The prepared native and PAO-modified GNPs were characterized by absorbance spectroscopy, and TEM (Figure 2). Maximal absorption for native GNPs was at 525 nm, which corresponds to the GNPs at around 30 nm in diameter [34]. With the abovementioned techniques, we estimated that the average diameter was 27.3 ± 5.7 nm, confirmed by TEM. For this analysis, 127 particles were counted. The same value for GNP–PAOs was 29.7 ± 1.6 nm (TEM). The difference between the average sizes determined by these techniques could be explained by the drying of the oligonucleotide hydrophilic layer on GNP–PAOs allocated to the mesh grid before TEM. Michen et al. [35] studied similar effects when preparing GNPs stabilized with bovine serum albumin. In our research, oligonucleotides of small size (around 5 kDa) were used to modify GNPs, whereby a hydrophilic layer formed due to the presence of hydrophilic groups of adenine. Moreover, GNPs and PAO were conjugated in buffer with high ionic strength, which caused linear conformation of the oligonucleotide and necessary stabilization of the GNPs [36]. According to the modeling and experimental work of Michen et al. [35], the difference in the size of the modified nanoparticles is due to differences in the environment when analyzing dissolved (DLS) and dried (TEM) preparations.

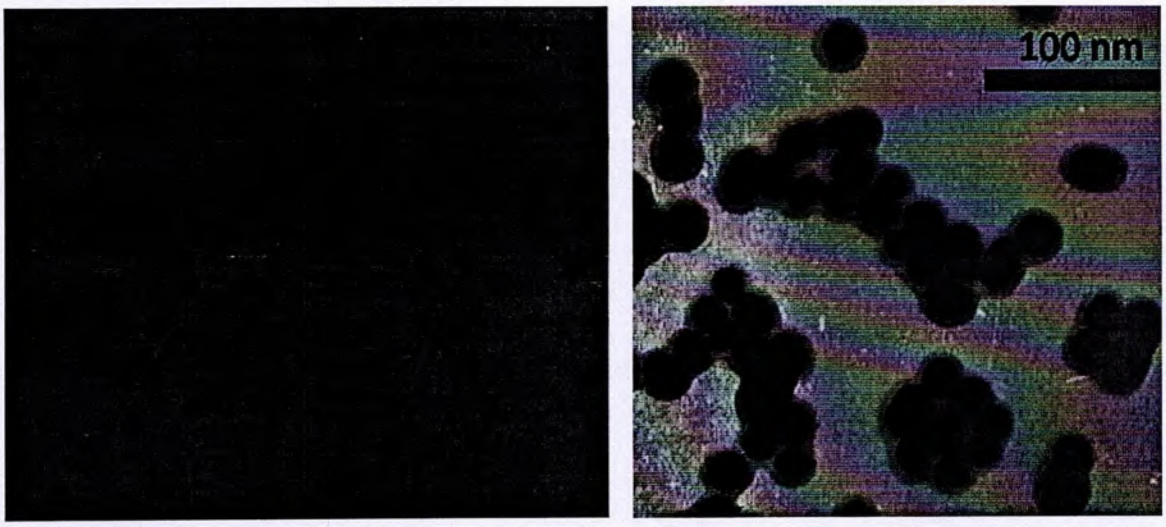

(a) (b)

Figure 2. Transmission electron microscopy (TEM) images of unmodified GNPs (a) and PAO-modified GNPs (b).

Characterization of gold nanoparticles modified with PAO, as well as native GNPs, was provided by DLS technique. To show the impact of the oligonucleotide sequence, nanoparticles were added to the water solution with known concentration of antimony (III), and all the samples were then measured in three replicates. Unmodified GNPs showed no sufficient increase in size before (28.8 ± 5.0 nm) and after (38.6 ± 8.2 nm) addition of antimony ions (Figure 3). This indicates that in the absence of surface modification, interaction did not take place. In contrary to this result, presence of the oligonucleotide sequence on the gold surface leads to the formation of complexes detected by this technique. Thus, modification of GNPs by PAO led to an increase in the diameter of a carrier to 57.8 ± 5.3 nm compared to freshly synthesized nanoparticles (28.8 ± 5.0 nm). Addition of antimony (III) to the reaction media led to an increase in the average diameter due to the formation of aggregates (128.9 ± 4.2 nm). This difference indirectly confirms the contribution of the oligonucleotide sequence to the interaction with antimony (III) ions, and demonstrates the possibility of applying this type of modification for the detection of target ions.

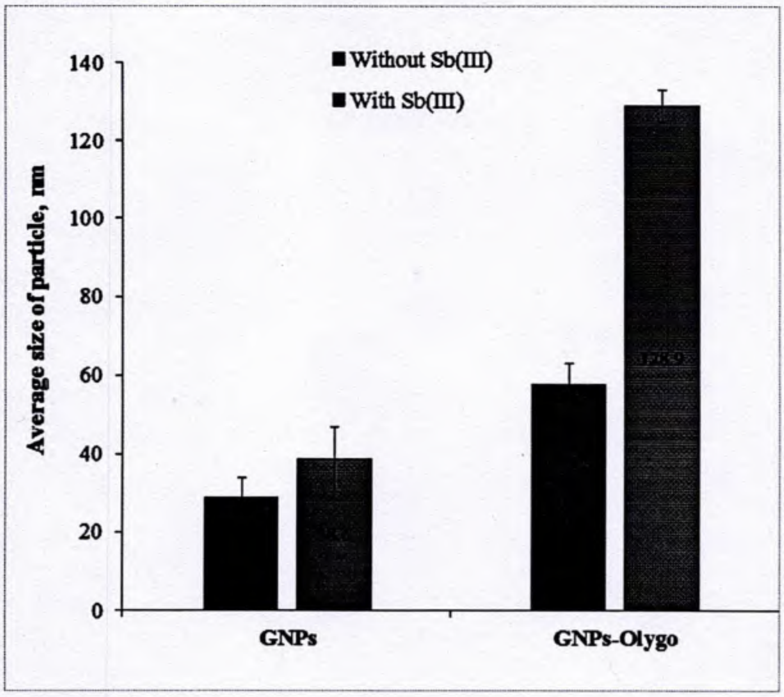

Figure 3. Results of dynamic light scattering (DLS) characterization of native and PAO-modified gold nanoparticles in absence and presence of antimony at 10 ng/mL in the solutions (n = 3).

3.3. Colorimetric Detection of Antimony (III)

A simple assay protocol was developed using the obtained GNP–PAO conjugate for colorimetric determination of Sb^{3+} in water. To appreciate the detectable minimal concentration of Sb^{3+}, different amounts of Sb^{3+} aqueous solution were added to the solution of PAO–GNPs. At low concentrations of Sb^{3+}, the color of the solution is pale red (due to the dilution of PAO–GNPs). As the concentration of Sb^{3+} increases, the additional amount of target ions results in an immediate color change to blue. We can observe the interaction results by the naked eye. In addition, the optical density at 620 nm was measured. This wavelength has been chosen in previous studies on colorimetry [21]. According to experimental data, when comparing the optical densities at 595 and 620 nm for the entire studied range of metal ions, it was revealed that the maximum signal (A = 0.8) for antimony ions was reached at 620 nm. The signal in the presence of other ions at 595 nm is minimized when the wavelength is changed to 620 nm. The chosen wavelength of 620 nm corresponds to the absorbance band of the formed gold aggregates. The obtained dependence of optical density intensity over the Sb^{3+} concentrations is given in Figure 4.

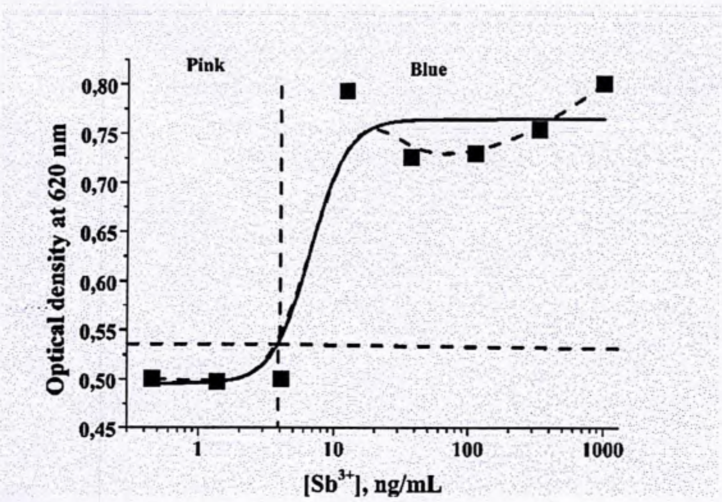

Figure 4. Calibration curve for Sb^{3+} detection (with the use of GNP–PAO conjugate). The value of 0.55 indicates the absorbance of gold conjugate at 620 nm in the absence of antimony. The points above and to the right of optical density 0.5 correspond to the blue color of the final reaction mixture, and the points below and left of this level correspond to pink ($y = 0.76 + (0.50-0.76)/(1 + (x/6.6)^{3.19})$, ($R^2 = 0.95$)). All experiments were undertaken in three replicates. Standard deviations from the mean were in the range 2.1%–5.8%.

The concentration of 10 ng/mL caused sharp structural changes with loss of gold conjugate stability in the solution. The interaction of aptamers with the target can be characterized by a gentle interaction curve if saturation occurs slowly. However, in some cases, the transition from a change in properties occurs abruptly, when saturation with the analyte leads to a loss of system stability. The same characterization of dependence was observed by Gordon et al. [37]. Figure 4 clearly demonstrates that sharp changes of optical density can be formally described by four-parametric equation. This fitting was done for estimation of analytical characteristics of the developed technique. However, taking into account the absence of the working range, this technique cannot be characterized by the "added-founded" method. Figure 5a shows the absorbance spectra of the reaction mixture containing PAO–GNPs in the presence of different concentrations of antimony (III). As can be observed, the spectrum varies depending on the concentration of the determined ions. When the Sb^{3+} concentration increased from 5.0 to 20 ng/mL, an additional band and shoulder between 600 and 730 nm at the absorbance spectrum occurred and optical density at 620 nm was increased, respectively. At the same time the position of the main absorbance peak for gold nano-dispersed particles remains the same with a slow shift to the right from 529 nm for the GNP–PAOs without antimony to 542 nm for the GNP–PAOs at high antimony concentration.

If the position of the absorption peak is unchanged, an additional shoulder appears on the right side of the spectrum (600–730 nm).

In a range of 0-3 ng/mL, the color solution was red. However, after 10 ng/mL Sb^{3+} was added, the solution turned purple due to Sb^{3+}-stimulated aggregation corresponding with absorbance and DLS data (Figure 5b). This figure indicates the similarity of the behavior of parameters. Thus, growth of optical density (Figure 5b, blue curve) correlated well with the nanoparticle size determined by DLS (Figure 5b, red curve). Therefore, the presence of Sb^{3+} at concentrations of 10 ng/mL or higher leads to aggregation of modified GNPs.

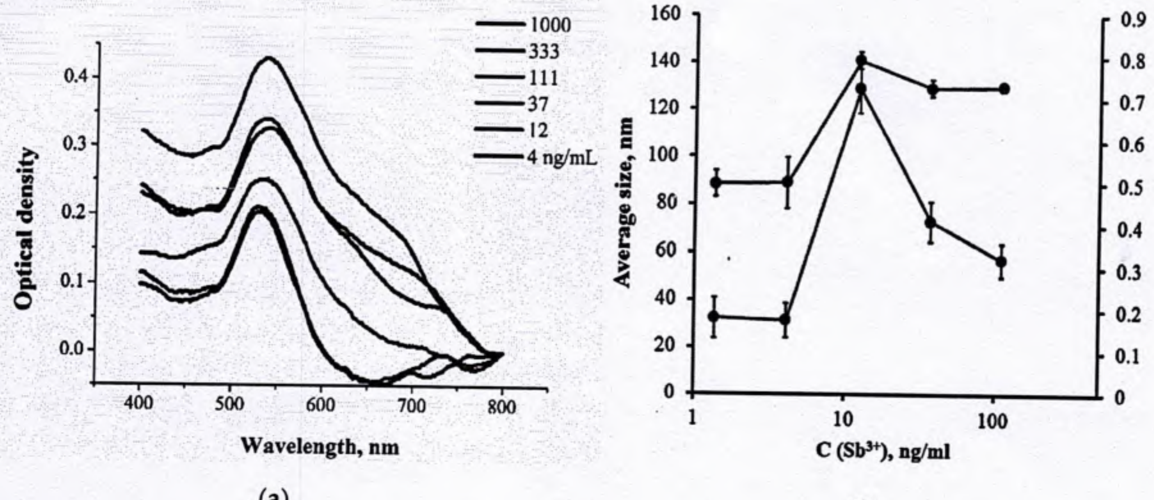

(a)

(b)

Figure 5. (**a**) The absorbance spectra of PAO-immobilized GNPs after different additions of Sb^{3+} (normalized spectra, after subtracting the corresponding background signal); (**b**) the value of optical density (lower) and average hydrodynamic diameter (upper) of conjugated GNPs. All experiments were undertaken in three replicates.

Characterization of PAO–GNPs by TEM additionally confirmed aggregate formation (Figure 6). The concentration of Sb^{3+} estimated as 10 ng/mL corresponds to the ion's permissible levels in drinking water [6].

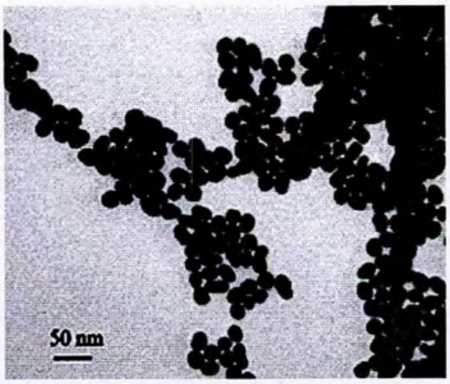

Figure 6. TEM image of PAO-modified GNPs after interaction with Sb^{3+} (10 ng/mL).

3.4. Selectivity Test

It is well known that the chemical composition of water in natural environments varies in accordance with the predominance of weathering, dissolution of atmospheric gases, and leaching of salts from ore [38]. Indeed, natural (e.g., river, lake, spring) waters have a different composition [39]. In the study we tried to cover the maximum diversity of ions by considering both widely presented environmental contaminants and agents influenced by such types of reaction [40] to make sure there is no influence of external ions.

Figure 7 demonstrates the difference in intensities of optical density at 620 nm. As seen, insignificant nonspecific changes were observed. Only Sn^{4+} and As^{3+} influence the determination of Sb^{3+}. However, the influence from As^{3+} is only observed when its concentration exceeds 1 mg/L, whereas an allowable concentration of As^{3+} in a drinking water is 0.01 mg/L [41]. As for the tin ion (Sn^{4+}), finding it in this form is almost impossible. Moreover, the content of tin ions is not standardized in drinking water. Despite this, we note this effect in this study.

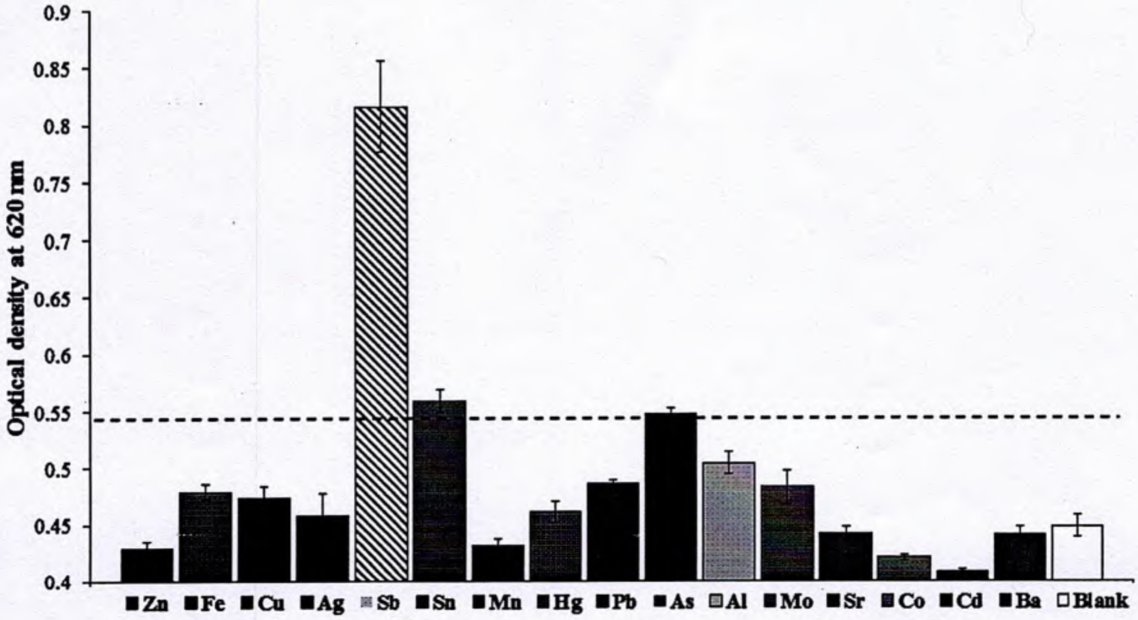

Figure 7. The values of A620 for GNP–PAOs after adding 50 ng/mL ions. The value of 0.55 indicates the absorbance of gold conjugate at 620 nm in the absence of antimony. The dashed line indicates the border between background staining (red, below this line) and reliable signal (optical density, blue,

above this line). Concentrations of the corresponding ions used: Sr^{2+}, Ba^{2+} - 10 mg/L; Mo^{2+}, Mn^{2+}, Zn^{2+}, Hg^{2+}, Co^{2+}, Ag^{+}, Cd^{2+}, Cr^{3+}, As^{3+}, Cu^{2+}, Pb^{2+}, and Fe^{3+}—1 mg/L. All experiments were undertaken in three replicates.

Alkali metal ions (Na^{+}, K^{+}, Li^{+}, and Cs^{+}) did not affect the assay results up to the concentrations of 22.5 mg/L, and the optical density value continued to correspond to the blank solution. Earth alkali metals (Mg^{2+}, Sr^{2+}, and Ba^{2+}) did not influence the conjugate PAO–GNPs' stability, at least at 10 mg/L and Ca^{2+} at 13.5 mg/L. Nickel ions (Ni^{2+}) at 4 mg/L did not cause the aggregation of the used PAO-modified GNPs. Such ions as Mo^{2+}, Mn^{2+}, Zn^{2+}, Hg^{2+}, Co^{2+}, Ag^{+}, Cd^{2+}, Cu^{2+}, and Fe^{3+} were taken at the concentration 1 mg/L, and aggregation did not occur. Chromium ions (Cr^{3+}) did not influence the stability of conjugates at 1 mg/L but influenced it at 1.8 mg/L. It should be noted that even the first concentration exceeded the maximum permissible level for drinking water. The chosen anions did not alter optical density even at 22.5 mg/L for chloride, 20.5 mg/L for sulfate, and 20.0 mg/L for nitrate ions. The low influence of other ions as interferences is explained by the selective interaction of the oligonucleotide sequence with Sb to induce aggregation.

3.5. *Real sample analysis.*

To further demonstrate the applicability of this method, commercial drinking water was applied as a diluter for stock solution of Sb^{3+}. The absence of Sb^{3+} in water samples is confirmed by a quality certificate from the manufacturer. Different concentrations of Sb^{3+} ions (0.5–1000 ng/mL) spiked the water sample with its following testing. The results presented in Figure 8 indicate this method is free from the matrix effect of drinking water. The relationship between optical density and Sb^{3+} concentration continues to be the same as for the calibration curve. Due to a sharp change in optical density at a concentration of 10 ng/mL, we can only identify positive or negative results. A blue color indicates a positive result, and red shows a negative result of Sb^{3+} assays.

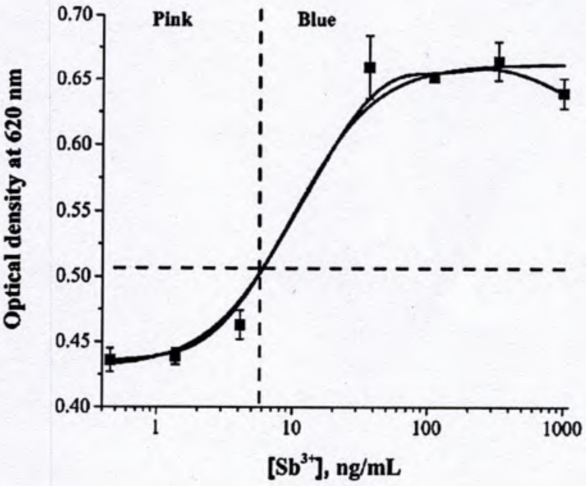

Figure 8. Dependence of optical intensity for detecting Sb^{3+} in drinking water (n = 3). The points above and to the right of optical density 0.5 correspond to the blue color of the final reaction mixture, and the points below and left this level correspond to pink ($y = 0.66 + (0.43-0.66)/(1 + (x/10.05)^{1.38})$, ($R^2$ = 0.98)). All experiments were undertaken in three replicates.

3.6. *Estimation of Analytical Characteristics*

The simple and rapid analytical technique developed was characterized with the following analytical parameters. The first calibration curve obtained when ions were diluted by the distilled water is shown in Figure 4. Despite the development of positive–negative analysis, this calibration curve can be conditionally described by the four-parameter sigmoidal equation ($y = A2 + (A1-A2)/(1 + (x/x0)^p)$) to demonstrate the nonlinear dependence. In accordance with this fitting, the detection limit was estimated as 3.2 ng/mL of antimony ions with a relatively narrow range of detectable concentrations from 4.2 ng/mL to 10.5 ng/mL. Such a narrow distribution is explained by the loss of stability of applied PAO–GNP conjugate. Color transition is observed by the naked eye when the concentration of antimony reached 10 ng/mL. Similar results were obtained when distilled water was changed to actual drinking water (Figure 8). The detection limit of antimony in the real sample was estimated as 2.0 ng/mL, with the range of determined concentrations from 3.7 ng/mL to 25 ng/mL. The average error of detection is from 0.3% to 3.8% in inter-assay. According to these data, our results are promising in analytical sensitivity (LOD = 10 ng/mL), duration of analysis (2 min), and reproducibility (error of determination is less than 3.8% in three replicates). The present study confirmed the applicability of developed colorimetric techniques to determine Sb^{3+} as compared to the known methods. Table 1 shows publications related to Sb^{3+} determination by the different analytical techniques.

Table 1. Described assays for the determination of antimony.

№	Heavy metal	Sensing unit	Detection method	LOD, Dynamic range	Probe	Ref.
			Sophisticated instrumental methods			
1	As^{3+}, Sb^{3+}	Gold film electrode	Anodic stripping voltammetry	As^{3+}: 1.12 ng/mL 5.5–0.5 μg/mL Sb^{3+}: 0.56 ng/mL 2.6–0.6 μg/mL	Copper	[42]
2	Sb^{3+}	Silver nanoparticle-modified screen-printed electrodes		0.083 ng/mL 0.012–0.11 μg/mL	Seawater samples and pharmaceutical preparations	[43]
3	Sb^{3+}	Gold nanoparticle-modified carbon screen-printed electrodes		0.115 ng/mL 0.012–0.11 μg/mL	Seawater samples, drug samples	[44]
4	Sb^{3+}	Mercury film screen-printed electrode		1.54 ng/mL 1.2–10.1 ng/mL	Pharmaceutical preparations and seawater	[12]
5	Sb^{3+}	Quercetin-5′-sulfonic acid	Adsorptive stripping voltammetric method	3.6 pg/mL (60s) and 1.6 pg/mL (180s) 1.0–5.0 ng/mL	Tap water and a commercial mineral water	[45]
6	As^{3+}, Sb^{3+}	AgNPs as a modifier	Electrothermal atomic absorption spectrometry	As^{3+}: 0.022 ng/mL Sb^{3+}: 0.046 ng/mL	Seawater and tap water	[9]
7	As^{3+}, Sb^{3+}	GNPs		As^{3+}: 2.3 ng/mL Sb^{3+}: 3.0 ng/mL	Seawater and tap water	[10]
8	Sb^{3+}	-	Trap-flame atomic absorption spectrometry	0.75 ng/mL 5.0–10.0 ng/mL	Tap and mineral water	[46]
9	Sb^{3+}, Sb^{5+}	EDTA and pyridine-2,6-dicarboxylic acid for chelating reaction with Sb	Anion exchange high-performance liquid chromatography	Sb^{5+}: 0.5 μg/mL Sb^{3+}: 0.8 μg/mL 5–200 μg/mL	Hot spring samples from New Zealand	[18]
10	Sb^{3+}	-	Electrothermal atomic absorption spectrometry	0.45 μg/mL 0-50 μg/mL	Soils and alfalfa samples	[8]

11	Sb^{3+}	-	Hydride generation coupled to atomic fluorescence spectroscopy	0.08 µg/mL 0.25–250 µg/mL	Soils and alfalfa samples	[8]
12	Sb^{3+}	-	Multi-syringe flow injection analysis with hydride generation-atomic fluorescence detection	0.08 ng/mL 0.2–5.6 ng/mL	Hard drinking water, filtered and diluted lake water	[13]
13	Sb^{3+}	BSA activated (TGA)-capped CdTe quantum dot nano-sensor	Fluorescence	0.0294 ng/mL 0.10–22.0 µg/mL	Artificial pond water, spring water, sewage	[47]
14	Sb^{3+}	-	Atmospheric pressure glow discharge atomic emission spectrometry	0.14 ng/mL 0.5–100 ng/mL	Groundwater samples	[48]
15	Sb^{3+}	Absorbance at 198 nm after hydride generation	UV-visible molecular absorption spectrophotometry with diode-array detection	3–440 µg/mL	PVC sample	[7]
16	Sb^{3+}, Bi^{3+}	Pyrogallol red	β-correction spectrophotometry	0.05–5.0 µg/mL 0.2–3.2 µg/mL	River, tap, and industrial wastewater	[14]
16	Sb^{3+}, Sb^{5+}	Pyrogallol (complexing agent)	UV–vis spectroscopy	Sb^{5+}: 1.26 µg/mL Sb^{3+}: 4.84 µg/mL	Commercial sample of Glucantime®	[15]
17	Sb^{3+}	Bromopyrogallol red	spectrophotometry	0.2 µg/mL 5.19±0.16–10.52±0.15 mg/mL	Samples of Glucantime	[16]
			Non-instrumental methods			
18	Sb^{3+}	Yellow potassium iodoantimonite $KSbI_4$	Colorimetry	0.6 µg/mL 0–5 µg/mL	Contaminated waters	[17]
19	Sb^{3+}	GNPs modified with PAO	Colorimetry	2.0 ng/mL (instrumental LOD) 10 ng/mL (visual LOD)	Drinking water	This study

3.7 The discussion of the interaction mechanism of antimony (III) with poly-A modified gold nanoparticles

The mechanism of interaction of metals and metalloids with DNA and proteins has become of interest to researchers since the successful use of compounds against tropical diseases began [49]. In particular, antimony preparations were used against leishmaniasis [50]. To understand the mechanism, previous investigations are helpful. In some investigations, antimony acts as a complexation agent when interacting with organic compounds, with the resulting salts as stibogluconate or meglumine antimonite due to their properties to provide hydroxyl groups [49]. In the investigation by Baiocco et al., authors [51] studied the mechanism of action of an anti-leishmaniosis drug with antimony compounds as the main components. Some molecules targeting antimony, trypanothione synthetase and trypanothione synthetase [52], are involved in this mechanism. Influencing the oxidative stress of bacteria also happens when antimony (III) blocks the reduction of the above-mentioned enzyme by NADPH and interacting with two catalytical cysteines (Cys52 and Cys57) in the active center [53].

Demicheli et al. [54] studied the interaction of antimony (V) with adenine nucleosides. Since the mechanism of interaction of antimony with targets in human organisms is not clear, the authors tried to understand how the interaction of this agent with nucleosides and nucleotides is possible. For its study, adenine was chosen as the nitrogen base. Authors used circular dichroism and NMR studies. Based on the obtained results, they concluded that Sb(V) seems to bind to the ribose moiety. This means that antimony can bind to ribose-containing compounds as ribonucleosides.

Investigation of antimony (V) compounds with DNA showed no interactions [55]. Contrary to these results, linking of antimony (III) to DNA structures was estimated by short column capillary electrophoresis-ICP-MS assay [55]. During this investigation, authors confirmed interaction of ribose moieties. Thus, having preliminary studies on this subject in hand, we assume that, most likely, trivalent antimony interacts with ribose nucleotide residues. In this case, the antimony (III) ion is involved in the complexation and convergence of several gold nanoparticles modified with poly-A sequences. Upon critical approach, the modified particles lose stability and forms an aggregate.

4. Conclusions

We propose a novel, simple, and selective colorimetric assay for Sb^{3+} ions using gold nanoparticles conjugated with poly-A oligonucleotide. This approach is based on an 3333 of modified gold nanoparticles after the addition of Sb^{3+} into the solution as seen by the naked eye. The color of the resulting mixture turns from pink to blue at 10 ng/mL, corresponding to the maximum permissible level of target analyte in drinking water. Advantages of this assay are its ease of detection, high sensitivity, and selectivity. The demonstrated approach and research results will allow the use of aggregation methods for the determination of metal ions and the development and study of the capabilities of this technique. The developed method is promising for determining the presence of Sb^{3+} in drinking water due to the identity of the detection limit of the developed method and the maximum permissible concentration of antimony (III) in drinking water.

Author Contributions: Conceptualization, A.N.B., M.S.G. and A.V.Z.; Methodology, A.N.B., M.S.G. and N.S.K.; Software, N.S.K.; Writing-Original Draft Preparation, A.N.B. and N.S.K.; Writing, Review, and Editing, A.V.Z., B.B.D., A.N.B.; Visualization, A.N.B. and N.S.K.; Supervision, A.N.B., A.V.Z. and B.B.D.

Funding: This work was financially supported by Russian Science Foundation (project # 19-44-02020) and Department of Science and Technology (project # DST/INT/RUS/RSF/P-28G). The authors are grateful to the researchers of the A.N. Bach Institute of Biochemistry: A.N. Antipov for help in the formation of ions collection; and S.M. Pridvorova and V.A. Grigoriev for transmission electron microscopy.

Conflicts of Interest: The authors declare no conflict of interest.

References

1. Sundar, S.; Chakravarty, J. Antimony toxicity. *Int. J. Environ. Res. Public Health* **2010**, *7*, 4267-4277.
2. Herath, I.; Vithanage, M., Bundschuh, J. Antimony as a global dilemma: Geochemistry, mobility, fate and transport. *Environ. Pollut.* **2017**, *223*, 545-559.
3. Filella, M. Antimony interactions with heterogeneous complexants in waters, sediments and soils: A review of data obtained in bulk samples. *Earth-Sci. Reviews* **2011**, *107*, 325-341.
4. He, M.; Wang, N.; Long, X.; Zhang, C.; Ma, C.; Zhong, Q.; Wang, A.; Wang, Y.; Pervaiz, A.; Shan, J. Antimony speciation in the environment: Recent advances in understanding the biogeochemical processes and ecological effects. *J.f Environ. Sci.* **2019**, *75*, 14-39.
5. Wilson, S.C.; Lockwood, P.V.; Ashley, P.M.; Tighe, M. The chemistry and behavior of antimony in the soil environment with comparisons to arsenic: A critical review. *Environ. Pollut.* **2010**, *158*, 1169-1181.

6. Council of the European Communities Council Directive Relating to the Quality of Water Intended for Human Consumption (80/778/EEC). *Official Journal L* **1980**.

7. Sanz, J.; Gallarta, F.; Galban, J.; Castillo, J.R. Antimony determination by hydride generation — UV-visible molecular absorption spectrophotometry with diode-array detection. *Fresenius' Zeitschrift für Analytische Chemie* **1988**, *330*, 510-515.

8. De Gregori, I.; Pinochet, H.; Fuentes, E.; Potin-Gautier, M. Determination of antimony in soils and vegetables by hydride generation atomic fluorescence spectrometry and electrothermal atomic absorption spectrometry. Optimization and comparison of both analytical techniques. *J. Anal. Atomic Spectrom.* **2001**, *16*, 172-178.

9. Gunduz, S.; Akman, S.; Baysal, A.; Kahraman, M. The use of silver nanoparticles as an effective modifier for the determination of arsenic and antimony by electrothermal atomic absorption spectrometry. *Spectrochim. Acta B* **2010**, *65*, 297-300.

10. Gunduz, S.; Akman, S.; Baysal, A.; Culha, M. The use of gold nanoparticles as an effective modifier for the determination of arsenic and antimony by electrothermal atomic absorption spectrometry. *Microchim. Acta* **2011**, *172*, 403-407.

11. Serrano, N.; Díaz-Cruz, J.M.; Ariño, C.; Esteban, M. Antimony-based electrodes for analytical determinations. *TrAC Trends in Anal. Chem.* **2016**, *77*, 203-213.

12. Renedo, O.D.; González, M.J.G.; Martínez, M.J.A. Determination of antimony (III) in real samples by anodic stripping voltammetry using a mercury film screen-printed electrode. *Sensors* **2009**, *9*, 219-231.

13. Semenova, N.V.; Leal, L.O.; Forteza, R.; Cerdà, V. Antimony determination and speciation by multisyringe flow injection analysis with hydride generation-atomic fluorescence detection. *Anal. Chim. Acta* **2005**, *530*, 113-120.

14. Abbaspour, A.; Baramakeh, L. Simultaneous determination of antimony and bismuth by beta-correction spectrophotometry and an artificial neural network algorithm. *Talanta* **2005**, *65*, 692-699.

15. González, M.J.G.; Renedo, O.D.; Martínez, M.J.A. Simultaneous determination of antimony(III) and antimony(V) by UV–vis spectroscopy and partial least squares method (PLS). *Talanta* **2005**, *68*, 67-71.

16. Rath, S.; Jardim, WF.; Dórea, J.G. A simple spectrophotometric procedure for the determination of antimony (III) and (V) in antileishmanial drugs. *Fresenius J. Anal. Chem.* **1997**, *358*, 548-550.

17. Tighe, M.; Edwards, M.M.; Cluley, G.; Lisle, L.; Wilson, S.C. Colorimetrically determining total antimony in contaminated waters and screening for antimony speciation. *J. Hydrol.* **2018**, *563*, 84-91.

18. Lintschinger, J.; Koch, I.; Serves, S.; Feldmann. J.; Cullen, W.R. Determination of antimony species with high-performance liquid chromatography using element specific detection. *Fresenius J. Anal. Chem.* **1997**, *359*, 484-491.

19. Fogg, A.G.; Burgess, C.; Burns, D.T. Use of basic dyes in the determination of anions, particularly as a means of determining antimony, thallium, and gallium. *Talanta* **1971**, *18*, 1175-1196.

20. Hu, M.; Chen, J.; Li, Z.Y.; Au, L.; Hartland, G.V.; Li, X.; Marquez, M.; Xia Y. Gold nanostructures: engineering their plasmonic properties for biomedical applications. *Chem. Soc. Reviews* **2006**, *35*, 1084-1094.

21. Berlina, A.N.; Zherdev, A.V.; Pridvorova, S.M.; Gaur, M.S.; Dzantiev, B.B. Rapid visual detection of lead and mercury via enhanced crosslinking aggregation of aptamer-labeled gold nanoparticles. *J. Nanosci. Nanotechnol.* **2019**, *19*, 5489-5495.

22. Du, J.; Zhu, B.; Chen, X. Urine for plasmonic nanoparticle-based colorimetric detection of mercury Ion. *Small* **2013**, *9*, 4104–4111.

23. Ullah, N.; Mansha, M.; Khan, I.; Qurashi, A. Nanomaterial-based optical chemical sensors for the detection of heavy metals in water: Recent advances and challenges. *TrAC Trends in Anal. Chem.* **2018**, *100*, 155-166.

24. Zhou, W.; Saran, R.; Liu, J. Metal sensing by DNA. *Chem. Reviews* **2017**, *117*, 8272-8325.

25. Chen, Z.; Wang, X.; Cheng, X.; Yang, W.; Wu, Y.; Fu, F. Specifically and visually detect methyl-mercury and ethyl-mercury in fish sample based on DNA-templated alloy Ag–Au nanoparticles. *Anal. Chem.* **2018**, *90*, 5489-5495.

26. Yang, D.; Liu, X.; Zhou, Y.; Luo, L.; Zhang, J.; Huang, A.; Mao, Q.; Chen, X,; Tang L. Aptamer-based biosensors for detection of lead(ii) ion: a review. *Anal. Meth.* **2017**, *9*, 1976-1990.

27. Gan, Y.; Liang, T.; Hu, Q.; Zhong, L.; Wang, X.; Wan, H.; Wang P. In-situ detection of cadmium with aptamer functionalized gold nanoparticles based on smartphone-based colorimetric system. *Talanta* **2019**, 120231.

28. Zhou, M.; Lin, T.; Gan, X. Colorimetric aggregation assay for silver(I) based on the use of aptamer modified gold nanoparticles and C-Ag(I)-C interaction. *Microchim. Acta* **2017**, *184*, 4671-4677.

29. Zhang, L.; Chen, X.R.; Wen, S.H; Liang, R.P.; Qiu. J.D. Optical sensors for inorganic arsenic detection. *TrAC Trends in Anal. Chem.* **2019**, *118*, 869-879.

30. Huang, J.; Su, X.; Li, Z. Metal ion detection using functional nucleic acids and nanomaterials. *Biosens. Bioelectron.* **2017**, *96*, 127–139.

31. Frens, G. Controlled nucleation for the regulation of the particle size in monodisperse gold suspensions. *Nature Phys. Sci* **1973**, *241*, 20-22.

32. Tan, D.; He, Y.; Xing, X.; Zhao, Y.; Tang, H.; Pang, D. Aptamer functionalized gold nanoparticles based fluorescent probe for the detection of mercury (II) ion in aqueous solution. *Talanta* **2013**, *113*, 26-30.

33. Zhu, Q.; Liu, G.; Kai, M. DNA aptamers in the diagnosis and treatment of human diseases. *Molecules (Basel)* **2015**, *20*, 20979-20997.

34. Kreibig, U.; Genzel, L. Optical absorption of small metallic particles. *Surface Sci.* **1985**, *156*, 678-700.

35. Michen, B.; Geers, C.; Vanhecke, D.; Endes, C.; Rothen-Rutishauser, B.; Balog, S.; Petri-Fink, A. Avoiding drying-artifacts in transmission electron microscopy: Characterizing the size and colloidal state of nanoparticles. *Sci. Reports* **2015**, *5*, 9793.

36. Mirkin, C.A.; Letsinger, R.L.; Mucic, R.C.; Storhoff, J.J. A DNA-based method for rationally assembling nanoparticles into macroscopic materials. *Nature* **1996**, *382*, 607-609.

37. Gordon, C.K.L.; Wu, D.; Feagin, T.A.; Pusuluri, A.; Csordas, A.T.; Eisenstein, M.; Hawker, C.J.; Niu, J.; Soh H.T. Click-PD: A quantitative method for base-modified aptamer discovery. *ACS Chem. Biol.* **2019**, doi: 10.1021/acschembio.9b00587.

38. Hounslow, A. *Water Quality Data: Analysis and Interpretation*, 1st ed.; Boca Raton: CRC Press, London New York, 2018; 416 p.

39. Hem, J.D. Study and Interpretation of the chemical characteristics of natural water, 3rd ed.; US Geological Survey: Charlottesville, U.S., 1985, 264 p.

40. Berlina, A.N.; Zherdev, A.V.; Dzantiev, B.B. Progress in rapid optical assays for heavy metal ions based on the use of nanoparticles and receptor molecules. *Microchim. Acta* **2019**, *186*, 172.

41. WHO World Health Organization (WHO); Guidelines for Drinking-Water Quality, 4th ed.; WHO Library Cataloguing-in-Publication Data: Switzerland. **2011**.

42. Hamilton, T.W.; Ellis, J.; Florence, T.M. Determination of arsenic and antimony in electrolytic copper by anodic stripping voltammetry at a gold film electrode. *Anal. Chim. Acta* **1980**, *119*, 225-233.

43. Renedo, O.D.; Martínez, M.J.A. A novel method for the anodic stripping voltammetry determination of Sb(III) using silver nanoparticle-modified screen-printed electrodes. *Electrochem. Commun.* **2007**, *9*, 820-826.

44. Renedo, O. D.; Martínez, M.J.A. Anodic stripping voltammetry of antimony using gold nanoparticle-modified carbon screen-printed electrodes. *Anal. Chim. Acta* **2007**, *589*, 255-260.

45. Rojas, C.; Arancibia, V.; Gómez, M.; Nagles, E. High sensitivity adsorptive stripping voltammetric method for antimony(III) determination in the presence of quercetin-5′-sulfonic acid. Substituent effect on sensitivity. *Sens. Actuators B* **2013**, *185*, 560-567.

46. Unutkan, T.; Koyuncu, İ.; Diker, C.; Fırat, M.; Büyükpınar, Ç.; Bakırdere, S. Accurate and sensitive analytical strategy for the determination of antimony: Hydrogen assisted T-shaped slotted quartz tube-atom trap-flame atomic absorption spectrometry. *Bull. Environ. Contam. Toxicol.* **2019**, *102*, 122-127.

47. Ge, S.; Zhang, C.; Zhu, Y.; Yu, J.; Zhang, S. BSA activated CdTe quantum dot nanosensor for antimony ion detection. *Analyst* **2010**, *135*, 111-115.

48. Zhu, Z.; Yang. C.; Yu, P.; Zheng, H.; Liu, Z.; Xing, Z.; Hu, Sh. Determination of antimony in water samples by hydride generation coupled with atmospheric pressure glow discharge atomic emission spectrometry. *J. Anal. Atomic Spectrom.* **2019**, *34*, 331-337.

49. Ong, Y.C.; Roy, S.; Andrews, P.C.; Gasser, G. Metal compounds against neglected tropical diseases. *Chem. Rev.* **2019**, *119*, 730-796.

50. Eddaikra, N.; Ait-Oudhia, K.; Kherrachi, I.; Oury, B.; Moulti-Mati, F.; Benikhlef, R.; Harrat, Z.; Sereno, D. Antimony susceptibility of Leishmania isolates collected over a 30-year period in Algeria. *PLoS Negl .Trop. Dis* .**2018**, *12*, e0006310.

51. Baiocco, P.; Colotti, G.; Franceschini, S.; Ilari, A. Molecular basis of antimony treatment in leishmaniasis. *J. Medic. Chem.* **2009**, *52*, 2603-2612.

52. Krauth-Siegel, R.L.; Comini, M.A. Redox control in trypanosomatids, parasitic protozoa with trypanothione-based thiol metabolism. *Biochim. Biophys. Acta – Gen. Subj.* **2008**, *1780*, 1236-1248.

53. Colotti, G.; Fiorillo, A.; Ilari, A. Metal-and metalloid-containing drugs for the treatment of trypanosomatid diseases. *Front. Biosci.* **2018**, *23*, 954-966.

54. Demicheli, C.; Frézard, F.; Lecouvey, M.; Garnier-Suillerot, A. Antimony(V) complex formation with adenine nucleosides in aqueous solution. *Biochim. Biophys. Acta – Gen. Subj.* **2002**, *1570*, 192-198.

55. Li, Y.; Liu, J.M.; Han, F.; Jiang, Y.; Yan, X.P. Probing interactions of antimony species with DNA by short column capillary electrophoresis coupled with inductively coupled plasma mass spectrometry. *J. Anal. Atomic Spectrom.* **2011**, *26*, 94-99.